THE LOSS IN SOLID POLES OF

SYNCHRONOUS MACHINES ON LOAD

by

VICTOR STUART RAMSDEN, B.E.(Elec.), M.Eng.Sc.

Submitted for the degree of Doctor of Philosophy

at

The University of Aston in Birmingham

February, 1972

SUMMARY

The loss in solid poles of synchronous machines on load may be caused by several travelling waves and the thesis is directed towards a discussion of the problems arising from the superposition of these waves and of the effect of the superposed main field, which is stationary relative to the poles.

The major part of the work is concerned with the effect of a superposed parallel steady field on the permeability and losses for an alternating field in mild steel. Experiments show that, for a given surface alternating field strength, the steady field decreases the loss, which may be accurately calculated by a linear theory if the steady field strength is greater than the alternating field strength. Otherwise a non-linear theory which allows for unsymmetrical hysteresis loops is required for strong alternating fields, and a limiting non-linear theory is developed, but not tested.

A consideration of the usual linear theory for the loss induced by a travelling wave shows that it may be written in terms of an eddy-current reaction parameter leading to simple normalised curves, and that the tangential field strength of significant travelling waves is likely to be fairly strong in typical large machines. The superposition of waves which induce different frequencies in the rotor may therefore cause an oscillation between linear and non-linear behaviour, with variations around the rotor periphery caused by interference between pairs of winding harmonics and by the variation of the steady main field. It is emphasised, however, that the main field is perpendicular to the travelling fields in a smooth rotor, and it is believed that its effect will only be significant in regions where it is very strong, where it will both reduce the permeability and make the behaviour more linear.

ACKNOWLEDGEMENTS

INDEX

LIST OF SYMBOLS

M.K.S.A. units are used

A	vector potential (Wb/m), cross-sectional area (m^2)
A_s	surface area
a	radius
B	flux density (T), total flux density which is stationary relative to the rotor (Ch. 2 and appendix 8.2), resultant flux density for perpendicular fields
$\triangle B$	total change of flux density
$B_\triangle$	$\triangle B/2$
$\hat{B}, \check{B}$	upper peak and lower peak of an incremental loop
B_b	biasing flux density $(\hat{B} + \check{B})/2$
B_m	peak of a normal hysteresis loop
B_s	saturation flux density (chs. 3 and 4), surface flux density (section 5.4)
B_o	saturation flux density (section 5.4)
b	lamination thickness (m)
C_m	ratio of field m.m.f. to armature m.m.f. (when this is in the d-axis) for the same fundamental flux density
D	stator bore (ch. 2), rotor diameter (ch. 6) (m)
d	depth of penetration $\sqrt{\rho/\omega\mu_o\mu}$ (m)
E	electric field strength (V/m)
e	non-dimensional electric field strength
E_f	voltage induced by the field (V)
F	m.m.f. (A)
F_{a1}	fundamental armature (stator) m.m.f.
F_f	field (rotor) m.m.f.
f	frequency (Hz)
f_1	fundamental frequency

G   amplifier gain

g   air gap   (m)

H   magnetic field strength (A/m), resultant field
           strength for perpendicular fields

$\triangle H$ total change of field strength

$H_\triangle$ $\triangle H/2$

$\hat{H}, \check{H}$ upper peak and lower peak of an incremental loop

H_b biasing field strength $(\hat{H} + \check{H})/2$

H_m peak of normal hysteresis loop

h $H_b/H_\triangle$

I   r.m.s. line current   (A)

I_A r.m.s. phase current   (A)

J   current density (A/m^2)

K   current loading (A/m)

K_H normalised tangential field strength (eqn. 6.44)

K_B normalised radial flux density (eqn. 6.48)

K_P normalised torque, or loss at constant velocity
           (eqn. 6.60)

k   integer indicating winding harmonic pair number

k_d distribution factor

k_p pitch factor

k_s slot-width factor

k_w total winding factor

L   self inductance, mean path length, pole length

M   mutual inductance, modulus of Bessel function
           of the first kind

m $\sqrt{\omega \mu_o \mu_\triangle /\rho} = 1/d$ (m^{-1})

N   turns in series per pole and phase

N_1 turns on primary coil

N_2 turns on secondary coil

P   power loss (W/m^2)

p   number of pole pairs, non-dimensional
           instantaneous loss (section 5.4)

Q	non-dimensional eddy-current reaction factor $1/\beta d\mu_r \tanh\beta g$
q	slots per pole and phase
R	winding resistance, Kuyper's normalised loss factor (eqn. 8.24)
R_L	load resistance
r	radial distance, series resistance
s	slot width
T	turns in series per phase
t	time (s)
u	coordinate of separating surface
v	velocity of wave relative to the rotor (m/s)
V	terminal voltage
W_h	hysteresis energy loss (J/m^3)
W_{hb}	hysteresis energy loss of incremental loop
X_d, X_q	direct and quadrature axis synchronous reactance
X_{ad}	direct axis magnetising reactance
x, y, z	space coordinates
Z	conductors in series per slot, wave impedance (real part)
Z_L	load impedance
α	hysteresis angle, pole arc
β	phase-change coefficient (rad/m)
β_1	fundamental phase-change coefficient
δ	depth of penetration $\sqrt{2\rho/\omega\mu_o\mu}$, $\sqrt{2\rho/\omega(B_o/H_\Delta)}$ (section 5.4) (m)
$\dot{\gamma}$	complex skin-effect factor (eqn. 6.19)
ε	fractional pitch = ratio of coil span to pole pitch
ϑ	surface power-factor angle
ϑ_1	electrical space angle relative to a fixed point on the stator ($\mathcal{L}$ of A-phase coils)

$\vartheta_2 = \vartheta_1 - \omega_1 t$ electrical space angle relative to the peak of the fundamental stator m.m.f.

ϑ_3 electrical space angle relative to a fixed point on the rotor (d-axis)

λ wavelength   (m)

λ_1 fundamental wavelength

λ_s slot pitch

μ relative d.c. permeability

μ_o magnetic constant   ($4\pi \times 10^{-7}$ H/m)

μ_n normal relative permeability

μ_Δ incremental relative permeability (with superposed parallel fields)

$\mu_\perp$ relative permeability with superposed perpendicular fields

μ_{rev} reversible relative permeability (the limit reached by μ_Δ for very small values of H_Δ)

μ_i initial relative permeability (reversible normal permeability)

$\dot{\mu}_e$ complex effective a.c. permeability (eqn. 3.13)

μ_r rotor relative permeability

μ_s stator relative permeability

ν rate of change of μ_n with H_m

ν_Δ rate of change of μ_Δ with H_Δ

ρ resistivity   (Ωm)

τ pole pitch   (m)

τ_1 fundamental pole pitch

ϕ flux (Wb), circumferential direction, flux per unit length (section 5.4), load power-factor angle

ϕ_n phase shift relative to the stator current of the n'th harmonic tangential surface field strength ($\angle \dot{H}_{xo}$)

ϕ_{dk} half the relative phase shift between the k'th pair of surface field harmonics

$90° + \psi$ electrical angle between the rotor d-axis and the peak of the fundamental armature m.m.f. (fig. 2.10)

ω frequency (rad/s)

ω_1 fundamental frequency

Subscripts

a   armature (stator), applied

av   time average (e.g. $H_{av} = \frac{1}{T}\int_0^T H \, dt$)

b   bias, the amplitude average of unsymmetrical variations (e.g. $H_b = (\hat{H} + \check{H})/2$)

e   eddy current

g   gap

h   hysteresis

l   longitudinal

m   maximum

n   harmonic space order, normal (permeability)

o   surface value (ch. 6)

r   rotor

s   stator, slot, surface

t   transverse

$6k\omega$ indicates resultant of a pair of winding harmonics inducing frequency of $6k\omega$

Superscripts

.   complex number

*   complex conjugate

^   upper peak value

v   lower peak value

1. INTRODUCTION

This thesis is concerned with the loss in solid poles of
synchronous machines caused by harmonics of the armature current field.
Many of the sections are also relevant to negative-sequence (asymmetrical
load) and slot-ripple pole-face loss, to machines with laminated poles,
to induction motors and to other electromagnetic devices. Modern large
2-pole turbo-generators are made with solid rotors for mechanical reasons,
and many other synchronous machines are built with solid poles for
electrical reasons; laminating the poles reduces the pole-face loss, but
also reduces desirable damping currents during transient behaviour or
asynchronous starting. Usually the armature m.m.f. harmonic loss is the
major pole-face loss in these machines.

The design of a machine often hinges on an estimation of the
full-load losses. Care must be taken to limit the temperature rise and
there is often a monetary penalty for machines designed with excessive
losses.[1] For large fully water-cooled generators the temperature rise
is no longer a limiting factor, but the machine size for a given output
depends on the loss weighting, and hence on the losses.[2] With a low loss
weighting, which could occur with a machine for a nuclear power station,
the length (and hence price) can be reduced until the present limit on
transient reactance X'_d is reached; but if expensive fuels are concerned,
giving a high loss weighting, the length must be increased (allowing
a reduction of stator current loading and hence load losses). A
comparison of the cost associated with the total losses and the cost
associated with the size (materials, transport, installation, etc.)
determines the final length. If desired, the air gap of a
turbo-generator can be chosen to give a minimum loss penalty,[3] as load
losses decrease with an increase of air gap, whilst the excitation loss
increases. An accurate estimation of load loss is therefore desirable.

Pole-face loss forms an important part of the load loss in solid-
rotor machines,[3] and the armature m.m.f. harmonic component of this

rose as machine ratings increased.   Tested values of turbo-generator negative-sequence resistance, a measure of fundamental-wavelength, double-frequency loss in the rotor, tripled from 2% to 6% as machine ratings increased from 60 MW to 300 MW during the period 1946 - 1964. Over the same period the average stator current loading also tripled.[1] In general, load losses are proportional to the square of the current loading, but pole-face loss also depends on the air gap, which increases with the current loading to limit the decrease of short circuit ratio, for steady-state stability. Because the wavelengths of the armature m.m.f. harmonics are less than the fundamental, the m.m.f.-harmonic loss has probably not risen as fast as the negative sequence resistance, or as the current loading. The increase of air gap effected an actual decrease in the slot ripple component of pole-face loss, by decreasing the ripple.

For turbo-generators, the average m.m.f.-harmonic pole-face loss is of the order of 10 - 25 kW/m^2, and 5% load unbalance causes an additional loss of the same order. Removing the heat generated in the rotor surface presents a problem for fully water -cooled machines, as the air in the air gap is not renewed.[2] (A uniformly distributed loss of the order of 50 kW/m^2 causes a 100°C temperature rise in a surface rotating at 200 m/s with forced air ventilation,[4] which is about the maximum tolerable mean rotor temperature.[2]) The problem is accentuated by the non-uniform distribution of m.m.f.-harmonic loss, which may cause high local heating in parts which are also highly stressed mechanically, such as the endbells. Recent calculations[5] showed that the m.m.f. harmonics can cause a peak loss of 754 kW/m^2 in that part of the endbell extending into the air gap region, where the gap between the endbell and the stator is much less than the normal gap between rotor and stator. Loss concentrations around rotor surface discontinuities, like bolt holes, are also a serious problem.

The pole-face loss problem is not confined to large machines. Losses in the rotor surface of small solid-rotor hysteresis motors

may limit their output power at high excitations.[6]

Work at the University of Aston in Birmingham on m.m.f. -
harmonic loss in solid-rotor synchronous machines was begun by
Adderley.[7] He isolated many problems which were not satisfactorily
accounted for in previous publications:-

1) Non-linear B/H curve for iron

2) Hysteresis

3) Presence of main field

4) Superposition of harmonics

5) Rotor position relative to armature m.m.f.

6) Rotor shape (e.g. slots, wedges, grooves, length,
    pole shape)

7) Air-gap curvature

8) Stator slots

9) Stator winding depth and position

Not all these problems are present in every machine. The first
three relate to magnetic rotors and are not a problem for non-magnetic
endbells; the questions of rotor position and shape are largely
irrelevant for hysteresis motors with smooth rotors; curvature is of
most importance for machines with a large air gap to diameter ratio,
such as turbo-generators.

The final four points concern the machine geometry and their
incomplete solution relates more to the complexity of the solution than
to a lack of understanding. Curvature and rotor shape were considered by
several authors,[3,8,9] but the effects on m.m.f.-harmonic loss of stator
slotting and the actual shape and position of the stator winding were
largely neglected (stator slots were usually accounted for by increasing
the air gap by Carter's factor, based on a uniform, homopolar m.m.f.).
Solutions to these four problems are not given in this thesis, although
a thorough understanding of the existing theory for simple geometries,
which is discussed here, helps in finding solutions, or at least may
suggest appropriate approximations.

There has been some lack of understanding of certain features of the first five points, and a discussion of these features forms the major part of this thesis. Superposition of harmonics is always a problem in a non-linear medium, and there is an additional complication for pole-face loss in synchronous machines as several space harmonics of the air-gap field induce currents of the same frequency in the rotor, resulting in regions of maximum and minimum loss. The amplitude and position of the maximum loss is of importance for all types of rotor, and the average loss for rotors with salient poles or slots depends on the rotor position relative to the armature field. Some authors considered the interaction of the harmonics and as many other neglected it. Adderley discussed the question in some detail and showed that the phase of the harmonics had been inadequately considered. The air-gap field in normal machines is discussed in chapter 2 and the rotor position is also considered.

The present theory for the calculation of pole-face loss due to eddy currents assumes a linear B/H curve (constant permeability), and some authors included a method of using what they thought was an appropriate value of permeability. It is known that a superposed steady field may change the B/H curve and hysteresis loss, throwing doubt on the choice of permeability or B/H curve. A few authors[132-136] considered the presence of the main field – which is stationary relative to the rotor – in the calculation of slot-ripple loss, but although they did not say so, they used results for a small a.c. field parallel to a steady field, when in fact the linear theory showed the harmonic fields in the rotor to be large and perpendicular to the main field. A survey of papers on superposed fields, given in chapter 3, showed that further experiments were needed; there had been few experiments on permeability, hysteresis loss or eddy current loss using solid iron, those experiments which had been conducted on solid or laminated iron had not covered the full range of the variables, and there had been no comparison of calculated and measured eddy current

losses. Results for permeability and hysteresis loss in solid iron
with and without a superposed parallel field are given in chapter 4,
considerable attention being paid to the reliability of the usual
ballistic method of making such measurements. These results are used
to compare calculated and measured eddy current losses in chapter 5,
and to derive some results for a superposed perpendicular field in
appendix 8.4.

The experiments with superposed fields showed that the effect
of the steady field on permeability and hysteresis loss depends on the
relative amplitudes of the fields. In chapter 6 the existing theory
for the calculation of pole-face loss is discussed, with emphasis on
the amplitude of the harmonic fields inside the rotor, and on the
effect of permeability. Chapters 2 - 6 provide the necessary
background for the discussion in the later half of chapter 6
of some effects of the superposed steady field and of the
superposition of the harmonics.

Chapter 6 is also used in appendix 8.5 to help summarise the
contribution of previous authors to the calculation of pole-face loss.
This is not placed in the main part of the thesis because it is in the
nature of a post-script to Adderley's work.

2. ARMATURE WINDING HARMONICS AND MAIN FIELD

2.1 Introduction

The recognised causes of power losses in the rotor pole faces of present synchronous machines under normal conditions are the armature slots and the armature winding harmonics. Additional loss occurs if the armature currents are non-sinusoidal or unbalanced.

Two forms of loss are produced by the stator slotting. 'Slot-ripple' loss (or 'tooth-ripple' loss) is the result of relative motion between the rotor and the local dips of air-gap flux density at the stator slots.[10] 'Reluctance pulsation' loss occurs only if the rotor surface is not smooth (e.g. slots or salient poles, the phenomenon being similar to that which occurs in an inductor alternator) and it can be reduced by correctly shaping the rotor.[11]

The winding harmonics can also be divided into two categories, but the loss mechanism is the same for each.[12] The 'phase-band' harmonics arise from the connection of the armature winding into a finite number of phases, and the 'slot' harmonics arise from the discontinuous distribution of the winding (i.e. its concentration into a finite number of relatively large discrete conductors). A symmetrical polyphase set of sinusoidal currents flowing through such an armature winding produces a travelling m.m.f. which is neither sinusoidal nor of constant shape. The fundamental of this wave is of constant amplitude and velocity, and when the rotor moves with it at synchronous speed it induces no loss in the rotor; but because the wave is not of constant shape there are m.m.f. harmonics which move relative to the rotor.

In this chapter the total armature m.m.f. variation relative to the rotor is found by subtracting the fundamental m.m.f. from the total m.m.f. By considering two windings of different pitch it is shown that the peak phase-band m.m.f. variation is not always at the peak of the fundamental m.m.f., contrary to previous belief.[13,14]

A mathematical analysis shows that the position of the peak phase-band variation is determined by the sign of the winding factors, as mentioned by Adderley, and confirms that the peak slot-harmonic variation always occurs at the position of zero fundamental armature m.m.f., as was known earlier[12,13], but was forgotten in one recent paper.[5]

The superposition of the induced voltage or current harmonics in the rotor, from which the loss is calculated, follows the same rules as the superposition of the m.m.f. harmonics, for constant permeability, and this is discussed in chapter 6. The total m.m.f. variation may be found useful for future consideration of variable permeability because the induced voltage can be calculated from the applied flux density if the field in the air gap of the induced current is small. If the eddy-current reaction is large, however, the resultant flux density tends to zero and the induced current is equal and opposite to the variation of stator current (or current loading) relative to the rotor, so this variation is also discussed in this chapter. The total m.m.f. and current-loading variations are also useful for estimating the amplitude of the magnetic field variations in the rotor. The m.m.f. gives the applied flux density, equal to the resultant flux density for weak eddy-current reaction, and the current loading gives the resultant tangential field strength for strong eddy-current reaction. In practice, the reduction of the applied variations by the air gap must be considered before the rotor surface field and induced voltage or current are calculated. This is best done by determining the reduction of each harmonic and then recombining to give the total variation.

A brief discussion of the relation between the m.m.f. variations and the main field over the pole face of an actual machine concludes this introductory chapter on the problem of m.m.f.-harmonic loss.

2.2   Total variation of armature m.m.f. relative to the rotor

2.2.1   Phase-band harmonics

Since the fundamental armature m.m.f. wave is of constant amplitude, the variations of m.m.f. on a rotor travelling at synchronous speed can be found by subtracting the fundamental wave from the total wave, as sketched in fig. 2.1 for a 3-phase, $60°$-spread infinitely-distributed, full-pitched winding.
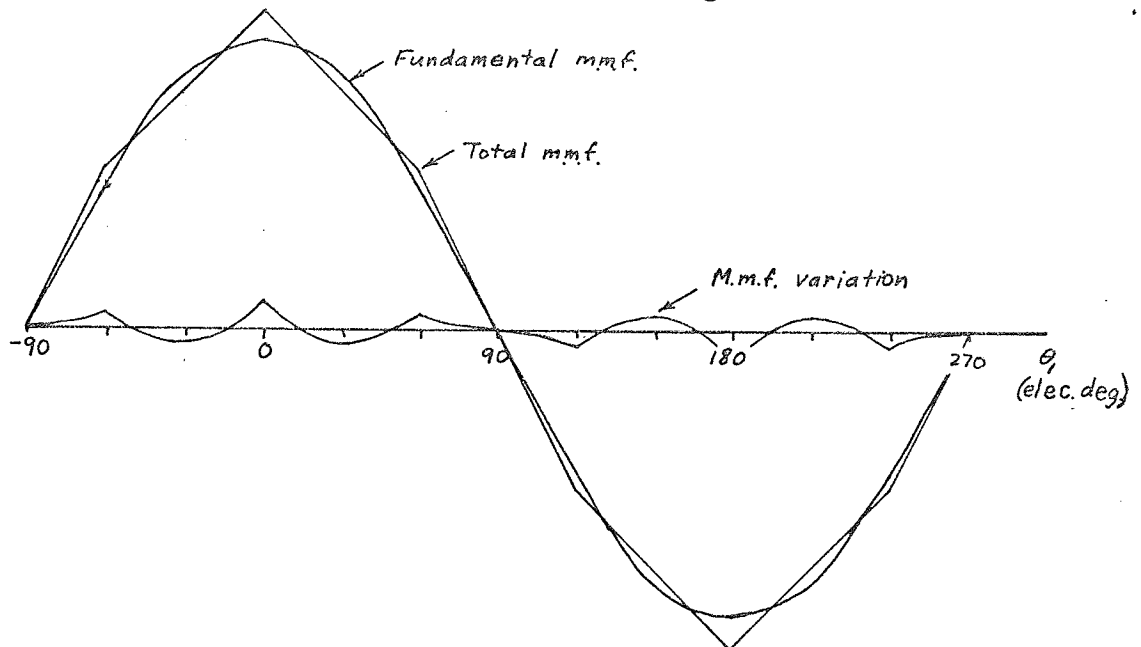
Fig. 2.1 Difference between fundamental and total armature m.m.f. of an infinitely-distributed, full-pitched winding when the current in one phase is a maximum.

As the shape of the stator m.m.f. wave changes, the variation relative to the rotor changes. Fig. 2.2 shows the stator m.m.f. at $10°$ intervals in time from which the variations relative to the rotor shown in fig. 2.3 were obtained. (In drawing figs. 2.2 and 2.3 the current in phase A is taken to be $\frac{1}{2N} \cos \omega_1 t$; the origin of the electrical angle relative to the stator ϑ_1 is taken at the centre-line of A-phase coils; $\vartheta_2 = \vartheta_1 - \omega_1 t$ is the electrical angle relative to the peak of the fundamental armature m.m.f., which is in line with some point on the rotor surface.) The variation shown in fig. 2.3 is seen to be a travelling wave of varying amplitude and shape, moving backwards relative to the rotor. The peak-peak amplitude of the wave is also plotted in fig. 2.3,

showing that the amplitude is greater at the peak of the fundamental m.m.f. ($\vartheta_2 = 0$) than at the point of zero fundamental m.m.f. ($\vartheta_2 = -90°$).

The variations of m.m.f. with time at any point on the rotor surface can be obtained by a cross-plot of several curves like those shown in fig. 2.3, or they can be obtained directly from fig. 2.2 since the rotor moves forwards 10 electrical degrees for each $10°$ interval in time. These variations with time are also shown on fig. 2.2, at $10°$ intervals of ϑ_2, together with the amplitude of the fundamental m.m.f. ($\frac{3}{\pi} 0.955 \cos \vartheta_2$) at each point.

An example of the effect of short pitching or of increasing the number of phases is shown in figs. 2.4 and 2.5. These are drawn for a pitch of 5/6, equivalent to a 6-phase, 12-zone, full-pitched winding, following the method outlined for figs. 2.2 and 2.3. The amplitude of the m.m.f. variations is reduced and there is almost no difference in the amplitudes at $\vartheta_2 = 0$ and $\vartheta_2 = -90°$; the frequency, however, is predominantly $12\omega_1$ at $\vartheta_2 = 0$ and $6\omega_1$ at $\vartheta_2 = -90°$.

Earlier work on these lines was done by Rüdenberg[12] (1924), Adderley[7] (1968) and Gault[15] (1941). Rüdenberg showed the difference between the stator m.m.f. wave at two different times, and rather misleadingly called this difference the harmonics, instead of the difference between the fundamental and the total m.m.f. Adderley showed the time variations of the stator m.m.f. relative to rotor as given here in fig. 2.2. Gault was concerned with rotor-bar currents in induction motors, and instead of considering the stator m.m.f. distribution he considered the stator

current loading distribution. He did this because the rotor-bar
resistance is small, allowing the rotor current loading to be equal
and opposite to the stator current loading, analogous to the case
of strong eddy-current reaction in a solid rotor.
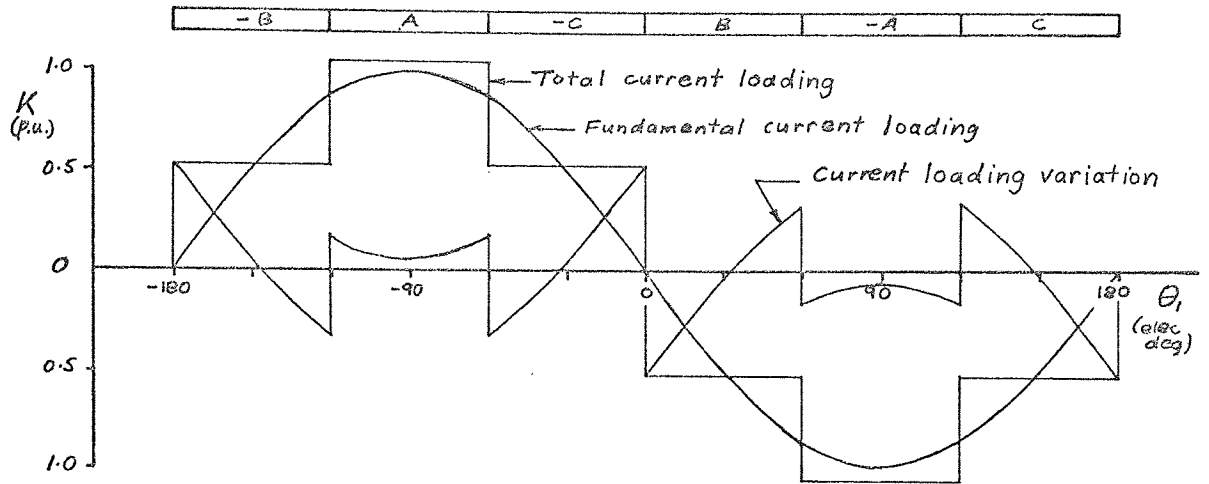
Fig. 2.6 Difference between the fundamental
and total armature current loading of an
infinitely-distributed, full-pitched winding
when the current in phase A is a maximum $(\omega_1 t = 0)$.
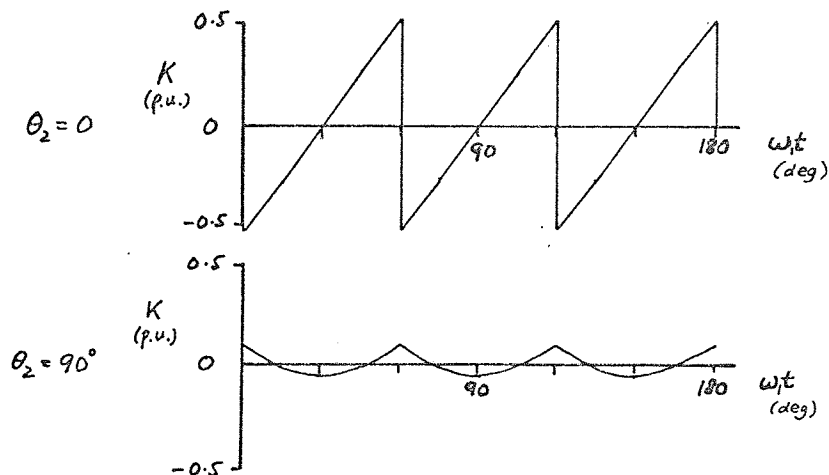
Fig. 2.7 Variation of current loading with
time at two points on the fundamental wave
$(\vartheta_2 = 0$ and $90^\circ)$ for an infinitely-distributed,
full-pitched winding.

Gault obtained results for a 3-phase infinitely-distributed
winding with 2/3 pitch, and the results are also applicable to a
full-pitched, infinitely-distributed winding. Taking the peak
fundamental armature current loading as 1 p.u., the difference
between the total wave and the fundamental at time $\omega_1 t = 0$ is
shown in fig. 2.6, and the time variation of current loading at
$\vartheta_2 = 0$ and $\vartheta_2 = 90^\circ$ is shown in fig. 2.7. (ϑ_2 is measured from the

zero crossing of the fundamental current loading, where the fundamental m.m.f. is a maximum)

The variation of fig. 2.6 is the derivative with respect to distance of the m.m.f. variation of fig. 2.1.

2.2.2 Slot harmonics

In most practical machines the winding is not infinitely distributed, but consists of discrete conductors, which introduce steps in the m.m.f. waveform or pulses in the current loading. Clearly these steps or pulses have a maximum amplitude where the m.m.f. is changing most rapidly and the current loading is a maximum, i.e. at $\vartheta_2 = 90^\circ$. Similar curves to those already given could be drawn to include the effect of the discrete conductors, or, on the other hand, the effect can be seen separated from the phase-band harmonics by considering a winding with as many phases as conductors per pole. This was done by Rüdenberg[12] to give the m.m.f. waveforms shown in fig. 2.8(a). The equivalent current loading waveforms are given in fig. 2.8(b).
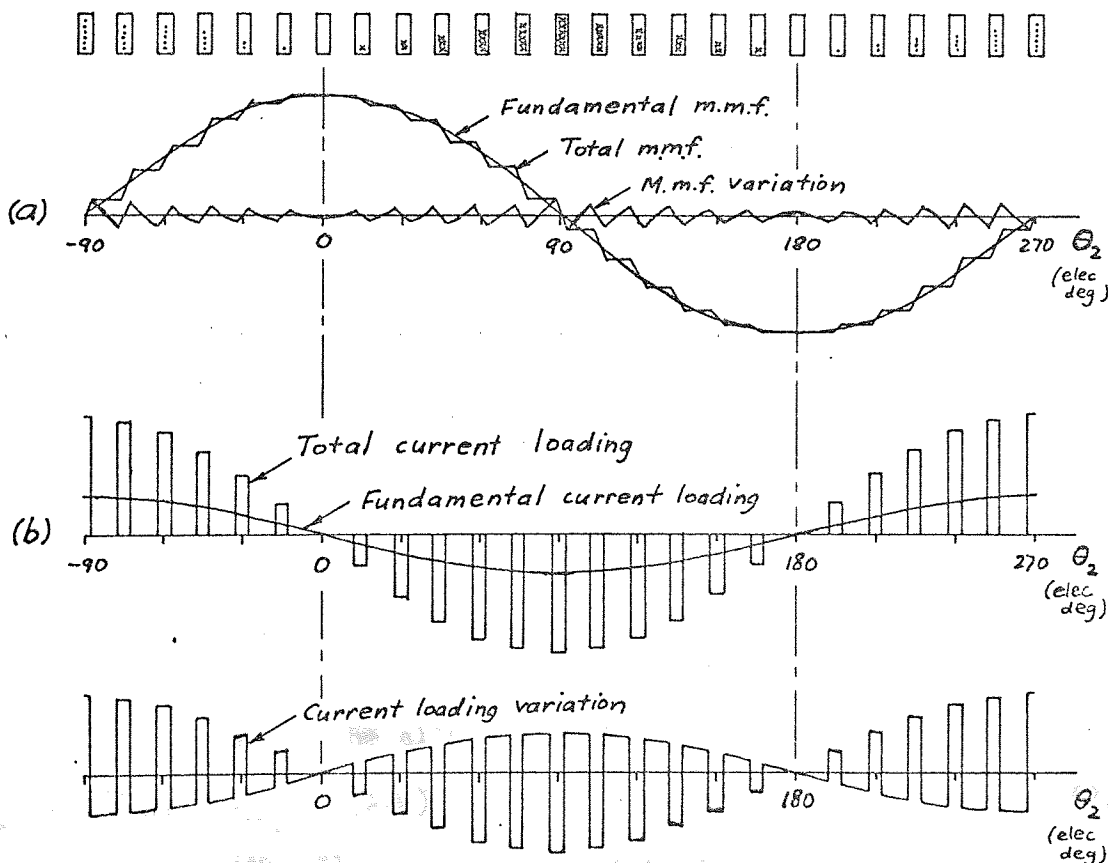
Fig. 2.8   Total slot-harmonic variations
(a) M.m.f.
(b) Current loading

2.3 Armature winding harmonics

2.3.1 M.m.f.

The m.m.f. wave of a 3-phase, 6-zone, integral-slot winding excited with balanced, sinusoidal currents, with the current in phase A equal to $\sqrt{2}I_A\cos\omega_1 t$ and the origin of ϑ_1 at the centre-line of the phase-A coils, is given by

$$F_a = \hat{F}_1\cos(\vartheta_1-\omega_1 t) + \hat{F}_5\cos(5\vartheta_1+\omega_1 t) + \hat{F}_7\cos(7\vartheta_1-\omega_1 t) + \ldots$$
$$\ldots + \hat{F}_{6k\pm1}\cos((6k\pm1)\vartheta_1\mp\omega_1 t) + \ldots \tag{2.1}$$

where $\quad \hat{F}_n = \dfrac{6\sqrt{2}}{\pi}NI_A\dfrac{k_{wn}}{n}\qquad (A) \tag{2.2}$

$\quad N$ = turns in series per pole and phase

$\quad k$ = 1,2,3 ....

The winding factor k_{wn} is the product of the distribution factor k_{dn}, the pitch factor k_{pn} and the slot-width factor k_{sn}.

$$k_{wn} = k_{dn}k_{pn}k_{sn}$$

where $\quad k_{dn} = \dfrac{\sin\frac{nw}{2}}{q\sin\frac{nw}{2q}}\quad,\quad k_{pn} = \sin n\varepsilon\frac{\pi}{2}\;,\; k_{sn} = \dfrac{\sin\frac{ns}{2}}{\frac{ns}{2}}\;$ (appendix 8.1)

$\quad w$ = width of phase band (elec deg)

$\quad q$ = slots per pole and phase

$\quad \varepsilon$ = fractional pitch = ratio of coil span to pole pitch

$\quad s$ = slot width (elec deg)

2.3.2 Current loading

The corresponding current loading wave is given by

$$K_a = \frac{\partial F}{\partial x} = \beta_1\frac{dF}{d\vartheta_1} = -\hat{K}_1\sin(\vartheta_1-\omega_1 t) - \hat{K}_5\sin(5\vartheta_1+\omega_1 t) - \hat{K}_7\sin(7\vartheta_1-\omega_1 t) - \ldots$$
$$\ldots -\hat{K}_{6k\pm1}\sin((6k\pm1)\vartheta_1\mp\omega_1 t) - \ldots \tag{2.3}$$

where $\quad \hat{K}_n = n\beta_1\hat{F}_n\qquad (A/m) \tag{2.4}$

$\quad \beta_1 = \dfrac{2\pi}{\lambda_1} = \dfrac{2p}{D}$ = fundamental phase-change coefficient (rad/m)

and $\quad \lambda_1$ = fundamental wavelength (m)

$\quad D$ = stator bore (m)

$\quad 2p$ = no. poles

$\hat{K}_n$ may be written in the alternative form

$$\hat{K}_n = \sqrt{2}(\text{a.c.})k_{wn}\qquad (A/m) \tag{2.5}$$

where $(\text{a.c.}) = \dfrac{6TI_A}{\pi D} = \dfrac{ZI_A}{\lambda_s}$ = r.m.s. current loading (A/m)

$\quad T$ = 2pN = turns in series per phase

$\quad Z$ = conductors in series per slot

2.4 Armature m.m.f. harmonics relative to the rotor

The following discussion is given in terms of the m.m.f. wave, and similar arguments can be used for the current-loading wave, with similar conclusions.

The m.m.f. wave of eqn. 2.1 can be written in terms of an angle ϑ_2 relative to the peak of the fundamental m.m.f. (which is opposite some point on the rotor, depending on the load), using $\vartheta_2 = \vartheta_1 - \omega_1 t$.

$$F_a = \hat{F}_1 \cos\vartheta_2 + \hat{F}_5 \cos(5\vartheta_2 + 6\omega_1 t) + \hat{F}_7 \cos(7\vartheta_2 + 6\omega_1 t) + \ldots$$
$$\ldots + \hat{F}_{6k\pm1} \cos((6k\pm1)\vartheta_2 + 6k\omega_1 t) + \ldots \tag{2.6}$$

The armature m.m.f. relative to the rotor consists of a fixed fundamental and a series of harmonics travelling backwards, pairs of harmonics inducing the same frequency in the rotor.

2.4.1 Time variation

The variation of F_a with time relative to the rotor at the peak of the fundamental ($\vartheta_2 = 0$) is a series of cosine terms having even symmetry about $\omega_1 t = 0$, $30°$, $60°$, etc. At the zero of the fundamental ($\vartheta_2 = 90°$) the m.m.f. variation is a series of sine terms with odd symmetry about $\omega_1 t = 0$, $30°$, $60°$, etc. These facts agree with the time variations shown in figs. 2.2 and 2.4.

2.4.2 Space variation

The variation of F_a with position may be shown by combining the pairs of $6k\pm1$ harmonics which induce the same frequency $6k\omega_1$ in the rotor.

$$F_{6k\omega} = F_{6k-1} + F_{6k+1}$$
$$= \hat{F}_{6k\omega} \cos(\eta_k + 6k\vartheta_2 + 6k\omega_1 t) \tag{2.7}$$

where
$$\hat{F}^2_{6k\omega} = \hat{F}^2_{6k-1} + \hat{F}^2_{6k+1} + 2\hat{F}_{6k-1}\hat{F}_{6k+1}\cos2\vartheta_2 \tag{2.8}$$

$$\tan\eta_k = \frac{\hat{F}_{6k+1} - \hat{F}_{6k-1}}{\hat{F}_{6k+1} + \hat{F}_{6k-1}} \tan\vartheta_2 \tag{2.9}$$

Equation 2.7 shows that the resultant of each pair of $6k\pm1$ space harmonics relative to the rotor is a modulated travelling wave of varying amplitude and wavelength.

The wavelength is slightly greater or slightly less than $\frac{\lambda_1}{6k}$, depending on ϑ_2 and the relative values of F_{6k-1} and F_{6k+1} . Only if F_{6k-1} and F_{6k+1} have the same magnitude is the wavelength constant at $\frac{\lambda_1}{6k}$.

The amplitude also depends on ϑ_2 and the relative values of the two $6k\pm1$ m.m.f.'s. At the peak of the fundamental ($\vartheta_2=0$),

$$F_{6k\omega} = (\hat{F}_{6k+1} + \hat{F}_{6k-1}) \cos 6k\omega_1 t \qquad (2.10)$$

and at the zero of the fundamental ($\vartheta_2=90^o$),

$$F_{6k\omega} = (\hat{F}_{6k+1} - \hat{F}_{6k-1}) \sin 6k\omega_1 t \qquad (2.11)$$

Thus if $\hat{F}_{6k+1}$ and $\hat{F}_{6k-1}$ have the same sign, the maximum variation occurs at $\vartheta_2=0$, whilst if the two components have opposite signs, the maximum occurs at $\vartheta_2=90^o$. This was noted by Adderley[7].

If the two components are of equal amplitude, eqn. 2.7 may be simplified to illustrate these results.

If $\hat{F}_{6k-1} = \hat{F}_{6k+1}$, then $F_{6k\omega} = 2\hat{F}_{6k-1}\cos\vartheta_2\cos(6k\vartheta_2+6k\omega_1 t)$ $\qquad (2.12)$

If $\hat{F}_{6k-1} = -\hat{F}_{6k+1}$, then $F_{6k\omega} = 2\hat{F}_{6k-1}\sin\vartheta_2\sin(6k\vartheta_2+6k\omega_1 t)$ $\qquad (2.13)$

2.4.3 Space variation for an actual winding

The sign of a harmonic is that of its winding factor, $k_{wn} = k_{dn} k_{pn} k_{sn}$ (eqn. 2.2). The slot-width factor is positive except for very high harmonics, as shown in appendix 8.1. The pitch and distribution factors may be positive or negative, but certain rules exist. (There are useful graphs of k_{pn} and k_{dn} in Say[16], and tables in Liwschitz-Garik[17]. It should be noted, however, that the expression $k_{pn} = \cos n(1-\varepsilon)\frac{\pi}{2}$ used by Say and others does not give the correct sign of k_{pn} for n = 3,7,11,15.... when the origin of ϑ_1 is taken at the centre-line of the coils of one phase, as done here, rather than 90° away at the centre of a phase band, as done by Say.) The distribution factors for a pair of $6k\pm1$ phase-band harmonics ($k\neq q$) with a 60° phase-spread winding have opposite signs, and those for a slot-harmonic pair (k=q) have the same sign for any winding. The pitch factors for a pair of phase-band harmonics may have the same or opposite signs, but those for a slot-harmonic pair always have

2.4.3.1 Phase-band harmonics ($k \neq q$, $2q$, ...)

The above rules show that for a 60° phase-spread winding the maximum amplitude of the resultant of a pair of phase-band harmonics occurs at the peak of the fundamental m.m.f. ($\vartheta_2 = 0$) if the pitch factors of the pair have opposite signs, and occurs at the zero of the fundamental m.m.f. ($\vartheta_2 = 90^{\circ}$) if the pitch factors have the same sign.

These conclusions agree with the figures given in section 2.2.1. The pitch factors for a full-pitched winding have opposite signs for all pairs of harmonics, so the maximum resultant of each pair occurs at $\vartheta_2 = 0$, and the total variation is therefore also a maximum at $\vartheta_2 = 0$, as shown in figs. 2.2 and 2.3.

The pitch factors of pairs of harmonics for 5/6 pitch have alternately the same sign (k odd, n = 5,7;17,19;....) and opposite signs (k even, n = 11,13;23, 25;....). Thus the total winding factors for the pairs of harmonics n = 5,7; 17,19;.... have opposite signs and the maximum resultant of each pair occurs at $\vartheta_2 = 90^{\circ}$, and similarly the n = 11,13; 23,25; .... pairs have maxima at $\vartheta_2 = 0^{\circ}$. It may also be shown, using the method below, that the minima of the n = 11,13; 23,25;.... pairs are much less than the maxima of the n = 5,7; 17,19; .... pairs, so the dominant pairs at $\vartheta_2 = 90^{\circ}$ are the n = 5,7; 17,19; .... pairs giving dominant frequency of $6\omega_1$. The other points illustrated in figs. 2.4 and 2.5, namely the dominant frequency of $12\omega_1$ at $\vartheta_2 = 0$ and the approximately constant resultant variation over the pole face, can be obtained in a similar way.

The amplitude of the resultant of a pair of $6k \pm 1$ harmonics expressed as a fraction of the peak fundamental m.m.f. is, from eqn.2.8,

$$\left(\frac{\hat{F}_{6k\omega}}{\hat{F}_1}\right)^2 = \left(\frac{\hat{F}_{6k-1}}{\hat{F}_1}\right)^2 + \left(\frac{\hat{F}_{6k+1}}{\hat{F}_1}\right)^2 + 2\left(\frac{\hat{F}_{6k-1}}{\hat{F}_1}\right)\left(\frac{\hat{F}_{6k+1}}{\hat{F}_1}\right)\cos2\vartheta_2 \qquad (2.14)$$

where $\dfrac{\hat{F}_n}{\hat{F}_1} = \dfrac{k_{dn}\, k_{pn}\, k_{sn}}{n\; k_{d1}\, k_{p1}}$ $\quad (k_{s1} \simeq 1)$ $\qquad\qquad (2.15)$

Since the slot-width factor is nearly the same for each harmonic of a pair, families of curves can be plotted showing $\dfrac{\hat{F}_{6k\omega}}{\hat{F}_1 k_{sn}}$

against ϑ_2. This is done in figs. 2.9 (a) and (b) for the first and second pairs of harmonics (n = 5,7;11,13) for a 60°-spread winding of 5 and 6 slots per pole and phase respectively, with several practical pitches.

These curves show the variable amplitudes of the resultant m.m.f.'s, and how the coil pitch controls the position of the maximum. They illustrate the fact that the pitch factors for the 5th and 7th harmonics are rarely of the same sign, giving a maximum resultant at $\vartheta_2 = 90^o$, and when they are, the pitch factors for the 11th and 13th harmonics are large (k_{p5} and k_{p7} have the same sign for $0.800 \leqslant \varepsilon \leqslant 0.857$). Thus it is impossible to obtain a small armature reaction m.m.f. variation at $\vartheta_2 = 0$ (unless q=1, when all harmonics are slot harmonics). A final decision on the best pitch for minimum rotor surface loss may depend on the rotor angle at rated load and on the effects of superposition, these being discussed later in this chapter and in chapter 6.

2.4.3.2 Slot harmonics (k=q, 2q....)

The winding factors for a slot harmonic pair always have opposite signs so the maximum slot-harmonic variation always occurs at the zero of the fundamental m.m.f. ($\vartheta_2 = 90^o$). This is in agreement with the more direct reasoning of section 2.2.2.

The magnitude of $k_{pn} k_{dn}$ for a slot harmonic is equal to $k_{p1} k_{d1}$ and the slot-width factors for a pair of harmonics are approximately equal. So, from eqn. 2.15, the amplitudes of the first pair of slot harmonics, expressed as a fraction of the fundamental, are $\dfrac{k_s}{6q-1}$ and $\dfrac{k_s}{6q+1}$, which are both approximately equal to $\dfrac{k_s}{6q}$ when $q \geqslant 2$. Using eqn. 2.13, this gives the p.u. resultant as

$$\frac{\hat{F}_{6q\omega}}{\hat{F}_1} = \pm \frac{2 \, k_{s(6q)}}{6q} \sin \vartheta_2 \, \sin(6q\vartheta_2 + 6q\omega_1 t) \qquad (2.16)$$

where the +ve sign applies if k_p for the 6q-1 harmonic is +ve and vice versa. The total slot-harmonic variation is therefore zero at $\vartheta_2 = 0$, has a dominant wavelength $\dfrac{\lambda_1}{6q} = \lambda_s$, and moves backwards at synchronous

speed relative to the rotor. These results also agree with section 2.2.2.

2.5 Rotor position and main flux density

2.5.1 Introduction

The position of the rotor relative to the fundamental armature m.m.f., and hence relative to the points of maximum and minimum m.m.f. harmonic variations, depends on the parameters of the machine and the load. The situation is sketched in fig. 2.10 for a salient-pole machine, showing the fundamental armature m.m.f. F_{a1} lagging the direct axis by $90+\psi$ elec deg. The main flux density B on the rotor surface, due to the resultant of F_{a1} and the rotor excitation m.m.f. F_f, is also shown as a function of angle ϑ_3 relative to the rotor direct axis. The slot-ripple loss depends on B , and it may also affect the rotor B/H curve appropriate for the m.m.f. harmonics. The distribution of the m.m.f. harmonic variations over the pole face is shown in a more detailed example in section 2.6.
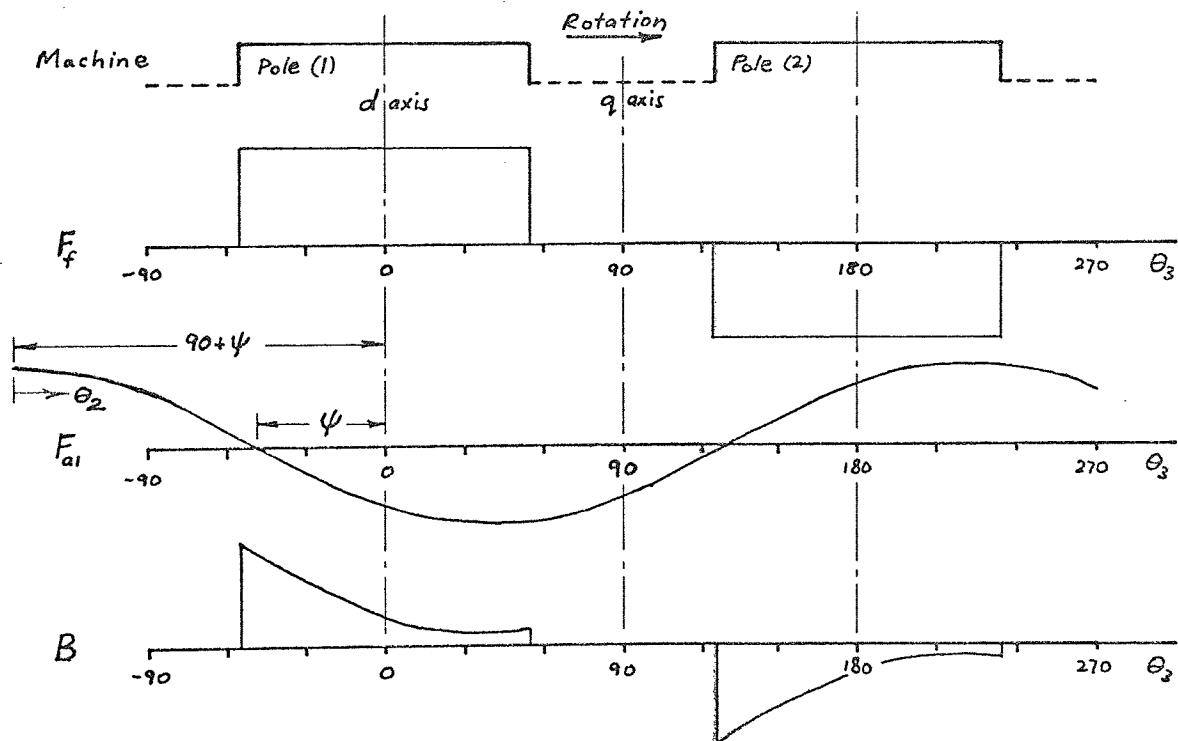
Fig. 2.10 Air-gap field distributions for a salient-pole machine

2.5.2 Rotor position

The rotor position may be estimated using the 2-axis theory from which the phasor diagram of fig. 2.11 is obtained. From the figure,

$$\tan \psi \quad = \frac{IX_q + V\sin \phi}{IR_a + V\cos \phi} = \frac{\frac{X_q}{X_L} + 1}{\frac{R_a}{R_L} + 1} \quad \tan \phi \qquad (2.17)$$

where $X_L = \frac{V}{I} \sin \phi$, the load reactance

$R_L = \frac{V}{I} \cos \phi$, the load resistance
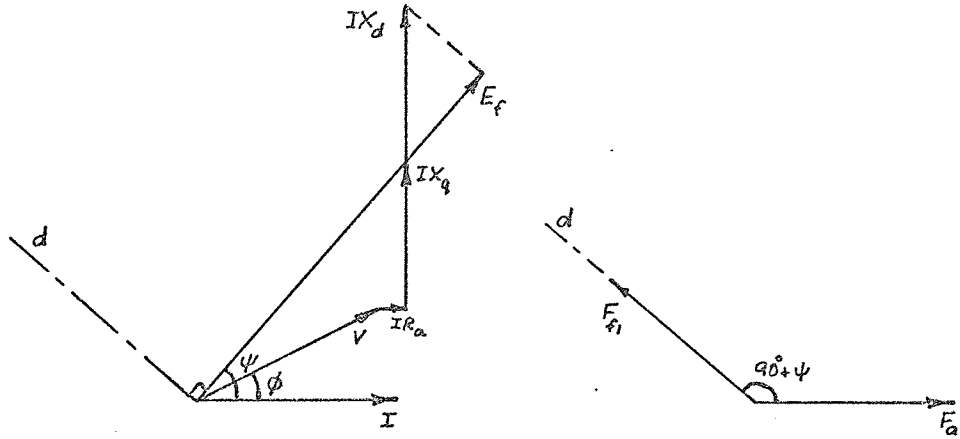
Fig. 2.11   Synchronous machine phasor diagram
(Generator, lagging power factor)

$\frac{R_a}{R_L} \ll 1$ for normal non-zero power factor loads, and ψ can

be plotted in terms of $\frac{X_q}{X_L}$ and ϕ . Instead of $\frac{X_q}{X_L}$, a more convenient

parameter is $\frac{X_q}{Z_L}$ (where $Z_L = \frac{V}{I}$, the load impedance, which equals

1 p.u. at rated load) and this is used to plot the characteristics for ψ

in fig. 2.12 from

$$\tan \psi \quad \approx \quad (\frac{X_q}{Z_L \sin \phi} + 1) \tan \phi \qquad (2.18)$$

In practice $R_a \ll X_q$, and the only curves which are affected

by the exact value of R_a are the zero power factor curves in the region

of $\frac{X_q}{Z_L} = \frac{X_q}{X_L} = \pm 1$.

2.5.3 Main flux density

In appendix 8.2 an expression for the main flux density over a

pole face is derived, neglecting saturation. For pole face (1) of fig.

2.10 the expression can be written

$$\frac{B}{B_{fo}} = \frac{B_{fo}}{B_{fo}} (E_f + \frac{IX_{ad}}{C_m} \cos (\vartheta_2 + 90° + \psi)) \qquad (2.19)$$

where $E_f = V\cos(\psi - \phi) + IR_a \cos\psi + IX_d \sin\psi$ (2.20)

B_{fo} = flux density distribution giving voltage V on no load

$\hat{B}_{fo}$ = peak of B_{fo}

C_m = ratio of field m.m.f. to d-axis armature m.m.f. for the same fundamental flux density.

2.5.4   M.m.f. harmonics

When the rotor is displaced relative to the peak of the fundamental armature m.m.f. by $90° + \psi$, it is also displaced from the m.m.f. harmonic variations by the same angle. The armature m.m.f. variations discussed in section 2.4 may be written in terms of angle ϑ_3 relative to the d-axis of the rotor using $\vartheta_2 = \vartheta_3 + 90° + \psi$.

For example, eqn. 2.8 becomes

$$\hat{F}^2_{6k\omega} = \hat{F}^2_{6k-1} + \hat{F}^2_{6k+1} + 2\hat{F}_{6k-1}\hat{F}_{6k+1} \cos 2(\vartheta_3 + 90° + \psi)$$ (2.21)

2.6   Example

As an example of the preceding sections, the main flux density and the resultant amplitudes of two pairs of m.m.f. harmonics are plotted over the pole face of a 30 kW salient-pole machine in figs.2.13(a) and (b) for short-circuit and rated-load conditions. Further details of the machine (Ginsberg and Jokl no. 4) are given in appendix 8.2.

At rated load (0.8 lagging power factor) eqn. 2.17 gave $\psi = 61.1°$, and on short circuit $\psi = 90°$. B was calculated from eqn. 2.19.

The armature winding has a pitch of 2/3 for which all m.m.f. harmonics, except triplens, have the same magnitude of pitch factor, and the pitch is therefore equivalent to full pitch as regards the harmonic content. All phase-band harmonics have maximum resultants at $\vartheta_2 = 0$, and only the slot harmonics have maxima at $\vartheta_2 = 90°$. The figures show the resultant amplitudes of the first pair of phase-band harmonics (n=5,7) and the first pair of slot harmonics (n=29,31), calculated from eqn. 2.21 expressed in terms of $\dfrac{\hat{F}_{6k\omega}}{\hat{F}_1 k_{sn}}$ (as for fig. 2.9).

It can be seen that the average amplitude of m.m.f. variation over the pole face depends on the rotor position. The average phase-band variation is smaller on rated load than on short circuit (for this pitch),

whilst the average amplitude of the slot-harmonic variations is larger. The rotor position may, therefore, affect the average loss on the pole face; this is discussed further in chapter 6, section 6.4.2.

It is also apparent that the main flux density distribution is different for the two load conditions, but that B tends to be small where the phase-band m.m.f. variation is large (for this pitch) and large where the slot-harmonic variation is large. These facts are, of course, a direct consequence of the relative positions of F_{a1} and the m.m.f. harmonic variations. The maximum amplitude of B occurs near the trailing edge of the pole on rated load and is of the order of twice the no-load flux density, neglecting saturation (see also appendix 8.2).

2.7 Conclusion

It was shown that the winding harmonic variations may be a maximum or a minimum at the peak of zero of the fundamental armature m.m.f. depending of the signs of the winding factors. In particular, for a 3-phase 60°-spread winding the position of the maximum phase-band variation depends on the winding pitch, and a fractional pitch in the range of $0.857 \geqslant \epsilon \geqslant 0.800$ gives a minimum variation of the first pair of phase-band harmonics on the axis of maximum fundamental armature m.m.f. For all windings the slot-harmonic variation is a maximum on the axis of zero fundamental m.m.f. It was also shown that the harmonic analysis agreed with the more direct method of plotting the total armature field, and it is thought that such plots of total m.m.f. and current loading may be of further use in estimating the total field variations on the rotor surface, and ultimately the loss.

The fact that the position of the rotor relative to the fundamental armature m.m.f. may affect the loss on two counts was introduced. The rotor position determines the average resultant amplitude of a pair of harmonics over the pole face, and it influences the main flux density distribution.

The non-uniform amplitude of the main flux density over a pole face was illustrated, and an idea of the maximum amplitude obtained.

(The fact that the maximum occurs where the resultant m.m.f. slot-harmonic variation is large will need to be remembered when slot-ripple variations are important, as both induce the same frequency in the rotor.) The peak main flux density predicted by the calculation neglecting saturation may over estimate the actual density (appendix 8.2) and further work is needed.

3.1 Introduction

It has been known for a long time that the permeability and losses in iron for a varying magnetic field may be changed by a steady field. For example, remanent magnetism is one source of a steady field, and in 1873 Rowland[18] reported a reduction of permeability of virgin iron (iron which has not been magnetised since heat treatment) caused by the accidental application and removal of a large field. Many reversals of the test magnetic force could not remove the effect of the remanent magnetism. In 1904 Searle[19] carried out a more systematic series of experiments, and his fig. 3 is sketched here in fig. 3.1, showing the reduction in permeability and hysteresis loss for a loop of constant H limits with increasing levels of remanent magnetism.
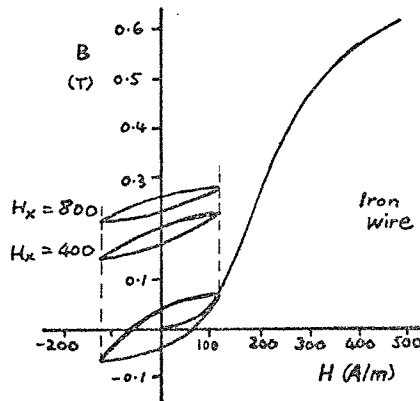
Fig. 3.1 The effect of remanent magnetism on small
hysteresis loops.
H_x = amplitude of previous magnetising force (A/m)

The steady field may also come from an external source (the earth's field is a naturally occuring example). In 1887 Lord Rayleigh[21] obtained up to 80% reductions in permeability for small field variations in the presence of a large steady magnetising force, and some hysteresis loops about a non-zero value of H were obtained by Ewing[20] in 1885. Fig. 3.2 is a sketch of Ewing's fig. 44, showing the 'incremental' loops.
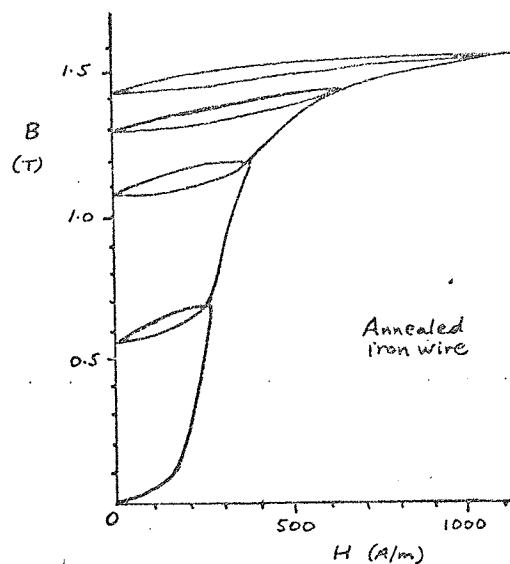
Fig. 3.2   Incremental hysteresis loops formed by
          removing and reapplying a magnetising force.

The effects of a steady field have been put to practical use

in instruments for the measurement of steady magnetic fields, in d.c.

excited reactors for the control of alternating currents, and to

increase the magnetising current of transformers for load testing of

alternators.   On the other hand, the d.c. component of current in

radio transformers, rectifier circuit smoothing chokes and cathode

reactors is unavoidable and can be annoying.

Many experiments were performed to obtain data for such

transformers, reactors, etc., and the results form a large proportion

of the available information on superposed fields.   This chapter

reviews the   data   relating to soft magnetic materials.

3.2 Steady field with parallel varying field

3.2.1 Incremental permeability, μ_Δ

3.2.1.1 Definition

If, after demagnetisation, a specimen of iron is subjected to a magnetising force, H_m, and the field strength is subsequently changed by ΔH causing a change of flux density ΔB, then the incremental permeability is the ratio $\mu_\Delta = \dfrac{\Delta H}{\mu_o \Delta B}$. The definition is illustrated in fig. 3.3. Curve (i) shows an incremental loop beginning at the point (H_m, B_m) on the normal magnetisation curve, i.e. at the peak of a normal hysteresis loop, and (ii) shows an incremental loop on the descending part of the normal loop. In keeping with the definition of normal permeability $(\mu_n = \dfrac{H_m}{\mu_o B_m})$ μ_Δ can be written as

$$\mu_\Delta = \frac{H_\Delta}{\mu_o B_\Delta} \quad \text{where } H_\Delta = \tfrac{1}{2}\Delta H, \; B_\Delta = \tfrac{1}{2}\Delta B$$
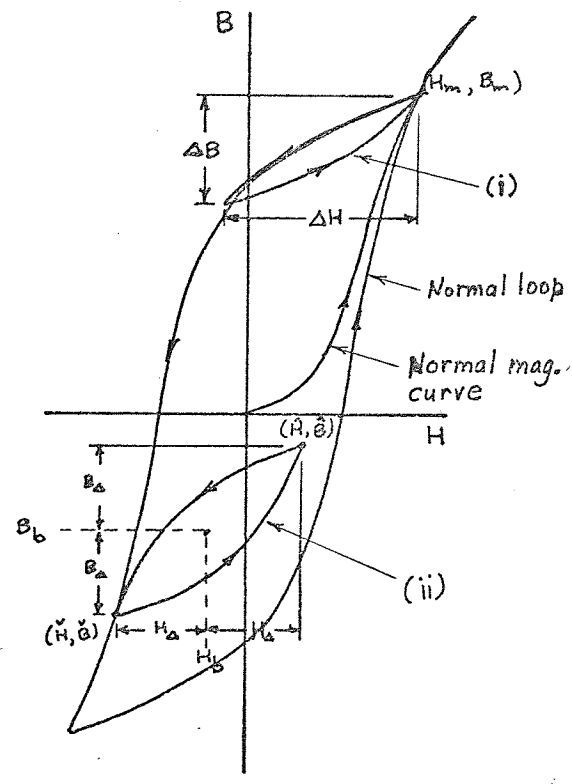
Fig. 3.3 Quantities relating to incremental loops

Also illustrated in fig. 3.3 are the symbols for the extremities of an incremental loop $(\hat{H}, \hat{B})$, $(\check{H}, \check{B})$, for the amplitude averages $H_b = \dfrac{\hat{H}+\check{H}}{2}$, $B_b = \dfrac{\hat{B}+\check{B}}{2}$, and for the size of the loop $H_\Delta = \tfrac{1}{2}\Delta H$, $B_\Delta = \tfrac{1}{2}\Delta B$.

3.2.1.2 Prediction of μ_Δ

Several authors observed that the position and shape of an incremental loop changed for repeated cycles. For an incremental loop on the normal magnetisation curve the lower tip of the incremental loop rose above the normal loop. The effect is illustrated by curve (i) in fig. 3.3 and confirmed in chapter 4. If this drift of an incremental loop is neglected, the shape of the normal loop may be used to calculate

μ_Δ for an incremental loop on the normal magnetisation curve, as the first part of such a loop is then along the normal loop. This was hinted at by Spooner[23](1923) and suggested by Lanchester[24](1933). Conversely, any technique of predicting μ_Δ for incremental loops on the normal magnetisation curve amounts to predicting the shape of the normal hysteresis loops, and since there is no method at present for doing this, the difficulty is evident.

Assuming, however, that a normal hysteresis loop is available, the incremental permeability for a set of incremental loops beginning from the same point on the normal magnetisation curve is given by the slopes of the dotted lines shown in fig. 3.4(a). The general shape of the variation of μ_Δ against H_Δ sketched in fig. 3.4(b) is similar to the variation of normal permeability against H_m.

(a)   (b)
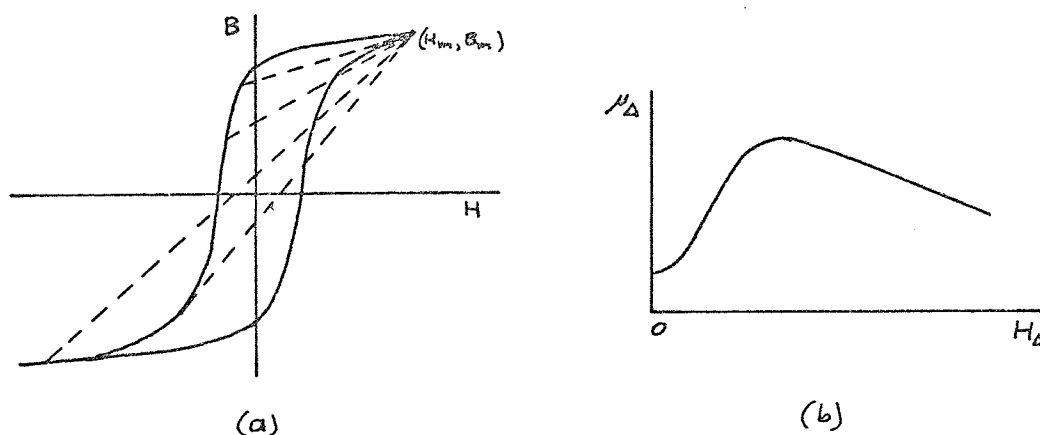
Fig. 3.4 Variation of μ_Δ against H_Δ , for constant $(\hat{H}, \hat{B})$ equal to (H_m, B_m), predicted from a normal hysteresis loop.

It is even more difficult to predict μ_Δ for incremental loops not on the normal magnetisation curve, for in general μ_Δ depends on the previous magnetic history as well as on the amplitude of the incremental loop. The problem is illustrated in figs. 3.5 and 3.6.

There have, however, been several attempts to produce empirical formulae for μ_Δ . The available formulae for small values of H_Δ were reviewed by Bozorth[22]. The limit of μ_Δ when H_Δ tends to zero is called the reversible permeability μ_{rev} $\left(\mu_{rev} = \lim_{H_\Delta \to 0} \frac{H_\Delta}{\mu_0 B_\Delta} \right)$. In 1910 Gans[25] observed that μ_{rev} was largely determined by B_b alone for
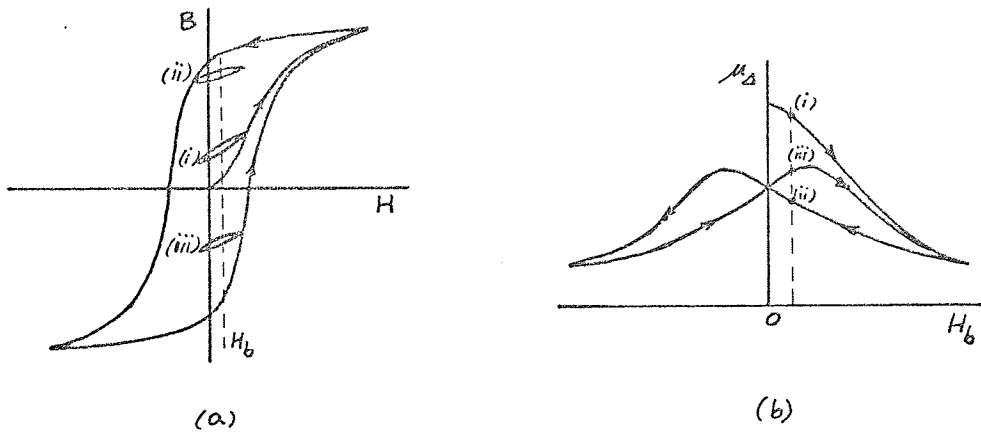
Fig. 3.5 μ_Δ against H_b for a fixed H_Δ.
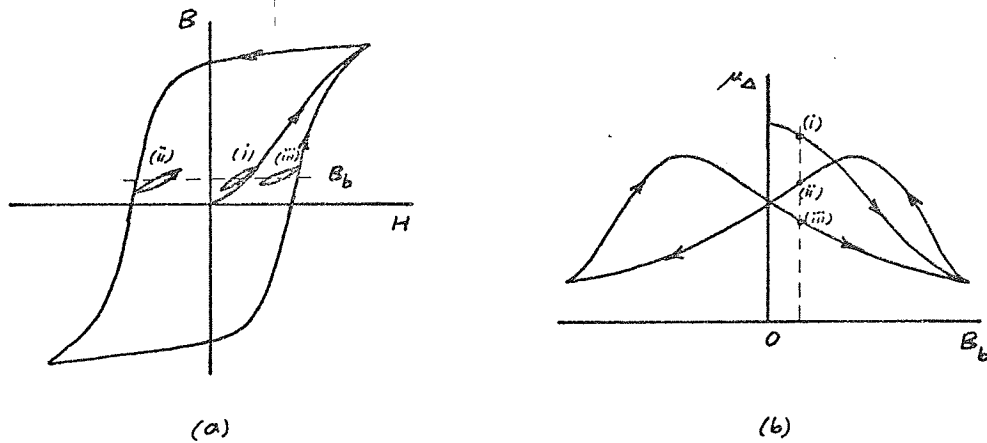
Fig. 3.6 μ_Δ against B_b for a fixed H_Δ.

several materials (soft iron, annealed steel, hardened steel, nickel),

the curves of fig. 3.6 (b) being very close together. Also, when

μ_{rev} was expressed in terms of μ_i, the initial normal permeability

$\left(\mu_i = \lim\limits_{H_m \to 0} \dfrac{B_m}{\mu_0 H_m}\right)$ and B_b was expressed in terms of the saturation flux

density B_s, the curves of $\dfrac{\mu_{rev} - 1}{\mu_i - 1}$ against $\dfrac{B_b - \mu_0 H_b}{B_s}$ were close to

coincidence for the different materials. In 1911 Gans[25] expressed the

mean curve in the parametric form

$$\left.\begin{array}{l} \dfrac{B_b - \mu_0 H_b}{B_s} = \coth x - \dfrac{1}{x} = L(x) \\[4mm] \dfrac{\mu_{rev} - 1}{\mu_i - 1} = 3\left(\dfrac{1}{x^2} - \dfrac{1}{\sinh^2 x}\right) = \dfrac{dL(x)}{dx} \end{array}\right\} \qquad (3.1)$$

The curve is shown in fig. 3.7 (labelled on the usual

assumptions that $\frac{\mu_{rev} - 1}{\mu_i - 1} \approx \frac{\mu_{rev}}{\mu_i}$ and $\frac{B_b - \mu_o H_b}{B_s} \approx \frac{B_b}{B_s}$). It seems to

represent quite closely the actual curve for ferromagnetic

materials whose domains have no direction of easy magnetisation[22].

Once μ_{rev} is found, Ebinger[27](1930) suggested that, for

values of H_Δ up to 8 A/m, μ_Δ may be found from the linear relation

$$\mu_\Delta = \mu_{rev} + \nu_\Delta H_\Delta \qquad\qquad (3.2)$$

This was by analogy with Rayleigh's law for normal permeability

$$\mu_n = \mu_i + \nu H_m .$$

Ebinger plotted $\frac{\nu_\Delta}{\nu}$ against $\frac{B_b}{B_s}$ for a variety of materials (the exact

materials were not specified), for incremental loops on the normal

magnetisation curve, and found that the points lay reasonably close to

a single curve, also shown in fig. 3.7.

The curve of $\frac{\mu_{rev}}{\mu_i}$

shows that μ_{rev} becomes much

less that μ_i as the steady

biasing field strength

increases. The curve of $\frac{\nu_\Delta}{\nu}$

shows that the variation of μ_Δ

with H_Δ also decreases

considerably, and at high

biasing levels, μ_Δ is almost

independent of H_Δ .
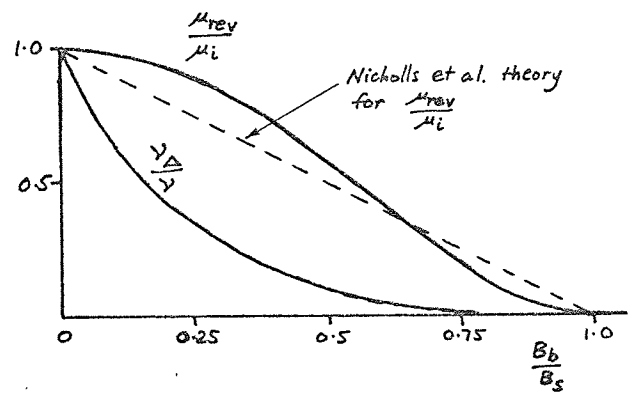
Fig. 3.7 $\frac{\mu_{rev}}{\mu_i}$ and $\frac{\nu_\Delta}{\nu}$ against $\frac{B_b}{B_s}$.

In 1929, Sizoo[28] confirmed that, for 3% Si steel, μ_{rev} was

dependent on the average flux density alone, but that for values of H_Δ

greater than about 1 A/m, μ_Δ depended significantly on the previous

magnetic history (see section 3.2.3.5). Sizoo did not apply the

maximum possible pre-magnetisation (H_m), and it is likely that for

larger values of H_m, values of H_Δ smaller than 1 A/m would have been

needed to avoid the effects of previous magnetic history. (see chapter

4, section 4.5). Thus care must be taken when using Ebinger's formula,

eqn.3.2, if H_Δ is of the order of 1 A/m.

For larger values of H_Δ , and for incremental loops on the normal magnetisation curve, Ebinger suggested two further formulae, following the work of Spooner[23] in 1923. Spooner noticed an approximately linear relation between μ_Δ and ΔB, for incremental loops of the same peak flux density (fig.3.16), and gave the formula

$$\mu_\Delta = \mu_{Bm} (a + b \Delta B) \qquad (3.3)$$

where μ_{Bm} is the normal permeability of the material for the flux density B_m at the upper peak of the incremental loop ($\mu_{Bm} = \dfrac{B_m}{\mu_o H_m}$), and 'a' and 'b' are constants dependent on B_m but independent of the material (fig. 3.8).

The results using this formula were shown to be accurate to 10 or 20% for materials which did not have exceptionally low or exceptionally high remanent flux densities, and for values of ΔB which were neither very small, nor greater than B_m.
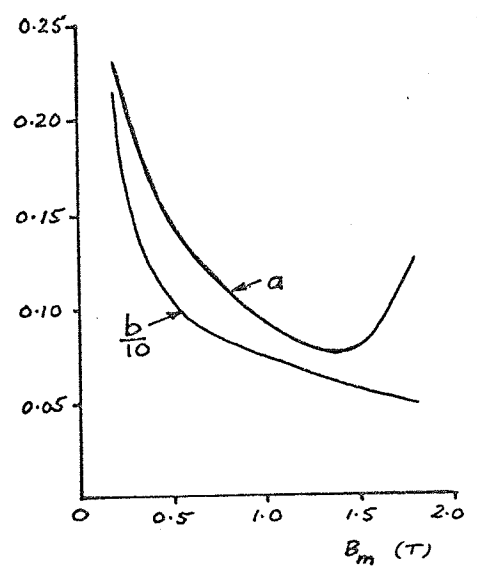
Fig. 3.8 Constants 'a' and 'b' for Spooner's eqn.
$\mu_\Delta = \mu_{Bm} (a+b \Delta B)$
with ΔB in tesla.
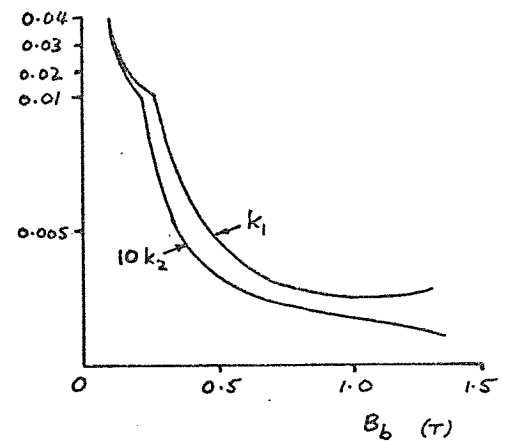
Fig. 3.9 Constants k_1 and k_2 for Ebinger's eqn.
$\mu_\Delta = \mu_{bn} \sqrt{k_1 + k_2 B_\Delta}$
with B_Δ in tesla.

Ebinger's two formulae were expressed in terms of the normal permeability μ_{bn} corresponding to the biasing flux density:

$$\mu_\Delta = \mu_{bn} (A + B.B_\Delta) \qquad (3.4)$$

$$\mu_\Delta = \mu_{bn} \sqrt{k_1 + k_2 B_\Delta} \qquad (3.5)$$

He thought that B_b and μ_b were more likely to be known than B_m and H_m,

and the constants A, B and k_1, k_2 were plotted against B_b, the shape of the curves being similar to those in fig. 3.8. The curves for k_1 and k_2 are shown in fig. 3.9. The accuracy of eqn. 3.4 was similar to that of Spooner's eqn. 3.3, but eqn. 3.5 was more accurate, especially for small B_Δ .

The above formulae of Spooner and Ebinger were most accurate for the permeability of incremental loops at the peak of a normal loop. Spooner felt that his formula could be used for other incremental loops, but his investigations on this point were not extensive (the values of B_Δ he used were always only 10% of $\hat{B}$, for example), and as already mentioned Sizoo showed that μ_Δ depended significantly on previous magnetic history (by 10% or more) as H_Δ increased.

An attempt to allow for previous magnetic history in the calculation of current transformer magnetising current was made by Nicholls et al. in 1969[29]. Their method assumed that the ascending part of incremental loops on the descending part of a normal loop could be represented by the normal magnetisation curve, suitably scaled, as shown in fig. 3.10. The representation was not based on direct observations of B/H loops, and awaits experimental confirmation. Certain relations for μ_Δ can be derived, however, and it can be shown that the relation for μ_{rev} agrees with the work of Gans, as follows.

The normal magnetisation curve is scaled and translated in the B direction, and just translated in the H direction, giving the co-ordinates of a point $(\hat{H}, \hat{B})$ at the peak of an incremental loop as

$$
\left.
\begin{aligned}
\hat{B} &= B_n \frac{B_s - \check{B}}{B_s} + \check{B} \\
\hat{H} &= H_n + \check{H}
\end{aligned}
\right\} \qquad (3.6)
$$

where the symbols are explained in fig. 3.10.
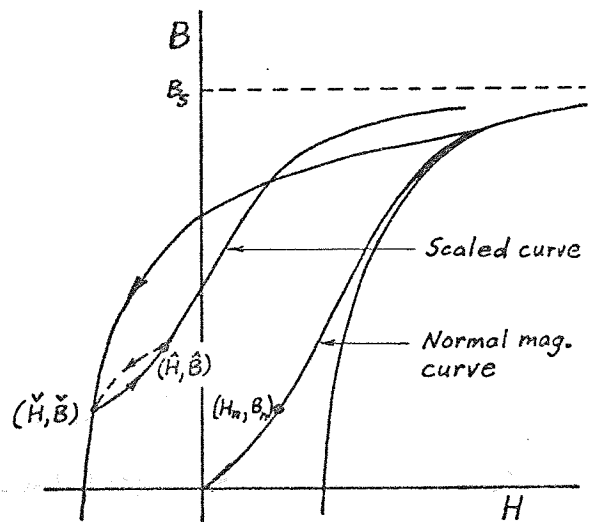
Fig. 3.10 Representation of ascending part of incremental loop.

The incremental permeability is therefore given by

$$\mu_\Delta = \frac{\Delta B}{\mu_o \Delta H} = \frac{\hat{B} - \check{B}}{\mu_o(\hat{H}-\check{H})} = \frac{B_n}{\mu_o H_n} \cdot \frac{B_s - \check{B}}{B_s} = \mu_{n2}(1 - \frac{\check{B}}{B_s}) \qquad (3.7)$$

where μ_{n2} is the normal permeability for $H_n = \Delta H = 2H_\Delta$.

This equation can be written in terms of B_b and B_Δ , since $\check{B} = B_b - B_\Delta$, to give an expression similar to eqns. 3.3 and 3.4 used by Spooner and Ebinger:

$$\mu_\Delta = \mu_{n2}(1 - \frac{B_b}{B_s} + \frac{B_\Delta}{B_s}) \qquad (3.8)$$

For vanishingly small ΔH, $\mu_\Delta = \mu_{rev}$, $\mu_{n2} = \mu_i$ and $\check{B} = B_b$, so that eqn. 3.7 gives

$$\frac{\mu_{rev}}{\mu_i} = 1 - \frac{B_b}{B_s} \qquad (3.9)$$

This is the straight line shown in fig. 3.7 and is a reasonable approximation to the curve obtained by Gans.

For loops which are slightly larger, but not so large that B_b is very different from $\check{B}$, eqn. 3.7 together with Rayleigh's law for μ_n gives

$$\mu_\Delta = (\mu_i + \nu 2H_\Delta)(1 - \frac{B_b}{B_s}) = \mu_i(1 - \frac{B_b}{B_s}) + 2\nu(1 - \frac{B_b}{B_s}) H_\Delta .$$

Using eqn. 3.9,

$$\mu_\Delta = \mu_{rev} + 2\nu(1 - \frac{B_b}{B_s}) H_\Delta$$

and by comparison with eqn. 3.2,

$$\frac{\nu_\Delta}{\nu} = 2(1 - \frac{B_b}{B_s}) . \qquad (3.10)$$

The plot of $\frac{\nu_\Delta}{\nu}$ from eqn. 3.10 is shown in fig. 3.11 together with Ebinger's curve. This shows that, for small incremental loops on the descending part of a normal loop, the method of Nicholls et al. predicts a much greater variation of μ_Δ with H_Δ than was measured by Ebinger for small loops on the normal magnetisation curve. The experimental verifications of this prediction and the predictions of

eqns. 3.7 and 3.8 are considered in chapter 4, section 4.5.3.

No other
attempt to allow for
previous magnetic
history was discovered.
Magnetic hysteresis has
two effects, causing an
incremental loop to be
inclined away from the
normal magnetisation
curve, as shown by
loop (i) in fig. 3.3,
and causing the slope
of a loop such as
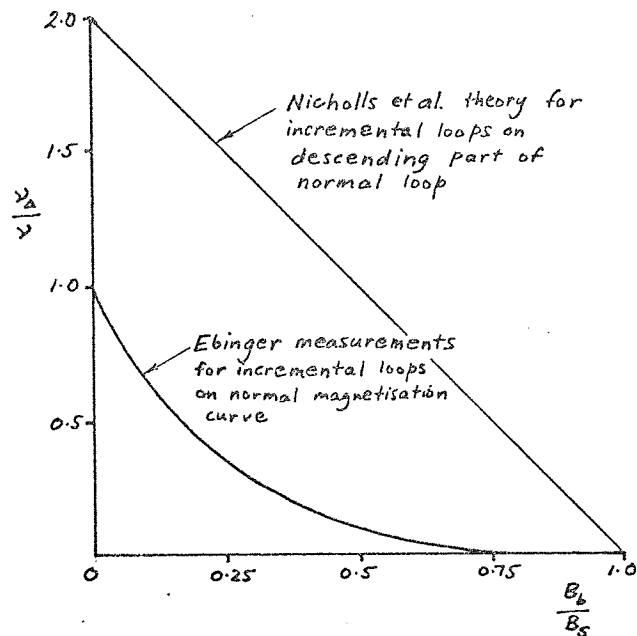
Fig. 3.11 Comparison of $\dfrac{\nu_\Delta}{\nu}$

(ii) in fig. 3.3 to be different from the slope of a loop on the

normal magnetisation curve (figs. 3.5 and 3.6). Both these hysteresis

effects were neglected by Johnson et al.[30] and Chernovets et al.[31] for

incremental loops with large ΔB in the calculation of d.c.-controlled

reactor characteristics. Good agreement with experiment was obtained

by assuming that the incremental loops followed the normal magnetisation

curve.

To summarise, the methods available for calculating μ_Δ for

incremental loops on the normal magnetisation curve are:

1) the methods of Gans and Ebinger for small loops

2) the formulae of Spooner and Ebinger for medium sized loops

3) the normal magnetisation curve for large loops

4) the use of a family of normal hysteresis loops

Incremental loops of small and medium size not on the normal

magnetisation curve depend on the previous history and the only method

available is that of Nicholls et al, which was not directly verified by

experiment, although it was shown here that the method agrees with Gans'

results for very small loops.

3.2.1.3 Reported results for μ_Δ

The methods of measuring μ_Δ may be classified according to whether the field strength is varied suddenly, slowly, or periodically. Measurements by periodic (a.c.) methods may depend on waveform and be affected by eddy currents, so a discussion of these is left until section 3.2.3. In this section results obtained by the first two methods are reviewed.

In 1873 Rowland[18] used the method of sudden changes of field strength, the 'ballistic' method, on unlaminated ring specimens. He measured flux density with a heavily damped galvanometer connected to a secondary winding, and field strength was deduced from the magnetising current. The relevant results were those showing the effect of residual magnetism on permeability, but they are only of value in a qualitative way because the value of field strength which was applied and removed to cause the remanent magnetism was not given, and the unmagnetised specimen was virgin iron (i.e. demagnetised by heat treatment as the process of demagnetisation by reversals was not in practice then) which could have contained an unknown amount of remanent magnetism. Results for the same specimen in both the magnetised and virgin state were only given for 'Burden's Best' iron; these are plotted in fig. 3.12(a) as μ_Δ against B_Δ and in fig. 3.12(b) as μ_Δ against H_Δ.
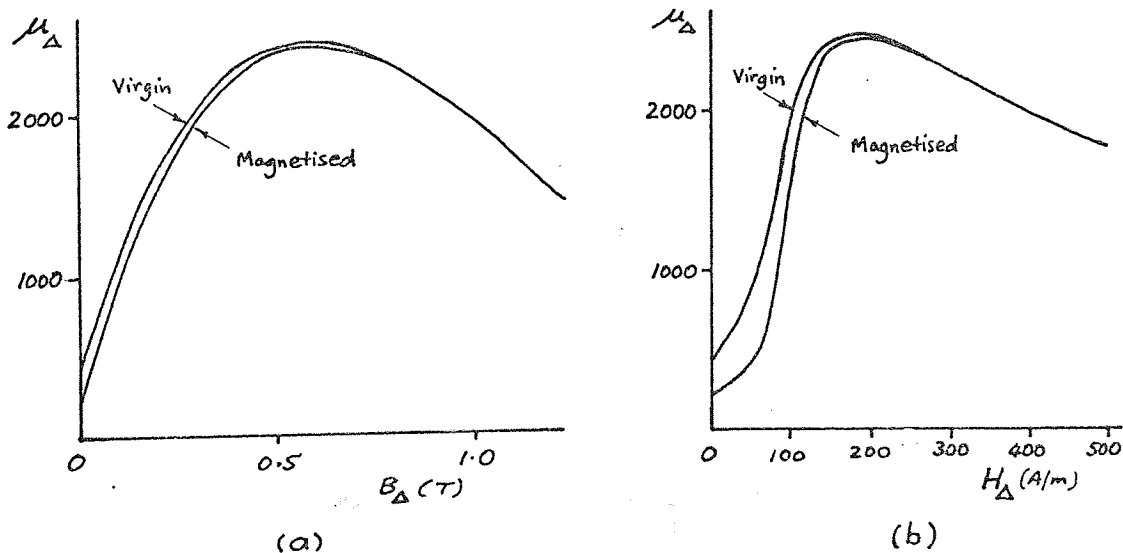
Fig. 3.12 Effect of remanent magnetism on permeability, 'Burden's Best' iron (from Rowland, tables I and II)

It can be seen that the permeability was reduced by the premagnetisation when compared on a basis of the same amplitude of B or of H, but only for values of H or B below the knee of the normal magnetisation curve.

The next person to report on the permeability of magnetised specimens was Searle in 1904.[19] He used the ballistic method on a square of 0.34 mm 'tagger plate' laminations.* The first experiments relevant to this discussion followed up Rowland's experiment on the effect of residual magnetism. Searle demagnetised the iron by slowly reducing a 90 Hz alternating current, he applied a known magnetising force H_m which was reversed 50 times before removal to give the magnetisation, and he used several values of H_m. The experiments thus measured the permeablity of incremental loops of zero H_b, with the iron at the remanent point of several main loops before the incremental loops were performed, as illustrated in fig. 3.13.

The results were plotted in two ways as shown in fig. 3.14. The variation of permeability with field strength is shown in fig. 3.14 (a) and in fig. 3.14 (b) the ratio $\frac{\mu_\Delta}{\mu_n}$ is plotted against field strength, where μ_n is the normal permeability for
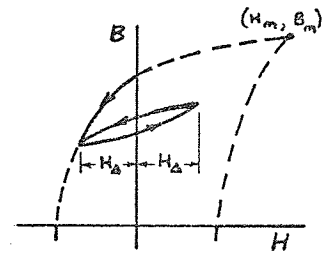
Fig. 3.13 Type of incremental loop considered by Searle.

$H_n = H_\Delta$. Each curve is for a constant value of H_m, i.e. for incremental loops on the same main loop, and the curve for $H_m = 0$ gives μ_n.

(a)

(b)
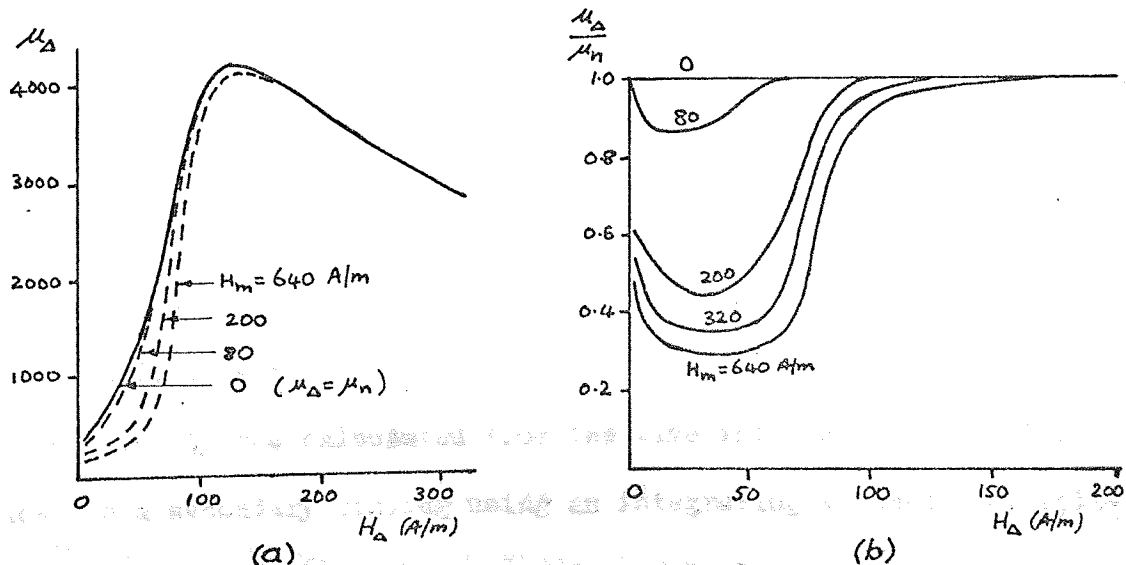
Fig. 3.14 Incremental permeability on several main loops with $H_b = 0$, compared with normal permeability, 'tagger plate'. (from Searle, figs. 6 and 7)

Rowland's results were confirmed, and in addition the curves show that μ_Δ for $H_b = 0$ may be very dependent on the amplitude of the magnetic history, being very much reduced by large premagnetising forces for H_Δ below the knee of the normal magnetisation curve.

Searle also measured the permeability of incremental loops at the peak of a main loop, i.e. on the normal magnetisation curve. His results were again presented in two ways, as shown in fig. 3.15. The reduction of permeability with increasing H_b is clearly shown in fig. 3.15 (a), and fig. 3.15 (b) shows that as H_Δ becomes greater than H_b the permeability returns to normal (except for $H_b \leq 100$ A/m, which is approximately equal to the coercive force).
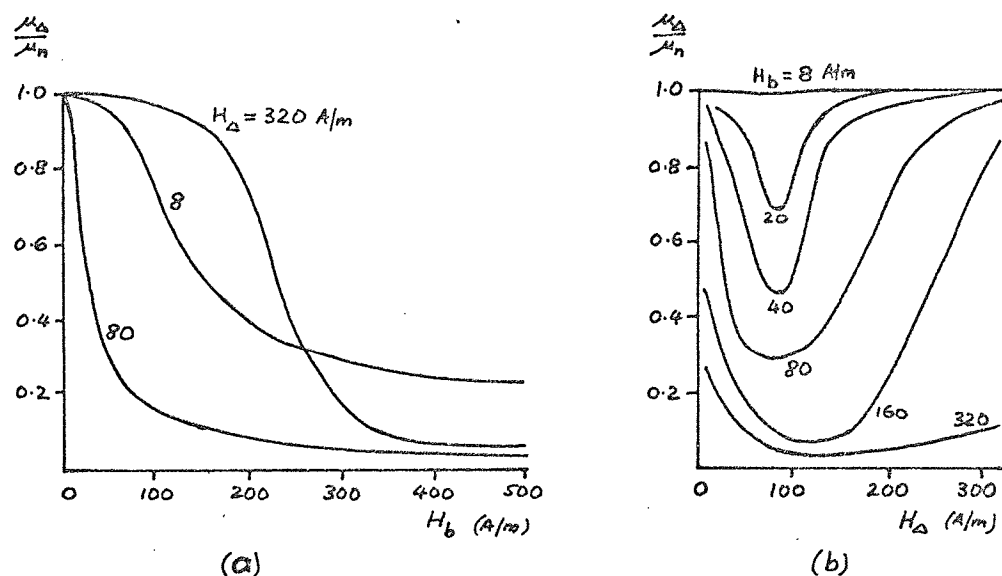
Fig. 3.15 $\dfrac{\mu_\Delta}{\mu_n}$ for incremental loops on the normal magnetisation curve, tagger plate (from Searle, figs. 11 and 12)

The next detailed investigation of incremental permeability came in 1923 when Spooner[23] used results obtained by Chubb & Spooner in 1915,[33] and by himself in 1921,[34] to deduce his formula for calculating μ_Δ. Chubb and Spooner studied incremental loops on the normal magnetisation curve using the method of slowly varying field strength on a 3333 kVA transformer with a silicon steel core. As for the ballistic method the field strength was calculated from the magnetising current, but the flux density was calculated from the time integral of the voltage induced in a secondary winding using an integrating voltmeter or volt-second meter. The magnetising current was slowly varied and recorded at

each revolution of the volt-second meter. No further details of the
meter were given. The method was checked, however, by comparing a normal
hysteresis loop for a 250 kVA transformer obtained by this method and by
the ballistic method. The two loops were almost identical and had areas
agreeing to within a fraction of one percent.

Spooner presented his results by plotting μ_Δ against ΔB
for incremental loops of the same maximum flux density B_m . Some of his
curves are shown in fig. 3.16, where the permeability is plotted against
$B_\Delta = \frac{\Delta B}{2}$, rather than against ΔB, which enables an easier comparison
with the normal permeability (when $B_\Delta = B_m$, $\mu_\Delta = \mu_n$). The
approximately linear relation between μ_Δ and B_Δ can be seen, which was
the basis of eqn. 3.3.
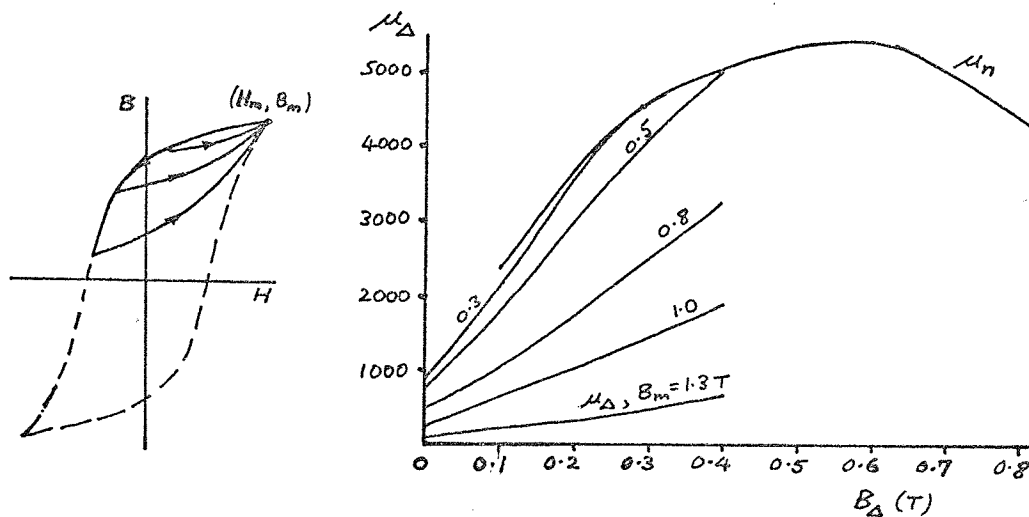
Fig. 3.16 μ_Δ on normal magnetisation curve, transformer
laminations (from Spooner, fig. 3)

The ballistic method was used by Sugiura [35] in 1931 to obtain
B/H curves for an iron tube when polarised in several directions. Fig. 3.17
shows his results for incremental loops on the normal magnetisation curve
with constant values of parallel polarising field strength. The
variation of μ_Δ could be deduced from these curves, and would show the
reduction of μ_Δ for values of H_Δ less than H_b , as indicated by Searle's
results. It is also interesting to note that the B/H curves are
approximately linear for such values of H_Δ .

Sims and Clay [36] in 1935 compared several methods of measuring
μ_Δ , using a ring of 0.40 mm stalloy (4% Si) laminations. A few of their
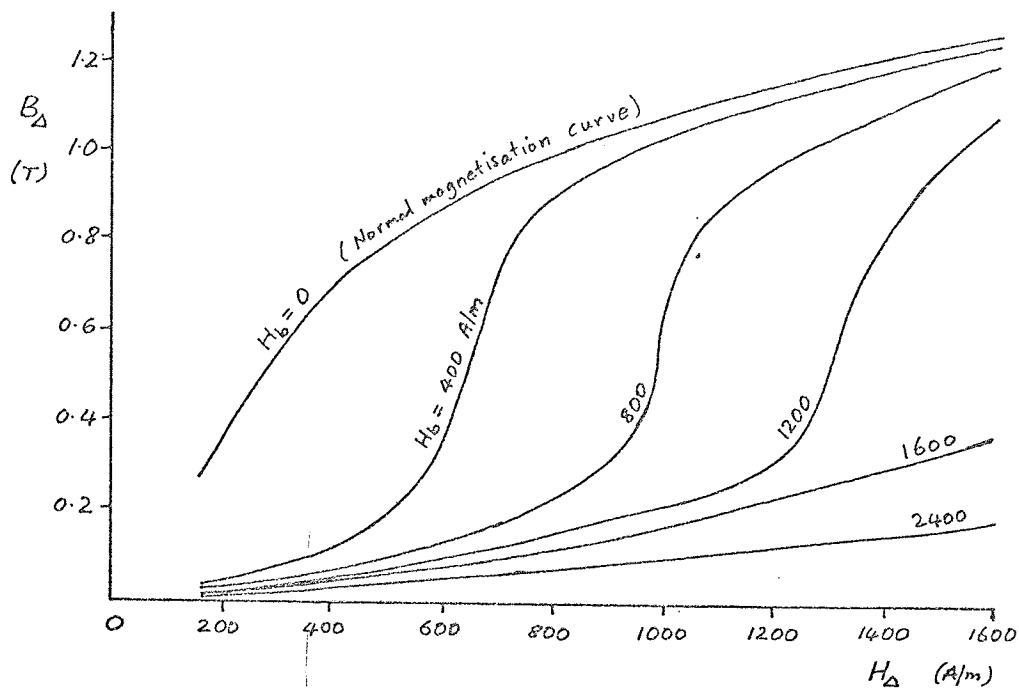
Fig. 3.17 B/H curves for incremental loops on normal magnetisation curve, iron tube (from Sugiura, fig. 25)

curves obtained with the ballistic method showing μ_Δ for incremental loops on the normal magnetisation curve are given in fig. 3.18, together with the normal permeability. Once again a marked reduction of permeability can be seen, and there is a tendency for μ_Δ to be independent of H_Δ for the larger values of H_b (H_Δ was always less than H_b in these tests).

There were no other results reported for the incremental permeability of steel, using either the ballistic method or the slowly-varying field strength method.
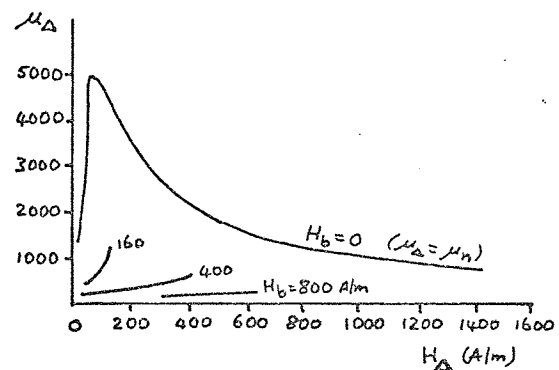
Fig. 3.18 μ_Δ on normal magnetisation curve, stalloy (from Sims and Clay, fig. 21)

* 'tagger plate' was a sheet transformer iron supplied by C.A. Parsons, Newcastle-on-Tyne. No details of its composition were given.

Several experiments have been performed to determine the
hysteresis loss when a steady field is superposed on a changing field,
by either the ballistic method or the method of slowly changing field
strength. In general, the results showed a decrease of hysteresis loss
as the steady field increased, keeping H_Δ constant, and an increase of
hysteresis loss keeping B_Δ constant, until high values of B_Δ were
used, when the loss showed a decrease. The results also showed that the
magnetic history of the specimen may have an effect on the loss.

In 1893, Ewing and Klaassen[37], using a magnetic curve tracer
with a soft-iron specimen, showed the decrease of area of incremental
loops of constant H_Δ on the normal magnetisation curve as the biasing
field increased. Besides measuring the permeability of incremental loops
at points on a main loop such that $H_b = 0$ (fig. 3.13), Searle[19] also
showed that the hysteresis loss of such loops of constant H_Δ decreased
as the biasing (remanent) flux density increased. The ballistic
experiments on the square of tagger plate were supported by magnetometer
measurements on a specimen of iron wire (fig. 3.1). Wilson et al.[38] in
1909 compared the effects of the two different forms of magnetic
treatment used by Ewing and by Searle. For rings of stalloy and lohys
laminations they showed that the hysteresis loss when only remanent
magnetism was present (i.e. $H_b = 0$) was up to 20% greater than the loss
for loops on the normal magnetisation curve, for loops of the same B_Δ
and H_Δ .

After these preliminary experiments, further work concentrated
on the hysteresis loss for loops on the normal magnetisation curve. In
1912 experiments were reported by Holm[39] and by Rosenbaum[40]. Holm
carried out two series of tests by the ballistic method on a ring of
0.50 mm laminations. The first series was for a constant maximum flux
density, $B_m = 1.46$ T, and varying B_Δ from 0.14 to 1.46 T (fig. 3.16).
In the second series B_Δ was kept constant at 0.14 T and B_m varied from

0.14 to 1.54 T. The results showed that the area of a displaced loop was greater than the area of the normal (undisplaced) loop of the same B_Δ, and the increase was 4.5 times for the most displaced loop in the second series of tests.

Rosenbaum carried out one series of tests by the ballistic method on a small (0.75 kW) square transformer core of 0.35 mm laminations. He kept B_Δ constant at 0.48 T and varied B_m from 0.48 to 1.54 T. He found that the hysteresis loss (W_{hb}) could be approximated to within 10% by the relation

$$W_{hb} = W_h + \alpha_R B_b^{2.6} \qquad (3.11)$$

where W_h = loss of unbiased loop of same B_Δ

α_R = positive constant.

Rosenbaum's work was extended to cover a varying B_Δ by Ball[41] in April 1915, who suggested the formula

$$W_{hb} = (\eta + \beta_B B_b^{1.9}) B_\Delta^{1.6}$$
$$= W_h + (\beta_B B_\Delta^{1.6}) B_b^{1.9} \qquad (3.12)$$

where $W_h = \eta_s B_\Delta^{1.6}$ = loss of unbiased loop according to the Steimetz law

β_B, η_s = positive constants

Ball's formula was based on ballistic experiments on rings of 0.35 mm laminations of 2.5% Si steel and 'standard' low carbon steel. The rings had a ratio of mean diameter to radial thickness of 2.5:1, much smaller than the value of 8:1 recommended by B.S.2454 : 1954[42]. (According to Hughes[43], however, the hysteresis loss deduced from the loop plotted with the average flux density as determined experimentally is only very slightly greater than the actual hysteresis loss, for rings such as those used by Ball). Furthermore, the exponents of B_b and B_Δ given by Ball were only average exponents and there was some variation with both B_Δ and B_b. For example, with B_Δ = 0.2 T the exponent of B_b was more like 2.3 than 1.9, a value closer to Rosenbaum's 2.6. These variations are to be expected, as has been shown by detailed examinations of the Steimetz index[37,44].

Thus Ball's formula is to some extent approximate, but its most serious limitation is the small range of B_Δ for which it applies. The range of B_b covered by Ball was from 0 to 1.0 T, but that of B_Δ was only from 0.05 to 0.2 T. The behaviour of the hysteresis loss for larger values of B_Δ was given by Chubb and Spooner[33] in September, 1915, using their method discussed in the previous section. Some of their results are shown in fig. 3.19, from which it can be seen that at the higher values of B_Δ the loss decreased as B_b increased, requiring the constant α_R to be negative, contrary to the increase of loss with displacement predicted by Ball. Also, in the discussion[45], Spooner calculated the exponent of B_b from his data and showed that it decreased from 2.35 to 1.09 as B_Δ increased from 0.1 to 0.9 T.
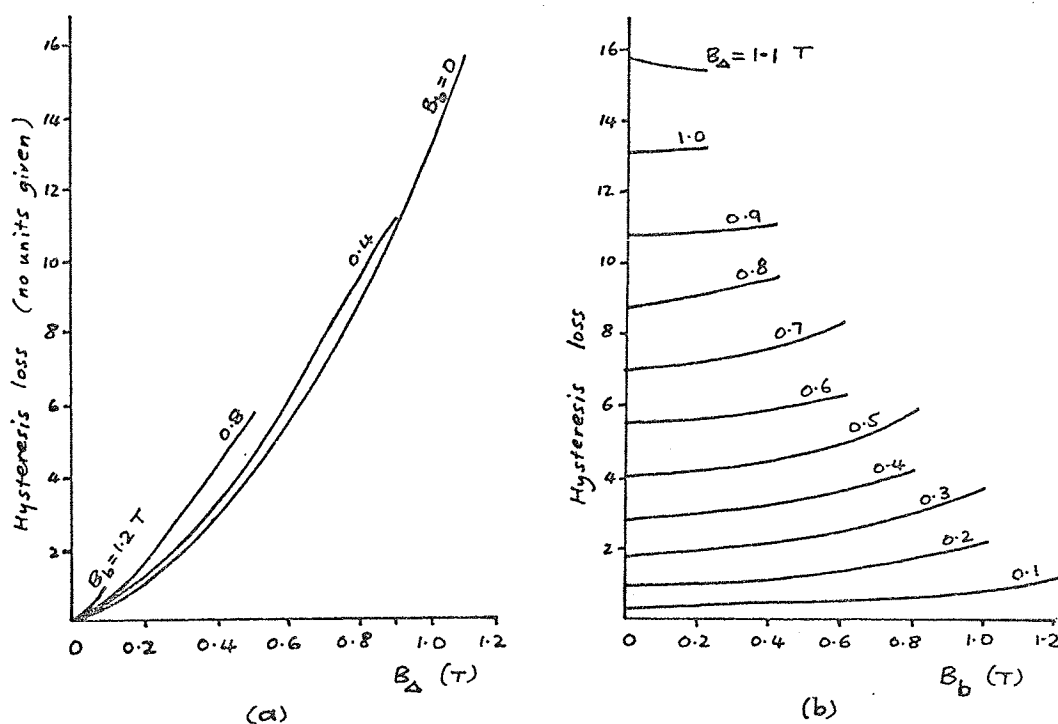
Fig. 3.19 Hysteresis loss for incremental loops on normal magnetisation curve, silicon steel (from Chubb and Spooner)

Spooner published some further results in 1921.[34] These were for incremental loops at several points on a normal hysteresis loop as shown in fig. 3.20 (a) and were obtained by the ballistic method on rings of electrical sheet steel. Spooner plotted the hysteresis loss expressed as a fraction of the loss of the normal loop on which the incremental loop was situated, which obscured the effect of the previous history on the loss. Curves such as those shown in fig. 3.20 (b) can, however, be drawn from Spooner's tabulated results, showing the variation

of the loss with the loop displacement (peak flux density $\hat{B}$). The
incremental amplitude (B_Δ) was 10% of the displacement. A comparison
of points 5 and 2 in fig. 3.20 (b) shows that the loss may vary by
about 30% for loops of the same amplitude and displacement
(B_Δ = 0.12 T in this case, 10% of the displacement of 1.2 T).
Fig. 3.20 (b) is for 1% Si steel. The results for 2.25% Si steel were
slightly different in that the loss at the peak of a normal loop could
be less than the loss for a loop of the same displacement at some other
position, in agreement with the results of Wilson et al. mentioned at
the beginning of this section.
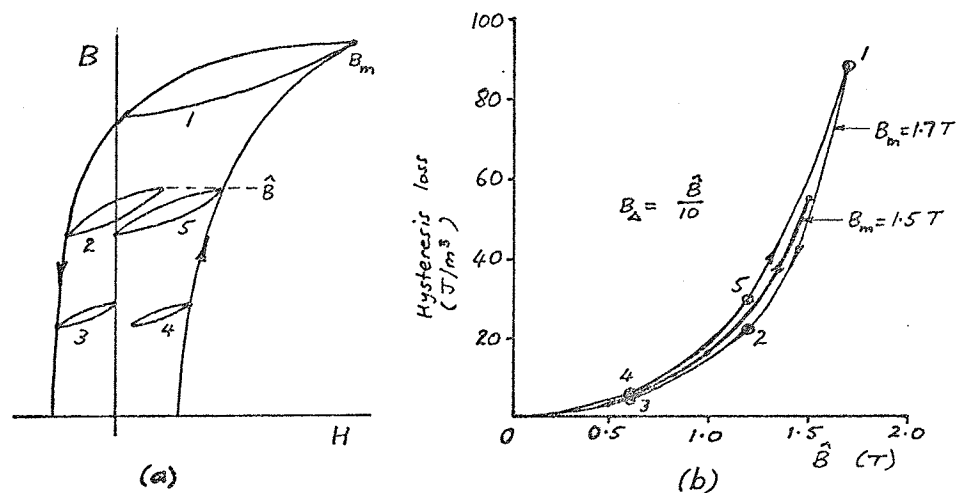
Fig. 3.20 Hysteresis loss for incremental loops at several
points on a normal loop, 1% Si steel (from Spooner, table 111,
ring C)

Further work on the effect of magnetic history on hysteresis
loss using the ballistic method was reported by Greig & Shurmer in
1953.[46] Their results for a ring of 3.5% Si iron, with incremental
loops of amplitude B_Δ up to 0.15 T on a normal loop of B_m = 1.0 T,
showed the loss to be dependent on B_b and B_Δ only, the loss being the
same for loops of the same B_b and B_Δ on each side of the normal loop.

3.2.3   A.C. test methods

3.2.3.1   Introduction

This section refers to test methods for obtaining permeability and losses when a periodic field at power frequency or higher is superposed on a steady field. The results may differ from those obtained by the ballistic or slowly varying field methods because of the effect of waveform distortion and eddy currents. Waveform distortion may affect the results in three ways: by changing the relation between peak, r.m.s. and fundamental amplitudes, by making the time average of flux density or current not equal to the amplitude average, and by causing additional losses. Eddy currents increase the measured loss and decrease the measured permeability (because H_Δ is larger for a given B_Δ).

3.2.3.2   Waveform distortion

Fig. 3.21 shows the current and flux density waveforms for a displaced loop, (a) for sinusoidal flux density and (b) for sinusoidal current. The effect of the displacement is to introduce even harmonics into the distorted waveforms, making the time average $(H_{av} = \frac{1}{T} \int_0^T H \, dt)$ unequal to the amplitude average $(H_b = \frac{\hat{H} + \check{H}}{2})$. The ballistic or slowly varying field methods naturally give amplitude averages for the bias fields. In an a.c. test the bias field would normally be the time average.

(a)   (b)
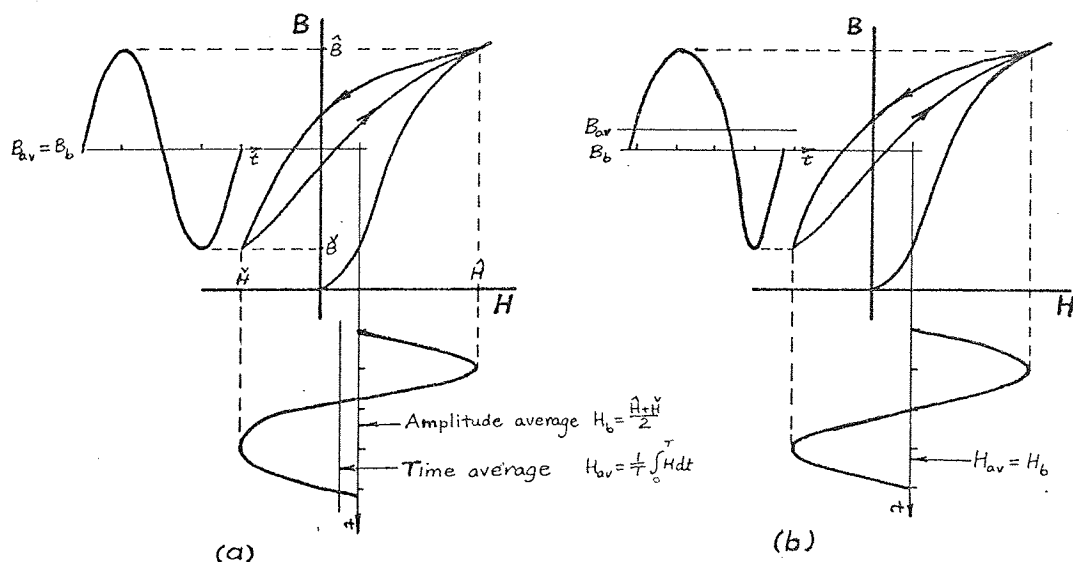
Fig. 3.21   Waveform distortion with superposed fields
           (a) sinusoidal B_Δ
           (b) sinusoidal H_Δ

The distortion of B or H means that the permeability can be defined in several ways, as the ratio of peak, r.m.s., or fundamental quantities. This problem is common to a.c. tests with no biasing field, but is worse for tests with a biasing field, where the harmonics are larger. The relevant British standard[47] recommends the latter definition; measurements comparing the three definitions are reported in section 3.2.3.5.

The addition of the even harmonics made it especially difficult to measure peak flux density in the past. The normal method of measurement is to full-wave rectify and average the voltage induced in a secondary coil $\left(\Delta\emptyset = \int_{t_1}^{t_2} e \, dt \text{ where } e = 0 \text{ at } t = t_1 \text{ and } t_2 \text{ when } B = \check{B} \text{ and } \hat{B} \right)$. When even harmonics are present the zeros of the e.m.f do not occur at 180° intervals, and in the past special adjustable contact-time commutators were needed. Nowadays semi-conductor rectifiers would ensure cut-off at the zeros of e.m.f.

Waveform distortion may cause additional losses in the iron specimen and in the exciting circuits. The additional eddy-current loss in the iron is constant only for thin laminations with a constant r.m.s. alternating flux density. The problem of harmonic losses in the exciting circuits is of two types. One type also occurs in experiments without superposed d.c. and arises when the flux density is meant to be sinusoidal, and losses are measured with a bridge or a.c. potentiometer. The harmonics of the non-sinusoidal current cause losses in the resistance of the exciting circuit. But the power supplied by the source is at fundamental frequency only, the iron acting as a frequency converter to produce the harmonic power. This power is included in the input to the specimen, and is therefore included in fundamental frequency measurements made by a bridge or a.c. potentiometer. A wattmeter, on the other hand, works from the true current and voltage and gives the net power into the iron.

The other type of harmonic loss problem occurs when special circuits are used to superpose the steady field, and is caused by harmonic currents flowing in these circuits. The losses can be eliminated, or

Further waveform distortion may be caused by the impedance of the a.c. exciting circuit. For example, in sinusoidal flux density experiments, non-sinusoidal current flowing through series impedance produces a non-sinusoidal voltage drop, distorting the voltage applied to the specimen. Various feedback techniques have been proposed to reduce this effect.

3.2.3.3 Circuits

Several different circuit arrangements have been used for the superposition of a steady field on a periodic field with a minimum of distortion.

(a) One winding D.c. and a.c. supplies are connected in parallel or in series and applied to the exciting winding, as shown in figs. 3.22 (a) and (b) respectively. The parallel circuit provides independent
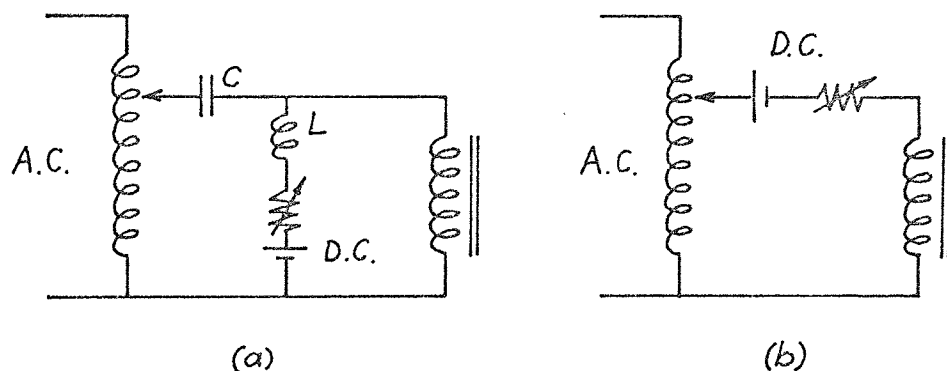
Fig. 3.22 One-winding circuits for supplying steady and
periodic fields
(a) parallel
(b) series

control of the two supplies. The impedance of the series blocking capacitor (C) may cause distortion of the a.c. voltage if sinusoidal flux is required. If sinusoidal current is required, extra series impedance may be added in addition to C, but the non-sinusoidal voltage across the parallel branch may cause harmonic losses in the d.c. supply circuit and distortion of the winding current (owing to the subtraction of the parallel branch harmonic currents) unless the blocking inductance (L) is large. The parallel circuit is recommended by B.S. 933: 1941[47] and was used by Carter and Richards (1950)[48],

Mondal et al. (1966)[49] and Choudhury et al. (1967)[50]. Only sinusoidal flux was considered, and for low ranges of B_Δ (up to 0.1 T) the circuit was used together with an Owen bridge[50] (which introduces significant series impedance). For higher ranges of B_Δ (up to 1.3 T) an electrostatic wattmeter, bridged - T network or feedback technique was used[49,50].

The series circuit can be made suitable for sinusoidal current by adding a large series air-cored reactor, according to the level of a.c. voltage available. A series resistor would not be used because it would reduce the direct current, and the reactor should be air-cored to avoid a decrease of inductance by the direct current and to avoid extra iron losses. The circuit can be rearranged slightly for sinusoidal flux by providing a variable d.c. supply to a low series resistance. At all times there is some interaction between the a.c. and d.c. controls, and a further disadvantage is that both d.c. and a.c. must flow through the current and power measuring instruments. Only experiments with sinusoidal flux were reported using the series circuit. Charlton and Jackson (1925)[51] used the circuit as shown in fig. 3.22 (b), and it was used with modifications to reduce the series impedance and interdependence of a.c. and d.c. by Chubb and Spooner (1915)[33], Edgar (1933)[52] and Sims and Clay (1935)[36]. Values of B_Δ up to 1.8 T were used by Edgar.

(b) <u>Two windings</u> The steady field is produced by exciting a second winding with d.c. as shown in fig. 3.23. Independent control and measurement of the a.c. and d.c. is possible, a low series impendance for sinusoidal flux can be achieved, and a resistor or an air-cored reactor can be inserted in the a.c. circuit for sinusoidal current.

Apart from the fact that two windings are required, the main disadvantage is that a large air-cored reactor (L) is needed in the d.c. circuit to limit the induced alternating current which would cause additional losses and contribute
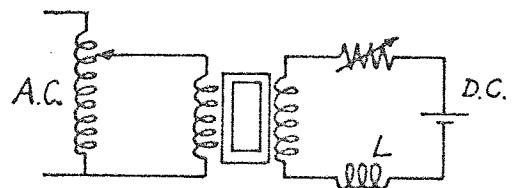
Fig. 3.23 Two-winding circuit for superposing steady and periodic fields

to the periodic field. The circuit was used by Rosenbaum (1912)[40], Niwa and Asami (1923)[53], Ebinger (1930)[27] and Kresadlo (1969)[55] with sinusoidal flux, and by Niwa et al. (1924)[54] with sinusoidal current. The maximum value of B_Δ used by Kresadlo was 2.0 T, and that of H_Δ used by Niwa et al. was 3200 A/m.

(c) <u>Two cores</u>   An arrangement of two identical cores, each with two windings, is used to eliminate the induced alternating currents in the d.c. windings, these windings being connected in series in such a sense that the induced alternating voltages oppose one another. Two possible arrangements are shown in fig. 3.24.
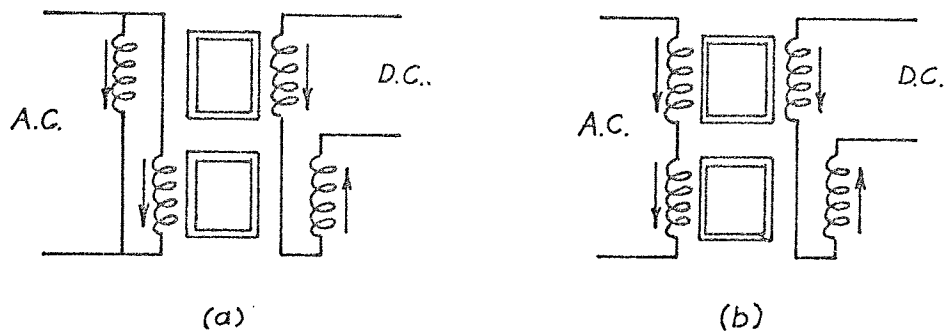
<u>Fig. 3.24</u>   Two-core circuits for superposing steady and
periodic fields
(a) Parallel
(b) Series

For sinusoidal flux the voltage across the a.c. windings should be sinusoidal (neglecting the voltage drop in the winding resistance). This can be achieved with the parallel circuit of fig. 3.24 (a). Because of the sinusoidal flux the voltages induced in the d.c. windings are sinusoidal and may oppose exactly to give zero alternating current in the d.c. circuit. The current in each a.c. winding does contain even harmonics, but because the even harmonics are in opposite directions,   they may flow around the loop formed by the parallel a.c. windings. Thus no even harmonics are present in the supply current and distortion due to series resistance apart from the winding resistance is reduced.

The series circuit of fig. 3.24 (b) is worse than the parallel circuit for sinusoidal flux because alternating currents flow in the d.c. circuit, and waveform distortion is not reduced. In fact the flux cannot

be sinusoidal as the currents required by each winding for sinusoidal flux are different, an impossibility with a series connection. Thus the alternating voltages induced in the d.c. windings contain even harmonics and even harmonic currents flow in the d.c. circuit. The voltage across each a.c. winding is different owing to the even harmonics, but these are equal and opposite and the resultant voltage across both windings may be sinusoidal. An equilibrium value is reached by the even harmonic currents in the d.c. circuit as they tend to reduce their source, the flux distortion. This was confirmed by Charlton and Jackson[51], who observed a substantially constant a.c. current in the d.c. circuit as the d.c. circuit resistance was varied.

Neither circuit can be used with complete effectiveness if sinusoidal current is desired. The series circuit would be suitable, apart from the even harmonic currents in the d.c. circuit. The parallel circuit is unsuitable for sinusoidal current in the same way that the series circuit is unsuitable for sinusoidal flux. Different voltages are required across each winding for sinusoidal currents, and the parallel connection prevents this. The total supply current may be sinusoidal as even harmonic currents can flow around the parallel circuit loop. No alternating currents flow in the d.c. circuit, however, because the induced alternating voltages oppose exactly (they are the same in the d.c. circuit, neglecting the a.c. winding resistance).

The two-core circuits have been applied mostly in d.c. controllable reactors (including transductors and magnetic amplifiers) rather than in iron testing. The circuits were investigated by Coales in 1908[56], and the production of second harmonic currents in the d.c. side was discussed by Boyajian (1924)[57], Charlton and Jackson (1925)[51] and Johnson et al. (1949)[30]. The first use of the method for iron testing was by Vallauri in 1911[58], who used the parallel connection for sinusoidal flux, and this idea was revived by Choudhury et al. in 1966[59]. Shiner (1967)[60] claimed that this circuit was in use at his firm, but in fact the circuit he described is a variation of the series connection (a single a.c. coil is

wound over both cores). The series connection was also used by Goldschmidt (1930)[61] for very small values of B_Δ . The two-core methods were not used with sinusoidal current, and their application for this purpose was not discussed (although Boyajian [57] used the parallel connection with sinusoidal total current). .

(d) <u>Feedback</u> All the above methods suffer from the disadvantages that very low series resistance is necessary to obtain sinusoidal flux of a reasonable amplitude, or that a very high series impedance is required for sinusoidal current (necessitating a high alternating voltage). These disadvantages can be largely overcome by using feedback. Electronic amplifiers are required, so feedback was first applied to magnetic testing in 1953, and to incremental testing circuits in 1967. No relevant results were reported. A discussion of feedback methods is therefore left till chapter 5, section 5.3.2, where their application for sinusoidal current is considered, and to appendix 8.3.

3.2.3.4 <u>Eddy-current effects</u>

Specimens for the measurement of permeability by a.c. methods are usually in the form of a ring or square of laminations. If B_a is the space average flux density in the core of area A, and H_s is the applied field strength on the mean path of length 1 , then the complex a.c. permeability $\dot{\mu}_e$ is defined by

$$\dot{\mu}_e = \frac{B_a}{\mu_o H_s} \tag{3.13}$$

This may be written in terms of the e.m.f. E_i induced in the a.c. winding of N turns and the alternating current I , assuming sinusoidal variations, as

$$\dot{\mu}_e = \frac{E_i}{\mu_o j\omega AN} \frac{1}{NI}$$

$$= \frac{1}{\mu_o \omega AN^2} (\omega L - jR_e) \tag{3.14}$$

where $\frac{E_i}{I} = R_e + j\omega L$ is the impedance of the a.c. winding less the d.c. resistance. Thus measurements of impedance suffice to determine μ_e. Unlike d.c. permeability, the a.c. permeability does not relate flux

density and field strength at a point, but is a property of the core as a whole.

By using linear eddy-current theory for the thick lamination problem it may be shown (ref 22, p.770; ref 62, p. 251) that

$$\dot{\mu}_e = \frac{2\mu \sinh \frac{\dot{\alpha} b}{2}}{\dot{\alpha} b \cosh \frac{\dot{\alpha} b}{2}} \qquad (3.15)$$

where μ = d.c. permeability, assumed constant throughout the lamination.

   b = lamination thickness

$$\dot{\alpha} = \frac{1+j}{\delta} \quad , \quad \delta = \sqrt{\frac{2\rho}{\omega \mu_o \mu}}$$

Therefore

$$\frac{|\dot{\mu}_e|}{\mu} = \frac{\sqrt{2}\delta}{b} \sqrt{\frac{\cosh \frac{b}{\delta} - \cos \frac{b}{\delta}}{\cosh \frac{b}{\delta} + \cos \frac{b}{\delta}}} \qquad (3.16)$$

This is the same as the ratio $\frac{|\phi|}{|\phi_o|}$ where $\phi = B_a A$ is the total a.c. flux and $\phi_o = \mu \mu_o H_s A$ is the flux if there were no eddy currents.

$\frac{|\dot{\mu}_e|}{\mu}$ is plotted against $\frac{b}{\delta}$ in fig. 3.25, from which it can be seen that $|\dot{\mu}_e|$ is about 2% less than μ when $b = \delta$, and is more than 10% less when b is more than 1.5 δ. For a typical lamination thickness of 0.35 mm, resistivity of 4×10^{-7} Ωm and d.c. permeability of 500, $b = \delta$ at a frequency of 1700 HZ. The variation of $|\dot{\mu}_e|$ with μ for several frequencies with such a lamination thickness and resistivity is shown in fig. 3.26. At a frequency of 50 HZ $|\dot{\mu}_e|$ is practically equal to μ for usual values of μ, but at 5000 HZ $|\dot{\mu}_e|$ can be much less than μ and, in addition, variations of μ produce smaller variations of $\dot{\mu}_e$.

Unfortunately, the simple classical theory just outlined does not always give reliable results, especially when the depth of penetration is close to or less than the sheet thickness. Careful experiments to compare a.c. and d.c. permeabilities (with no superposed steady field) were reported in 1935 by Webb and Ford [63]. Experiments were carried out on 0.4mm lohys sheet (0.2% Si, $\rho = 1.4 \times 10^{-7}$ Ωm) at 50 HZ and on
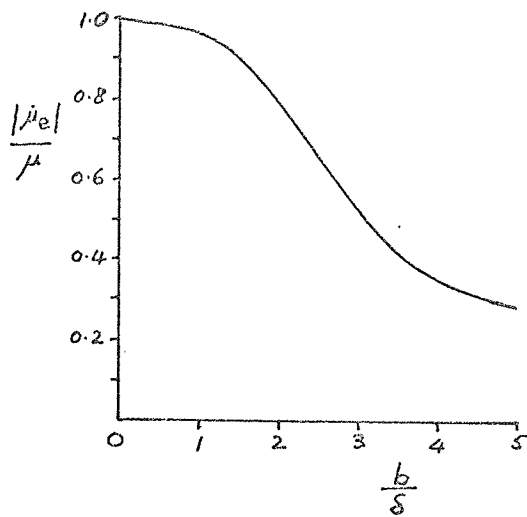
Fig. 3.25 A.c. permeability (as a
fraction of d.c. permeability) for a
core of laminations, plotted against
lamination thickness/depth of
penetration.
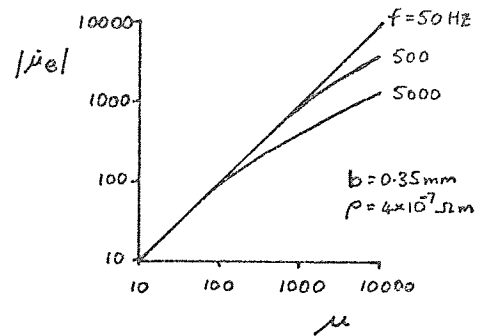
Fig. 3.26 Variation of a.c.
permeability with d.c.
permeability for a typical
lamination at several
frequencies.

o.3 mm stalloy sheet (4% Si, $\rho = 5.5 \times 10^{-7}$ Ωm) [75] at 50 HZ and 500 HZ.
Peak values of B and H were recorded in the a.c. tests, and the results
for lohys are shown in fig. 3.27. It can be seen that a reduction of
permeability with increase of frequency occurred, the reduction being a
maximum in the region of maximum permeability, as predicted by the above
classical theory (fig. 3.26). No reduction was observed for stalloy at
50 HZ, but there was a reduction in the region of maximum permeability
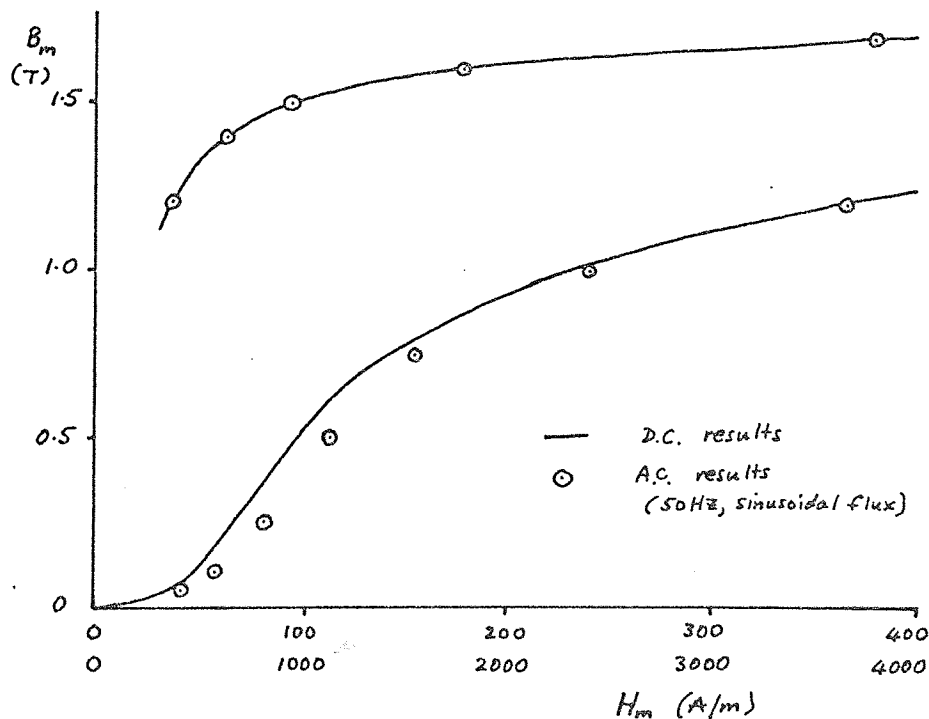
Fig. 3.27 Comparison of a.c. and d.c. B/H curves on 0.4mm
lohys sheet (from Webb and Ford)

at 500 HZ. The reductions, however, were greater than is predicted by the classical theory. For lohys at H_m = 115 A/m, μ = 4300, $\frac{b}{\delta}$ = 0.99 at 50 HZ and fig. 3.25 gives $\left|\frac{\dot{\mu}_e}{\mu}\right|$ = 0.98, compared to the observed value of 0.82. For stalloy at H_m = 115 A/m, μ = 5600, $\frac{b}{\delta}$ = 1.41 at 500 HZ giving $\left|\frac{\dot{\mu}_e}{\mu}\right|$ = 0.91, compared to the observed value of 0.75.

Webb and Ford made no comparisons between theory and experiment. The discrepancies can possibly be explained by considering the domain structure of the sheet. Waveform distortion cannot be the cause as sinusoidal flux was used for the results quoted above, and current distortion would have increased as H_m increased, while the difference between a.c. and d.c. permeabilities decreased.

A simplified domain model was considered by Bishop and Lee in 1963[64], and for very small fields they calculated the variation of the real and imaginary parts of $\frac{\dot{\mu}_e}{\mu_i}$ with $\frac{b}{\delta_i}$, where μ_i is the d.c. permeability for small fields and δ_i is the corresponding depth of penetration. They found that the reduction of permeability with frequency was more than that predicted by the classical theory, the extra reduction depending on the domain half-width to sheet thickness ratio $\frac{a}{b}$. Assuming the theory to hold also for the region of maximum d.c. permeability (implying no irreversible wall movements) and replacing μ_i by μ , a value of $\frac{a}{b}$ = 0.6 gives the measured values of $\left|\frac{\dot{\mu}_e}{\mu}\right|$ for stalloy at both frequencies. This requires a domain width 2a of 0.36 mm, slightly high for non-oriented sheet, but of the correct order of magnitude. For lohys, however, $\frac{a}{b}$ = 2.5 is necessary, implying an impossibly high domain width of 2.0 mm. (Bloor and Martin (1959)[65] measured domain widths in the range 0.01 to 0.075 mm for 0.3 mm non-oriented 2.79% Si iron sheet, and widths up to 1.0 mm have been measured for single crystals and grain-oriented sheets (ref. 22, p. 536 and refs. 66 - 68)).

The domain theory is still being developed to allow for complex domain structures (as occur in non-oriented sheets), for non-magnetic inclusions, for domain-wall bowing, and for non-uniform wall

mobilities [67-70]. Such developments may enable more accurate
calculations of a.c. permeability and eddy-current loss.

Another explanation for the shortcomings of the simple
classical theory was put forward by Peterson and Wrathall in 1936[71], who
suggested that laminations might not be homogeneous. They used classical
theory to show that a thin surface layer of low permeability (caused by
the rolling process) would be sufficient to produce the observed
discrepancies. Experiments on materials with the surface etched off and
on laminations with a thin surface layer of copper supported the theory.

3.2.3.5 μ_Δ by a.c. methods

Early measurements of μ_Δ by a.c. methods were concerned with
its variation along the normal magnetisation curve and around a normal
hysteresis loop (figs. 3.5 and 3.6). Experiments by Smith[72] and Fondiller
and Martin[73] in 1921 showed the general 'butterfly loop' shape of the
variation, but complete details of the specimen and circuits were not
given. H_Δ was kept constant and results for only one, small value were
published in each paper. Smith used a frequency of 500 HZ and eddy
current effects were evidently large, as he said that the maximum a.c.
permeability was one fifth of the maximum d.c. permeability. Fondiller
and Martin used 1000 HZ. In 1929 Sizoo[28] considered several small values
of H_Δ (0.044 to 5.6 A/m) and showed the variation of μ_Δ as a function of

(a)

(b)
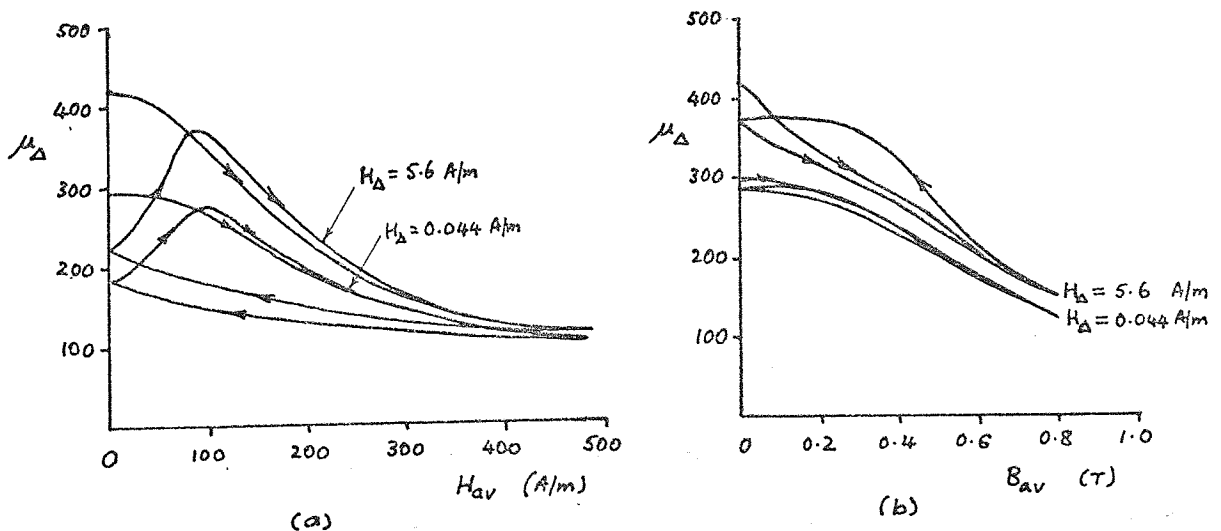
Fig. 3.28   Variation of μ_Δ around a normal hysteresis loop
(from Sizoo)

both H_{av} and B_{av} around one normal
loop. A frequency of 500 HZ was used,
but the thickness of the 3% Si steel
laminations in his sample was not
specified. Some of his results are
shown in fig. 3.28 and it can be seen
that μ_Δ depends on the previous
magnetic history for $H_\Delta > 0$. Results
were reported by Goldschmidt[61] in
1930 for the variation of
reversible permeability around
several normal hysteresis loops,
and fig. 3.29 shows the variation

Fig. 3.29 Variation of
reversible permeability
around several normal loops
(from Goldschmidt)

with H_{av}. The sample consisted of steel wires of unspecified diameter
and the frequency was not given either.

Later measurements of μ_Δ by a.c. methods were only concerned
with its variation along the normal magnetisation curve (i.e. at the
peaks of normal hysteresis loops). Ebinger (1930)[27] presented results in
the form of the curves and equations already mentioned in section 3.2.1.2
(fig. 3.9, and eqns. 3.4 and 3.5). He considered values of B_Δ up to
0.23 T , B_{av} up to 1.5 T, and claimed the results were valid for all
normal steel laminations at power and telephone frequencies. No exact
details of the samples and frequencies were given. In 1933 Edgar[52]
reported measurements on three grades of silicon-steel laminations, using
ring samples and a frequency of 60 HZ with sinusoidal flux. The r.m.s.
value of alternating current was recorded, and the results presented in the
form of B/H curves, as shown in fig. 3.30. (The curves were in fact
continued up to H_Δ (r.m.s.) $\simeq$ 9000 A/m, with the voltage form factor
varying by 9% from 1.111 at the higher flux densities.)

Comparisons of three a.c. methods with the ballistic method
were published by Sims and Clay in 1935[36]. Sinusoidal flux at power
frequency was used on a ring sample of 0.40 mm stalloy laminations.
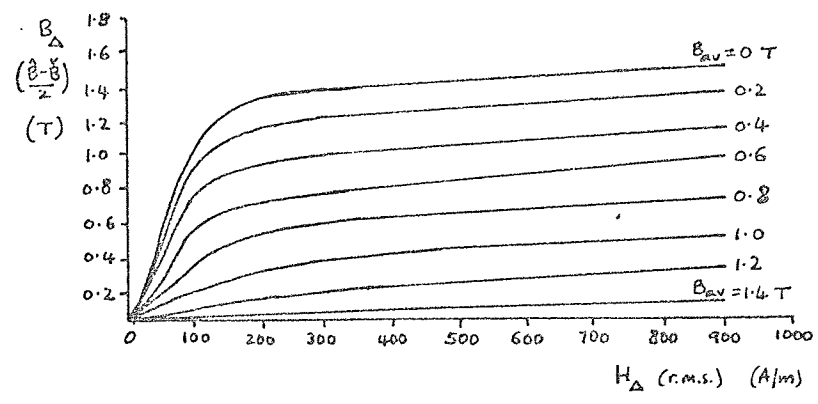
Fig. 3.30 A.C. B/H curves at several direct flux densities, 0.48 mm, 2.5% Si steel laminations (from Edgar)

The a.c. methods gave μ_Δ in terms of peak, r.m.s. and fundamental quantities, for constant values of H_{av}. Some of the results are shown in fig. 3.31 for H_{av} = 545 A/m. (The ballistic tests have already been discussed in section 3.2.1.3, fig. 3.18). Eddy-current effects were shown to be small by check tests without superposed d.c., and the difference between the curves was attributed to current waveform distortion. Because of the peaky nature of the current wave, the fundamental and r.m.s. values of H_Δ were less than the peak value, leading to a higher μ_Δ (curves 2 and 3 above curve 4). Curve 4 obtained from peak values is below curve 1 from ballistic tests because of the difference between the amplitude and time averages of the steady field strength $\left(H_b \text{ and } H_{av}\right)$ mentioned in section 3.2.3.2 (fig. 3.21 (a)). With sinusoidal flux, H_b can be much greater than H_{av}, so the set of ballistic results to compare with curve 4

(a)

(b)

Curve 1 : ballistic
" 2 : fundamental
" 3 : r.m.s.
" 4 : peak
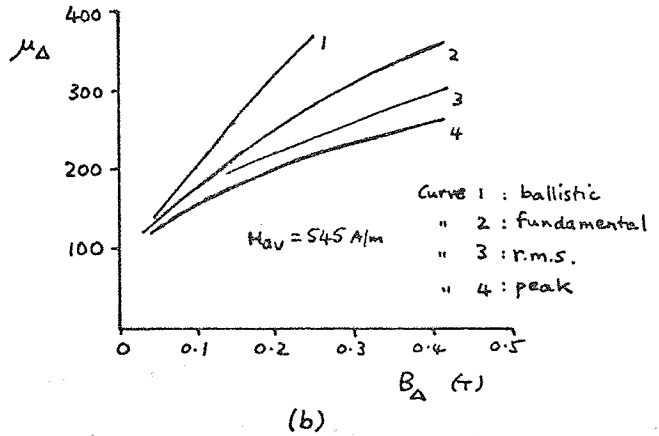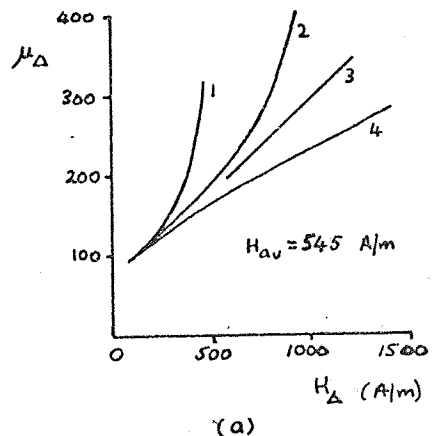
Fig. 3.31 Comparison of μ_Δ by a.c. and ballistic methods, 0.40 mm stalloy (from Sims and Clay, fig. 23)

A.C. methods with sinusoidal flux and constant H_{av}.

should in fact be for incremental loops with higher values of H_b, which have lower permeabilities. Further measurements regarding the effects of waveform distortion were made by Sims and Spinks (1938)[74], confirming the work of Sims and Clay.

Measurements of both the angle and modulus of μ_Δ were made by Carter and Richards (1950)[48]. Ring samples of several grades of silicon-steel sheet were used with frequencies of 50 HZ and 800 HZ and B_Δ in the range 0.0001 to 0.1 T. Most readings, however, were taken at 800 HZ, and with B_Δ in the range 0.0001 to 0.01 T, as the authors were interested in the design of smoothing chokes for telephone exchanges. $\mu_\Delta \angle \vartheta$ calculated from impedance measurements with an Owen bridge (and therefore in terms of fundamental amplitudes) was tabulated for fixed values of B_Δ at several values of H_{av}. A plot of some of the results for 0.35 mm super-stalloy (4.3% Si) (fig. 3.32) shows the decrease of μ_Δ with increase of H_{av}, and, as the frequency increases, the decrease of μ_Δ and the increase of $\angle \vartheta$ owing to eddy currents.

(a) Angle (b) Amplitude
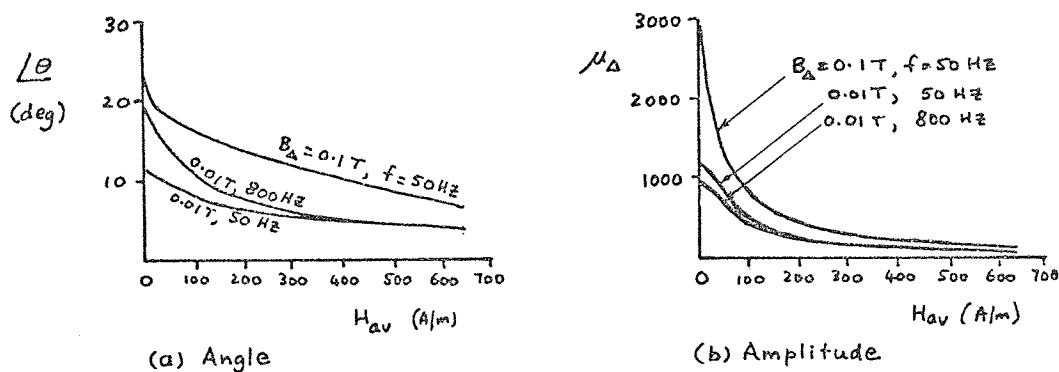
Fig. 3.32 Complex incremental permeability ($\mu_\Delta \angle \vartheta$) as a function of H_{av} at several frequencies and alternating flux densities, 4.3% Si iron (from Carter and Richards, table 2)

Sheet steel manufacturers in Great Britain [75-77] publish data for their products (oriented and non-oriented silicon steel) in the form of graphs of μ_Δ against H_{av} at constant B_Δ, as shown in fig. 3.32 (b), for B_Δ in the range 0.001 T to 0.5 T and for frequencies from 50 HZ to 500 HZ. Results for B_Δ = 0.5 T (only given by the Steel Company of Wales) would probably be subject to waveform distortion, as shown by Sims and Clay (fig. 3.31). An American manufacturer[78] published results in a form more suitable for comparison with the normal permeability, and covered a

wider range of B_Δ (fig. 3.33). Exact circuit details were not given,
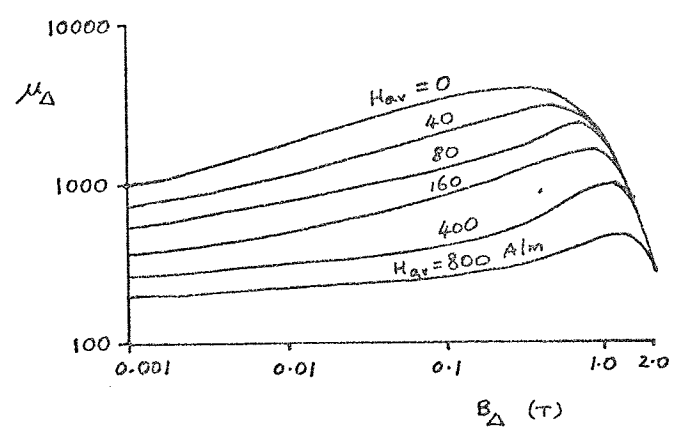
Fig. 3.33 μ_Δ as a function B_Δ for several values of H_{av}, 0.35 mm, 3.6% Si steel laminations at 60 HZ with μ_Δ from r.m.s. quantities. (from ref. 78)

so the distortion cannot be assessed. The core dimensions were given, however, and these were not very suitable for magnetic testing[42,43], the core being rectangular with a thickness to length ratio of 1:3 in one direction and 1:5 in the other.

Measurements of μ_Δ on a solid specimen using an a.c. method were reported recently by Langman (1970)[79]. H_Δ was of the order of 125 A/m, very small for the steel used, which was representative of that used in railway lines, having a maximum normal permeability of 160 at 3000 A/m. The change of flux for H_Δ = 125 A/m with a superposed field was considered to be too small for measurement with a galvanometer and search coil, so a.c. at a frequency of 5 kHZ was used, allowance for eddy currents being made with the classical constant permeability theory.

It was stated that preliminary tests showed that μ_Δ did not change measurably when H_Δ was varied between 5 and 125 A/m. Unfortunately, the values of H_{av} used for these preliminary tests were not mentioned, and the only check on the validity of the constant permeability theory was for $H_b \simeq 0$, where μ_Δ agreed with the normal permeability measured ballistically. (On the basis of earlier work, however, the theory should be satisfactory, as the variation of μ_Δ with H_Δ decreases as H_{av} or H_b increases; see Sims and Clay, fig. 3.18, for example).

Langman's results for μ_Δ were presented in the form shown in fig. 3.34 (a). Since H_Δ was small, and μ_Δ did not vary for changes of H_Δ, μ_Δ can be taken to be the reversible permeability μ_{rev} and the time average fields H_{av}, B_{av} equal to the amplitude averages H_b, B_b. Langman gave a curve of B_b against H_b, so fig. 3.34 (a) may be used to plot the permeability in the form used by Gans, i.e. $\frac{\mu_{rev}}{\mu_i}$ against $\frac{B_b}{B_s}$. This is done in fig. 3.34 (b), with $\mu_i = 52$ and $B_s = 2.2$ T , and it can be seen that there is fair agreement with Gans' formula (eqn. 3.1), giving further confidence in both Langman's method and the formula.
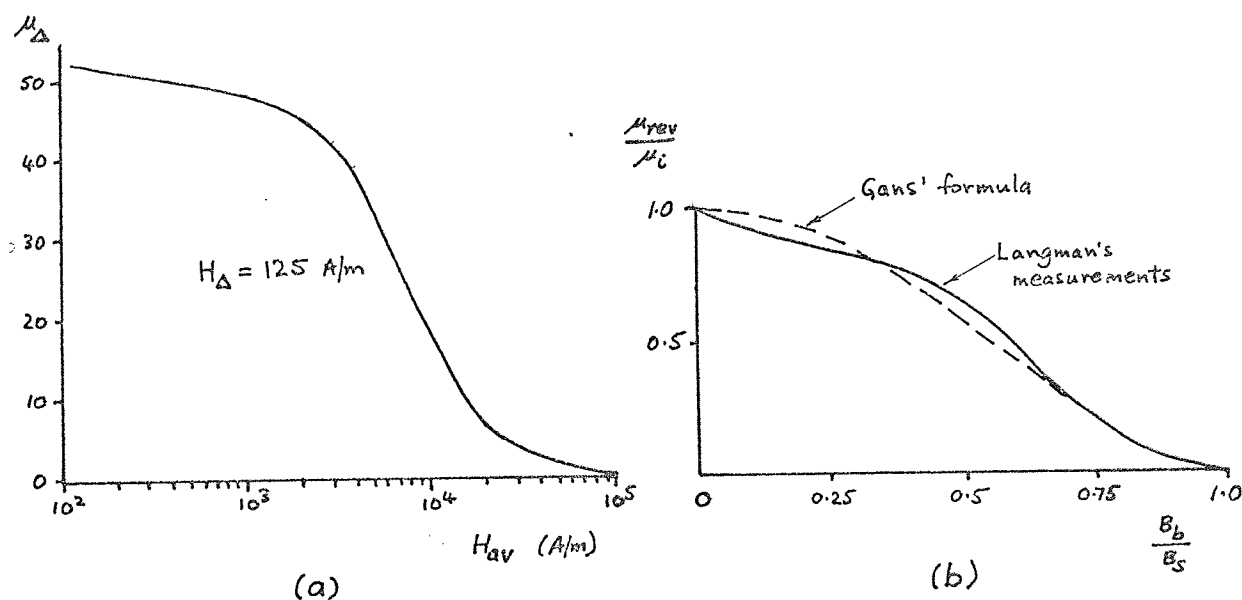
Fig. 3.34   Langman's results for rail steel
(a) Original form
(b) Gans' form

3.2.3.6   Losses by a.c. methods

All the useful published measurements of loss by a.c. methods for incremental loops on the normal magnetisation curve were made with a wattmeter and one of the circuits of figs. 3.22 (b) and fig. 3.23. Most of the results were with sinusoidal flux with a sample of silicon-iron laminations. No work on solid iron was reported.

Rosenbaum's results obtained by the ballistic method were mentioned in section 3.2.2. The same tests were carried out with a.c. and a wattmeter. After separation of eddy current losses, assumed to be proportional to f^2 and constant for the tests at constant B_Δ, the remaining hysteresis losses agreed with the ballistic results to within 1%

at $H_{av} = 0$ and to within 5% at the higher values of H_{av}. Allowance was made for the difference between H_{av} and H_b in comparing the two methods. Differences were put down to non-uniform flux distribution in the transformer-core sample which was not an ideal shape for magnetic testing. Agreement between ballistic and wattmeter methods was also obtained by Vallauri[58].

In 1923 Niwa and Asami[53] measured hysteresis loss in rings of 3.35% Si steel laminations. To avoid eddy-current loss the laminations were only 0.0825 mm thick and a frequency of 50 HZ used. A plot of total losses against frequency at constant B_Δ was linear, confirming that eddy current loss was negligible. The ranges of B_Δ and B_b ($B_{av} = B_b$ for sinusoidal flux) were similar to those covered by Chubb and Spooner (see section 3.2.2) and the results (fig.3.37(b)) for incremental loops on the normal magnetisation curve were like those shown in fig. 3.19. They said their results could be described to within 10% by a formula of the type proposed by Ball (eqn. 3.12), but they observed a decrease of loss with B_b for $B_\Delta > 1.0$ T, so their conclusion could not apply for such values of B_Δ.

Niwa and Asami also studied the losses of incremental loops at positions around a normal hysteresis loop. Unlike some of Spooner's results discussed in section 3.2.2 (fig. 3.20) they found that for a given B_Δ and B_b the loss was practically independent of the position on the normal loop, agreeing with the work of Greig and Shurmer (also mentioned in section 3.2.2). But only one normal loop was considered for each value of B_Δ, the normal loop was not the same for each value of B_Δ, and the amplitudes of the normal loops ($B_m = 1.3$ T for $B_\Delta = 0.1$ T and $B_m = 1.6$ T for $B_\Delta = 0.2$ T) were less than the maximum used by Spooner. Niwa and Asami also plotted the loss as a function of H_{av} and showed it to be practically a single-valued function of H_{av} as well as of B_b.

Losses for other materials were plotted against H_{av} for constant values of B_Δ by Charlton and Jackson (1925)[51], Mondal et al (1966 and 1967)[49,50], and Kresadlo (1969)[55]. Only incremental loops on the normal magnetisation curve were considered, the flux was sinusoidal, and eddy

current loss was included in the plotted loss. Niwa and Asami's results are given in fig. 3.37 (a). Charlton and Jackson's curves for 0.55 mm U.S. electric sheet at 60 HZ were similar, except that curves for values of B_Δ up to 1.47 T were given and the loss decreased as H_{av} increased for B_Δ greater than 1.1 T.

Mondal et al. in 1966 compared the loss at 50 HZ in a sample of stalloy laminations measured with an electrostatic wattmeter and an Owen bridge. Measurements were taken up to B_Δ = 1.25 T, and the wattmeter results were similar to those of Niwa and Asami. Distortion of the current waveform caused the Owen bridge measurements to be up to 50% higher than the wattmeter measurements at the higher values of H_{av} (discussed by the authors, and earlier[80], and see section 3.2.3.2). In 1967 Mondal et al. reported losses for stalloy at 50 HZ again, obtained using a current-feedback circuit with the Owen bridge. The authors did not compare their new results with the previous results, and when this is done it can be seen that the new losses increase much more rapidly as H_{av} increases. Later results for stalloy at 50 HZ and H_{av} = 0 obtained by Mondal et al. (1967)[81] with an electrostatic wattmeter agreed with the 1966 results. No details about the 1966 stalloy sample were given, so we do not know if it was the same as the first or second 1967 sample, which were of slightly different form, but containing sheet of the same thickness (0.38 mm). However, because of the strange shape of the curves obtained by the authors with the current-feedback circuit, these results should be treated with caution (the curves showed an initial decrease of loss with H_{av} as well as the later rapid increase).

Kresadlo measured losses in 0.12 mm orthoperm laminations, using a wattmeter and values of B_Δ up to 2.0 T. Frequencies from 10 to 70 HZ were used, and he showed that the losses did not obey classical theory. His results for 30 HZ are shown in fig. 3.35, and it can be seen that they are generally similar to Niwa and Asami's (fig. 3.37 (a)), apart from the peak at high values of B_Δ .

Edgar (1933)[52] carried out work on similar lines to that of

Rosenbaum and Niwa and Asami,
obtaining hysteresis loss as a
function of B_Δ for various
constant values of B_b, using
sinusoidal flux (when $B_{av} = B_b$) at
60 HZ. He used ring specimens of
various grades of silicon-steel
laminations, separated eddy current
loss, and achieved a wide range of
B_Δ and B_{av}. His results for
hysteresis loss were given in the
two forms used by Chubb and Spooner

Fig. 3.35 Total loss for incremental
loops on normal magnetisation curve,
0.12 mm orthoperm sheet, 30HZ (from
Kresadlo)

(fig.3.19), as shown in fig. 3.36 for low-silicon steel, the curves for
high-silicon steel being of similar shape.
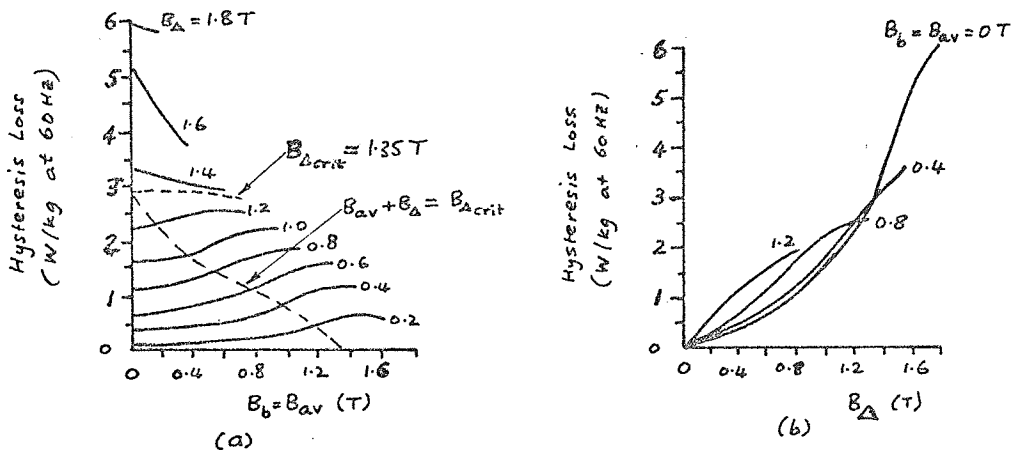
Fig. 3.36 Hysteresis loss for incremental loops on the normal
magnetisation curve, 0.48 mm, 2.5% Si steel laminations,
sinusoidal flux (from Edgar)

These curves confirmed what was suspected by Chubb and Spooner,
that the hysteresis loss at low values of B_Δ eventually begins to decrease
as B_b increases, just as at high values of B_Δ the loss always decreases
as B_b increases. A line may be drawn on fig. 3.36 (a) showing where
$B_\Delta + B_b = (B_\Delta)_{crit}$. The curves appear to change their trend of
increasing with B_b at points along this line.

The work of Niwa and Asami was continued by Niwa, Sugiura and
Matura (1924)[54]. They noted first that the areas of some ballistically
obtained normal hysteresis loops given in the earlier paper were within 1%

of the hysteresis losses measured by the a.c. method, further confirming that the eddy current loss was negligible. Then, using sinusoidal current instead of sinusoidal flux, they measured the loss for incremental loops on the normal magnetisation curve. The results are compared with the sinusoidal flux results in figs. 3.37 (a) and (b), and it can be seen that differences are not large, being greatest where the loss is most sensitive to the loop position (given by H_{av} and B_{av}). The differences can be explained by using fig. 3.21 and noting, for example, that an incremental loop with sinusoidal flux and a given H_{av} will be slightly further up the normal magnetisation curve than a loop with sinusoidal current and the same H_{av}.
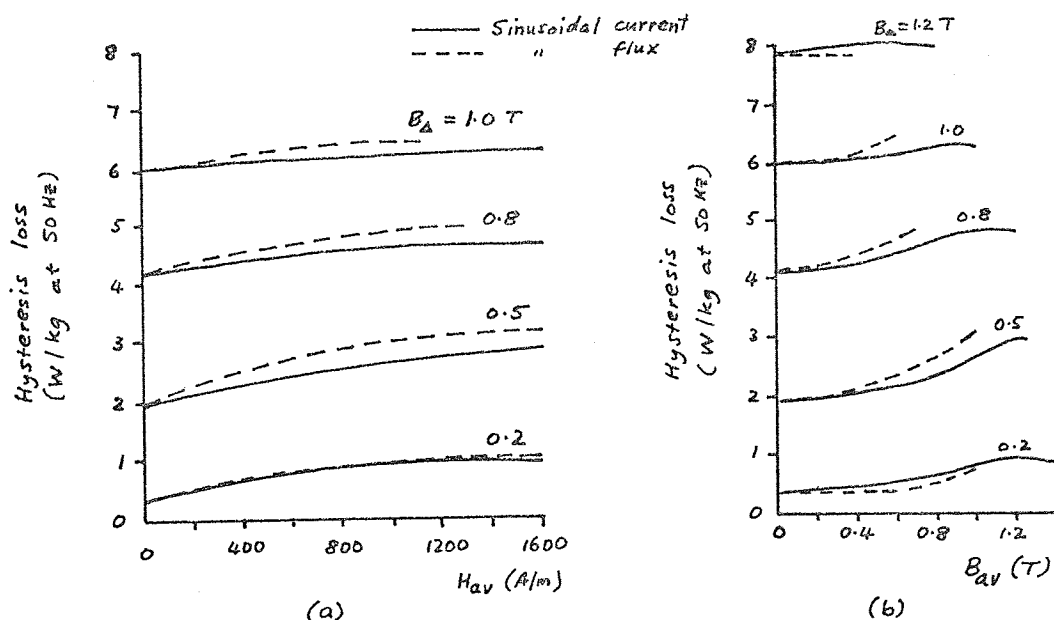
Fig. 3.37 Hysteresis loss for incremental loops on the normal magnetisation curve for sinusoidal flux and sinusoidal current, 3.35% Si steel laminations (from Niwa and Asami figs. 16 & 18, and Niwa et al. figs. 27 & 28)

Niwa et al. also plotted the variation of hysteresis loss with B_Δ for constant values of H_b, for sinusoidal current, as shown in fig. 3.38. Results were not given in terms of H_Δ except for values of H_Δ greater than H_b, for which a linear relation between hysteresis loss W_{hb}, H_Δ and H_b applied:

$$W_{hb} = a + b H_\Delta - c H_b \qquad (3.17)$$

They found this relation to hold also for the results of Chubb and Spooner,

with different values for the constants a , b and c.
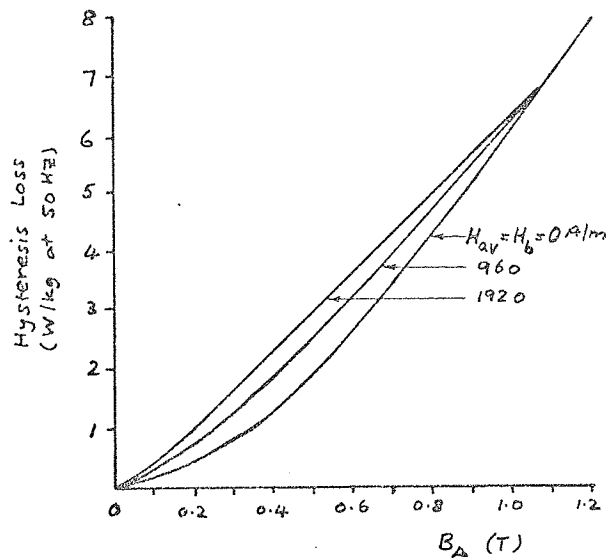
Fig. 3.38 Hysteresis loss for
incremental loops on normal magnetisation
curve, 3.35% Si steel sheet (from Niwa
et al., fig. 29) sinusoidal current

The only other reported results for losses at constant H_Δ were

those of Smith[72] and of Fondiller and Martin[73], both in 1921. Their

measurements of μ_Δ were discussed in section 3.2.3.5 where it was stated

that eddy-current effects were probably considerable. Only one, small

value of H_Δ was used for the loss measurements, as for the permeability

measurements, and the variation of loss along the normal magnetisation

curve and around a normal hysteresis loop was very similar to the variation

of μ_Δ ; in fact this was all Smith said about his loss results. Smith

plotted μ_Δ against B_{av} and Fondiller and Martin gave the loss as a function

of H_{av} . The form of the results is shown in figs. 3.5 and 3.6 and it can

be seen that the magnetic history had a large effect.

3.3 Steady field with non-parallel varying field

3.3.1 Work before 1931

In 1909, Gans[83] measured the effect of a superposed steady perpendicular field on the permeability of several materials for very small varying fields μ_{rev}. (Gans mentioned that earlier work had been done on the effect of a transverse field with larger varying fields, but his reference[82] was to an article which was mainly a bibliography of pre-1900 work, and there was insufficient time to study this work. In view of the state of the art before 1900, and of the later work, it is unlikely that much of importance is omitted). Disc specimens were placed inside a long solenoid, giving a longitudinal field, and this was placed between the poles of an electromagnet, giving the steady transverse field. Both fields were in the plane of the disc. The ballistic method was used to measure μ_{rev} for increasing values of the steady field, and the results were compared with μ_{rev} for parallel fields, as shown in fig. 3.39 for soft iron. This shows that μ_{rev} was reduced by the perpendicular field, but not as much as by the parallel field. The difference between the permeabilities at $B_b = 0$ was attributed to experimental error; difficulty was experienced in determining demagnetising factors and the flux density inside the samples. No expression was found for the transverse reversible permeability valid for all materials, like that found for the

Fig.3.39 Comparison of reversible permeability with superposed perpendicular and parallel fields, soft iron (from Gans)

parallel reversible permeability (eqn. 3.1), and the effect of a cyclic change of the steady field (previous magnetic history effect) was not reported.

Some experiments with larger values of varying longitudinal field were reported by Goldschmidt in 1910[84]. His sample was a wrought-iron tube which formed part of the magnetic circuit of a moving-coil meter. A coil wound around the tube produced the longitudinal field H_1, and a

conductor along the centre of the tube produced the transverse field H_t , so the resultant flux lines followed helical paths. Cyclic variations of H_l were carried out for several fixed values of H_t (of unspecified previous history). The results of only two tests were published, however, and these were in essential agreement with the later, more extensive results of Sugiura (figs. 3.41 and 3.42), except that Goldschmidt observed no change in hysteresis loss as H_t increased for loops of constant peak flux density $\simeq 1.6$ T, compared to a decrease observed by Sugiura.

3.3.2 Sugiura's experiments

In 1931 Sugiura[35] examined the effect of a polarising steady field on the hysteresis loops of a longitudinal field, for angles between the two fields of from 0 to 90 deg. As a translation of the paper (in Japanese) was not available, the following discussion is based on the extensive synopsis in English and on the figures which had captions in English. Sugiura used the ballistic method with a long cylindrical iron tube sample. The longitudinal field was produced by a coil wound around the tube, and the polarising field was of a helical shape produced by a combination of fields from conductors passing through the tube and around it. Points noted included the following:

(a) A transverse polarising field H_t reduced the longitudinal flux density B_l obtained on reversing the longitudinal field H_l , giving B_l/H_l curves as shown in fig. 3.40. The transverse field reduced the longitudinal permeability, and made the B_l/H_l curves more linear. (In obtaining these curves, H_t was increased from zero before reversals of H_l were made. Reversing H_t , to establish the transverse field on the normal magnetisation curve, before reversing H_l, made little difference, and it can therefore be assumed that for the results in fig. 3.40 the starting point of the field was on the normal magnetisation curve in the transverse direction.)

(b) The hysteresis loops of the longitudinal field remained symmetrical in the presence of a transverse field, fig. 3.41. The
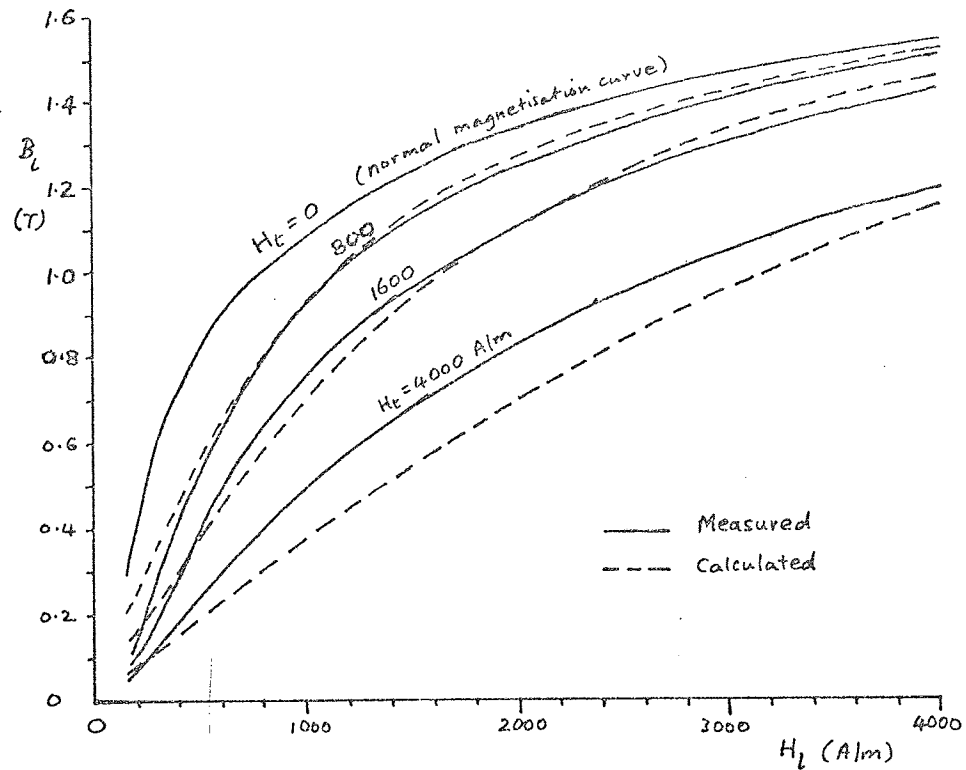
Fig.3.40 Effect of increasing values of steady transverse field H_t on B/H curves in the longitudinal direction, iron tube (from Sugiura, figs. 5 and 6, with a calculated curve for H_t = 4000 A/m added)

hysteresis loss decreased as H_t increased, both for loops of the same peak flux density and of the same peak field strength, fig.3.42. It can also be seen from fig.3.41 (b) that a loop of given peak field strength became more elliptical as H_t increased.
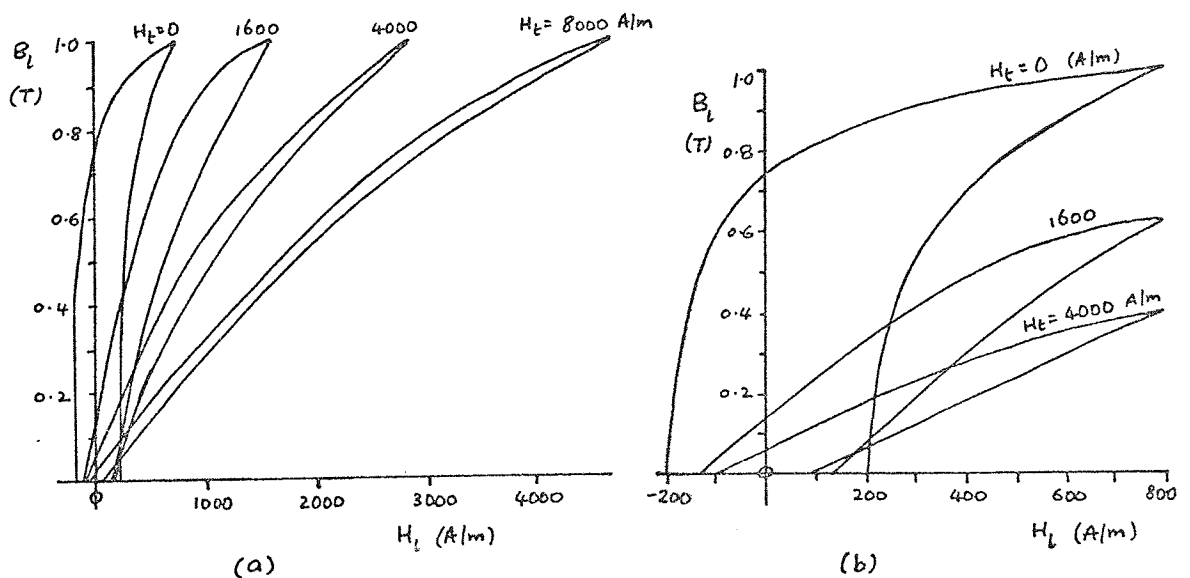
Fig.3.41 Effect of steady transverse field on longitudinal field hysteresis loops, iron tube (from Sugiura, figs. 13 and 16)
(a) constant peak longitudinal flux density
(b) constant peak longitudinal field strength

(a)   (b)
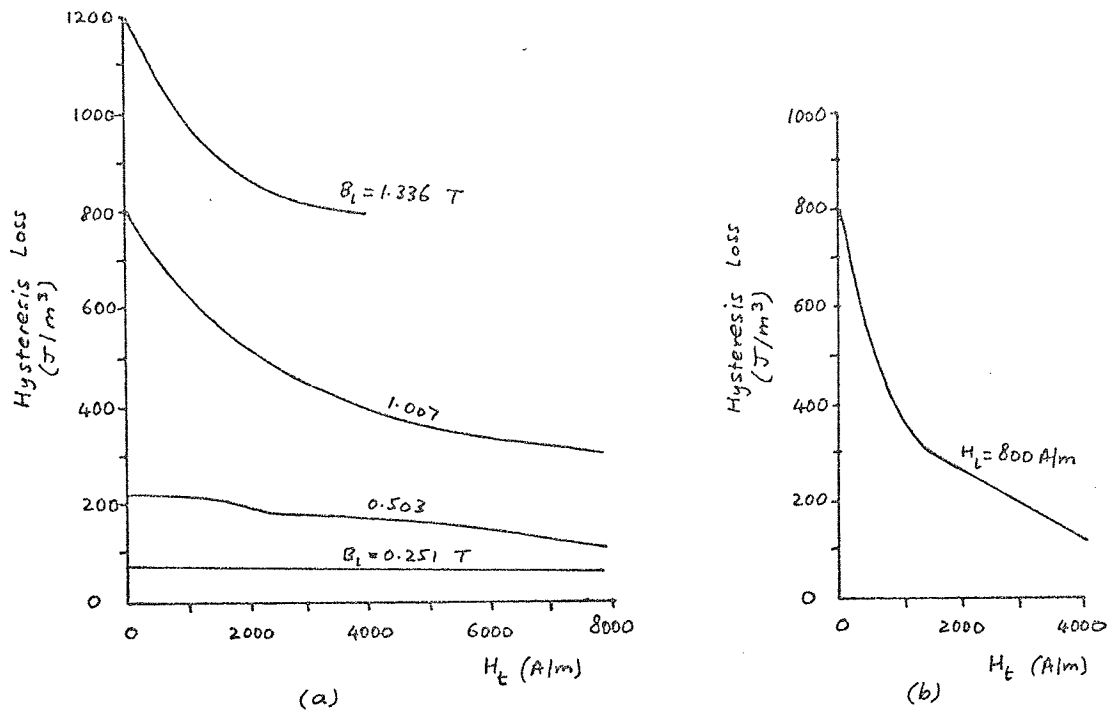
Fig.3.42   Longitudinal field hysteresis loss as a function of steady transverse field, iron tube   (from Sugiura, figs. 15 and 17)

(a)   constant peak longitudinal flux density

(b)   constant peak longitudinal field strength

(c)   The closer the polarising field H_p was to the longitudinal direction, the greater was the reduction in the longitudinal permeability, except when $H_1 \gg H_p$, as illustrated by the magnetisation curves in fig. 3.43. The curves at low values of H_1 are in agreement with Gans' results for μ_{rev} (fig.3.39).

(d)   The hysteresis loops became unsymmetrical as the angle between the polarising field and the longitudinal direction decreased, and the behaviour of the hysteresis loss depended on the amplitude of H_p and whether H_1 or B_1 was kept constant, fig.3.44 (there were insufficient results for more specific conclusions).
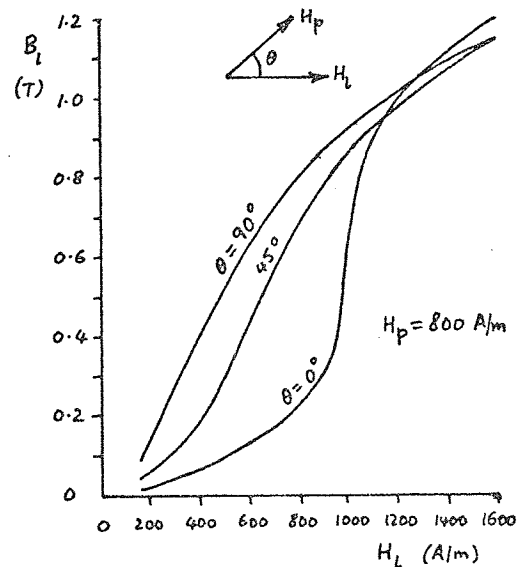
Fig.3.43 Effect of angle ϑ between polarising field H_p and longitudinal direction on the longitudinal field magnetisation curves, iron tube (from Sugiura, fig.21)
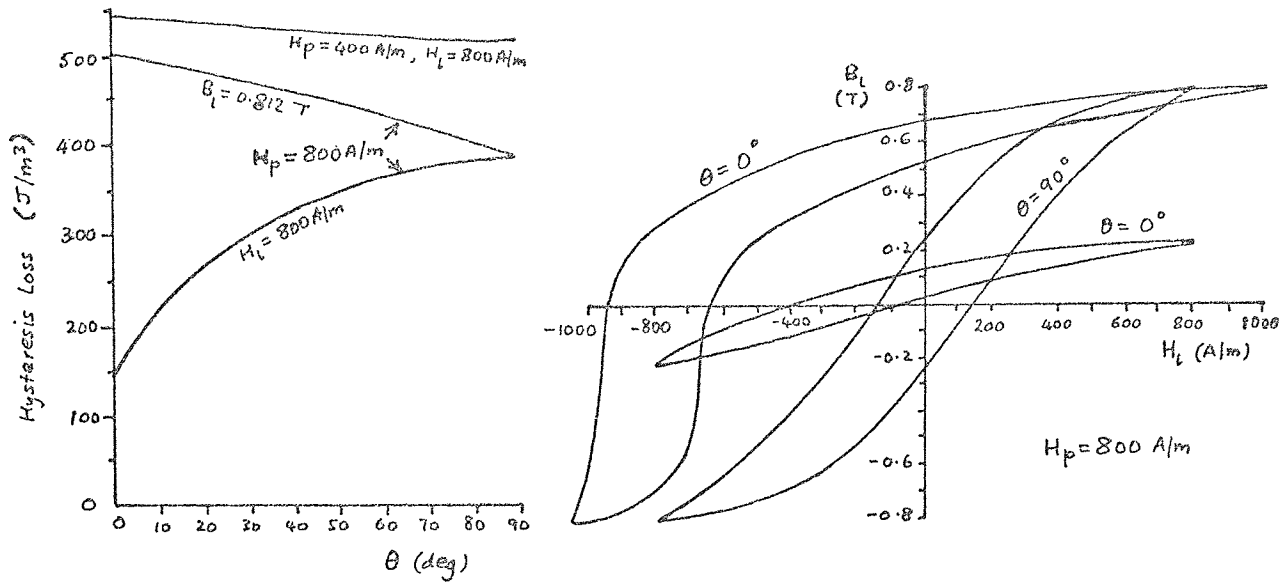
Fig.3.44 Effect on longitudinal field hysteresis loops and hysteresis loss of angle ϑ between polarising field and longitudinal direction, iron tube (from Sugiura, figs. 36 and 37)

Sugiura made some calculations of the B_l/H_l curves mentioned in (a) above, shown by the broken-line curves in fig.3.40. He neglected hysteresis, so that the relation between the resultant field strength $H = \sqrt{H_l^2 + H_t^2}$ and the resultant flux density B was given by the normal magnetisation curve, and so that B could be taken to be in the same direction as H. The longitudinal component of B was then given by $B_l = B \cdot \dfrac{H_l}{H}$. It can be seen that the largest differences between measured and calculated curves occur where $H_l < H_t$, where most of the flux change is rotational. The neglect of rotational hysteresis tends to over-estimate B_l, as shown in fig.3.45, and over-estimations occur for the smaller values of H_t, where one would expect rotational hysteresis to be greatest. The cause of the under-estimations is not clear.
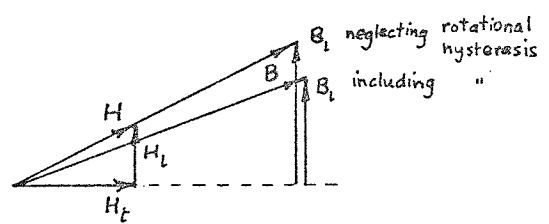
Fig.3.45 Illustrating over-estimation of B_l by neglect of rotational hysteresis

3.3.3 Later work

Measurements of a.c. loss in thin ferromagnetic wires were reported by Harrison et al.[85] in 1936 and by Webb [86] in 1938. A polarising field H_t was applied parallel to the axis of a wire, and thus everywhere perpendicular to the circular alternating field of a current passed along the wire. Both authors reported a considerable decrease of a.c. resistance as the polarising field increased with the alternating current constant. Webb's results for soft-iron wire of 0.5mm diameter at 1 MHz are shown in fig.3.46 (a).
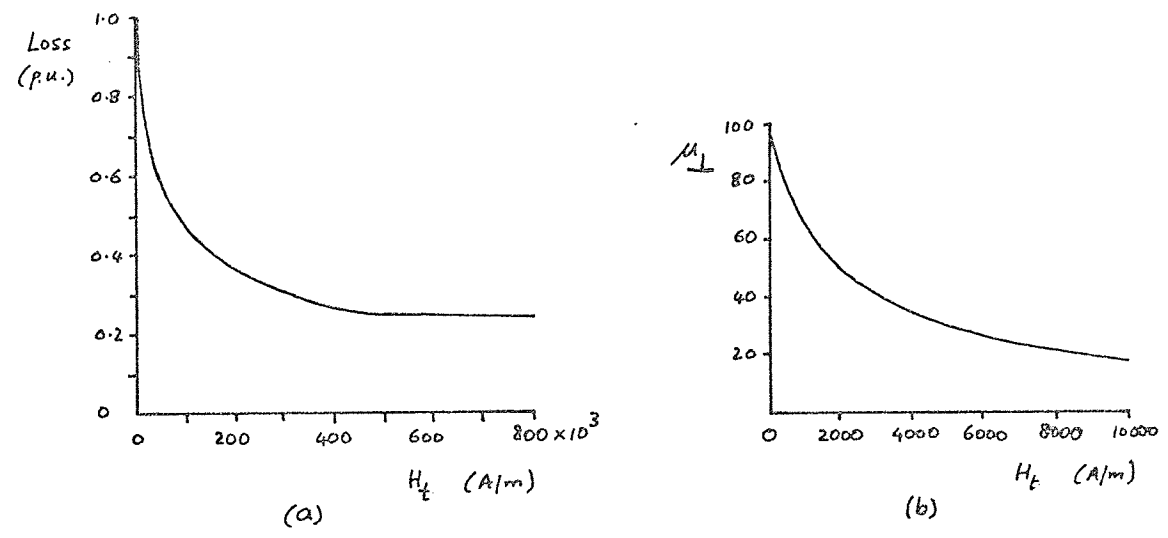
Fig.3.46 Change of (a) loss at 1 MHz and (b) calculated d.c. permeability caused by superposed steady perpendicular field with constant alternating current, 0.5 mm dia. soft-iron wire (from Webb)

From the measured a.c. resistance, Webb calculated an average d.c. permeability over the wire section using classical constant permeability theory, fig.3.46 (b). The decrease of permeability with H_t observed by earlier workers can be seen. Webb, however, did not mention the amplitude of the alternating current or field, so the applicability of the theory cannot be assessed.

Working with mumetal, Harrison et al. observed a small hysteresis effect as H_t varied, but Webb found no hysteresis effect for any of his samples.

The decrease of a.c. loss in a cylindrical sample caused by a superposed steady perpendicular field with a constant alternating field strength was further confirmed by Beck and Kelly in 1948 [87]. They used

an iron pipe of wall thickness 1.3 mm at 60 Hz. Dynamic B/H loops from an oscilloscope display showed the decrease of loss and permeability, but because of eddy currents the loops were much more elliptical and of much greater area than loops of the same flux density amplitude given by Sugiura (fig.3.41). No calculations of the losses were made.

Bozorth (1951)[22] suggested that hysteresis loops in the presence of a perpendicular biasing field, as shown in fig.3.41, could be calculated by a method similar to that used by Sugiura for the magnetisation curves, to an accuracy limited by the width of the hysteresis loop. (Bozorth assumed that the resultant flux density followed a normal hysteresis loop as H_1 varied, when it is more likely to follow an incremental loop as described in section 3.5.2, fig.3.53. This should not affect the calculation of the B_1/H_1 curves in fig.3.40 because these relate peak values of B_1 and H_1 and the peak resultant flux density lies on the normal magnetisation curve, as shown in fig.3.53.) He also gave curves showing that a perpendicular superposed steady field was less effective in reducing the reversible permeability than was a parallel superposed field, confirming Gans' results (fig.3.39).

The advantages of using a transverse polarising field in a controlled reactor were mentioned by Libkind and Dorzhko (1967)[88]. In particular they mentioned the increased linearity of the B_1/H_1 curves, giving a sinusoidal alternating current, and the decreased a.c. losses. They developed a theory for calculating various characteristics of a reactor with transverse field control, based on a prediction of the B_1/H_1 curves by the method used by Sugiura. Their source for the method was a paper by Zaitsev (1948)[89], which is not available in Great Britain. No direct experimental check on the calculated B_1/H_1 curves was given by Libkind and Dorzhko.

A.c. tests were reported by Choudhury et al. (1967)[81] which showed the loss at constant alternating flux density increasing slightly as a function of a perpendicular biasing flux density. A toroidal sample of 0.38 mm stalloy laminations was used, and the frequency was 50 Hz,

indicating negligible eddy current effects. The perpendicular field was produced by placing the sample between the poles of an electromagnet, rather than by passing a current through conductors in a hollow in the toroid section. As the core was of a clock-spring construction the longitudinal, transverse and resultant fields were all in the plane of the sheet. Their loss measurements with no biasing field agree with their earlier work, as mentioned in section 3.2.3.6, and the measurements with a biasing field were confirmed by displaying dynamic B/H loops. Although Choudhury et al. referred to Sugiura's work, they did not give any explanation of the difference between their results and his (fig.3.42 (a)) which showed the loss decreasing with increasing H_t .

A similar arrangement to that of Choudhury et al. was used by Dietrich[90] for determining the effect of a superposed perpendicular field on the B/H curves of turbogenerator rotor steels (containing C, Si, Mn, Cr, Mo, Ni, V). He used a ballistic method and obtained results similar to those of Sugiura, plotting permeability curves as shown in fig.3.47 (derived from B_1/H_1 curves like those in fig.3.40) and hysteresis
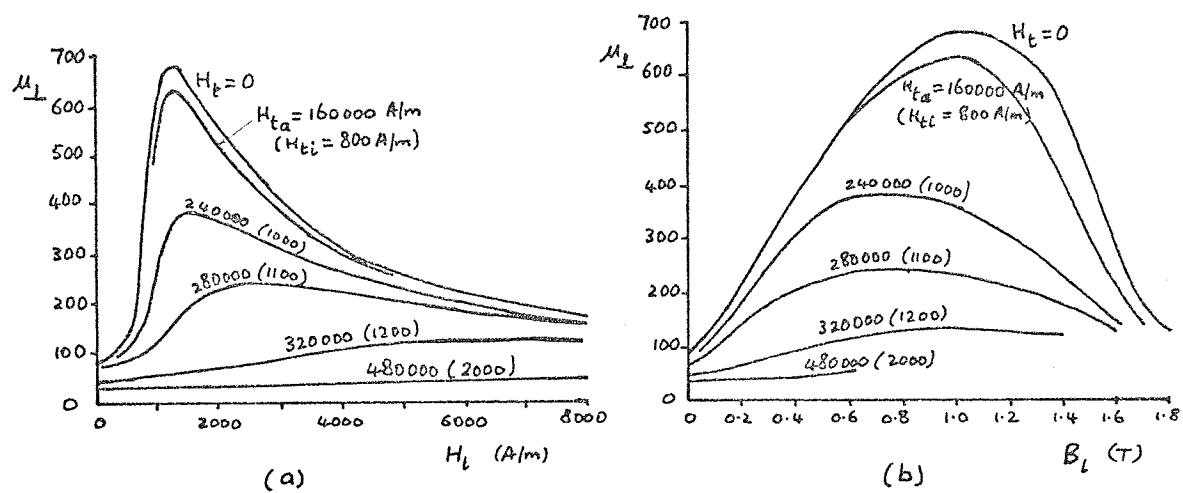
Fig.3.47 Permeability curves for a turbo-generator rotor steel with superposed perpendicular field (from Dietrich)

H_{ta} = transverse field strength in air

H_{ti} = estimated transverse field strength in the iron

loops of decreasing area like those in fig.3.41(b). Dietrich made no theoretical calculations, and it is in fact not possible to make calculations of the type made by Sugiura, because Dietrich did not

measure the transverse field when the longitudinal field was present, and because an estimated demagnetisation factor was used to give the transverse field strength inside the sample H_{ti} . (An idea of the error present in the calculated values of H_{ti} can be obtained by considering one point on the B_1/H_1 curves and carrying out a calculation by Sugiura's method. At $H_1 = 8000$ A/m, fig. 3.47 states that a value of $H_{ti} = 2000$ A/m reduced B_1 from 1.7 T to 0.5 T . But the calculated resultant field strength is $H = 8250$, giving $B = 1.71$ T and $B_1 = B \cdot \dfrac{H_1}{H} = 1.64$ T . Thus a much larger H_{ti} would theoretically be needed to reduce B_1 as far as the measured value.)

3.4   Steady field with a travelling field

Direct experiments to measure the effect of a steady field on a travelling field received little attention until recently when, in 1966 and 1967, Chernovets and Kozulin published two papers on rotating-field controllable reactors[31,32]. In the first paper experimental and theoretical results were given, and the second paper contained more details of the experiments.

The reactor considered had the general shape of an induction motor with an unwound, unslotted stator, zero air gap, and a wound, slotted stationary rotor. A cross-section is shown in fig.3.48(a) from which it can be seen that a normal 3-phase a.c. winding was at the top of the slots, but that the d.c. winding returned inside the core, confining the steady field to the back of the slots. The core consisted of 0.35 mm electrical steel laminations, and the a.c. winding had 4 poles.

(a)   (b)
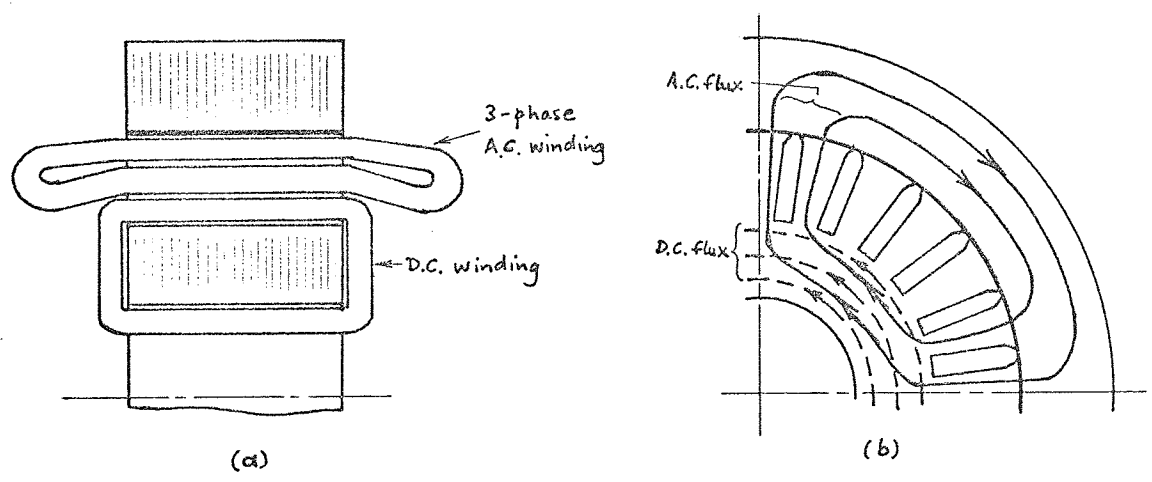
Fig.3.48 Rotating-field controllable reactor

(a)   cross-section

(b)   flux paths

A sketch of the a.c. and d.c. flux paths in fig.3.48(b) shows that where both fluxes existed they were mainly parallel, and the theory was developed on this basis. Hysteresis effects were neglected and the normal magnetisation curve was used to calculate the relation between the fundamental alternating flux density (B_Δ') and alternating field strength (H_Δ') in the core behind the slots, assuming sinusoidal H .

(as discussed near the end of section 3.2.1.2, and see also fig.3.49). The same relation was calculated from experimental results after allowances were made for m.m.f. drops in other parts of the core. Only values of H'_{Δ} approximately equal to the steady field strength were considered, and fair agreement was obtained. The steady field strength was strong, being greater than or equal to 10000 A/m.
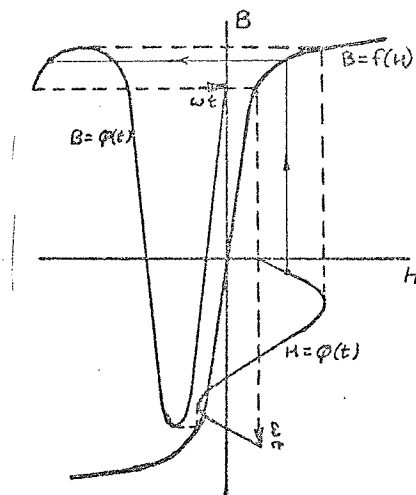
Fig. 3.49 Use of normal magnetisation curve to calculate B/H characteristics with a superposed parallel steady field.

3.5   Effect of the varying field on the steady field

3.5.1   Parallel fields

When a varying field is superposed on a steady field there is, in general, a change of average flux density or field strength. Fig.3.50 shows the change of biasing flux density B_b produced by superposing a varying field H_Δ with a constant biasing field strength H_b . The steady flux density, originally at the peak of a normal hysteresis loop (H_b, B_m), increases with a small incremental loop (fig.3.50(a)) and decreases with a large one (fig.3.50(b)). For a given incremental loop, the values of H_b and B_b are unique, and curves of B_b against H_b for constant B_Δ or H_Δ may be drawn.
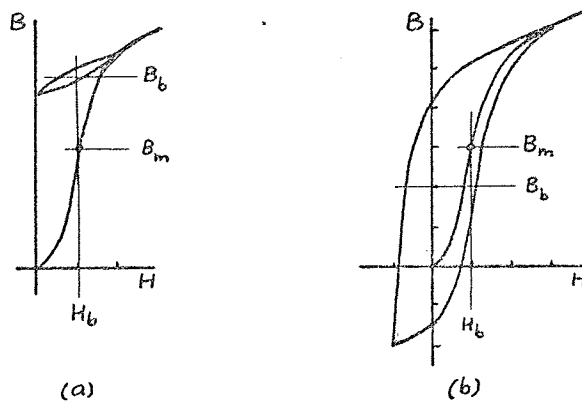
Fig.3.50 Illustrating the change of biasing flux density caused by incremental excitation about a constant field strength

(a)   small incremental loop

(b)   large incremental loop

With a.c. excitation the steady flux density or field strength usually measured is the time average $(B_{av}$ or $H_{av})$ which may be different from the amplitude average $(B_b$ or $H_b)$, depending on the waveform (section 3.2.3.2). Fig.3.51 compares plots of B_{av} against H_{av} at constant values of B_Δ given by Niwa and Asami [53] with sinusoidal flux and by Niwa et al.[54] with sinusoidal current, for 3.35% Si steel laminations. (further details of their experiments were given in section 3.2.3.6). Sinusoidal flux curves were given by Edgar[52], and the permeability $\dfrac{B_{av}}{\mu_o H_{av}}$ was tabulated by Carter and Richards[48], both for silicon-steel laminations. Curves at constant H_Δ for annealed iron were given by

Bozorth[22] for low values of H_b and unspecified waveform.

Fig. 3.51 Effect of alternating field on average flux density and field strength, with sinusoidal flux or sinusoidal current, 3.35% Si steel laminations (from Niwa and Asami, fig. 3, and Niwa et al. fig. 2)
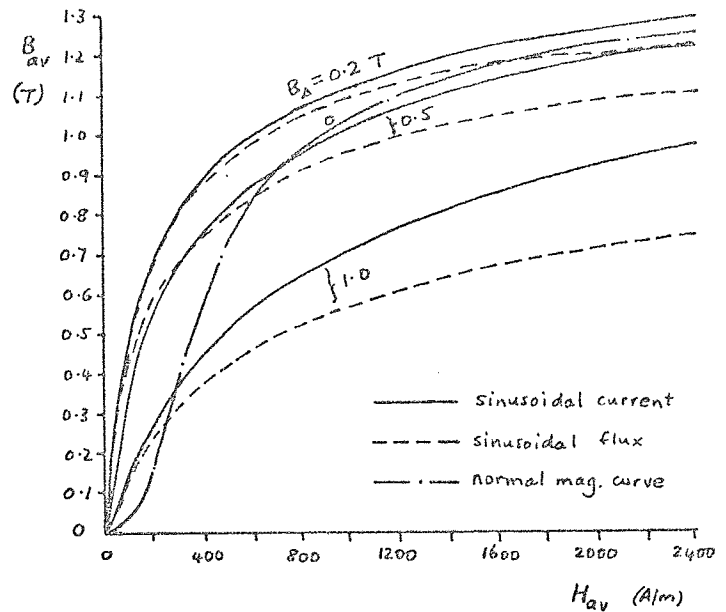
The increase of average flux density with small superposed a.c. fields was used at one time as a means of detecting radio waves[91]. It was believed that the increase of flux density was due to a removal of hysteresis as the alternating field shook the iron molecules. Other observers at the time thought that the same effect caused the decreased area of a normal hysteresis loop traced by the average field with a superposed alternating field. Ewing's experiments[20] of 1885 (mentioned in section 3.1) should have been sufficient to indicate that the real cause was the formation of incremental loops and the measurement of average quantities. The question was not fully resolved until Niwa et al. (1934)[54] observed the loops on a cathode ray tube. They carefully showed that the normal loop traced by the main field was unaffected by the alternating field, provided the maximum resultant field strength was constant.

3.5.2 Non-parallel fields

When an alternating field is superposed on a perpendicular field of steady field strength there is a change in the steady flux density owing to the non-linearity of the iron. Let the steady field be in the transverse direction, of field strength H_{to} and flux density B_t, and let the varying field be in the longitudinal direction, H_l and B_l. If B_t is initially on the normal magnetisation curve with value B_{to}, and H_l is zero, then as H_l increases, B_t may either increase or decrease depending on its initial amplitude, as illustrated in fig. 3.52. If the transverse field begins below the point of maximum permeability, B_t will increase (fig.3.52(a)) and if the transverse field begins above this point, B_t will decrease (fig.3.52(b)). (It is assumed that the resultant flux density B follows the normal magnetisation curve as the resultant field strength H increases, i.e. rotational hysteresis is neglected.) By taking the component of B in the longitudinal direction, fig.3.52 also illustrates the calculation of the B_l/H_l curves in fig.3.40. For a linear B/H curve the resultant, longitudinal and transverse flux densities would be B', B'_l and B_{to} respectively.
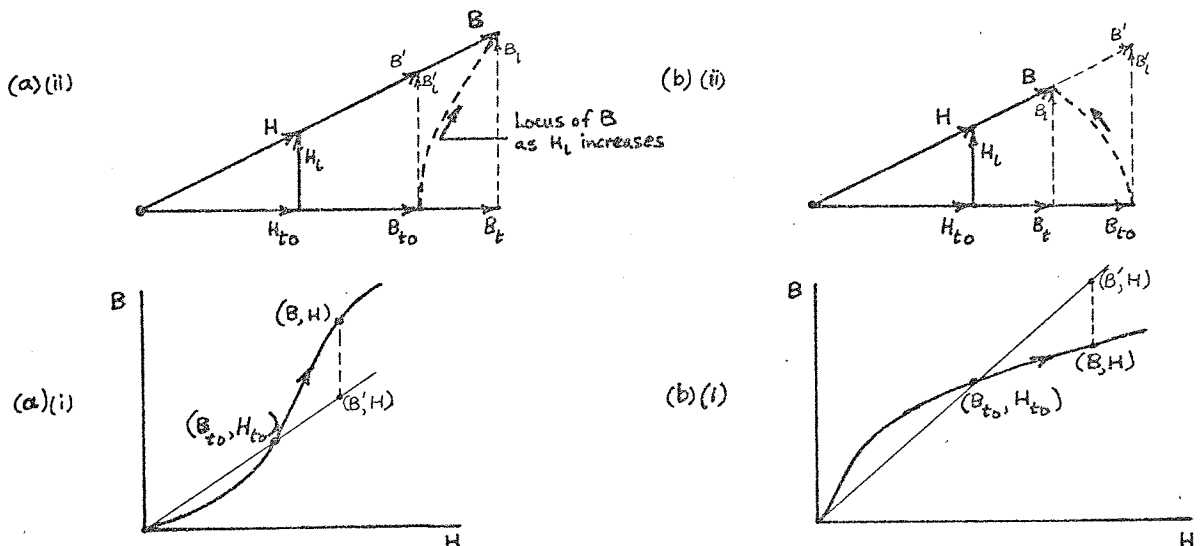
Fig.3.52 Illustrating effect of non-linear B/H curve on transverse flux density B_t as longitudinal field H_l is applied
(i) B/H curves
(ii) Vector diagrams
(a) Starting values B_{to}, H_{to} below point of maximum permeability
(b) B_{to}, H_{to} above point of maximum permeability

If H_1 is alternated slowly after reaching a maximum value H_{1m}, B_1 will change sign, but the resultant field will reach a minimum value in the transverse direction when $H_1 = 0$ and then increase to its previous value (but in a different direction) as H_1 goes to $-H_{1m}$. The next half cycle of H_1 will see a return of the resultant field to the original direction. Thus for each half cycle of H_1 the resultant field will follow an incremental loop, as illustrated in fig. 3.53, neglecting rotational hysteresis. B_t will change as H_1 cycles, because the incremental loop, like the normal magnetisation curve, is not a straight line through the origin.
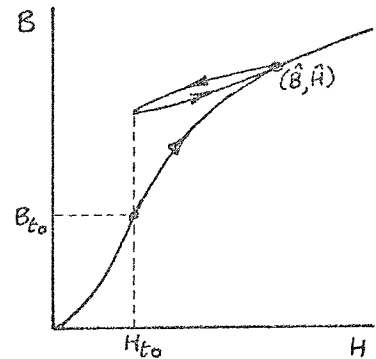
Fig.3.53 Incremental loop formed by resultant field when longitudinal field H_1, superposed on constant transverse field H_{to}, is cycled. The peak point $(\hat{B}, \hat{H})$ is reached when $H_1 = \pm H_{1m}$, i.e. twice per cycle of H_1.

The value of B_t during the initial increase and subsequent cycles of H_1 was measured by Goldschmidt in 1910 [84]. (Goldschmidt actually chose the longitudinal direction for the steady field, because (as mentioned in section 3.3.1) his sample was a wrought iron tube forming part of the magnetic circuit of a galvanometer. This enabled the longitudinal flux density to be measured without reversals of the longitudinal field strength. To be consistent with the above discussion, the steady field is assumed to be in the transverse direction, and the varying field in the longitudinal direction.) His results are shown in fig. 3.54. The starting point for B_t was close to the normal magnetisation curve, just below the point of maximum permeability, and an initial increase of B_t can be seen. It can also be seen that the initial curve is different from the subsequent cycles, and that B_t changes at twice the frequency of H_1. Such changes of B_t have been used in the cross-field modulator or frequency doubler [95].

Curves similar to fig. 3.54 were given by Beck and Kelly

for rapid variations of H_l
(60 Hz) and only the varying
component of B_t was shown. The
loops were much fatter than
those in fig.3.54, possibly
because of large eddy currents
in their 1.3 mm thick iron pipe
(discussed in section 3.3.3).

Other workers were
concerned with the time
average of B_t (B_{tav}) for
sinusoidal variations of
H_l at frequencies near 50 Hz .
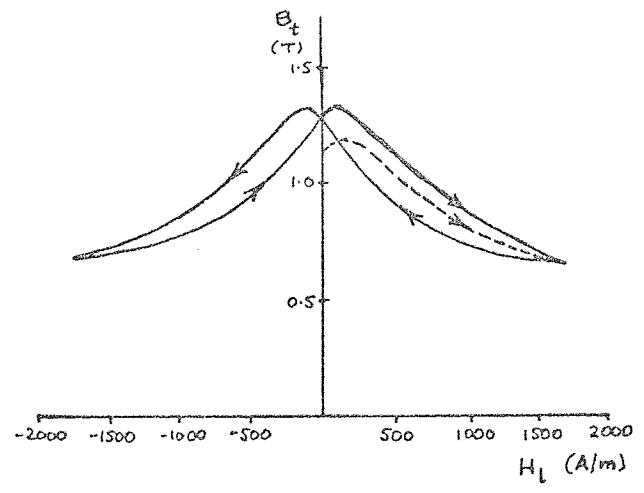
Fig.3.54 Variation of transverse flux
density as longitudinal field increases
from zero and then cycles, with
transverse field strength H_{to} constant,
wrought iron (from
Goldschmidt, fig.11)

Plots of the transverse direction magnetisation curves (B_{tav} against
H_{to}) for several values of H_{lm} were given for an iron tube by Sugiura[35],
as shown in fig.3.55. Cross plots of such curves (i.e. B_{tav} against
H_{lm} for several values of H_{to}) were given for iron wire by Ashworth[93]
and for an iron pipe by Beck and Kelly[87]. Eddy currents could have
been significant in all of the above tests.

The magnetisation curves
in fig.3.55 show similar features
to the curves with parallel super-
posed fields given in fig.3.51.
With perpendicular fields, however,
the effect of sinusoidal variations
of B_l was not studied, and neither
was the effect of keeping B_t
constant at the initial value
B_{to} (rather than H_t constant
at H_{to}).

As for parallel
superposed fields, much early
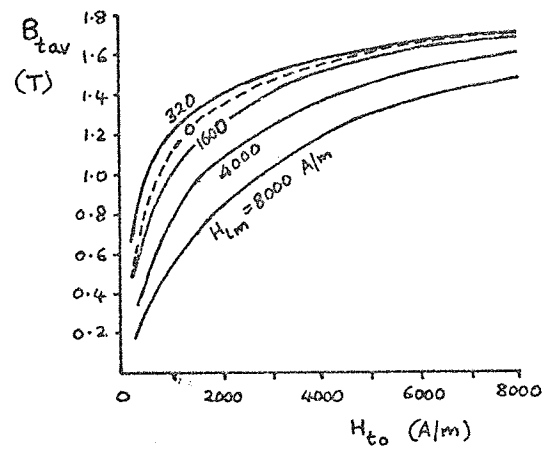
Fig.3.55 Transverse direction
magnetisation curves: time average
transverse flux density B_{tav}
against steady transverse
field strength H_{to} for several
values of
superposed alternating longitudinal
field strength of peak amplitude
H_{lm}, iron tube (from Sugiura, fig.39)

work with perpendicular fields was concerned with the decrease of area of a hysteresis loop traced by the average biasing flux density (B_{tav} above) for slow cyclic variations of the biasing field strength (H_{to} above) with a superposed alternating field (H_{lm} above). Examples of the effect were given by Finzi (1891)[92], Goldschmidt (1910)[84], Williams (1917)[94] and Sugiura (1931)[35]. Calculations were made by Williams but unfortunately the reference given is only an abstract, and the original paper is not available. The abstract mentions that good agreement was obtained for soft-iron although there was a distinct rotational hysteresis for hard specimens, but details of the calculation method were not given in the abstract. Other available methods for calculating either the transverse or longitudinal flux density were based on the normal magnetisation curve. All hysteresis effects, such as the incremental loops followed by the resultant flux density, were neglected on the basis that little error would be introduced for large longitudinal or transverse fields. In addition to the calculations of longitudinal flux density given by Sugiura[35], Bozorth[22] or Libkind and Dorzhko[88] (mentioned in section 3.3) the calculations of transverse flux density in magnetic cross valves by Higa (1955)[118] and in controlled reactors by Libkind and Dorzhko[88] may be mentioned. Besides the neglect of hysteresis in the above treatments, eddy currents were also neglected, and no discussion was given of their possible effects (e.g. effect of change of waveshape and amplitude of the alternating longitudinal field with depth).

3.6 Time decrease of μ_Δ

In 1934 Webb & Ford[96] reported that the application of a large magnetising force, such as is involved in the demagnetisation of a specimen, may cause an increase in the values of normal and incremental permeability obtained at low flux densities, this increase then disappearing approximately exponentially with time. The 'time-decrease of permeability' occurs whether d.c. or a.c. methods of measurement are used, and may require days or even weeks to be effectively completed. It is only considerable below about $B_\Delta = 0.1$ T, and varies greatly with the field strength. It also depends on the nature of the material, being especially high in high-silicon steels. The presence of a polarising force reduces the effect, but each change of polarising force re-initiates the decrease.

A percentage difference was defined as $D = \dfrac{\mu_I - \mu_F}{\mu_F} \cdot 100$, where μ_I is the permeability measured after 2 minutes and μ_F that measured after 2 weeks. In Table 3.1 the maximum value of D and the value of H_Δ for which it occurs are shown for a few of the materials considered by Webb and Ford.

TABLE 3.1   MAXIMUM TIME-DECREASE OF PERMEABILITY

Specimen	H_Δ for D_{max} (A/m)	D_{max} (%)
1. Low-carbon steel, solid	--	1
5. Low-silicon iron, sheet (Lohys)	4	8
18. High-silicon iron, sheet	1.44	115
19. High-silicon iron, solid	1.44	90
10. Nickel iron, sheet	1.04	2
20. Aluminium iron, solid	4.8	36

The values in Table 3.1 were obtained by comparing μ/H curves. When μ/B curves were compared, Webb and Ford found that the maximum time-decrease for a given B_Δ was considerably less than that for a given H_Δ, and that the maximum occurred at roughly $B_\Delta = 0.0008$ T for all materials tested. They also measured losses at a given flux density, and found that although there was a time-decrease below $B_\Delta = 0.005$ T, the maximum decrease, even in a high-silicon material, was only about 5%.

3.7 Conclusion

The chapter surveyed existing knowledge on the effect of a superposed steady field on the permeability and losses for an alternating field in soft-iron. Considering the permeability first, for parallel fields, and for incremental loops on the normal magnetisation curve of the same biasing field strength, fig. 3.17 summarises the behaviour of μ_Δ : there is a large reduction in μ_Δ for values of H_b greater than H_Δ , and a tendency for μ_Δ to be independent of H_Δ for such values of H_b. Results for incremental loops of the same biasing flux density (fig. 3.30) show a steady decrease of permeability as B_b increases and and increasing tendency for the permeability to be independent of H_Δ .

For perpendicular fields, measurements were taken with the biasing field strength held constant, and the results show that the permeability decreases and becomes independent of the amplitude of the alternating field (fig. 3.40) and the alternating field hysteresis loops become more elliptical (fig. 3.41). (Measurements on the type of steel used in modern turbo-generators were made (fig. 3.47), but there is doubt about the values given for the steady field inside the steel.)

The reduction of permeability is greater for parallel fields than for perpendicular fields, except when the alternating field strength is greater than the steady field strength (fig. 3.43). Measurements with an angle between the superposed fields in the range $0°$ to $90°$ were made by only one person and the results lie between the results for parallel and perpendicular fields (fig. 3.43).

The effect of the previous history of the steady field on the alternating-field permeability was studied for parallel fields only. The general butterfly-loop shape of the curves for μ_Δ

(fig. 3.6) was established by a.c. methods. Eddy-current effects were probably large, however, only a few, small values of H_Δ were used, and few normal hysteresis loops were considered. Results by other methods were taken for $H_b = 0$ only (fig. 3.14) and show that the previous history is important, at least for alternating fields below the knee of the normal magnetisation curve.

When the steady field is parallel to the alternating field the permeability μ_Δ may be approximately predicted by several methods, depending on the amplitude of the alternating field, although the methods have not been checked for modern steels and apply only to incremental loops on the normal magnetisation curve. One method was put forward for incremental loops on the descending branch of a normal loop, but there was no experimental verification. For superposed non-parallel fields, calculations of permeability have only been made for perpendicular fields, neglecting hysteresis, and there were differences between measured and calculated values (fig. 3.40). The only attempt to define a suitable value of permeability for a travelling field with a superposed steady field was in a machine where the fields were mostly parallel (fig. 3.48) and fair agreement was obtained between experimental results and calculations assuming the fields to be parallel.

Turning now to hysteresis loss, the effect of a superposed parallel steady field depends on whether H_Δ or B_Δ is kept constant. Most results were taken with B_Δ constant, and show an increase for values of B_Δ below a critical value (in the range 1.0 to 1.5 T) and a decrease for values of B_Δ above this value (fig. 3.36). In addition, the rate of increase of loss as B_b increases for the smaller values of B_Δ begins to decrease when the sum of B_b and B_Δ exceeds the critical flux density. The

approximate law put forward by Ball (eqn. 3.12) for calculating
the hysteresis loss of an incremental loop from the loss of an
unbiased loop is only valid for small values of $B_\triangle$, and for
values of B_b such that $B_\triangle + B_b < B_{crit}$. The few results taken
with $H_\triangle$ constant indicate that the loss always decreases as the
steady field increases, but the complete range of $H_\triangle$ was not
covered.

The effect of a superposed perpendicular steady field is
to decrease the hysteresis loss for loops of the same flux density
or field strength amplitude (fig. 3.42), although for loops of
the same flux density amplitude one or two people observed no
change or even a slight increase. No law was put forward for
calculating the loss. The decrease of loss with perpendicular
fields may be more or less than the decrease with parallel fields,
depending on the loop amplitude (fig. 3.44), but insufficient
results are available for more general conclusions.

There is some doubt about the effect of previous magnetic
history on the hysteresis loss, as the complete range of the
variables was not covered, although it appears that there may be
an effect for parallel fields if the amplitude of the previous
history is sufficiently large (fig. 3.20). No measurements were
taken with perpendicular fields.

Some measurements of loss were made with both parallel
and perpendicular fields in which eddy-current losses were
considerable, and for constant values of alternating field strength
the variation of the loss followed the variation of the permeability.
No attempt was made to calculate the losses from measured values of
permeability, and insufficient information was given for this to
be done.

It was shown that the alternating field may change the
steady flux density or field strength, and that with a.c. excitation
the steady field measured depends on the waveform of the alternating

field. With parallel fields, the total field follows incremental loops like those shown in fig. 3.50, from which either the average flux density or field strength may be deduced. With perpendicular fields, the steady field strength was always held constant and the 'steady' flux density varied as shown in fig. 3.54, with a double-frequency component.

The chapter concluded with a short review of the phenomenon of the 'time-decrease' of μ_Δ , showing that this is only important for small amplitudes of the alternating field, and is always less than 1% for low-carbon (mild) steel.

4.   EXPERIMENTS ON PERMEABILITY AND HYSTERESIS LOSS WITH A

        SUPERPOSED PARALLEL STEADY FIELD

4. 1   Introduction

        The previous chapter showed that few experiments had been
performed on the magnetic behaviour of mild steel with a superposed steady
field. This chapter describes some experiments on permeability and
hysteresis loss with a superposed parallel steady field in the absence of
eddy currents. In the next chapter calculations of eddy current loss using
these results are compared with measurements, and in chapter 6 the results
are used to derive the permeability with a superposed perpendicular field.

        The type of steel used was one already in use at the University
of Aston in Birmingham for the study of losses caused by a travelling field.
It was originally chosen because its magnetic properties were as close as
possible to those of the solid poles of salient-pole machines. The ranges
chosen for the amplitudes of the steady and varying fields were those likely
to be encountered in the pole-face loss problem, as discussed in
chapter 6.

        Three methods were used for the permeability measurements,
because at the time the investigations were begun it was thought that there
could be some difference between results obtained with the ballistic and
slowly varying field methods. Results using the different methods are
compared in this chapter, and the measurements are also compared with the
previous experience discussed in chapter 3.

        The chapter begins with a section on normal permeability and
hysteresis loss, for later comparison with the superposed field results,
and to establish confidence in the measurements.

4.2 The specimen

The specimen was a ring of mild steel, EN1A grade 4 (B.S.970) of chemical composition C 0.11%, S 0.25%, Mn 1.15%. It was formed by cutting a disc from a length of circular bar and turning the disc to produce a homogeneous ring of circular section. The outside diameter of the ring was determined by the maximum diameter of bar available, and the inside diameter made large enough to ensure less than 0.1% error in calculating permeability from the field strength at the mean diameter and the average flux density over the section[42, 43, 97] (the ratio of mean diameter to radial thickness was 18:1). The choice of inside diameter also reduced errors in the calculation of eddy current loss (in chapter 5 it is assumed that the toroid is equivalent to a solenoid of infinite length).

Table 4.1 Details of the specimen

Dimensions:

Outside diameter, D_o	18.97	cm
Inside diameter, D_i	17.01	cm
Thickness (cross-section dia.), d	1.004	cm
Mean diameter, $D = \frac{1}{2}(D_o + D_i)$	17.99	cm
Mean magnetic path length, $L = \pi D$	56.5	cm
Cross-sectional area, $A = \frac{\pi}{4}d^2$	0.791	cm^2
Surface area, $A_s = \pi^2 dD$	178.5	cm^2
Volume, $V = \frac{\pi^2}{4}d^2 D$	44.8	cm^3

Windings:

Flux coil, N_2	1320	turns
Magnetising coil, N_1	2040	turns

The heat treatment was the same as that given to the steel already in use at the university. The ring was heated to 850°C and allowed to cool in the furnace overnight.[98] Scale was removed and the surface made smooth by light hand rubbing with fine emery cloth.

The dimensions of the ring were then measured with a vernier rule and micrometer (table 4.1). The outside and inside diameters were measured at 8 places around the ring, and the averages taken. The thickness (cross-section diameter) of the ring was measured at 4 places in 4 directions; the results showed that the shape of the ring section was the same at each

place, although slightly elliptical, the maximum section diameter being 4% greater than the minimum. The thickness was calculated as the average of the 16 measurements of thickness. The other quantities in the table were derived according to the formulae given there.

Two coils were wound on the ring. The first was wound directly on to the bare surface for the measurement of flux. This flux coil was a single layer of SWG 30 (0.315 mm dia.) enamel-covered wire wound in 6 groups of 220 turns, completely covering the ring apart from 6 small gaps for future access to the ring surface. The second, magnetising, winding contained 6 layers of SWG 18 (1.22 mm dia.) enamel-covered wire wound in 6 groups of 340 turns, and the layers moved around the ring in alternate directions to cancel the effective circumferential turn of a single layer. Both windings were thus nearly uniformly distributed around the ring, ensuring uniform flux and that any unknown irregularity in the ring would not unduly affect the readings.

The numbers of turns on each winding were decided from the requirements that the iron should be driven to saturation with a magnetising current of not more than 5 A, and that the flux-coil output should be sufficient to record a B/H loop performed in about 20 minutes at a constant rate of change of flux (these requirements are discussed further in section 4.3.1). The diameter of the magnetising-winding wire was chosen to be as small as possible for a resistance of less than 2Ω, to allow a current of 5 A from a 10 V supply. The temperature rise of the coil at 5 A was calculated to be about 70°C. By experiment, the temperature rise was only 48°C after half an hour, when some varnish began to melt. Since the full load current was only needed for a few minutes in the measurements of permeability and losses, the temperature rise in practice was always small.

4.3   Normal permeability and hysteresis loss

4.3.1 Method

4.3.1.1 Introduction

There are three methods available for permeability and hysteresis measurements of solid ring specimens avoiding the effects of eddy currents[97]:

a) ballistic method, in which the magnetising current is changed discontinuously

b) slowly-varying method, in which the magnetising current is changed slowly

c) uniformly-varying method, in which the magnetising current is varied in such a way as to keep $\frac{dB}{dt}$ constant, i.e. a uniform rate of change of flux density.

The ballistic method is used in conjunction with a ballistic galvanometer or flux meter for measuring the flux, and has been used since the time of Rowland (1873)[18]. The slowly-varying method requires an integrator for flux measurement, and was used for example by Chubb and Spooner (1915)[33]. The uniformly-varying method needs no integrator for measuring flux, since $\frac{dB}{dt}$ is maintained constant and a measurement of $\frac{dB}{dt}$ and time suffices. This method was used by Peck on large transformers in 1901[99] and compared with the ballistic method by Morris and Langford in 1911[100].

Morris and Langford's experiments showed some differences between the ballistic and uniformly varying flux methods, and in 1952 Astbury[97] considered the question still unsettled. In 1954 Ross[101] compared the slowly-varying method with the ballistic method on several materials and found differences less than 1%, the order of the experimental error, except for materials with very steep B/H curves, such as Mumetal, with which their apparatus could not cope. Mazzetti and Soardo[102], however, gave results in 1966 comparing the ballistic and uniformly-varying methods for one specimen, which happened to be Mumetal. They found no difference.

The apparatus used by Mazzetti and Soardo showed such promise for rapid, accurate determinations of B/H curves that it was decided to use a similar technique and at the same time confirm the comparison between methods a), b) and c) for mild steel. Furthermore, the ballistic methods used by Mazzetti and Soardo, Ross, and Morris and Langford had involved an instrument for measuring flux different from that used in the slowly-varying or uniformly-varying methods, but with the apparatus used by Mazzetti and Soardo it was in fact possible to use the same device in all methods, thus eliminating many errors possible in previous tests.

4.3.1.2 Circuits used (fig. 4.1)

The circuit used by Mazzetti and Soardo was all electronic. The magnetising current was supplied from a d.c. amplifier and the flux measured with an operational integrator (operational amplifier of high open loop gain with a feedback capacitor). Such units have since been used by Warner (1967) [103] and Erdmann (1968) [104]. The magnetising current could be controlled in any desired fashion (e.g. at very low or audio frequency) by the input voltage to the d.c. amplifier. The amplifier used by Mazzetti and Soardo, and built for this project, had a frequency response flat from 0 to 1.3 kHz, and 1 dB down at 2.4 kHz at full voltage on no load. Thus it could be used for sudden or slow changes of current.

For the ballistic and slowly varying methods, the voltage input to the amplifier came from a low power d.c. supply (stabilised electronic or dry cell) in series with an on-off and reversing switch and a ten turn potentiometer. The sudden changes in current for the ballistic method were achieved by using the reversing switch and the slow changes by slowly varying the potentiometer.

To achieve uniformly varying flux, Mazzetti and Soardo wound on a second flux coil and used the difference between the voltage induced in this coil and a constant voltage, after high-gain integration, as the input to the magnetising-current amplifier. The constant voltage was obtained from a special bistable circuit which changed state each time the magnetising current reached the required positive or negative value so that

symmetrical loops were performed. Thus the output of the bistable was a square wave and so was the rate of change of flux. A similar method was used by Warner, but instead of the special bistable he used a circuit containing standard differential amplifiers, NOR gates and a flip-flop. The method is actually an application of voltage feedback, used by McFarlane and Harris[105] and discussed further in appendix 8.3. The instability problems mentioned by McFarlane were overcome by Warner, and Mazzetti and Soardo, by placing an operational integrator in the forward path of the feedback loop.

4.3.1.3 Drift

Two further details of the circuit used by Mazzetti and Soardo relate to the d.c. amplifier for the magnetising current and to the flux measuring circuit. The d.c. power amplifier was of very low long term drift (< 50 μV) and had equal gains in the positive and negative directions (to within 0.1%) enabling an accurate zero current to be set and symmetric reversals to be made (50 μV produced a field of only 0.1 A/m on the present specimen).

Their flux measuring circuit contained an amplifier of very low long term drift (0.01 μV referred to the input) which corresponded to a rate of change of flux of 0.01 μWb/sec. The error due to this drift in a 20 minute loop of maximum flux density 1.0 T in a specimen of area 25 mm^2 and with a flux coil of 100 turns amounted to 0.2%. For the specimen described in section 4.2, with its larger cross-sectional area and number of flux-coil turns, the error for a 20 minute loop of maximum flux density 1.0 T would only be approximately 0.005%. Such a good (and expensive) amplifier as that used by Mazzetti and Soardo was thus not required, and one with a long term drift of 0.5 μV (referred to input) was used, giving an error for the above loop of 0.25%. For faster loops, (including the ballistic method) the error was reduced in proportion to the time of the loop.

4.3.1.4 Recording of field quantities

The field strength H was assumed uniform over the ring and equal

to $\frac{N_1 I}{L}$ (N_1 and L are defined in table 4.1). The magnetising current I was therefore a measure of H, and it was given by the voltage drop across a small series resistor. This voltage was first amplified with a low power d.c. instrumentation amplifier of high input impedance and then read with a digital voltmeter. The gain of the amplifier was adjusted to make the reading direct in A/m or an easy multiple thereof.

In a similar fashion the output of the flux integrator was read on a digital voltmeter, and the gain of the flux measuring circuit adjusted to make the reading direct in teslas.

For the slowly varying and uniformly varying flux methods, the voltages proportional to B and H were applied to the X and Y inputs of an XY recorder, as well as to digital voltmeters. In addition, for the uniformly varying flux method, a program was written by a colleague, A.W. Scott, to enable a PDP - 9 digital computer to record on-line the voltages proportional to H and $\frac{dB}{dt}$, perform the integration, and print out the values of B and H for a complete loop. This enabled more accurate recording of saturated loops whose steep portions would have been very narrow on the XY recorder, provided a means of recording loops which were too fast for the XY recorder, and provided a verification of the integration.

4.3.1.5 Calibration

The calibrations of the B and H measuring circuits were based on measurements of voltage with the Solartron digital voltmeters (calibrated on an internal standard cell). For the B circuit, a fixed voltage was applied at the input for 60 s as measured on a stopwatch and the circuit allowed to integrate, after which the output voltage was measured. For the H circuit, a fixed current was passed through the magnetising winding, measured by the voltage drop across a 0.1 Ω standard resistor, and the amplifier output voltage measured.

The gains (G) required to make the circuits direct reading in teslas or A/m were calculated from the data of table 4.1 as follows:

B circuit: Flux coil e.m.f. $E_2 = N_2 A \frac{dB}{dt}$

Integrator output $\Delta E = G \int E_2 \, dt = N_2 A G \Delta B$

$\therefore$ For $\Delta E = \Delta B$, $G = \frac{1}{N_2 A} = 9.60$

H circuit: Amplifier output $E = G \, RI$. where R = small series
resistor $(25 \, m\Omega)$

$$= \frac{GRL}{N_1} H$$

$\therefore$ For $E = H$ (A/mm), $G = \frac{N_1}{RL} = 144.5$

The error in the use of the digital voltmeters was $\pm 0.1\%$
of the reading, giving an error of $\pm 1\%$ in permeability. (The error in
ΔB was $\pm 0.5\%$, from the sum of the errors in ΔE ($\pm 0.1\%$), A ($\pm 0.2\%$) and
G ($\pm 0.2\%$). The error in H was $\pm 0.4\%$ from the sum of the errors in E ($\pm 0.1\%$),
GR ($\pm 0.2\%$) and L ($\pm 0.1\%$).) The drift in the B circuit was less than
.05 mV/sec (i.e. .05 mT/sec) and in the H circuit less than .05mV (.05A/m).

4.3.2 Measurement of normal permeability and hysteresis loss

A few of the hysteresis loops taken by the uniformly-varying
flux method are given in fig. 4.2. The peaks of all the loops taken are
shown in fig. 4.7. The larger loops were recorded by computer (section
4.3.1.4) and the smaller loops ($H_m < 200$ A/m) with the operational
integrator and XY recorder where noise became a problem on the computer
line. There was no difference between the two methods of recording for
the medium loops. The inset on fig. 4.2 shows the remanent flux density
B_r and coercive force H_c of each loop plotted against the loop maximum
flux density B_m . This is used later to justify the limit set on the
investigation of the effect of magnetic history on incremental
permeability. Several of the loops were drawn to a large scale and their
areas measured with a planimeter. The mean of three consecutive readings
differing by less than 1% was used to calculate the hysteresis loss.
This is plotted together with the loss of incremental loops in figs. 4.26
and 4.27.

Before taking the above loops, the maximum rate of change of

flux that could be used without eddy-current errors was determined. Loops of maximum field strength 10000 A/m were recorded by computer with loop times from 2.46 s to 75.0 s. An increase of rate caused an increase of apparent remanent flux density and coercive force as shown by the difference between the slowest and fastest loops plotted in fig. 4.3. The apparent coercive force is plotted against the rate of change of flux in fig. 4.4, showing that a flux rate of less than 0.03 mWb/s, where there was no variation of coercive force, could be used. To be safe, a rate of change of about 0.015 mWb/s was used, corresponding to a loop time of 30 s for the larger loops. The oscillogram, reproduced in fig. 4.5, of the flux-coil output and the magnetising current shows that this uniform flux rate could be maintained for the whole cycle.

One of the loops was also taken by the slowly-varying flux method and by the ballistic method. Fig. 4.6 shows the XY recording of the slowly-varying method, together with points by the other methods.

A normal magnetisation curve taken by the ballistic method is shown in fig. 4.7, together with points from the other two methods. Complete reversals of current were used in the ballistic method, and B_m and H_m were recorded as the amplitude of each reversal was decreased in small steps to zero and increased again. (The uniformly-varying loops were only taken in descending order.) It was found that many more reversals were needed to give a steady change of flux at each step when the current was being decreased than when it was being increased, although the points eventually lay on the same curve. The number of reversals needed near the steep portion of the curve, $B_m \simeq 0.5$ T, was 150 during the decrease, and only 30 during the increase. The time taken for each reversal was also very long in this region of maximum permeability, because of eddy-currents in the solid specimen, and when demagnetisation was required later a careful procedure had to be followed.

It was found that an effective demagnetisation was produced by decreasing H_m from about 10000 A/m to zero in steps such that B_m was decreased by about 0.05 T at each step, with four reversals at each step,

and waiting for the flux to completely reverse. This procedure left a residual magnetism of 0.01 T, as measured by the difference between the positive and negative peaks of subsequent reversals. Later results on incremental permeability showed that the effect of this residual magnetism on permeability was always less than 1%.

The normal permeability calculated from the ballistic curve in fig. 4.7 $(\mu_n = \frac{B_m}{\mu_o H_m})$ is shown in fig. 4.8 plotted against H_m, and in fig. 4.9 against B_m.

4.3.3 Discussion of results

The shapes of the normal permeability curves are in agreement with those obtained by earlier workers[22]; in particular the tail on the μ_n/B_m curve (fig. 4.9) was often observed[22], and the initial portion of the μ_n/H_m curve (fig. 4.8) agrees with Rayleigh's observations[21], being practically linear up to $H_m = 50$ A/m. The logarithmic plot of hysteresis loss against flux density (fig. 4.27) shows that the Steinmetz law holds in distinct ranges of flux density, as was sometimes found earlier[44]. The loss is given by

$$W_h = 720 \, B_m^{1.78} \quad J/m^3 \quad \text{for} \quad 0.06 \, T \leqslant B_m \leqslant 1.0 \, T$$

$$W_h = 720 \, B_m^{2.31} \quad J/m^3 \quad \text{for} \quad 1.0 \, T \leqslant B_m \leqslant 1.8 \, T$$

Above 1.8 T the index decreases again, in agreement with other recent observations[108]. The amplitudes of the permeability and hysteresis loss also agree with earlier work for mild steel.[109]

The comparison between the three methods of measuring a hysteresis loop (fig. 4.6) shows that the difference between the methods is very small for a loop of medium peak flux density $(B_m=1.50 \, T; H_m=1840 \, A/m)$. The plot in fig. 4.7 of the peaks of other loops shows that the difference is likely to be small for other loops also. The figure shows that there was no consistent difference between the methods except for some of the higher values of H_m (8000 to 16000 A/m approx.) where the uniformly-varying method gave values of B_m about 0.5% higher than the

ballistic method. The experiments were not repeated as such a small difference would not affect the calculation of eddy-current loss, in view of the approximations necessary in the representation of the hysteresis loops. In addition, in later experiments the remanent flux density of several loops was measured by the ballistic and slowly-varying methods, and no differences were found between these and the uniformly-varying method results.

The results confirm and extend the only earlier comparison of the methods for mild steel. In 1954 Ross[101] compared the ballistic and slowly-varying methods for one hysteresis loop, of peak value H_m = 720 A/m. The methods gave the same value of peak flux density (1.0 T) and values of coercive force and remanence which differed by about 1%, the order of the experimental error.

The constancy of coercive force and remanent flux density above B_m = 1.65 T shown in fig. 4.2 shows that for this steel the steep portion of the hysteresis loop does not change for peak flux densities above 1.65 T (at which H_m = 3500 A/m). The curves also show that the relation $\frac{H_c}{H_{cm}} = \frac{B_r}{B_{rm}}$, where H_{cm} and B_{rm} are the maximum values of H_c and B_r, is not necessarily true. This relation was used by Nicholls et al.[29], without experimental justification, to calculate $\check{B}$ in eqn. 3.7 from a knowledge of H_{cm}, B_{rm} and an assumed shape of demagnetisation curve.

4.4   Permeability and hysteresis loss for incremental loops on the normal magnetisation curve

4.4.1 Method

The methods used for the measurement of incremental permeability and hysteresis loss of biased loops were similar to those used for the normal permeability and hysteresis loss. It was found most convenient to use the ballistic method for permeability, and the slowly varying method with the XY recorder when it was desired to record a complete incremental loop and find the hysteresis loss. As the three available methods gave the same results for normal loops, discussed in the previous section, it was expected that the results would be reliable, and a comparison of the ballistic method with the other two methods for several incremental loops confirmed this (fig. 4.29).

The circuit used was that of fig. 4.1 (a) with the addition of an extra variable d.c. source for the incremental loops, as shown in fig. 4.10. Both d.c. sources were connected via low drift chopper-stabilized operational amplifiers having unity closed-loop gain. These had a very low output impedance so neither d.c. source affected the other.
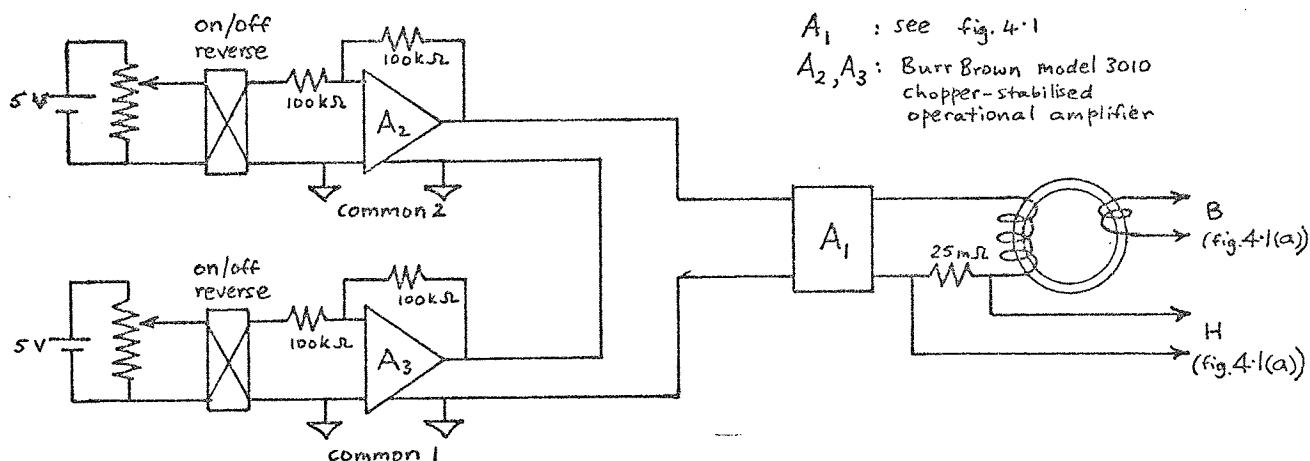
Fig. 4.10 Circuit for superposing two variable steady fields.

With this arrangement a particular incremental loop could be established by first setting one of the d.c. sources to give the required amplitude of the incremental loop (H_Δ). After switching this source off the other source was used to cycle the specimen down from about 10000 A/m in steps of 0.05 T to the required bias level (H_b) and cycled there until

the change of flux density was steady. The first source was then switched on again and reversed until the incremental change of flux density became constant. A loop was then traversed slowly (varying the first source by hand) for the measurement of hysteresis loss, or the peak points were read from the digital voltmeters for the measurement of permeability.

In the presence of a large biasing field the incremental flux density change $(2B_\Delta)$ could be read more accurately by resetting the integrator to zero at one of the peak points. H_Δ was already known accurately from the preliminary amplitude setting procedure. H_b was the same as the value before the first source was switched on again, and the biasing flux density B_b was calculated from the peak points of the incremental loop $(B_b = \frac{\hat{B} + \check{B}}{2})$.

In the above procedure a normal loop of amplitude H_b was established and then the incremental field was applied, as illustrated in fig. 4.11 (a). The alternative procedure of establishing a normal loop of amplitude $\hat{H}$ before applying the incremental field, illustrated in fig. 4.11 (b), was more difficult to perform rapidly and a few experiments showed that the results for permeability differed by 2% or less for small incremental loops ($H_\Delta < 500$ A/m) and by only 0.5% for a larger loop ($H_\Delta = 2500$ A/m). The difference in hysteresis loss was even smaller.
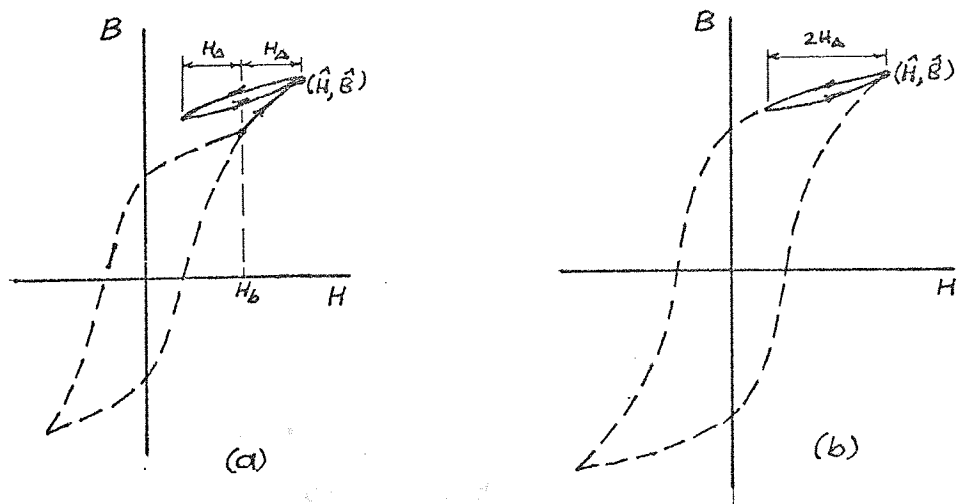
Fig. 4.11   Two ways of forming an incremental loop on the normal magnetisation curve.
(a) from normal loop of amplitude H_b
(b)   "   "   "   "   " $\hat{H}$

4.4.2 Incremental permeability

4.4.2.1 Experimental Results

Recordings of a few of the incremental loops studied are given in figs. 4.12, 4.13 and 4.14. The first two figures show a complete range of H_Δ, from small values to a value greater than H_b, and the third figure shows to a large scale a small incremental loop at the peak of a normal loop.

Plots of incremental permeability $(\mu_\Delta = \dfrac{B_\Delta}{\mu_o H_\Delta})$ are given in the following figures:

Fig. 4.15	μ_Δ	vs.	H_Δ	at constant	H_b
Fig. 4.16	μ_Δ	vs.	B_Δ	at constant	H_b
Fig. 4.17	μ_Δ	vs.	H_b	at constant	H_Δ
Fig. 4.18	μ_Δ	vs.	B_b	at constant	H_Δ
Fig. 4.19	μ_Δ	vs.	H_Δ	at constant	B_b
Fig. 4.20	μ_Δ	vs.	B_Δ	at constant	B_b

The first four figures were plotted directly from the results, and the last two were obtained from cross-plots of fig. 4.18.

Two further figures are given, mainly for comparison with the results of earlier workers. Fig. 4.21 is the low H_Δ part of fig. 4.19, using linear scales. Fig. 4.22 shows the permeability of sets of incremental loops with the same peak flux density (as considered by Spooner, fig. 3.16) obtained from fig. 4.20 by plotting lines of constant $\left(B_\Delta + B_b\right) = B_m$.

4.4.2.2 Discussion of results

Quantitative comparisons can be made between the measured results and the general formulae and curves given by Gans, Spooner and Ebinger, described in chapter 3, section 3.2.1.2. The equation for the initial linear section of the curve of normal permeability against H_m (fig. 4.8 (i)) is

$$\mu_n = 320 + 3.30\, H_m \tag{4.1}$$

giving $\mu_i = 320$ and $\nu = 3.30$. The reversible permeability for several values of biasing flux density was obtained from fig. 4.21 and is plotted in the form suggested by Gans in fig. 4.23, using $B_s = 2.1$ T.
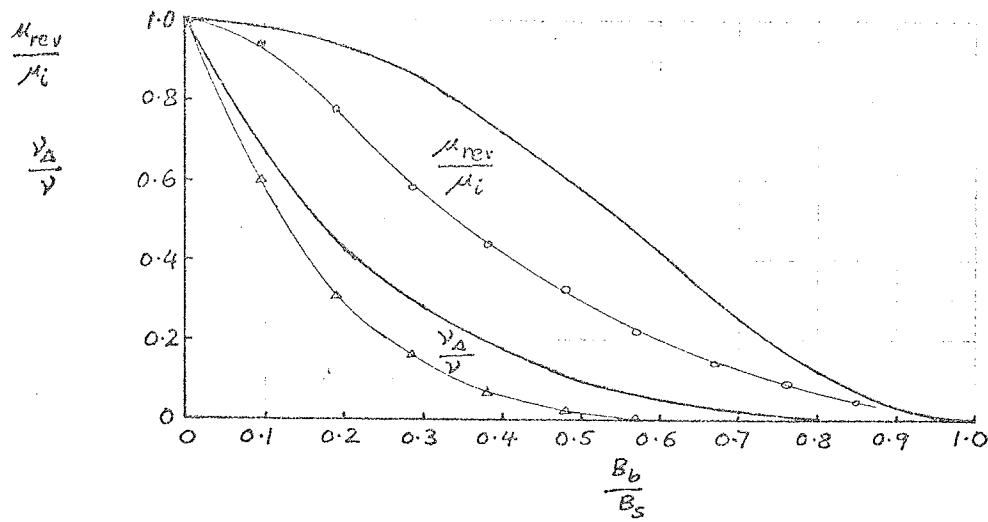
Fig. 4.23 Comparison of measured values of $\dfrac{\mu_{rev}}{\mu_i}$ and $\dfrac{\nu_\Delta}{\nu}$ with the curves given by Gans and Ebinger

—————— general curve for $\dfrac{\mu_{rev}}{\mu_i}$ given by Gans

o $\dfrac{\mu_{rev}}{\mu_i}$ measured from fig. 4.21

—————— general curve for $\dfrac{\nu_\Delta}{\nu}$ given by Ebinger

△ $\dfrac{\nu_\Delta}{\nu}$ measured from fig. 4.21

The agreement with Gans' curve is poor, and 100% errors could result if Gans' curve was used to predict reversible permeability for this steel, unlike other non-oriented steels considered by Bozorth[22] and the rail steel used by Langman (fig. 3.34).

For slightly larger values of H_Δ , Ebinger suggested the linear equation, eqn. (3.2). Fig. 4.21 shows that this law is valid for values of H_Δ up to 50 A/m at the lower biasing flux densities, and to higher values of H_Δ as B_b increases. Values of $\dfrac{\nu_\Delta}{\nu}$ are plotted in fig. 4.23, and whilst the experimental curve follows the general shape of Ebinger's curve, the numerical agreement is seen to be poor. Thus μ_Δ calculated from eqn. 3.2 as suggested in section 3.2.1.2 would contain large errors introduced by both the μ_{rev} and the ν_Δ terms.

Ebinger's other two equations (eqns. 3.4 and 3.5) are concerned with the variation of μ_Δ with B_Δ at a given steady flux density. Eqn. 3.4 predicts a linear relation between μ_Δ and B_Δ , and fig. 4.20 shows that such a relation holds approximately for values of B_Δ up to about 0.2 T, for most values of B_b . The comparison between the constants A and B in eqn. 3.4 calculated from fig. 4.20, and given by Ebinger is

shown in fig. 4.24. Once again the shapes of the curves are similar, but the numerical agreement is poor, especially for values of steady flux density below 1.0 T. Eqn. 3.5 predicts a quadratic relation between B_Δ and μ_Δ, and fig. 4.20 shows that this could hold approximately for only a slightly greater range of B_Δ than the linear relation.
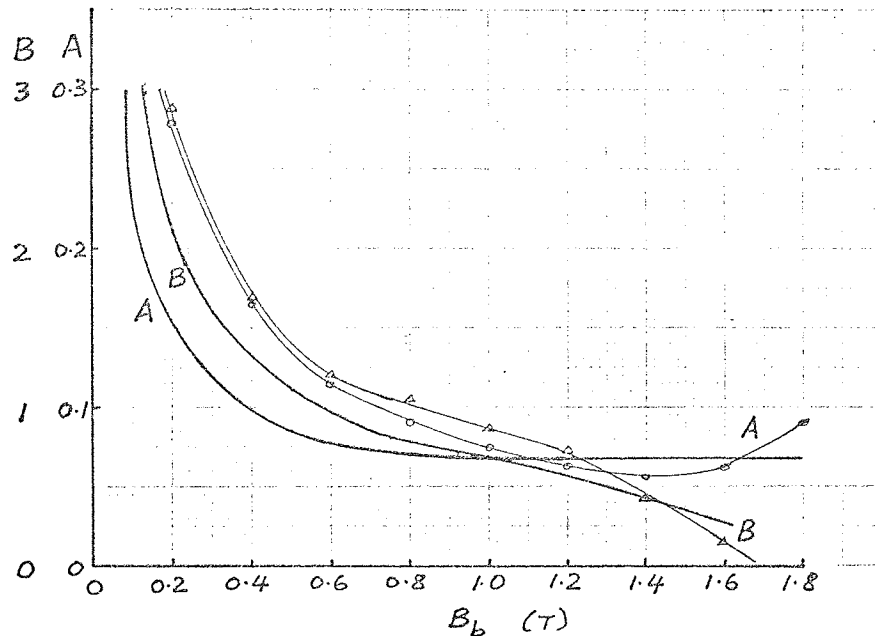
Fig. 4.24 Comparison of measured values of constants A and
B in eqn. 3.4, $\mu_\Delta = \mu_{bn}(A + B. B_\Delta)$, with the
curves given by Ebinger

—— curves given by Ebinger

o A ⎫
△ B ⎬ measured from fig. 4.20

A relation which holds over a much greater range of B_Δ than the equations suggested by Ebinger is eqn. 3.3, suggested by Spooner. This may be seen from fig. 4.22 which shows that there is a linear relation between μ_Δ and B_Δ for values of B_Δ up to at least $\frac{B_m}{2}$, for sets of incremental loops of the same peak flux density. The curves in fig. 4.22 are of similar shape to the results obtained by Spooner (fig. 3.16) and the measured values of the constants 'a' and 'b' in eqn. 3.3 are compared with Spooner's curves in fig. 4.25. The difference between the curves for 'b' is always less than 20%. The difference between the curves for 'a' is as high as 30% at some values of B_m, but the error introduced would be small at the higher vales of B_Δ where 'b' is the dominant constant.
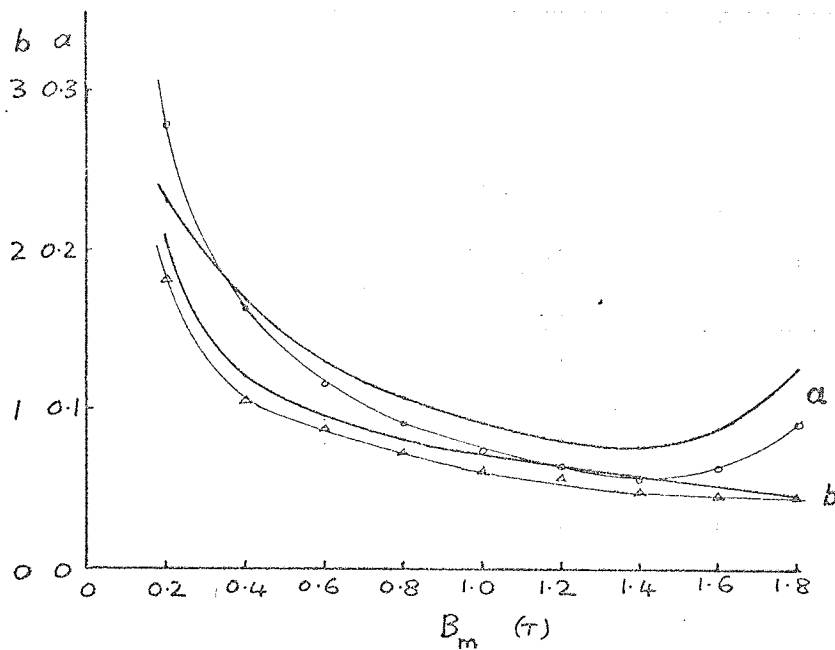
Fig. 4.25 Comparison of measured values of constants 'a'
and 'b' in eqn. 3.3, $\mu_\Delta = \mu_{Bm}(a+b\Delta B)$, with the
curves given by Spooner

—— curves given by Spooner
o a }
△ b } measured from fig. 4.22

It was mentioned in section 3.2.1.2 that μ_Δ could be

estimated from the normal magnetisation curve by neglecting hysteresis,

and this method was later illustrated in fig. 3.49. The results of

doing this for one value of biasing field (H_b = 900 A/m) are shown in

fig. 4.16, and it can be seen that the method over-estimates μ_Δ by a

factor of 4 for small incremental loops and by a progressively smaller

amount as the loop size increases. Other calculations show that

the over-estimations are less than about 20% if H_b is less than H_Δ

by about 500 A/m or more, or if H_b is greater than about 5000 A/m.

Instead of using the normal magnetisation curve to

calculate μ_Δ , the descending parts of a family of normal hysteresis

loops can be used (as illustrated in fig. 3.4). Three points

obtained by this method for H_b = 900 A/m are plotted in fig. 4.16,

and the agreement with the measured curve is much better than

that obtained by using the normal magnetisation curve, especially

for the smaller incremental loops. Values of μ_Δ calculated from

a family of normal hysteresis loops for the complete range of

biasing field are plotted in fig. 4.15, which shows that the permeability is always estimated with a percentage error not greater than about 10%.

The differences between the measured values of μ_Δ and the two methods of estimating μ_Δ from the normal magnetic characteristics are due to hysteresis. This is shown in the X-Y recording of an incremental loop and the tip of a normal loop in fig. 4.14. It can be seen that the slope of the incremental loop is a little less than the slope of the descending part of the normal loop which in turn is considerably less than the slope of the normal magnetisation curve (which follows very closely the ascending part of the normal loop).

Some general comments about the results for μ_Δ can be made. Considering first the behaviour of μ_Δ with a given biasing field strength, figs. 4.15, 4.16 and 4.17 show that:

1) $\mu_\Delta \simeq$ constant (μ_{rev}) if $H_\Delta < H_b$

2) $\mu_\Delta \ll \mu_n$ if $H_\Delta < H_b$ and H_b is large

3) $\mu_\Delta \simeq \mu_n$ if $H_\Delta > H_b$

These three points are illustrated by the X-Y recording of some incremental loops with $H_b = 900$ A/m in fig. 4.12. For small values of H_Δ the slopes of all the incremental loops (μ_Δ) are small and approximately equal to the reversible permeability for this particular value of H_b. As H_Δ begins to exceed H_b and negative values of H are achieved, the slope increases rapidly and approaches the values obtained with no biasing field. The results reported in earlier publications, discussed in chapter 3, also agree with the three points. There were the ballistic tests of Searle (fig. 3.15), Sugiura (fig. 3.17) and Sims and Clay (fig. 3.18), although only Sugiura had a solid, mild-steel specimen. Results obtained for laminated specimens by a.c. methods with constant values of biasing field strength were only plotted in terms of B_Δ, as shown in figs. 3.32 and 3.33. The

variation of μ_Δ indicated in fig. 3.33 is similar to that in fig. 4.16, although exact comparisons cannot be made because of the distortion problems illustrated in fig. 3.31. When the curves are replotted in terms of H_Δ the sharp change of permeability where $H_\Delta \simeq H_b$ is not present, which was also shown in fig. 3.31.

The behaviour when the biasing flux density is maintained at a given value is shown in figs. 4.18, 4.19 and 4.20, and the main difference from the behaviour with H_b constant is that μ_Δ does not return to normal when H_Δ is large. Thus for $B_b = 1.8$ T, μ_Δ is at a constant low value, equal to μ_{rev} for this particular value of B_b, apart from the 10% rise at $H_\Delta = 6000$ A/m (fig. 4.19). The only previously reported results plotted for constant values of steady flux density were those of Edgar (fig. 3.30) who used an a.c. method on silicon steel laminations, and they show the same general behaviour.

The various shapes which an incremental loop may take are illustrated in figs. 4.12 - 4.14. When H_Δ is less than H_b the loop is elliptical (figs. 4.12 , 4.14), and as H_Δ exceeds H_b (and μ_Δ tends to μ_n) it begins to resemble the normal hysteresis loop but it has unsymmetrical positive and negative portions (fig. 4.13). It may also be seen from these figures that an elliptical loop is associated with a high value of B_b, and an unsymmetrical one with a low value.

4.4.3 Hysteresis loss

The measurements of the hysteresis loss of incremental loops on the normal magnetisation curve were not as extensive as the measurements of permeability. Sufficient results were taken, however, to determine the main features of the effect of a biasing field on the hysteresis loss. The variation of the loss for given values of biasing field strength is shown in fig. 4.26 as a function of H_Δ and in fig. 4.27 as a function of B_Δ. Some approximate lines of constant biasing flux density are also drawn in fig. 4.26.

There is a difference between the behaviour of the loss at a given value of H_Δ and at a given value of B_Δ. Fig. 4.26 shows that the loss for a given H_Δ always decreased as the biasing field increased, whilst fig. 4.27 shows that the loss for a given B_Δ decreased as the biasing field increased only if B_Δ was greater than about 1.25 T. Below this value the biasing field caused an increase in loss.

It can be seen from fig. 4.26 that very small losses occurred when B_b was high and H_b was greater than H_Δ. The previous section showed that for these conditions μ_Δ, and hence B_Δ, was small. These points are illustrated by the X-Y recording in fig. 4.12 where the variation of the flux density amplitude and area of an incremental loop as H_Δ changes can be seen.

Earlier work, discussed in chapter 3, concentrated on the loss as a function of B_Δ. The only results for loss at given values of H_Δ were the few loops at one value of H_Δ given by Ewing and Klaassen[37] in a figure similar to fig. 3.1, and those given for H_b less than H_Δ by Niwa et al. (eqn. 3.17). There is no disagreement between the earlier work and the present results which confirm the decrease of loss observed at the higher values of B_Δ and the tendency of the loss at low values of B_Δ to increase and then decrease with increasing biasing field (fig. 3.37) although mild steel was not used by the earlier workers.

4.4.4 Effect of the varying field on the steady field

Curves of biasing flux density against biasing field strength for several values of H_Δ are given in fig. 4.28, where the normal magnetisation curve is distinguished by the broken line. The curves show that at constant biasing field strength the biasing flux density increases first and then decreases to a very low value as H_Δ increases and becomes greater than H_b. This change of average flux density is evident in the incremental loop recordings in fig. 4.12. On the other hand, at constant biasing flux density, the biasing field strength decreases slightly and then increases in step with the increase of H_Δ, except at high biasing flux densities where the incremental field has little effect.

The phenomenon and the earlier contributions were discussed in chapter 3, section 3.5.1. The earlier results were all obtained using a.c. methods and were mostly given in terms of B_Δ rather than H_Δ. The influence of the waveform under a.c. conditions was also mentioned.

4.5 Effect of magnetic history on incremental permeability

4.5.1 Method

In section 4.4 incremental loops on the normal magnetisation curve, i.e. at the peak of a normal loop, were considered. Results are now given for the permeability of incremental loops at other positions on a normal loop, as illustrated in figs. 3.5 and 3.6.

Apart from one set of results taken with uniformly-varying flux, the ballistic method was quicker and was used as described in section 4.4.1. The procedure was also similar, except that after setting the incremental loop amplitude H_Δ the biasing field strength H_b was cycled down from about 10000 A/m to the peak of the required normal loop (H_m, B_m), cycled there until the change of flux density was steady, and then H_b was reduced to the required level. The incremental loop was then performed as before, many reversals being needed to give a steady flux density change when μ_Δ was near a maximum.

4.5.2 Results

The incremental permeability was measured for incremental loops of several sizes (H_Δ = 5 to 7500 A/m) at many positions on several normal loops (H_m = 250 to 10000 A/m). As there is insufficient space to publish all the results, a selection showing the main features is given.

The variation of μ_Δ with H_b for incremental loops of H_Δ = 250 A/m at different points on the normal loop of amplitude H_m = 4000 A/m, B_m = 1.68 T is shown in fig. 4.29. The curve joins points taken with uniformly-varying flux. Points taken by the ballistic method for incremental loops on the same normal loop and on the normal magnetisation curve are also shown.

The effect of the size of the normal loop is shown in figs. 4.30 and 4.31 in which μ_Δ is plotted against H_b and against B_b for incremental loops of constant H_Δ (50 A/m) on several normal loops.

The effect of the same magnetic history on the permeability of incremental loops of different sizes is illustrated in figs. 4.32

and 4.33 where μ_Δ is plotted against H_b and against B_b for incremental loops on one normal loop (H_m = 4000 A/m, B_m = 1.68 T).

The results are summarised in figs. 4.34 and 4.35, which show the variation of μ_Δ with H_Δ for given values of H_b and B_b, for incremental loops at several positions on several normal loops.

4.5.3 Discussion of results

The good agreement shown in fig. 4.29 between the points taken ballistically and with uniformly-varying flux gives confidence in the use of the ballistic method for the measurements of μ_Δ.

Figs. 4.30 and 4.31 show that the effect of the previous magnetising force increased as its amplitude increased, until values of H_m greater than about 4000 A/m (such as 10000 A/m) were used, when little extra effect was produced. This coincides with the fact that the shapes of the normal loops with peak values greater than H_m = 4000 A/m, B_m = 1.68 T were similar, as shown by the plots of B_r and H_c in fig. 4.2.

In view of the above results, an idea of the maximum differences that existed between the permeability of incremental loops on the normal magnetisation curve and those with a different previous history can be obtained by considering incremental loops on the normal loop H_m = 4000 A/m. The curves in figs. 4.32 - 4.35 show that the differences were small if H_b or B_b was large, especially for large B_b, and that the differences were small if H_Δ was greater than 1000 A/m. For example, for B_b = 1.6 T, the differences were less than 10% for all values of H_Δ, and with H_Δ = 1000 A/m the differences were less than 10% for all values of H_b, and less than 20% for all values of B_b.

It can be seen that μ_Δ for values of H_Δ less than 1000 A/m could depend considerably on the previous magnetic history. Figs. 4.30, 4.32 and 4.34 show that, for incremental loops with the same H_b, μ_Δ on a normal loop was always less than or equal to μ_Δ on the normal magnetisation curve. The differences in μ_Δ increased as H_Δ decreased

and were generally largest for incremental loops on the descending part of a normal loop. The maximum difference recorded was for $H_\Delta = 5$ A/m, $H_b \simeq 200$ A/m where μ_Δ on the descending part of the normal loop $H_m = 4000$ A/m was only 23% of the value on the normal magnetisation curve. The behaviour for incremental loops of the same B_b was different. Figs. 4.31, 4.33 and 4.35 show that μ_Δ on a normal loop was not always less than μ_Δ on the normal magnetisation curve, μ_Δ being greater on the descending branch of a normal loop when B_b was more than about 0.5 T. Also, the differences were greatest for H_Δ in the range 100 - 500 A/m. For example, with $B_b = 1.0$ T the maximum difference was for an incremental loop of $H_\Delta = 250$ A/m on the descending branch of the normal loop $H_m = 4000$ A/m, for which μ_Δ was 310% of the value on the normal magnetisation curve, and with $B_b = 0$ T, the maximum difference was for $H_\Delta = 150$ A/m on the normal loop $H_m = 4000$ A/m, for which μ_Δ was 32% of the value on the normal magnetisation curve.

As H_Δ tended to zero, the differences between μ_Δ on the normal loop and μ_Δ on the normal magnetisation curve tended to decrease for incremental loops of the same B_b (fig. 4.35), although the differences were still of the order of a factor of 2 at $H_\Delta = 5$ A/m. An extrapolation of the curves to $H_\Delta = 0$ using a linear scale instead of the logarithmic scale of fig. 4.35 showed that differences of this order still existed at $H_\Delta = 0$, unless a sudden change of μ_Δ occurs as H_Δ tends to zero, which has not been noted before, and which did not occur with the present sample for the normal permeability (fig. 4.8). Thus, for this sample of mild steel, the reversible permeability μ_{rev} for incremental loops of the same B_b is probably not independent of the previous magnetic history.

Earlier experiments with soft iron on the effect of magnetic history on μ_Δ were discussed in chapter 3, sections 3.2.1.3 and 3.2.3.5. The results reported using the ballistic or slowly-varying flux methods were only for $H_b = 0$. The main results were those of Searle shown in fig. 3.14 (a) which covered a wide range of H_Δ and previous magnetising

force H_m , and the form of his curves agrees with the present results for H_b = 0 in fig. 4.34. Searle also found that little extra change of μ_Δ was produced by increasing H_m beyond a certain large value ($\simeq$ 1000 A/m for his sample of 'tagger plate') which agrees with the present results where H_m = 4000 A/m was the 'limiting' previous history (for both samples the limiting value was about ten times the field strength for maximum normal permeability).

Earlier results by a.c. methods were only for small values of H_Δ and contained uncertain eddy-current effects as frequencies were either unspecified or of the order of 500 Hz, and the thicknesses of the samples were not given. Even so, the general shapes of the curves given by Sizoo (fig. 3.28) and Goldschmidt (fig. 3.29) agree with the present results. Sizoo, however, found that for 3% Si steel μ_{rev} for incremental loops of the same B_b was independent of previous magnetic history, which does not agree with the above discussion of fig. 4.35. Bozorth[22] surveyed available results for μ_{rev} for a variety of materials and found that μ_{rev} tended to be independent of magnetic history for materials with a 'normal' domain structure, although Sizoo's results were the only ones quoted for steel. The results presented in this section show that μ_{rev} for EN1A mild steel does not have the same behaviour as for other materials with a similar 'normal' domain structure, and this is supported by the difference between measured values and Gans' curve for μ_{rev} on the normal magnetisation curve discussed earlier (section 4.4.2.2, fig. 4.23).

A method of scaling the normal magnetisation curve to calculate μ_Δ for incremental loops on the descending branch of a normal loop was discussed in chapter 3, section 3.2.1.2 (Nicholls et al). The method is embodied in eqn. 3.8 and curves representing this equation are compared with measured values in fig. 4.36. Incremental loops on the normal loop H_m = 4000 A/m were considered, and B_s was taken to be 2.1 T. It can be seen that the equation does not represent the measured variation of μ_Δ over the whole range of B_Δ . The relation
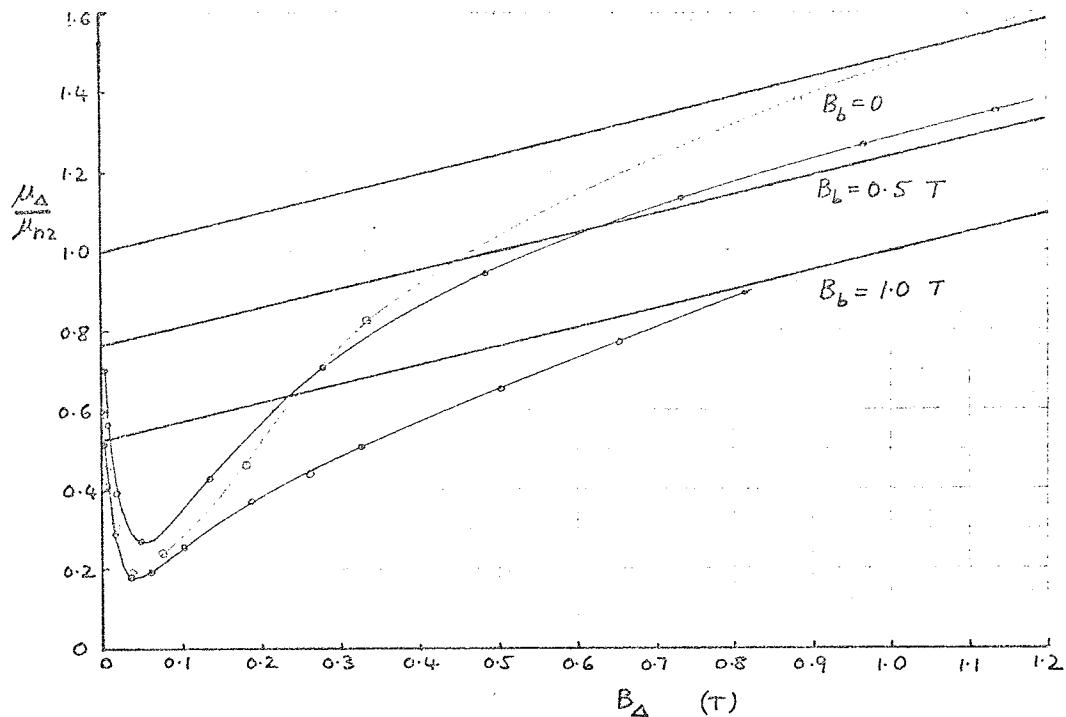
Comparison of measured values of $\dfrac{\mu_\Delta}{\mu_{n2}}$ for incremental loops on descending part of normal loop $H_m = 4000$ A/m, $B_m = 1.68$ T with curves calculated from eqn. 3.8 :

$$\left(\frac{\mu_\Delta}{\mu_{n2}} = 1 - \frac{B_b}{B_s} + \frac{B_\Delta}{B_s} \right)$$

——— calculated from eqn. 3.8

o   measured

could possibly be used, however, for large values of B_Δ (greater than about 0.5 T depending on B_b), or for very small values of B_Δ (0.001 T) if B_b is greater than 0.5 T. The maximum difference between the measured and calculated values occurred for B_Δ = 0.05 T, B_b = 0 T when the measured value of μ_Δ was 20% of the value given by eqn. 3.8. The discussion of eqn. 3.8 in section 3.2.1.2 indicated that the method should give reasonable results for very small values of B_Δ (eqn. 3.9 for μ_{rev} plotted in fig. 3.7 agreed with Gans' results), but that it should over-estimate μ_Δ for slightly larger values of B_Δ (eqn. 3.10 for $\dfrac{\nu_\Delta}{\nu}$ plotted in fig. 3.11 was above Ebinger's results). Both points are based on comparisons which were not valid for the test sample of mild steel as it was assumed in eqns. 3.9 and 3.10 that μ_{rev} and ν_Δ were single-valued functions of B_b. Nevertheless, as noted above, the method of Nicholls et al. does tend to give better results for very low values of B_Δ, and to over-estimate μ_Δ for slightly larger values of B_Δ.

4.6 Conclusion

The three methods of measuring a hysteresis loop, ballistic, slowly-varying flux and uniformly-varying flux, give the same results for EN1A mild steel, at least for fields up to $H_m \simeq 20000$ A/m, $B_m \simeq 2.0$ T. The ballistic method using an operational integrator instead of a ballistic galvanometer is suitable for rapid determinations of permeability and the slowly-varying flux method for a quick determination of a few hysteresis loops. The uniformly-varying method is suitable for automated computer measurements of many loops where the regular, square $\frac{d\phi}{dt}$ waveform is an advantage, or, because of the short time spent at high field strengths, for measuring loops of high peak field strength if overheating occurs with the other methods[103].

The permeabilities, biasing flux densities and shapes of incremental loops on the normal magnetisation curve may be classified according to the relative magnitudes of H_b and H_Δ, with some variations depending on the absolute magnitude of H_Δ :

(i)   When H_b is less than H_Δ, the incremental permeability is approximately equal to the normal permeability and the biasing flux density is low, but the incremental loop is an unsymmetrical ⌐ shape.

(ii)   When H_b is approximately equal to H_Δ, μ_Δ and B_b have intermediate values (between (i) and (iii)) and the loop is an unsymmetrical ⌐ shape.

(iii)   When H_b is greater than H_Δ, μ_Δ is much less than μ_n, B_b is high and the incremental loop is approximately elliptical. In addition, there is little variation of μ_Δ with H_Δ, and $\mu_\Delta = \mu_{rev}$.

Since, as H_b increases for a given value of H_Δ there is a transition zone of about 1000 A/m between the regions of high and low permeability, when H_Δ is less than about 1000 A/m the type of behaviour (i) is not so evident. When H_Δ is less than about 100 A/m, the incremental loop is approximately elliptical for all values of H_b.

The effect of previous magnetic history is small when either B_b or H_b is large ($B_b \gtrsim 1.5$ T, $H_b \gtrsim 2500$ A/m), or when H_Δ is greater

than about 1000 A/m.   At other times its effect can be considerable.

The permeability of incremental loops on the normal magnetisation curve may be calculated to within 10% from a set of normal hysteresis loops, for all values of H_Δ and H_b. For a limited range of H_Δ and H_b the normal magnetisation curve may be used for approximate calculations (errors $\simeq$ +20% if $H_\Delta \gtrsim (H_b + 500)$ A/m, or if $H_b \gtrsim 5000$ A/m). If a set of normal loops is not available, the method introduced by Spooner (eqn. 3.3) is fairly accurate for a wide range of incremental loops when Spooner's curves for the 'constants' a and b are used, and for mild steel greater accuracy could probably be obtained by using the present measured values for the constants (fig. 4.25). None of the above methods can be used for incremental loops not on the normal magnetisation curve, unless H_b, B_b or H_Δ are such that the effect of previous magnetic history is small, and no other accurate method is known.

The hysteresis loss of an incremental loop on the normal magnetisation curve for a given value of H_Δ is much less than the normal hysteresis loss if H_b is greater than H_Δ (attended by a high value of B_b). The loss for a given value of B_Δ may be increased by the biasing field, but only if B_Δ is less than about 1.25 T, which is similar to the behaviour observed by earlier workers for silicon steel.

5.   A.C. losses in solid iron with a superposed parallel steady field

5.1   Introduction

The results presented in chapter 4 showed that the permeability of incremental loops on the normal magnetisation curve was constant for a given value of H_b if H_Δ was less than H_b, and for values of H_Δ greater than H_b the incremental permeability was close to the normal permeability, but the incremental loops were unsymmetrical. In this chapter measurements of a.c. losses in the solid steel ring, mainly for values of H_Δ less than H_b, are compared with constant permeability theory. A theoretical indication of the results to be expected when H_Δ is greater than H_b is also given. As shown in chapter 3, such measurements and calculations have not previously been reported.

Sinusoidal current at 300 Hz was used for the tests. This frequency is equal to the frequency of the eddy currents induced in the rotor of a 50 Hz synchronous machine by the first pair of m.m.f. harmonics and thus produced comparable eddy-current and hysteresis losses. The choice of sinusoidal current was also made because of the similarity with the source of the m.m.f. harmonics, and it was particularly appropriate in the tests because the surface field strength was then completely specified by the known direct and alternating currents.

5.2   Constant permeability theory

5.2.1 Theory with hysteresis neglected

The sample used for the tests was the same as the one used for the permeability measurements, described in chapter 4, section 4.2. The magnetic field strength is known on the surface directly from the supply current, and inside the iron it obeys the diffusion equation

$$\nabla^2 \underline{H} = \frac{\mu_0 \mu_\Delta}{\rho} \frac{\partial \underline{H}}{\partial t} \tag{5.1}$$

The addition of a constant term H_b to $\underline{H}$ does not affect the equation and so the biasing field may be accounted for by using the appropriate value of μ_Δ .

Since the specimen was a toroid of circular section, the theory is developed in cylindrical coordinates, as shown in fig. 5.1. For the a.c. field the diffusion equation reduces to
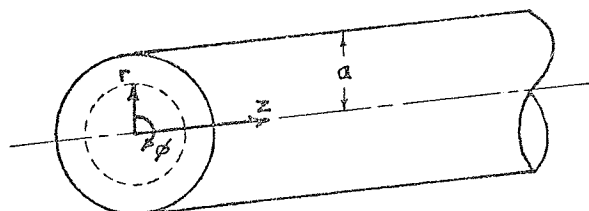
Fig. 5.1 Representation of the sample

$$\frac{\partial^2 H_z}{\partial r^2} + \frac{1}{r} \frac{\partial H_z}{\partial r} = \frac{\mu_0 \mu_\Delta}{\rho} \frac{\partial H_z}{\partial t} \tag{5.2}$$

since H_z is the only component of $\underline{H}$ and it is independent of ϕ and z .

By writing $H_z = \mathcal{Re}\, \dot{H} e^{j\omega t}$, eqn. (5.2) becomes

$$\frac{\partial^2 \dot{H}}{\partial r^2} + \frac{1}{r} \frac{\partial \dot{H}}{\partial r} - j m^2 = 0 \tag{5.3}$$

where

$$m = \sqrt{\frac{\omega \mu_0 \mu_\Delta}{\rho}} \tag{5.4}$$

The solution may be written in the form[110]

$$\dot{H} = A\, J_0 \left(j^{3/2}\, mr \right) + B\, Y_0 \left(j^{3/2}\, mr \right) \tag{5.5}$$

where J_0 and Y_0 are Bessel functions of zero order of the first and second kinds. The boundary conditions, $\dot{H}$ is finite at $r = 0$ and $\dot{H} = H_\Delta$ at $r = a$, give

$$\dot{H} = H_\Delta \frac{J_0 \left(j^{3/2}\, mr \right)}{J_0 \left(j^{3/2}\, ma \right)} \tag{5.6}$$

The electric field strength found from curl $\underline{H} = \frac{1}{\rho}\underline{E}$ is in the ϕ direction and is given by

$$E_\phi = -\rho\,\frac{\partial H_z}{\partial r} \,. \tag{5.7}$$

Letting $E_\phi = \mathcal{R}e\,\dot{E}\,e^{j\omega t}$ gives

$$\dot{E} = H_\Delta\,m\rho\,\frac{j^{3/2}\,J_1(j^{3/2}\,mr)}{J_0(j^{3/2}\,ma)} \,. \tag{5.8}$$

Tables of the modulus and phase of $J_0(j^{3/2}x)$ and $J_1(j^{3/2}x)$ were given by McLachlan[110]. Thus by putting

$$M_n(mr) = \left| J_n(j^{3/2}\,mr) \right| \tag{5.9}$$

$$\vartheta_n(mr) = \angle\,J_n(j^{3/2}\,mr) \tag{5.10}$$

$\dot{E}$ may be written

$$\dot{E} = H_\Delta\,m\rho\,\frac{M_1(mr)}{M_0(ma)}\,e^{\,j(\vartheta_1(mr)\,-\,\vartheta_0(ma)\,+\,\frac{3}{4}\pi)} \tag{5.11}$$

The loss may then be obtained in a convenient form by using the real part Z of the wave impedance at the iron surface.

$$Z = \mathcal{R}e\left(-\frac{\dot{E}}{\dot{H}}\right)_{r=a} = \mathcal{R}e\,\frac{(-\dot{E})_{r=a}}{H_\Delta} = m\rho\,\frac{M_1(ma)}{M_0(ma)}\cos\vartheta(ma) \tag{5.12}$$

where

$$\vartheta(ma) = \vartheta_1(ma) - \vartheta_0(ma) - \frac{\pi}{4} \tag{5.13}$$

is the power factor angle, the angle between $\dot{H}$ and $-\dot{E}$ at $r = a$. The loss per unit surface area is given by

$$P = \frac{1}{2}\,H_\Delta^2\,Z \,. \tag{5.14}$$

Z and $\cos\vartheta$ are plotted against μ_Δ in figs. 5.2 and 5.3, using the values of a, ω and ρ appropriate to the tests ($a = 5.02 \times 10^{-3}$m, $f = 300$ Hz, $\rho = 1.9 \times 10^{-7}$ Ωm) .

The wave impedance and power factor of a semi-infinite slab excited by an alternating magnetic field parallel to its surface are given by

$$Z_\infty = \frac{m\rho}{\sqrt{2}} \,, \quad \cos\vartheta_\infty = 0.707 \,. \tag{5.15}$$

These are also shown on figs. 5.2 and 5.3. It can be seen that the behaviour of the test ring at 300 Hz should be similar to that of a

semi-infinite slab when μ_Δ is greater than about 100, but when μ_Δ is less than this, as occurred in the presence of a superposed steady field, the behaviour should be different. For example, when $\mu_\Delta = 20$ (obtained for H_Δ less than 1000 A/m when $H_b = 5400$ A/m, fig. 4.15) the wave impedance and loss in the ring should be 35% less than in a semi-infinite slab and they should be directly proportional to μ_Δ rather than to the square root of μ_Δ. Also the power factor should be 0.520, and it should be approximately proportional to the square root of μ_Δ, rather than independent of μ_Δ.

For interest, the ratio $ma = \dfrac{a}{d}$, where d is the depth of penetration $\sqrt{\dfrac{\rho}{\omega\mu_o\mu_\Delta}}$, is also given as an abscissa on figs. 5.2 and 5.3. A value for this ratio greater than about 5 is required for the behaviour of the ring to be similar to that of a semi-infinite slab. For values of ma less than about 1 (not shown on the figures) the skin effect is small and there is uniform flux-density behaviour.

The likely sensitivity of the loss to a change of resistivity (due to a change of temperature, for example) can be shown by plotting a loss function used by McLachlan[110] and defined as

$$W\,(ma) = \frac{2}{ma}\;\frac{M_1(ma)}{M_0(ma)}\;\cos\vartheta\,(ma) \tag{5.16}$$

Thus

$$P = \frac{1}{2}\,H_\Delta^2\,\frac{\omega\mu_o\mu_\Delta\,a}{2}\,W\,(ma) \tag{5.17}$$

the influence of resistivity being confined to W (ma). The plot of W (ma) in fig. 5.2 shows that it has a stationary point at $ma = 2.5$, corresponding to $\mu_\Delta = 20$ for the test sample at 300 Hz and normal temperature. For conditions giving this value of permeability, then, the loss should not be sensitive to resistivity. Above $ma = 2.5$ the loss increases with ρ, and below $ma = 2.5$ the loss decreases as ρ increases. The power factor is a function of $ma = \sqrt{\dfrac{\omega\mu_o\mu_\Delta}{\rho}}\,a$ only, and is therefore as sensitive to resistivity as it is to permeability. The effect of frequency on the loss and power factor is the same as that of permeability, as the two always occur together as $\omega\mu_\Delta$.

5.2.2 Allowance for hysteresis

An allowance for hysteresis is made by using the concept of complex permeability, equivalent to an elliptical representation of a B/H loop. The X-Y recordings of incremental loops in figs. 4.12 and 4.14 show this to be a reasonable representation for $H_\Delta < H_b$. As described later the maximum value of H_Δ used in the a.c. tests was 1000 A/m, and fig. 4.2 shows that the normal loops of this peak value and below are not too far removed from an elliptical shape. The loop for $H_\Delta = 1000$ A/m in fig. 4.12 shows that the largest differences are likely to occur when the loop is unsymmetrical and $H_\Delta > H_b$. The advantage of using an elliptical representation is that the hysteresis loss can be characterised by one parameter, the phase $\propto$ of the complex permeability.

If the magnetic field strength at a point in the iron is $H = H_\Delta \cos \omega t = \mathcal{R}e \, H_\Delta \, e^{j\omega t}$ and the corresponding flux density is $B = B_\Delta \cos(\omega t - \propto) = \mathcal{R}e \, B_\Delta \, e^{j(\omega t - \propto)}$, B lagging H by the angle $\propto$, then the complex permeability $\dot{\mu}_\Delta$ is given by

$$\dot{\mu}_\Delta = \frac{B}{\mu_o H} = \mu_\Delta \, e^{-j\propto} \tag{5.18}$$

where $\mu_\Delta = \dfrac{B_\Delta}{\mu_o H_\Delta}$. The area of the loop is the hysteresis loss per unit volume per cycle, given by

$$W_{hb} = \oint H \, dB = \pi \, H_\Delta \, B_\Delta \sin \propto \tag{5.19}$$

[A complex permeability μ_e was discussed in chapter 3, section 3.2.3.4, in connection with measurements of μ_Δ by a.c. methods. This a.c., or effective, permeability relates the surface field strength to the average flux density over the core section and includes eddy-current effects. The integral $\oint H_s \, dB_a$ over a cycle gives the total loss (eddy + hysteresis) per unit volume per cycle.]

The hysteresis angle is taken to be the value which makes the area of the ellipse approximation equal to the area of the actual loop when the peak values of magnetic field strength and flux density are

the same for both. Thus eqn.(5.19) gives

$$\alpha = \arcsin \frac{W_{hb}}{\pi H_\Delta B_\Delta} \tag{5.20}$$

Values of α calculated from the results for hysteresis loss given in chapter 4, section 4.4.3, are plotted in fig. 5.4.

To calculate the total loss it is assumed that both μ_Δ and α are constant, and the theory follows that given in the previous section with $\overset{\circ}{\mu}_\Delta$ replacing μ_Δ, making the factor m complex. The evaluation of the modulii and phase angles of the Bessel functions is now more difficult because tables for $M_n(x)$ and $\vartheta_n(x)$ with x complex are not available. Aspden[111], however, considered the problem of eddy currents in solid cylindrical cores and plotted a loss function $L(ma)$, equal to McLachlan's loss function (eqn.5.16) divided by 2, for a few values of α. Aspden's curves are reproduced in fig. 5.5 together with curves calculated from the $\alpha = 0$ curve using the correction factor for a semi-infinite slab (see below). The figure shows that this correction factor should be sufficient for the present tests because the differences are small for $ma > 3$, and because the measured hysteresis angle (fig. 5.4) is small for values of H_Δ and H_b ($H_b > 500$ A/m, $H_\Delta < H_b$) which give low permeabilities and values of ma near 2.5.

Fig.5.5 Aspden's loss
function for a cylinder with
hysteresis compared with
curves calculated from the
 $\alpha = 0$ curve using the
semi-infinite slab
correction factor $\sqrt{1+\sin\alpha}$.

——— Aspden's curves

- - - - $\alpha = 0$ curve times
$\sqrt{1+\sin\alpha}$
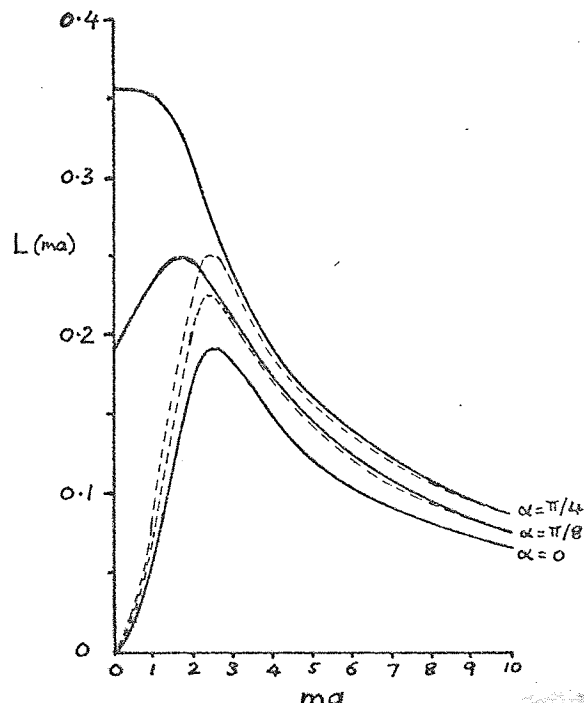
The total loss P_{e+h}, power factor angle ϑ_{e+h} and power factor in a semi-infinite slab were shown by Pohl[112] to be

$$P_{e+h} = P\sqrt{1+\sin\alpha}$$

$$\vartheta_{e+h} = \frac{\pi}{4} - \frac{\alpha}{2}$$

$$\cos\vartheta_{e+h} = 0.707\sqrt{1+\sin\alpha}$$

(5.21)

where P, $\pi/4$, 0.707 are the values in absence of hysteresis ($\alpha = 0$). The same correction factor $\sqrt{1+\sin\alpha}$ (sometimes written $\cos\frac{\alpha}{2} + \sin\frac{\alpha}{2}$ or $2\cos(\frac{\pi}{4} - \frac{\alpha}{2})$) applies to both the loss and the power factor only because the power factor angle in the absence of hysteresis is $\frac{\pi}{4}$. The appropriate formulae for the test ring should be

$$P_{e+h} = P\sqrt{1+\sin\alpha}$$

$$\vartheta_{e+h} = \vartheta - \frac{\alpha}{2}$$

$$\cos\vartheta_{e+h} = \cos(\vartheta - \frac{\alpha}{2})$$

(5.22)

where P and ϑ are given by eqns. 5.13 and 5.14 in the previous section.

5.3   Measurements

5.3.1   Resistivity

The resistivity of the steel used in the test sample was
measured by a colleague, A.L. Bowden, on an annealed bar of steel
from the same batch. The bar had a diameter of 3.70 cm and a length
of about 40 cm. The voltage drop between two probes near the centre
of the bar, 5 cm. apart, was plotted against the (d.c.) current which
entered and left the bar at the ends, and the gradient of this straight
line gave a value for resistivity at 23°C :

$$\rho = 1.9 \times 10^{-7} \ \Omega\text{m} \pm 2\% \ .$$

This value was used in the theoretical calculations; its
accuracy was not of great importance because the tests mostly covered
the region where the loss was insensitive to resistivity (eqn.5.17).

5.3.2   Method for a.c. loss measurements

5.3.2.1   Magnetising current supply

Circuits for superposing a.c. and d.c. were discussed in
chapter 3, section 3.2.3.3. A simple circuit suitable for
sinusoidal current is the series circuit with one magnetising winding,
fig. 3.22 (b), and this is the basis of the practical arrangement used,
shown on the left in fig. 5.6. To begin with, the circuit of fig.
4.10, used originally for superposing two variable steady fields, was
modified for a.c. and d.c. by replacing one of the d.c. sources with
a variable frequency signal generator. By virtue of the low output
impedance of the operational amplifiers, independent control of the
a.c. and d.c. was possible, and the frequency response of the power
amplifier A_1 was adequate to cope with frequencies up to 1 kHz.
Calculations then showed, however, that the voltage drop of the a.c.
and d.c. in the magnetising winding would be close to 10 V, the
maximum output voltage of A_1 , for the values of H_{Δ} and H_b of interest.
Therefore extra series impedance could not be added to achieve
sinusoidal current, and a feedback arrangement was necessary.

Two types of feedback circuit are available, and the theory

of these is given in appendix 8.3. The stability of the circuits is also discussed, as this has not been given before. The circuit chosen for the tests involves the feedback of a voltage proportional to the magnetising current with a high negative loop gain, this being the more stable method, an important point because the circuit was subject to step inputs when the steel was put in a cyclic condition. A small point to note is the insertion of the 1.5 μF capacitor C_1 . This prevented saturation of the feedback amplifiers due to feedback of the d.c. The phase shift of the 1.5 μF, 10 kΩ combination was small, preserving stability.

Referring to appendix 8.3, it can be seen that the circuit of fig. 5.6 increased the effective series resistance from 0.1 Ω to 100 Ω, and the effective supply voltage from 10 V to 100 V . An example of the waveforms obtained is given in fig. 5.7.

5.3.2.2 Measurement circuits and apparatus

The quantities measured were the loss, power factor, surface alternating field strength, biasing field strength and average flux density. The measuring circuits are shown on the right hand side of fig. 5.6, and they are similar to those used during the measurements of permeability (fig. 4.1 (a)) with the addition of a.c. meters and power measuring apparatus.

The total loss in the ring was obtained from the product of the flux-coil voltage and the magnetising current, thus excluding the magnetising-winding loss. Since the losses in the ring were small (less than 1 W), and the frequency was fairly high, an electronic multiplier was the least expensive device for obtaining the product, in view of the fact that low-power amplifiers were already available for the magnetising-circuit series resistance and the flux coil. With voltages proportional to the flux-coil voltage and magnetising current as inputs, the output of the multiplier was a signal alternating at twice supply frequency with a d.c. level proportional to the average power. The average was obtained with a digital voltmeter

of an integrating type which counted the voltage over 20 ms, eliminating all harmonics of 50 Hz.

The maximum multiplier output was 10 V and in general the output V_o was $\frac{XY}{10}$ for two inputs X and Y, each less than or equal to 10 V. After allowing for this, the amplifier gains G_e and G_i, and the turns ratio $\frac{N_2}{N_1}$, the expression used for the loss was

$$P = 10\, V_o \cdot \frac{N_1}{N_2 G_e} \cdot \frac{1}{G_i r} \cdot \frac{1}{A_s} \quad W/m^2 \qquad (5.23)$$

where r = magnetising circuit series resistance (Ω)
           A_s = surface area (m^2)

The multiplier was specified to have an error less than 1% of full output (10 V) for frequencies up to 5 kHz. It was found that by keeping one input close to the maximum of 7.0 V r.m.s. (10 V peak) the error was less than $\pm$ 1% of the reading if the average output was greater than 0.5 V. These conditions were satisfied in the tests by adjusting the amplifier gains G_e and G_i. Checks were made to ensure that these gains were the same on a.c. as they were on d.c., and that the connection of the multiplier produced no loading effect. Since the errors in G_e, G_i, A_s and r were all at least an order of magnitude less than the multiplier error, this error of $\pm$ 1% can be taken to be the error in the measurement of loss.

Power factor was obtained from the equation

$$\cos\vartheta = \frac{V_o}{XY} \qquad (5.24)$$

where X and Y are the true-r.m.s. multiplier input voltages and V_o is the average multiplier output voltage. True r.m.s. was measured, rather than the fundamental via a filter or waveform analyser, because the difference between the fundamental and true r.m.s. was small for the waveforms encountered.

The signal generator used in the tests had a variable phase output together with a d.c. output proportional to the phase angle which enabled the phase to be set to $\pm$ 0.05°. Thus an independent

measurement of ϑ was possible by forming Lissajous figures with the magnetising current signal and the flux-coil output, when these were sinusoidal. The maximum difference between angles measured by this method and those calculated from eqn. (5.24) was $\pm 1^\circ$, representing a maximum error of $\pm 4\%$ in the power factor (the angles were in the range of 50° to 65°).

The phase shifts through the flux-coil and magnetising current measuring circuits were also measured by the above method, and a phase lead of 1.3° existed in the magnetising current measuring circuit. A correction lying between 1% and 5%, depending on the measured power factor, was therefore subtracted from $\cos\vartheta$ and V_o.

The alternating field strength on the iron surface, H_A, is proportional to the alternating component I_A of the magnetising current:

$$H_A = \frac{N_1 I_A}{L} \quad .$$

(5.25)

I_A was obtained from the measurement with an electronic voltmeter of the amplified voltage drop across the series resistance r. An R-C network was inserted at the amplifier input to prevent saturation of the amplifier by the d.c. voltage from the direct component of current. This network was also necessary to prevent saturation of the multiplier by the product of the d.c. voltage and the flux-coil voltage, although the average power of this product would have been zero.

The integrating digital voltmeter, described above, was also used for measuring the biasing field strength H_b and the steady flux density B_{av} ($B_{av} \neq B_b$ because B_A was not sinusoidal, see chapter 3, section 3.2.3.2).

Calibration of the meters was performed using standard sources supplied with the meters. Checks were also made against other meters in the laboratory. The error in the use of the a.c. meters was less than $\pm 0.5\%$ of the reading, and in the d.c. meters less than $\pm 0.1\%$.

The frequency of the oscillator could be set to 300 Hz $\pm 0.2\%$ using a d.c. output proportional to frequency, and this was checked

with a frequency meter.

5.3.2.3 Procedure

The procedure followed similar lines to the measurement of μ_Δ. For the measurement of losses 'on the normal magnetisation curve' the steel was brought to a cyclic state by demagnetising to the required H_b in steps of 0.05 T from about 10000 A/m. Then, to avoid transients and the consequent introduction of a further magnetic history, the a.c. was raised slowly to the required H_Δ, and readings taken. For the measurement of losses 'on a normal hysteresis loop', the steel was demagnetised to the required H_m and then this steady field was reduced to the required H_b before slowly raising the a.c. Between each set of readings, the a.c. was switched off and the steel returned to the peak of the normal loop (H_m) and cycled a few times.

The average steady flux density B_{av} was obtained from the change of steady flux density as the a.c. was slowly increased. A reversals method with the a.c. on was not used, as this method resulted in a 1% increase in loss for the larger values of H_Δ.

5.3.3 Comparison of theoretical and measured losses

5.3.3.1 Incremental loops on the normal magnetisation curve

The measured losses are compared with curves given by the linear theory in fig. 5.8. For the theoretical curves, μ_Δ corresponding to a value of H_b and to a test value of surface alternating field strength H_Δ was read from fig. 4.17, Z was obtained from fig. 5.2, and P from eqn. 5.14 with hysteresis neglected or from eqn. 5.22 with hysteresis included ($\propto$ from fig. 5.4).

The error in the theoretical curves (which relied on measured values of μ_Δ, H_Δ, ω, ρ and a) can be obtained by first considering values of H_b greater than 4000 A/m where $\mu_\Delta \simeq 20$ for the values of H_Δ used. At this permeability the stationary point of W occurs (eqn. 5.17, fig. 5.2) and so eqn. 5.17 gives

$$P \propto H_\Delta^2\, \omega\, \mu_\Delta\, a \qquad (\mu_\Delta = 20,\ ma = 2.5) \qquad\qquad (5.26)$$

Adding percentage errors in H_Δ^2 ($\pm 2 \times 0.5\%$), ω ($\pm 0.2\%$), μ_Δ ($\pm 1\%$), a ($\pm 0.1\%$) gives an error in the theoretical values of P equal to $\pm 2.3\%$, say $\pm 2.5\%$. For values of H_b smaller than 4000 A/m, μ_Δ is greater than 20 and the behaviour of P approximates to that of a semi-infinite slab:

$$P \propto H_\Delta^2 \sqrt{\omega \mu_\Delta \rho} \qquad (\mu_\Delta \gg 20, \ ma > 5) \qquad (5.27)$$

The decreased sensitivity to μ_Δ compensates for the increased sensitivity to ρ, resulting in the same error in P, $\pm 2.5\%$, which is thus taken to be the maximum theoretical error over the whole range of H_b owing to measurement uncertainties.

The sum of the errors in the measurement of P ($\pm 1\%$) and in the theoretical prediction of P ($\pm 2.5\%$) is equal to $\pm 3.5\%$. Differences between the measured values of P and the theoretical curves of less than this value could therefore be due to measurement errors. Fig. 5.8 shows that for values of H_b greater than H_Δ the differences between the theoretical curves neglecting hysteresis and the measured losses are less than $\pm 3.5\%$. For such values of H_b, however, the inclusion of hysteresis in the theory improves the correlation with the measured points for H_Δ = 250 A/m and 500 A/m, but not for H_Δ = 750 A/m and 1000 A/m. This can be explained by considering H_Δ = 250 A/m and 1000 A/m as examples. The curves for μ_Δ in figs. 4.15 and 4.17 show that for H_Δ = 250 A/m, μ_Δ is strictly independent of H_Δ for values of H_b greater than 250 A/m, whereas for H_Δ = 1000 A/m, μ_Δ is not independent of H_Δ until H_b is as large as 4000 A/m, and for values of H_b less than this, μ_Δ decreases as H_Δ decreases. Thus for H_Δ = 250 A/m the linear theory should hold exactly, and the inclusion of hysteresis should be necessary. But for H_Δ = 1000 A/m, owing to the decrease of H_Δ with depth into the iron, the average permeability is less than the surface value used in the theory, leading to an over-estimate of loss which is counteracted by the neglect of hysteresis. It should be noted, however, that the inclusion of hysteresis only increased the theoretical loss by 10% or

less, for $H_b > H_\Delta$, there being no increase for H_b greater than three or four times H_Δ .

Owing to the limited output of the amplifier A_1 , values of H_b less than H_Δ could only be used for H_Δ = 250 A/m (or less). The measured losses for H_Δ = 250 A/m with $H_b <$ 250 A/m are less than predicted by the linear theory, which is consistent with the fact that μ_Δ decreases as H_Δ decreases for values of H_Δ less than 250 A/m. Also, differences between the actual shape of the B/H loop and the idealised elliptical shape are more pronounced for values of H_b less than H_Δ , as discussed in section 5.2.2, although such differences were small for this particular example ($H_\Delta \leq$ 250 A/m).

The validity of the linear theory for the test results can be further judged from the graphs of wave impedance (fig. 5.9) and power factor (figs. 5.10 and 5.11). According to the linear theory, the wave impedance and power factor should be independent of H_Δ . The measured results in figs. 5.9 and 5.10 show that this was true for values of H_b greater than 4000 A/m, coinciding with the region where μ_Δ was independent of H_Δ . The graphs of power factor for H_Δ = 250 A/m and 1000 A/m in fig. 5.11 confirm the comments above about the inclusion of hysteresis. It can be seen that the effect of hysteresis on power factor was more marked than its effect on loss, and that its inclusion is a definite improvement for H_Δ = 250 A/m. The effect of hysteresis on the power factor results for H_Δ = 500 A/m and 750 A/m (not shown) were similar to the results for H_Δ = 250 A/m and 1000 A/m respectively, as occurred with the loss results.

In addition to the above results, sinusoidal waveforms of flux were observed for values of H_b giving constant μ_Δ , compared with distorted waveforms for other values of H_b (e.g. the distorted waveform of e for H_b = 0 in fig. 5.7).

Throughout the tests the temperature of the steel was constant at 23°C, although at one particular high value of H_b the high direct current was allowed to heat the sample for about half an

hour giving a temperature rise of about 30° C, and no change in the loss was observed.

As mentioned in chapter 3, no earlier comparisons of measured and calculated eddy-current losses in soft iron with superposed fields were reported. Comparisons with a permanent magnet material, however, were recently reported by Copeland and Slemon[113]. For a value of H_Δ less than the coercive force, they compared the variation with frequency of measured and calculated values of phase shift, and the results indicated the applicability of the linear theory to such small incremental loop losses.

5.3.3.2 Incremental loops on the normal loop H_m = 4000 A/m

Measured values of loss and power factor for H_Δ = 250 A/m are compared with curves calculated by the linear theory, neglecting hysteresis, in fig. 5.12. Values of μ_Δ for the calculations were read from fig. 4.29. Hysteresis was not included because hysteresis loss was measured only for incremental loops on the normal magnetisation curve. Fig. 5.12 shows that the differences between the measured and calculated results are within the limits of experimental error for the higher values of H_b; the differences at the lower values are probably due to hysteresis loss and the variation of μ_Δ with depth.

Fig. 4.34 shows that μ_Δ is practically constant for values of H_Δ up to 250 A/m when H_b is equal to 1800 A/m or more. When H_b is less than 1800 A/m, μ_Δ tends to be more constant on the ascending branch of a normal loop than on the descending branch, since, on the ascending branch, μ_Δ does not decrease as H_Δ decreases (below H_Δ = 250 A/m) until H_b is less than about 250 A/m). This could explain why the measured values of loss and power factor have a greater tendency to be less than the calculated values for incremental loops on the descending branch of the normal loop (figs. 5.2 and 5.3 show that both P and $\cos\vartheta$ decrease as μ_Δ decreases). Regions where the measured values of loss or power factor are higher than the calculated values can be attributed to hysteresis, as in the previous section.

5.3.4 Steady flux density

Graphs of biasing flux density against biasing field strength under d.c. conditions were given in fig. 4.28. Under a.c. conditions, with sinusoidal current, the time average flux density B_{av} (measured in the tests) may not be the same as the amplitude average B_b because of waveform distortion, discussed in chapter 3, sections 3.2.3.2 and 3.5.1. In addition , since B_{av} depends on the amplitude of the a.c. excitation for a given value of H_b, for the solid steel ring in which H_Δ decreases with depth whilst H_b is constant, the value of B_{av} measured is an average value over the ring cross section, $\bar{B}_{av}$.

The effect of the decrease of H_Δ with depth was shown most clearly in the results for $H_\Delta = 250$ A/m, fig. 5.13. The earlier ballistic results showed that B_b decreased as H_Δ decreased below 250 A/m (an example is shown in fig. 4.12), and in fig. 5.13 it can be seen that the dotted curve for $\bar{B}_{av}$ lies below the ballistic curve for B_b and above the normal magnetisation curve. Waveform distortion probably increased $\bar{B}_{av}$ a little for values of H_b less than 250 A/m, but there was no distortion for values of H_b greater than 250 A/m.

5.4 Limiting non-linear theory for $H_A > H_b$

Consider a semi-infinite block of steel with an applied surface field strength H_s in the y direction as shown in fig. 5.14. Maxwell's equations curl $\underline{H} = \frac{1}{\rho} \underline{E}$ and curl $\underline{E} = -\frac{\partial \underline{B}}{\partial t}$ give

$$- \frac{\partial H}{\partial z} = \frac{1}{\rho} E \qquad \left. \right\} \qquad (5.28)$$

$$\frac{\partial E}{\partial z} = - \frac{\partial B}{\partial t} \qquad \left. \right\} \qquad (5.29)$$
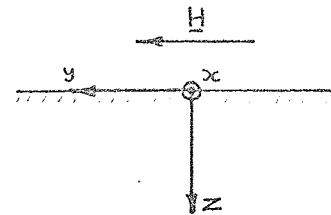
Fig. 5.14 Coordinate system and applied field for a semi-infinite block

The electric field is in the x direction, and the Poynting vector $\underline{N} = \underline{E} \times \underline{H}$ points into the block, along the positive z axis.

Differentiating (5.28) with respect to z and introducing (5.29) gives the diffusion equation

$$\frac{\partial^2 H}{\partial z^2} = \frac{1}{\rho} \frac{\partial B}{\partial t} = \frac{1}{\rho} \frac{\partial B}{\partial H} \frac{\partial H}{\partial t} \qquad (5.30)$$

Thus the permeability of interest in solving the diffusion equation is the differential permeability $\mu_d = \frac{1}{\mu_0} \frac{\partial B}{\partial H}$. In the linear theory with a superposed steady field, a set of B/H loops is represented by a straight line of slope $\mu_d = \mu_A$, or, for sinusoidal field variations, the set of B/H loops may be represented by a set of ellipses with a constant complex permeability, as described in section 5.2.2. For the present sample of steel the linear theory was suitable for small values of H_A, and, provided H_b was greater than H_A, for large values of H_A. But when H_b was less than H_A, and H_A was large, the shape of the B/H loops was close to the unsymmetrical step function shown in fig. 5.15.

Fig. 5.15 Representation of unsymmetrical B/H loop for large values of H_A and $H_b < H_A$.
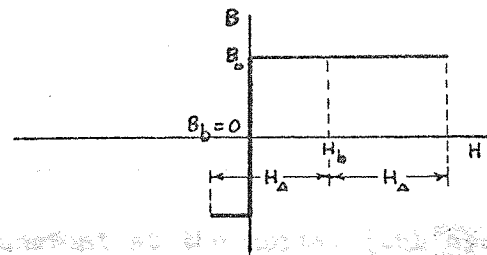
Note that $B_b = 0$ for the idealised representation, whereas in practice the value of B_b was not exactly zero, but close to it (fig. 4.28).

The effect of this type of loop on the loss was not measured because of the limitations of the power amplifier. Also, the theory for a cylindrical configuration with an unsymmetrical B/H loop is complicated, as it is even for a symmetrical step function representation[114]. However, an idea of the variation of the loss with H_b and H_Δ, and of the difficulties in the solution, can be obtained by considering a semi-infinite block.

For a symmetrical step B/H curve ($H_b = 0$, fig. 5.16 (a)) the loss per unit area in a semi-infinite block with a sinusoidal surface field strength of peak amplitude H_Δ was shown by MacLean[115] to be

$$P = 1.7 \times \frac{1}{2} \frac{\rho}{\delta} H_\Delta^2 \qquad (5.31)$$

where $\delta = \sqrt{\dfrac{2 \rho}{\omega \, B_0/\mu_\Delta}}$. By comparing eqn. (5.31) with eqn. (5.15) it can be seen that the loss is 1.7 times the loss given by the linear theory using a value of permeability $\mu_\Delta = \dfrac{B_0}{\mu_0 \, H_\Delta}$ corresponding to the
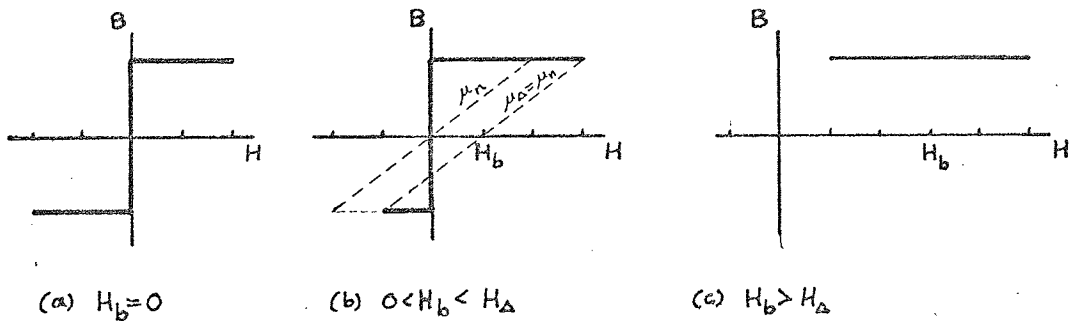
Fig. 5.16 Step function representation of B/H loop for different values of H_b with H_Δ constant

surface field strength H_Δ. On the other hand, with the step representation, when H_b exceeds H_Δ there is no change of flux density (fig. 5.16 (c)) and the loss is zero. Thus the loss may be expected to vary from a value greater than the linear value to a very low value as H_b increases. It is shown schematically in fig. 5.16 (b) that, for a given large value of H_Δ, μ_Δ remains constant at the normal (unbiased)

value as H_b increases from zero to a value close to H_Δ , and this is confirmed by the measured results for μ_Δ in fig. 4.17. The point of interest is whether as H_b increases the loss also remains at a constant high value, and decreases suddenly as H_b approaches H_Δ . It is shown below that the loss should not remain constant, but should decrease steadily as H_b increases.

Let the applied surface field strength H_s consist of a positive biasing component and an alternating component given by eqn. (5.32) and shown in fig. 5.17.

$$H_s = H_b + H_\Delta \sin \omega t = H_\Delta (h + \sin \omega t) \qquad (5.32)$$

where $h = \dfrac{H_b}{H_\Delta}$ and $0 \le h \le 1$. H_s is zero when $t = t_1$ and t_2 so the values of t_1 and t_2 are given by

$$\left. \begin{array}{l} \sin \omega t_1 = -h \ , \ \pi \le \omega t_1 \le \dfrac{3\pi}{2} \\[2mm] \sin \omega t_2 = -h \ , \ \dfrac{3\pi}{2} \le \omega t_2 \le 2\pi \end{array} \right\} \qquad (5.33)$$
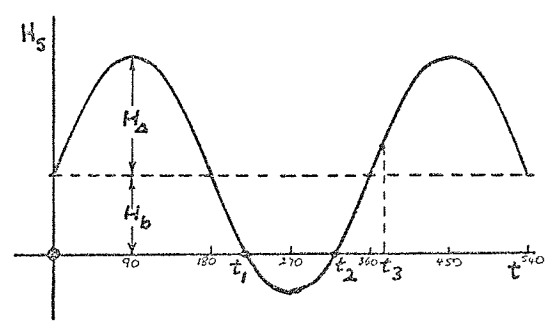
Fig. 5.17 Applied surface field strength

Imagine that in the beginning the alternating component is increased from zero so that the flux density in the iron is initially the saturation value $+ B_o$. As H_Δ exceeds H_b , a change of flux occurs when H_s is negative, i.e. when $t_1 < t < t_2$. The depth of penetration (δ_b) of this change of flux depends on the length of time for which H_s is negative, and hence on the ratio h . The negative flux density $-B_o$ in the surface layer of depth δ_b is changed back to the positive value when $t > t_2$ and H_s becomes positive, fig. 5.18, but because H_s was negative for less than half a cycle, the return to $+B_o$ is completed when $t = t_3$. Thus flux changes in the steel only occur over the depth δ_b during the time intervals $t_2 - t_1$ and $t_3 - t_2$,
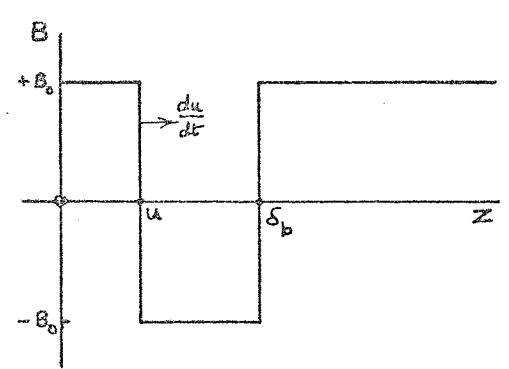
Fig. 5.18 Flux density inside the steel when H_s is positive and $t_2 < t < t_3$

and both δ_b and the time intervals decrease as H_b increases for a given value of H_Δ . Thus the loss should also decrease as H_b increases. The lower loss in a thin plate or rod[114, 117] compared to that in a semi-infinite block is a similar phenomenon, but with the advantage for theoretical studies of symmetrical positive and negative periods.

Expressions for δ_b, t_3 and the loss may be obtained by beginning with the theory outlined by MacLean[115] and later authors[1,115,116] for symmetrical magnetisation. To cope with the infinite rate of change of flux density at the surface separating regions of positive flux density $+B_o$ from regions of negative flux density $-B_o$, a flux per unit length $\varnothing$ is introduced, defined by

$$\varnothing = \int_z^\infty B \, dz \tag{5.34}$$

With the condition that $E = 0$ at $z = \infty$ this enables eqn. (5.29) to be replaced by

$$E = \frac{\partial \varnothing}{\partial t} \tag{5.35}$$

Let the distance of the separating surface from the surface of the block at any time be u , giving a velocity $\frac{du}{dt}$. For $z < u$, the rate of change of flux, and hence E, is

$$E = \frac{\partial \varnothing}{\partial t} = 2 B_s \frac{du}{dt} \quad , \qquad z < u \tag{5.36}$$

where B_s is the flux density at the block surface. Therefore, for $z < u$, at a given instant in time, E is independent of z and by eqn. (5.28) $\frac{\partial H}{\partial z}$ is also constant. Since $H = 0$ at the separating surface and $H = H_s$ at the block surface, the constant gradient $\frac{\partial H}{\partial z}$ is given by

$$\frac{\partial H}{\partial z} = - \frac{H_s}{u} \tag{5.37}$$

Substituting eqn. (5.37) into eqn. (5.28) gives

$$E = \rho \frac{H_s}{u} \tag{5.38}$$

Eliminating E from eqns. (5.36) and (5.38) gives

$$2u \frac{du}{dt} = \frac{d(u^2)}{dt} = \rho \frac{H_s}{B_s} \tag{5.39}$$

During the time when H_s is negative, $B_s = -B_o$, and eqn. (5.39) gives

$$\frac{d(u^2)}{dt} = - \frac{\rho H_\Delta}{B_o} (h + \sin \omega t) \quad , \quad t_1 < t < t_2 \qquad (5.40)$$

which on integrating gives

$$u^2 = - \frac{\rho H_\Delta}{\omega B_o} (h\omega t - \cos \omega t + C_1) \quad , \quad t_1 < t < t_2 \qquad (5.41)$$

The constant C_1 is found from the fact that $u = 0$ at $t = t_1$:

$$C_1 = -h \omega t_1 + \cos \omega t_1 \qquad (5.42)$$

and therefore

$$u^2 = - \frac{\delta^2}{2} (h (\omega t - \omega t_1) - \cos \omega t + \cos \omega t_1), t_1 < t < t_2 \qquad (5.43)$$

where δ is the depth of penetration for symmetrical magnetisation $(h = 0)$ given by

$$\delta = \sqrt{\frac{2 \rho H_\Delta}{\omega B_o}} \qquad (5.44)$$

Now $u = \delta_b$ when $t = t_2$, so eqn. (5.43) gives an expression for δ_b:

$$\delta_b^2 = - \frac{\delta^2}{2}(h (\omega t_2 - \omega t_1) - \cos \omega t_2 + \cos \omega t_1) \qquad (5.45)$$

H_s becomes positive at $t = t_2$ and the separating surface moves in from the origin again with $B_s = +B_o$ and therefore

$$u^2 = + \frac{\delta^2}{2} (h (\omega t - \omega t_2) - \cos \omega t + \cos \omega t_2), t_2 < t < t_3 \qquad (5.46)$$

Now $t = t_3$ when $u = \delta_b$, so equating eqn. (5.46) with $t = t_3$ and eqn. (5.45) gives an implicit expression for t_3:

$$h\omega t_3 - \cos \omega t_3 = h\omega t_1 - \cos \omega t_1 \qquad (5.47)$$

As ωt_1 is a known function of h (eqn. 5.33), ωt_3 may be found graphically.

Plots of $\frac{\delta_b}{\delta}$ and ωt_1, ωt_2, ωt_3 against h are given in figs. 5.19 (a) and (b), showing the decrease of δ_b and the time intervals $t_2 - t_1$ and $t_3 - t_2$ as h increases. Plots of $\frac{u}{\delta}$ against time for several values of h are given in fig. 5.19 (c).
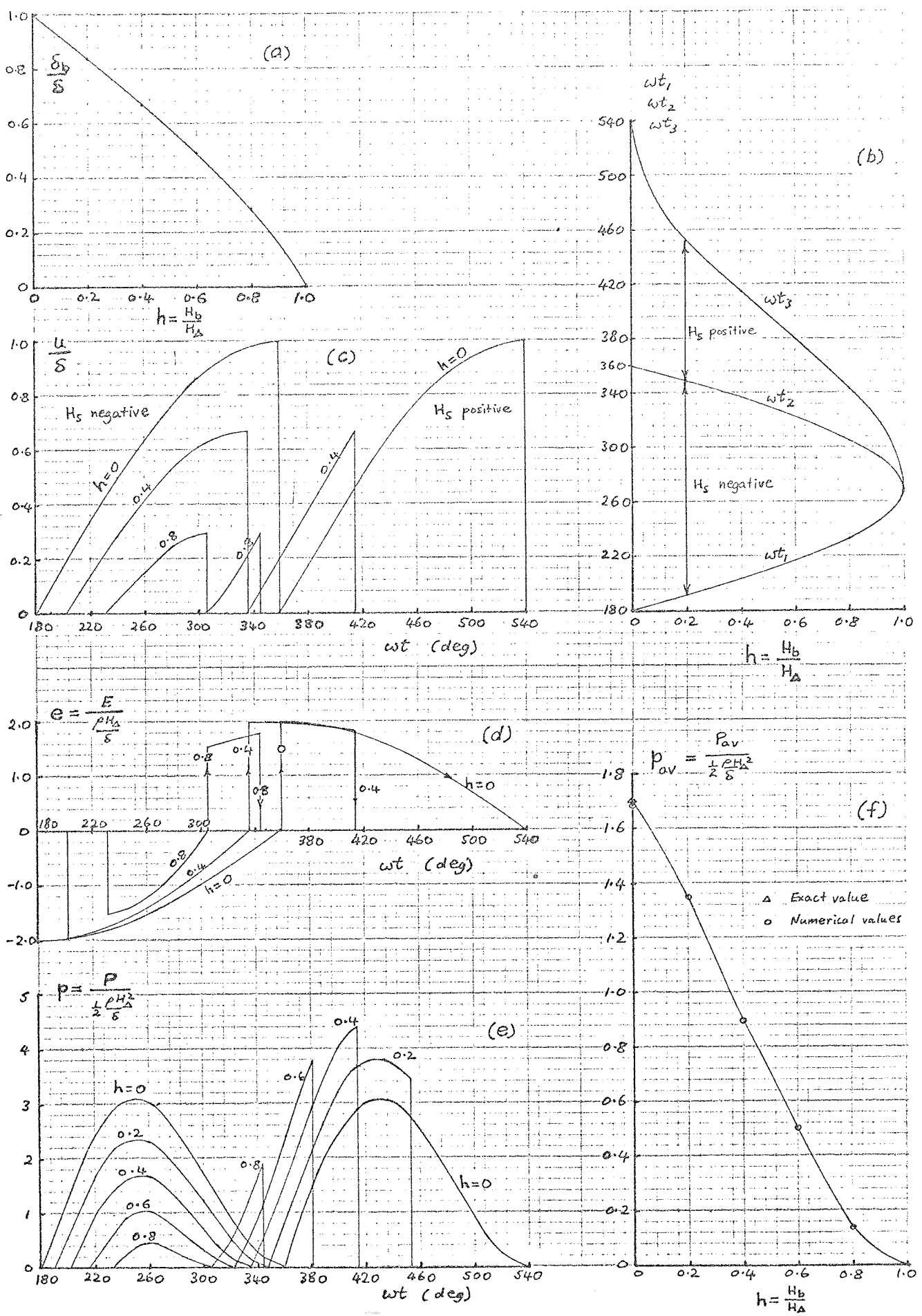
Fig. 5.19 Quantities relating to the calculation of loss in a semi-infinite slab of iron with unsymmetrical magnetisation using limiting non-linear theory.

(a) Depth of penetration (b) Time intervals (c) Separating surface
(d) Electric field strength (e) Instantaneous power (f) Average
power loss

The electric field strength may be found by substituting the expressions for u into eqn. (5.38), or into an equivalent non-dimensional form:

$$e = \frac{E}{\frac{\rho H_\Delta}{\delta}} = \frac{\delta}{\rho H_\Delta} \cdot \frac{\rho H_s}{u} = \frac{h + \sin \omega t}{\frac{u}{\delta}} \qquad (5.48)$$

($\frac{\rho H_\Delta}{\delta}$ is the amplitude of E at z = 0 by the linear theory, neglecting hysteresis)

The instantaneous power loss per unit surface area may be obtained from the magnitude of the Poynting vector

$$P_i = E H_s \qquad (5.49)$$

which in a non-dimensional form becomes

$$p = \frac{P_i}{\frac{1}{2} \frac{\rho H_\Delta^2}{\delta}} = 2 \frac{E}{\frac{\rho H_\Delta}{\delta}} \cdot \frac{H_s}{H_\Delta} = 2 e (h + \sin \omega t) \qquad (5.50)$$

($\frac{1}{2} \cdot \frac{\rho H_\Delta}{\delta}$ is the average value of P_i by the linear theory, neglecting hysteresis)

The average value of p over a cycle is given by

$$p_{av} = \frac{\omega}{2 \pi} \left[\int_{t_1}^{t_2} p_- \, dt + \int_{t_2}^{t_3} p_+ \, dt \right] \qquad (5.51)$$

where p_- and p_+ are the expressions for p when H_s is negative and positive. Each integral is of the form

$$\int_{t_1}^{t_2} \frac{2 (h + \sin \omega t)^2}{- h\omega t + \cos \omega t - C_1} \, dt \qquad (5.52)$$

which is difficult to evaluate analytically. The loss was therefore obtained numerically for h = 0, 0.2, 0.4, 0.6 and 0.8. Plots of e against time for these values of h are shown in fig. 5.18 (d) and the corresponding plots of p are shown in fig. 5.19 (e). The average value of each curve (by Simpson's rule) is plotted against h in fig. 5.19 (f). For h = 0 the numerical result (1.68) agrees well with the exact value ($\frac{16}{3\pi} = 1.70$), and as h increases to 1.0 the loss decreases steadily to

zero. Note that at h = 0.35, the loss is equal to the value
given by the linear theory $(p_{av} = 1.0)$.

As mentioned at the beginning of this section, the
unsymmetrical non-linear behaviour was not tested experimentally
because of insufficient output from the power amplifier. Also,
a more complicated theory would need to be developed for the
cylindrical sample.

5.5 Conclusion

The test results presented in this chapter show that for values of H_b greater than H_Δ the linear theory neglecting hysteresis may be used to predict the total power loss in solid mild steel, to within $\pm$ 3.5%. Hysteresis can be neglected because the hysteresis loss is mostly small, and because where hysteresis begins to be significant its effects are offset by a decrease of μ_Δ with H_Δ. As measured losses were never consistently greater than the calculated values by an amount which could not be attributed to hysteresis, it is concluded in addition that 'anomalous' losses due to the domain structure of the material are absent, at least when $H_b > H_\Delta$.

The linear theory may also be used to calculate power factor for $H_b > H_\Delta$, although the inclusion of hysteresis is necessary for small values of H_Δ (< 500 A/m).

For values of H_b less than H_Δ, it is likely that the loss for a given surface field strength H_Δ will decrease as H_b increases, even though μ_Δ does not change. Measurements would be needed to confirm this, to determine a suitable value of B_o for use in the limiting non-linear theory, and to determine the range of values of H_Δ covered by the theory.

Since B_b is large when H_b is greater than H_Δ (fig. 4.28) it may be concluded from the above that the linear theory is valid if B_b is a fixed large value. (This agrees with the fact that μ_Δ is nearly independent of H_Δ when B_b is large, fig. 4.19.) For small values of B_b, the limiting non-linear theory is more appropriate.

6. POLE-FACE LOSSES: LINEAR THEORY AND THE PROBLEM OF SUPERPOSITION

6.1 Introduction

In chapter 2 the main field and the source of the armature winding-harmonic fields in a synchronous machine were discussed, and in chapters 3, 4 and 5 some effects of a superposed steady field were considered. In this chapter a classical linear theory for the calculation of the loss caused by one travelling wave is explained, the important parameters are identified, including one new one, and the effect of permeability discussed. This theory is then applied to the calculation of the magnetic field and losses in two typical large machines and the results, together with the knowledge gained from the earlier chapters, are used to indicate the problems in allowing for the superposition of both a steady field and several travelling waves. Some possible future work of a fairly fundamental nature is indicated.

6.2 Linear theory for one travelling wave

6.2.1 Statement of the problem

To calculate the eddy-current losses in a rotor caused by a travelling field it is assumed initially that the air gap and depth of penetration are small compared to the rotor diameter, that the rotor surface is smooth, that the machine is infinitely long and that all permeabilities are constant. In addition it is assumed that the effects of eddy currents in the stator iron and copper are small, that stator slots may be neglected (apart from being the source of a ripple on the main flux) and that the stator winding may be represented by a thin current sheet. These assumptions enable a relatively simple linear theory to be developed in terms of rectangular coordinates in two dimensions, and is the approach which was followed by several authors[9,119 - 125] (appendix 8.5).

With the assumption of constant permeability, each harmonic of the stator current loading may be considered separately in the calculation of the resultant magnetic field. The source of a wave moving relative to the rotor is represented by a current sheet in an axial (z) direction on the stator surface (fig. 6.1) with a sinusoidal variation in time and a phase shift dependent on the peripheral (x) direction:

$$K = \hat{K} \cos (\omega t - \beta x) \qquad \text{A/m} \qquad (6.1)$$

where

ω = angular frequency of harmonic (rad/s)

$\beta = \pi/\tau$ $\qquad$ (m^{-1})

τ = pole pitch of harmonic $\qquad$ (m)
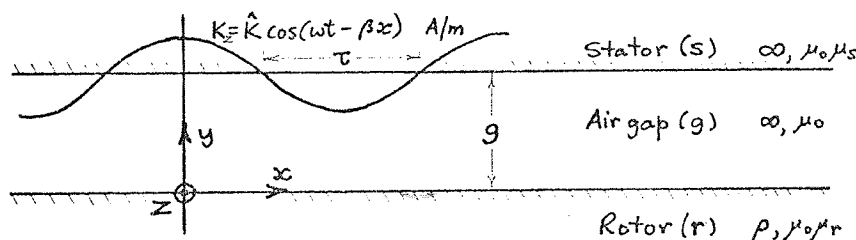
Fig.6.1 Configuration for the study of eddy currents induced in a solid rotor by a travelling wave

As shown in fig. 6.1, the stator is represented by a smooth semi-infinite half-space of infinite resistivity and permeability $\mu_0\mu_s$. The rotor is also represented by a smooth semi-infinite half-space, of resistivity ρ and permeability $\mu_0\mu_r$. The air gap of width g has infinite resistivity and permeability μ_0 . (Stoll and Hammond[124] showed that if the actual thicknesses of the stator and rotor are greater than $\frac{1}{\pi}$ times the pole pitch then the air-gap field, and hence losses, are the same as if the thicknesses were infinite. For the rotor of finite resistivity they further showed that if a strong skin effect is present, as is usually true, then the actual rotor thickness need only be greater than the depth of penetration $\delta = \sqrt{2\rho/\mu_0\mu_r\omega}$, or τ/π , whichever is the smaller)

6.2.2 Vector potential

The field distribution is found with the aid of a vector potential $\underline{A}$ defined by

$$\text{curl } \underline{A} = \underline{B} \tag{6.2}$$

$$\text{div } \underline{A} = 0 \tag{6.3}$$

because, with the assumed axial direction of source current and with no variation of geometry in the axial direction, the vector potential has only an axial component A . The two components of flux density may be found using eqn. 6.2, which gives

$$B_x = \frac{\partial A}{\partial y} , \qquad B_y = -\frac{\partial A}{\partial x} \tag{6.4}$$

The magnetic and electric fields are governed by the equations

$$\text{curl } \underline{H} = \underline{J} \tag{6.5}$$

$$\text{curl } \underline{E} = -\frac{\partial \underline{B}}{\partial t} \tag{6.6}$$

$$\text{div } \underline{B} = 0 \tag{6.7}$$

together with

$$\underline{B} = \mu_0\mu\underline{H} \tag{6.8}$$

$$\underline{J} = \frac{1}{\rho}\underline{E} \tag{6.9}$$

$$\text{div } \underline{J} = 0 \tag{6.10}$$

Substituting eqn. 6.2 in eqn. 6.5, using eqn. 6.8 , gives

$$\text{curl} \left(\frac{1}{\mu_o \mu} \text{curl } \underline{A} \right) = \underline{J} \tag{6.11}$$

Substituting eqn. 6.2 in eqn. 6.6 gives

$$\underline{E} = -\frac{\partial \underline{A}}{\partial t} - \text{grad } \psi \tag{6.12}$$

where ψ may be identified with an electrostatic potential. But since

the conductors extend to infinity in the $+z$ and $-z$ directions, and

there are no dielectrics, there is no possibility of charge

accumulating to produce an electrostatic potential. Therefore

$\text{grad } \psi = 0$ and

$$\underline{E} = -\frac{\partial \underline{A}}{\partial t} \tag{6.13}$$

Substituting eqn. 6.13 in eqn. 6.11, using eqn. 6.9, gives

$$\text{curl} \left(\frac{1}{\mu \mu} \text{curl } \underline{A} \right) = -\frac{1}{\rho} \frac{\partial \underline{A}}{\partial t} \tag{6.14}$$

Using the assumptions of constant permeability and no variation in

the z direction, eqns. 6.14 and 6.3 give

$$\frac{\partial^2 A}{\partial x^2} + \frac{\partial^2 A}{\partial y^2} = \frac{\mu_o \mu}{\rho} \frac{\partial A}{\partial t} \tag{6.15}$$

remembering that $\underline{A}$ has only a z component A .

Since the source current is assumed to vary sinusoidally with

t and x (eqn.6.1) and the permeability is constant, the field

quantities also vary sinusoidally and may be written in terms of

complex numbers, such as

$$K = \text{Re } \hat{K} e^{-j\beta x} e^{j\omega t} \tag{6.16}$$

$$A = \text{Re } \mathring{A} e^{-j\beta x} e^{j\omega t} \tag{6.17}$$

and eqn. 6.15 becomes

$$\frac{\partial^2 \mathring{A}}{\partial y^2} = \left(\beta^2 + j\frac{\omega \mu_o \mu}{\rho} \right) \mathring{A} = (\beta \dot{\gamma})^2 \mathring{A} \tag{6.18}$$

where

$$\dot{\gamma} = \sqrt{1 + \frac{j}{\beta^2 d^2}} \tag{6.19}$$

$$d = \sqrt{\frac{\rho}{\omega \mu_o \mu}} \tag{6.20}$$

Eqn. 6.18 may be solved for each region of fig. 6.1, the general

solution for region i being

$$\dot{A}_i = C_i \, e^{\beta \dot{\gamma} y} + D_i \, e^{-\beta \dot{\gamma} y} \tag{6.21}$$

where $\dot{\gamma} = 1$ for the air gap and stator (where $\rho = \infty$) and the six constants C_i and D_i are found from the boundary conditions expressing the decay of the field at $y = \pm \infty$ and the continuity of tangential field strength and tangential vector potential (i.e. eqns. 6.5 and 6.2) :

$$\dot{A} = 0 \quad \text{at} \quad y = \pm \infty \tag{6.22}$$

$$\left. \begin{aligned} \frac{1}{\mu_o} \frac{\partial \dot{A}_g}{\partial y} - \frac{1}{\mu_o \mu_s} \frac{\partial \dot{A}_s}{\partial y} &= \hat{K} \quad \text{at} \quad y = g \\[2mm] \frac{1}{\mu_o \mu_r} \frac{\partial \dot{A}_r}{\partial y} - \frac{1}{\mu_o} \frac{\partial \dot{A}_g}{\partial y} &= 0 \quad \text{at} \quad y = 0 \end{aligned} \right\} \tag{6.23}$$

$$\left. \begin{aligned} \dot{A}_s &= \dot{A}_g \quad \text{at} \quad y = g \\[2mm] \dot{A}_g &= \dot{A}_r \quad \text{at} \quad y = 0 \end{aligned} \right\} \tag{6.24}$$

The solution for the vector potential in the rotor is

$$\dot{A}_r = \frac{2\mu_s \mu_r \, e^{\beta \dot{\gamma} y}}{(\mu_s + 1)(\mu_r + \dot{\gamma}) \, e^{\beta g} - (\mu_s - 1)(\mu_r - \dot{\gamma}) \, e^{-\beta g}} \cdot \frac{\mu_o \hat{K}}{\beta} \tag{6.25}$$

The second term in this expression $\dfrac{\mu_o \hat{K}}{\beta}$ is the vector potential at the stator surface when the stator relative permeability μ_s is much greater than 1 and the rotor is absent (the first term equals 1 when $\mu_s \gg 1$, $y = 0$, $g = 0$, $\mu_r = 1$, $\rho = \infty$). The first term is non-dimensional and shows that the non-dimensional parameters determining the vector potential in the rotor are:

the stator relative permeability : $\qquad\qquad \mu_s$

the rotor relative permeability : $\qquad\qquad \mu_r$

the ratio of the air gap to the pole pitch : $\qquad \beta g = \pi g / \tau$

the ratio of the depth of penetration to the pole pitch: $\beta d = \pi d / \tau$

$$\left(\text{in } \dot{\gamma} = \sqrt{1 + j/\beta^2 d^2} \right)$$

P.T.O.

the ratio of the depth y to the pole pitch $\cdot$ $\qquad$ $\beta y = \pi y/\tau$

the ratio of the depth y to the depth of penetration $\cdot$ y/d

$$\left(\text{in } \beta \dot{\gamma} y = \sqrt{\beta^2 y^2 + j y^2/d^2}\right)$$

6.2.3 Simplifications of the expression for vector potential

6.2.3.1 Stator permeability

The vector potential is independent of the value of the stator permeability if this is sufficiently high. For example, with $\mu_s = \infty$, eqn. 6.25 becomes

$$\dot{A}_r = \frac{2\mu_r}{(\mu_r + \dot{\gamma})\, e^{\beta g} - (\mu_r - \dot{\gamma})\, e^{-\beta g}} \cdot \frac{\mu_o \hat{K}}{\beta} \cdot e^{\beta \dot{\gamma} y} \qquad (6.26)$$

An idea of the required size of μ_s can be obtained by gathering the terms containing μ_s in eqn. 6.25 and writing the resulting expression in the form

$$\dot{A}_r = \frac{\mu_r}{\cosh\beta g(\mu_r \tanh\beta g + \dot{\gamma})\left[1 + \dfrac{1}{\mu_s}\dfrac{\mu_r + \dot{\gamma}\tanh\beta g}{\mu_r \tanh\beta g + \dot{\gamma}}\right]} \cdot \frac{\mu_o \hat{K}}{\beta} \cdot e^{\beta \dot{\gamma} y} \qquad (6.27)$$

It may now be seen that if

$$\mu_s \gg \frac{\mu_r + \dot{\gamma}\tanh\beta g}{\mu_r \tanh\beta g + \dot{\gamma}} = \mu_s' \text{ (say)} \qquad (6.28)$$

then $\dot{A}_r$ is independent of μ_s and is given by

$$\dot{A}_r = \frac{\mu_r}{\cosh\beta g(\mu_r \tanh\beta g + \dot{\gamma})} \cdot \frac{\mu_o \hat{K}}{\beta} \cdot e^{\beta \dot{\gamma} y} \qquad (6.29)$$

(which is the same as eqn. 6.26 in terms of hyperbolic functions).

The inequality (6.28) does not generally require μ_s to be very high. For example if $\beta g \geqslant 2$, i.e. if $\pi g/\tau \geqslant 2$, then $\tanh\beta g = 1$ and (6.28) becomes $\mu_s \gg 1$. Also, μ_s' is certainly less than $\left|(\mu_r + \dot{\gamma}\tanh\beta g)/\dot{\gamma}\right|$, which in turn is less than $\left|\mu_r/\dot{\gamma} + 1\right|$, which has a maximum value of $\mu_r + 1$ when $\dot{\gamma} = 1$. Normally the skin effect is strong (see below) and $\left|\dot{\gamma}\right| > 1$, so that $\left|\mu_r/\dot{\gamma} + 1\right|$ is less than μ_r. Therefore a value of μ_s much greater than 1 is all that is required for the larger air gap to pole pitch ratios $(\pi g/\tau \geqslant 2)$, and for the smaller ratios a value of μ_s much greater than $\left|\mu_r/\dot{\gamma} + 1\right|$ is sufficient, where this is less than μ_r when the skin effect is strong. These

conclusions agree with Lawrenson et al.[125], who found that their results for the rotor surface flux density were unaffected by values of μ_s in the range 500 to ∞ (the maximum value of μ_r considered was 2500 and the skin effect was strong). Other authors either assumed that $\mu_s = \infty$ [119-123] or did not include the effect of the stator in their discussion[124]. Since the stator is normally made of high-permeability silicon-steel laminations it will be assumed that the vector potential is independent of μ_s and given by eqn. 6.29.

6.2.3.2 Strong skin effect

A second simplification can be made to the equations if the pole pitch is much greater than the depth of penetration, i.e. if the skin effect is strong, because from eqn. 6.19

$$\dot{\gamma} = \sqrt{1 + \frac{j}{\beta^2 d^2}} \simeq \frac{\sqrt{j}}{\beta d} = \frac{1+j}{\sqrt{2}\beta d} \quad \text{if} \quad \frac{1}{\beta^2 d^2} = \frac{\tau^2}{\pi^2 d^2} \gg 1 \qquad (6.30)$$

The expression now obtained for the vector potential in the rotor, from eqn. 6.29 using eqn. 6.30, is

$$\dot{A}_r = \frac{\sqrt{2}\beta d\mu_r}{\cosh\beta g(\sqrt{2}\beta d\mu_r \tanh\beta g + 1 + j)} \cdot \frac{\mu_o \hat{K}}{\beta} \cdot e^{\frac{1+j}{\sqrt{2}d} y} \qquad (6.31)$$

Thus, for the conditions $\mu_s \gg \mu_s'$ (eqn.6.28) and $1/\beta^2 d^2 \gg 1$ (eqn.6.30), the number of dimensionless parameters governing the vector potential is reduced from the six listed in the previous section to the three listed below:

the ratio of the rotor permeability to the skin-effect

factor $1/\beta d$: $\qquad\qquad\qquad\qquad\qquad\qquad \beta d\mu_r = \mu_r \pi d/\tau$

the ratio of the air gap to the pole pitch : $\qquad \beta g = \pi g/\tau$

the ratio of the depth y to the depth of penetration : $\quad y/d$

The ratio of the depth to the pole pitch (βy) is no longer important, and neither is the absolute value of the rotor permeability. Instead the ratio of the rotor permeability to the skin-effect factor is of interest.

6.2.3.3 Two types of behaviour with strong skin effect ($\frac{1}{\beta^2 d^2} \gg 1$)

Although three dimensionless parameters were listed above, two types of behaviour for $\dot{A}_r$ can be discerned depending on the value of the dimensionless ratio $Q = (\frac{1}{\beta d})/\mu_r \tanh\beta g$. When this is much greater than 1 , i.e. when $\mu_r \tanh\beta g$ is much less than the skin-effect factor $\frac{1}{\beta d}$, eqn. 6.31 shows that

$$\dot{A}_r = \frac{\sqrt{2}\beta d \mu_r}{\cosh\beta g(1+j)} \cdot \frac{\mu_o \hat{K}}{\beta} \cdot e^{\frac{1+j}{\sqrt{2}d} y} \quad \text{if } Q = 1/\beta d\mu_r \tanh\beta g \gg 1 \quad (6.32)$$

The significance of this expression can be seen by determining the tangential magnetic field strength on the rotor surface, which is equal to the current per unit length in the rotor. Using eqns. 6.4 and 6.8, eqn. 6.32 gives

$$\dot{H}_x = \frac{1}{\mu_o \mu_r} \frac{\partial \dot{A}_r}{\partial y} = \frac{\hat{K}}{\cosh\beta g} \quad \text{at } y = 0 \text{ if } Q \gg 1 \quad (6.33)$$

showing that H_x and the rotor current loading are equal to the stator current loading (i.e. complete reflection) apart from the $\frac{1}{\cosh\beta g}$ reduction factor (which is equal to 1 for small air gap to pole pitch ratios).

The second type of behaviour occurs when $\mu_r \tanh\beta g$ is much greater than $\frac{1}{\beta d}$, i.e. when $Q \ll 1$, and eqn. 6.31 shows that

$$\dot{A}_r = \frac{\mu_o \hat{K}}{\beta \sinh\beta g} e^{\frac{1+j}{\sqrt{2}d} y} \quad \text{if } Q = 1/\beta d\mu_r \tanh\beta g \ll 1 \quad (6.34)$$

The significance of this expression can be seen by considering the expression for the vector potential in the absence of eddy currents $\dot{A}_{ra}$, obtained from eqn. 6.29 by putting $\gamma = 1$ $(\rho = \infty)$

$$\dot{A}_{ra} = \frac{\mu_r \tanh\beta g}{\mu_r \tanh\beta g + 1} \cdot \frac{\mu_o \hat{K}}{\beta \sinh\beta g} \cdot e^{\beta y} \quad \text{if } \rho = \infty \quad (6.35)$$

and since $\mu_r \tanh\beta g$ is in this instance much greater than the skin effect factor which is greater than 1, eqn.6.35 gives

$$\dot{A}_{ra} = \frac{\mu_o \hat{K}}{\beta \sinh\beta g} \cdot e^{\beta y} \quad \text{if } \rho = \infty \text{ and } \mu_r \tanh\beta g \gg 1 \quad (6.36)$$

A comparison of eqns. 6.36 and 6.34 shows that the vector potential

at the rotor surface when $Q \ll 1$ is equal to the value in the absence of eddy currents, the 'applied' value.

The above two types of behaviour were discussed by Stoll and Hammond[124] for the same configuration as in fig. 6.1, but without the stator. They showed that the behaviour was determined by the ratio of the skin effect factor to the rotor permeability. The above discussion shows that when a stator of sufficiently high permeability is present $(\mu_s \gg \mu_s'$, eqn. 6.28) then the same arguments hold with the rotor permeability reduced by the factor $\tanh\beta g$. This means that the range of values of the skin effect factor which can lead to a complete reflection of the stator currents in the rotor may be considerably wider, and the range which can lead to no reduction of the applied vector potential by the eddy currents correspondingly narrower.

6.2.3.4 <u>The meaning of the dimensionless parameter $Q = 1/\beta d\mu_r \tanh\beta g$</u>

At any point the total (or resultant) field is the sum of the applied field and the field of the eddy currents. In terms of the vector potential in the rotor, this may be written

$$\overset{\circ}{A}_r = \overset{\circ}{A}_{ra} + \overset{\circ}{A}_{re}$$

where the potentials are in the z direction. When the skin effect is strong this may be used together with eqns. 6.31 and 6.35 to give the ratio of the eddy-current field to the total field on the rotor surface

$$\left(\frac{\overset{\circ}{A}_{re}}{\overset{\circ}{A}_r}\right)_o = 1 - \left(\frac{\overset{\circ}{A}_{ra}}{\overset{\circ}{A}_r}\right)_o = 1 - \frac{\mu_r \tanh\beta g}{\mu_r \tanh\beta g + 1} \cdot \frac{\sqrt{2}Q^{-1} + 1 + j}{\sqrt{2}Q^{-1}} \quad \text{if} \frac{1}{\beta^2 d^2} \gg 1$$

If $\mu_r \tanh\beta g \gg 1$ this reduces to

$$\left(\frac{\overset{\circ}{A}_{re}}{\overset{\circ}{A}_r}\right)_o = -\frac{1+j}{\sqrt{2}Q^{-1}}$$

so that

$$Q = \left|\frac{\overset{\circ}{A}_{re}}{\overset{\circ}{A}_r}\right|_o \quad \text{if} \quad \mu_r \tanh\beta g \gg 1 \text{ . and } \frac{1}{\beta^2 d^2} \gg 1 \qquad (6.37)$$

Q is therefore an eddy-current reaction factor, being the ratio of the eddy-current field to the total field. Strong eddy-current

reaction is indicated by $Q \gg 1$ and weak reaction by $Q \ll 1$.

Since $Q = 1/\beta d\mu_r \tanh\beta g = \dfrac{\tau \sqrt{\omega\mu_o}}{\pi \sqrt{\rho}\bar{u}_r \tanh(\pi g/\tau)}$, the eddy-current

reaction is increased by decreasing the values of resistivity, permeability and air gap, or by increasing the values of pole pitch and frequency. The pole pitch has the most influence on Q, especially if $g/\tau \ll 1$ (when $\tanh(\pi g/\tau) \simeq \pi g/\tau$) giving $Q \propto \tau^2$.

6.2.4 Magnetic field strength and flux density in the rotor

6.2.4.1 Tangential magnetic field strength

Remembering that $A = Re\ \dot{A}\ e^{-j\beta x}e^{j\omega t}$, the field strength components in the rotor obtained from eqn. 6.25 using eqns. 6.4 and 6.8 are

$$\dot{H}_x = \frac{1}{\mu_o\mu_r}\ \frac{\partial A}{\partial y} = \frac{\beta\dot{\gamma}\dot{A}_r}{\mu_o\mu_r} \qquad (6.38)$$

$$\dot{H}_y = -\frac{1}{\mu_o\mu_r}\ \frac{\partial A}{\partial x} = \frac{j\beta\dot{A}_r}{\mu_o\mu_r} \qquad (6.39)$$

where $H = Re\ \dot{H}\ e^{-j\beta x}e^{j\omega t}$.

The ratio of these two components depends only on $\dot{\gamma}$, since

$$\frac{\dot{H}_x}{\dot{H}_y} = \frac{\dot{\gamma}}{j} \qquad (6.40)$$

When the skin effect is strong, $\dot{\gamma}$ is given by eqn. 6.30, so that

$$\frac{\dot{H}_x}{\dot{H}_y} = \frac{1}{\sqrt{j}\beta d} \quad \text{and} \quad \left|\frac{\dot{H}_x}{\dot{H}_y}\right| = \frac{1}{\beta d} \quad \text{if} \quad \frac{1}{\beta^2 d^2} \gg 1 \qquad (6.41)$$

and the tangential (x) component of the field is greater than the radial (y) component by the skin-effect factor $\frac{1}{\beta d}$. The tangential component of the field on the rotor surface $\dot{H}_{xo}$ is therefore normally a good indication of the extent of saturation of the rotor iron, a fact mentioned by Kuyper[120] and Bratoljic[9]. Furthermore, eqn. 6.33 shows that $\dot{H}_{xo}$ is independent of the rotor properties if both the skin effect and the eddy-current reaction are strong.

The general expression for $\dot{H}_x$ when the skin effect is strong and $\mu_s \gg \mu_s'$ (eqn. 6.28) may be obtained by substituting eqn. 6.31 in eqn. 6.38 with $\dot{\gamma} = \frac{1+j}{\sqrt{2}\beta d}$ (eqn. 6.30)

$$\dot{H}_x = \frac{1+j}{\sqrt{2}\beta d\mu_r \tanh\beta g + 1 + j} \cdot \frac{\hat{K}}{\cosh\beta g} \cdot e^{\frac{1+j}{\sqrt{2}d}y} \qquad (6.42)$$

This confirms that $\dot{H}_x$ has a maximum value on the rotor surface ($y = 0$) when $Q = 1/\beta d\mu_r \tanh\beta g \gg 1$ given by

$$\dot{H}_{xm} = \frac{\hat{K}}{\cosh\beta g} \qquad (6.43)$$

In order to show the variation with Q of the amplitude of $\dot{H}_{xo}$ a ratio K_H is defined by

$$K_H = \left| \frac{\dot{H}_{xo}}{\dot{H}_{xm}} \right| = \frac{\sqrt{2}}{\sqrt{(\sqrt{2}\beta d\mu_r \tanh\beta g + 1)^2 + 1}} = \frac{Q^{1/2}}{(Q + Q^{-1} + \sqrt{2})^{1/2}} \qquad (6.44)$$

K_H is plotted as a function of Q in fig. 6.2. It tends to 1 when $Q \gg 1$, as expected, and decreases to Q when $Q \ll 1$.

6.2.4.2 Radial flux density

The behaviour of the radial (y) component of flux density is the same as the behaviour of the vector potential or total flux, and, as already indicated in section 6.2.3.3, is equal to the applied value when $\mu_r \tanh\beta g$ is much greater than the skin-effect factor $\frac{1}{\beta d}$, i.e. when the eddy-current reaction is weak ($Q \ll 1$).

The general expression for $\dot{B}_y$ when the skin effect is strong and $\mu_s \gg \mu_s'$ (eqn. 6.28) may be obtained by substituting eqn. 6.31 in eqn. 6.39, using eqn. 6.8

$$\dot{B}_y = \frac{j\sqrt{2}\beta d\mu_r \tanh\beta g}{\sqrt{2}\beta d\mu_r \tanh\beta g + 1 + j} \cdot \frac{\mu_o \hat{K}}{\sinh\beta g} \cdot e^{\frac{1+j}{\sqrt{2}d}y} \qquad (6.46)$$

This confirms that the maximum value of $\dot{B}_y$ occurs on the rotor surface when $Q = 1/\beta d\mu_r \tanh\beta g \ll 1$ given by

$$\dot{B}_{ym} = j\frac{\mu_o \hat{K}}{\sinh\beta g} \qquad (6.47)$$

and this is equal to the value when there are no eddy currents in the rotor and when the rotor permeability is high enough to make $\mu_r \tanh\beta g \gg 1$ (apply eqn. 6.39 to eqn. 6.36). $\dot{B}_{ym}$ is also the value when $\mu_r = \infty$. The ratio of $\dot{B}_y$ on the rotor surface to this maximum value is given by

$$K_B = \left| \frac{\dot{B}_{yo}}{\dot{B}_{ym}} \right| = \frac{\sqrt{2}\beta d\mu_r \tanh\beta g}{\sqrt{(\sqrt{2}\beta d\mu_r \tanh\beta g + 1)^2 + 1}} = \frac{Q^{-\frac{1}{2}}}{(Q + Q^{-1} + \sqrt{2})^{\frac{1}{2}}} \qquad (6.48)$$

K_B is plotted as a function of Q in fig. 6.2. It tends to 1 when $Q \ll 1$, as expected, and decreases to $1/Q$ when $Q \gg 1$.

From eqn. 6.35 the applied value of B_y on the rotor surface for any value of $\mu_r \tanh\beta g$ is given by

$$\dot{B}_{ya} = j \frac{\mu_r \tanh\beta g}{\mu_r \tanh\beta g + 1} \cdot \frac{\mu_o \hat{K}}{\sinh\beta g} = K_\mu \dot{B}_{ym} \qquad (6.49)$$

and is less than $\dot{B}_{ym}$ by the factor $K_\mu = \mu_r \tanh\beta g/(\mu_r \tanh\beta g + 1)$. The ratio K_B should therefore be increased by $1/K_\mu$ to obtain the ratio of the radial flux density to the actual applied value. This latter ratio was the one considered by Lawrenson et al.[125] in their discussion of the effect of eddy-current reaction on slot-ripple loss. In this problem, however, $\dot{B}_{ym}$ would be the applied flux density calculated by the usual conformal transformation method[126] because it is necessary to make the assumption $\mu_r = \infty$. Therefore K_B should be the appropriate ratio to use for obtaining the flux density in the presence of eddy-current reaction. (If desired, eqn. 6.49 could be used to determine the effect of a non-infinite rotor permeability on the calculated applied flux density.)

Lawrenson et al. did not identify the parameter $Q = 1/\beta d\mu_r \tanh\beta g$ as being of interest because they did not make the simplifying assumption of strong skin effect $(\frac{1}{\beta^2 d^2} \gg 1)$, although the assumption was valid for all their calculations (the minimum value of $\frac{1}{\beta^2 d^2}$ which occurred was 30).

6.2.4.3 Phase

For strong skin effect, the phase of $\dot{B}_y$ on the rotor surface relative to the stator current may be obtained from eqn. 6.46 and is given by

$$\angle \dot{B}_{yo} = \text{artan} (\sqrt{2}\beta d\mu_r \tanh\beta g + 1) = \text{artan}(\sqrt{2}Q^{-1} + 1) \qquad (6.50)$$

This is plotted in fig. 6.3. It tends to $+90°$ for $Q \ll 1$ and to $+45°$ for $Q \gg 1$.

Since there is no phase shift across the air gap ($\gamma = 1$ for the air gap in eqn. 6.21) the supply voltage to the stator has the same phase as $\dot{B}_{yo}$ and the power factor angle varies from a normal inductive angle of $90°$ to a smaller angle of $45°$ as the eddy-current reaction increases (neglecting the stator winding resistance).

The applied flux density $\dot{B}_{ya}$ is $90°$ ahead of the stator current (eqn. 6.49), and therefore the phase of $\dot{B}_{yo}$ relative to $\dot{B}_{ya}$ is $90°$ behind $\angle \dot{B}_{yo}$.

With strong skin effect, the phase of $\dot{H}_x$ relative to the stator current may be obtained from eqn. 6.42, and it lags $\dot{B}_y$ by $45°$ (also shown by eqn. 6.41). Therefore $\angle \dot{H}_{xo}$ tends to $+45°$ for $Q \ll 1$ and to $0°$ for $Q \gg 1$.

6.2.5 Loss

6.2.5.1 General

The power loss in the rotor per unit surface area may be conveniently found in terms of the field on the rotor surface by using the Poynting vector, and the average power is given by

$$P = -\frac{1}{2} \operatorname{Re}(E_z H_x^*)_{y=0} \qquad (6.51)$$

where * denotes complex conjugate.

Using eqns. 6.4, 6.13 and 6.17 it may be seen that

$$\dot{E}_z = -j\omega \dot{A} = -\frac{\omega}{\beta} \dot{B}_y \qquad (6.52)$$

giving

$$P = \frac{1}{2} \frac{\omega}{\beta} \operatorname{Re}(\dot{B}_y \dot{H}_x^*)_{y=0} = \frac{1}{2} \frac{\omega}{\beta} \left(\left| \dot{B}_{yo} \right| \left| \dot{H}_{xo} \right| \cos\vartheta \right) \qquad (6.53)$$

where ϑ is the angle between $\dot{B}_y$ and $\dot{H}_x$.

The loss is therefore proportional to the product of the radial flux density and the tangential field strength on the rotor surface. The term $\frac{\omega}{\beta}$ is equal to the velocity v of the wave relative to the rotor, and is approximately the same for all the

winding and slot ripple harmonics (being approximately synchronous speed for the winding harmonics and exactly this value for the slot-ripple harmonics). A relation between the values of $\dot{B}_y$ and $\dot{H}_x$ in the rotor may be obtained from eqn. 6.40, using eqn. 6.8,

$$\dot{H}_x = \frac{\dot{\gamma}}{j\mu_o\mu_r} \dot{B}_y \tag{6.54}$$

and this may be substituted in eqn. 6.53 to give general formulae for the loss in terms of either $\dot{H}_x$ or $\dot{B}_y$.

When the skin effect is strong, eqn. 6.54 becomes

$$\dot{H}_x = \frac{1}{\sqrt{j}\beta d\mu_o\mu_r} \dot{B}_y \qquad \text{if} \quad \frac{1}{\beta^2 d^2} \gg 1 \tag{6.55}$$

The angle ϑ between $\dot{H}_x$ and $\dot{B}_y$ is then $45°$, giving $\cos\vartheta = \frac{1}{\sqrt{2}}$, and the formulae for the loss per unit surface area are

$$P = \frac{1}{2} \cdot \frac{d}{\sqrt{2}\rho} \cdot v^2 B_{yo}^2 = \frac{1}{2} \frac{v^2 B_{yo}^2}{2\sqrt{\pi\mu_o\mu_r\rho f}} \qquad \text{if} \quad \frac{1}{\beta^2 d^2} \gg 1 \tag{6.56}$$

$$\text{or} \qquad P = \frac{1}{2} \cdot \frac{\rho}{\sqrt{2}d} \cdot H_{xo}^2 = \frac{1}{2} \sqrt{\pi\mu_o\mu_r\rho f} \; H_{xo}^2 \qquad \text{if} \quad \frac{1}{\beta^2 d^2} \gg 1 \tag{6.57}$$

Expressions for the loss in terms of the stator current may be obtained from eqns. 6.53, 6.56 or 6.57, using eqns. 6.44 or 6.48, and are given by

$$P = \frac{1}{2} v\mu_o \hat{K}^2 \frac{K_H K_B}{\cosh\beta g \; \sinh\beta g} \frac{1}{\sqrt{2}} = \frac{1}{2} \frac{d}{\sqrt{2}\rho} v^2 \mu_o^2 \hat{K}^2 \frac{K_B^2}{\sinh^2\beta g}$$

$$= \frac{1}{2} \frac{\rho}{\sqrt{2}d} \hat{K}^2 \frac{K_H^2}{\cosh^2\beta g} \tag{6.58}$$

Substituting for K_H and K_B in these gives expressions of the form used by earlier authors for the calculation of winding-harmonic loss. For example the first gives the form used by Kuyper[120], the second Barello[121] and the third Bratoljic[9]. For calculating slot ripple loss, an equivalent current sheet may be defined[124,125] using eqn. 6.47 where $\dot{B}_{ym}$ is the applied flux density when $\mu_r\tanh\beta g \gg 1$, e.g. $\mu_r = \infty$, as calculated by the conformal transformation method. Alternatively, since $|\dot{B}_{yo}| = K_B|\dot{B}_{ym}|$, eqn. 6.56 may be used.

The third relation in eqn. 6.58 is particularly useful if the

eddy-current reaction is strong ($Q \gg 1$) because $K_H = 1$ (fig.6.2).
In this case the loss varies as $(\mu_r \rho f)^{1/2} \cosh^{-2}(\pi g/\tau)$, and if
$\cosh^2(\pi g/\tau) \simeq 1$ ($g/\tau \ll 1$) giving complete reflection of the stator
current sheet in the rotor, the variation is as $(\mu_r \rho f)^{1/2}$. The
second relation is particularly useful if the eddy-current reaction
is weak ($Q \ll 1$) when $K_B = 1$. In this case the loss varies as
$v^2 (\mu_r \rho f)^{-1/2} \sinh^{-2}(\pi g/\tau) \propto \tau^2 f^{3/2} (\mu_r \rho)^{-1/2} \sinh^{-2}(\pi g/\tau)$, and if
$\sinh(\pi g/\tau) \simeq \pi g/\tau$ ($g/\tau \ll 1$) the variation is as $\tau^4 f^{3/2} (\mu_r \rho)^{-1/2} g^{-2}$.
A comparison of the two cases shows that for small air gap to pole
pitch ratios the loss depends considerably on the pole pitch and
air gap if the eddy-current reaction is small and is independent
of these if the eddy-current reaction is appreciable. The loss is
at all times proportional to the square of the current loading.

Omitting the $\cosh \pi g/\tau$ and $\sinh \pi g/\tau$ terms, the above
variations are the same as those given for strong skin effect by
Stoll and Hammond[124], who did not include a magnetic stator. Their
equations for P , however, corresponding to the two cases when
$K_B = 1$ and $K_H = 1$, contained a term $\exp(-2\pi g/\tau)$, where g was the
distance from the current sheet to the rotor, rather than the terms
$\sinh^{-2}(\pi g/\tau)$ or $\cosh^{-2}(\pi g/\tau)$, the equations being otherwise identical.
They did not discuss the variation of loss with pole pitch and gap
implied by the exponential term, and this variation is only small
if $g/\tau \ll 1$, when $\exp(\pi g/\tau) \simeq 1$. Since $\cosh x \simeq \exp x \simeq 1$ if $x \ll 1$, and
$\sinh x \simeq \cosh x \simeq \frac{1}{2} \exp x$ if $x \gg 1$, it is interesting to note that the
variation of the loss with the gap to pole pitch ratio is about the
same whether or not a magnetic stator is present, except when the
eddy-current reaction is weak and $g/\tau \ll 1$, in which case $P \propto (\tau/g)^2$
with the stator, being independent of g/τ without the stator. The
magnitude of the loss is only the same, however, when there is
complete reflection of the stator current sheet in the rotor (strong
eddy-current reaction and $g/\tau \ll 1$) being $(\tau/g)^2$ times greater with
the stator when $g/\tau \ll 1$ and the eddy-current reaction is weak, and

4 times greater when $g/\tau \gg 1$.

6.2.5.2 Variation of loss with rotor permeability and resistivity

The discussion in the previous section indicates that when the skin effect is strong, the loss for a given harmonic and geometry, i.e. given τ, f and g, may be proportional to either $\sqrt{\rho\mu_r}$ or $1/\sqrt{\rho\mu_r}$ depending on whether the eddy-current reaction is strong or weak. A suitable form for plotting the variation may be obtained from the first relation in eqn. 6.58, substituting for K_H and K_B from eqns. 6.44 and 6.48,

$$P = \frac{1}{2} v\mu_o \hat{K}^2 \frac{1}{\sqrt{2}\cosh\beta g \, \sinh\beta g} \cdot \frac{1}{Q+Q^{-1}+\sqrt{2}} \quad \text{if} \quad \frac{1}{\beta^2 d^2} \gg 1 \qquad (6.59)$$

The last term in eqn. 6.59 is the only one depending on the rotor properties and is a function of $Q \propto 1/\sqrt{\rho\mu_r}$. The variation of P with μ_r and ρ is therefore the same and may be shown by plotting

$$K_P = \frac{1}{Q+Q^{-1}+\sqrt{2}} = K_H K_B \qquad (6.60)$$

as a function of Q, which is done in fig. 6.2. The expected variation of K_P is shown, i.e. $K_P \propto Q$ when $Q \ll 1$ and $K_P \propto 1/Q$ when $Q \gg 1$. Also K_P is shown to reach a maximum value of $\frac{1}{2+\sqrt{2}}$ when $Q = 1$, i.e. when the magnitudes of the eddy current reaction field and the total field on the rotor surface are equal (eqn. 6.37).

The variation of loss with permeability and resistivity was also shown by Stoll and Hammond[124], and by Kuyper[120]. Kuyper plotted the dimensionless factor $R = K_P / \sqrt{2}\cosh\beta g \, \sinh\beta g$ against $1/\sqrt{2}\beta d\mu_r \propto 1/\sqrt{\rho\mu_r}$ for several values of g/λ (see appendix 8.5).

6.3 Examples of the linear theory

6.3.1 Machine data

Two machines are used to illustrate the theory, with particular emphasis on the field strength in the rotor and the effect of permeability on the losses. They are examples of large industrial machines - a 500 MVA 2-pole turbo-generator and a 60 MVA 6-pole salient-pole machine - and were among those used as examples by Adderley[7] (with the reference numbers Y and 1 E) although he neither calculated the rotor field strength nor discussed the influence of permeability. The relevant data is given in table 6.1. For convenience, data for an experimental machine used by Adderley is also given in table 6.1 and this will be referred to later.

6.3.2 Winding-harmonic results for one value of μ_r and one value of ρ

Table 6.2 gives the calculated values of skin-effect factor, eddy-current reaction factor, surface field strength and loss for some winding harmonics of the two industrial machines at rated current, including the 1st pair of slot harmonics for the turbo-generator (n=59, 61) and the 1st and 2nd pair of slot harmonics for the salient-pole machine (n=29, 31 and 59, 61). The slot-width factor (appendix 8.1) was included in every winding factor. The results are for μ_r = 100, a value near the middle of the likely range (10-2000)[125] on a logarithmic scale, and for ρ = 2.37 x 10^{-7} Ωm, a value appropriate for a temperature of about $70°$C and which gives the depth of penetration d = 1mm at 300 Hz.

The following points may be noted from the table:

1. $\frac{1}{\beta^2 d^2} \gg 1$ and $\frac{1}{\beta d} \gg 1$ for all harmonics, so that the assumption of strong skin effect is valid and $|\dot{H}_x| \gg |\dot{H}_y|$.

2. $0.1 < Q < 10.0$ so that the eddy-current reaction is neither very weak nor very strong. It is strongest for the low-order harmonics and weakest for the high-order ones. The reaction is about the same for the low-order harmonics (for the 7th harmonic $|\dot{H}_{xo}|$ is about 50% of the maximum possible value for the given geometry ($K_H \simeq 0.50$)

and $\left|\dot{B}_{yo}\right|$ is about 60% ($K_B \simeq 0.60$)) but for the slot harmonics the reaction is slightly weaker in the salient-pole machine ($\left|\dot{B}_{yo}\right|$ is about 90% of the maximum for both pairs of slot harmonics in the salient-pole machine, and about 80% for the turbo-generator 1st slot-Harmonic pair).

3. The difference between the stator current sheet $\hat{K}$ and the maximum possible tangential surface field strength $\dot{H}_{xm}$, which depends on the air-gap to pole-pitch ratio (eqn.6.43), is considerable for the higher harmonics of the turbo-generator and appreciable for the 2nd pair of slot harmonics of the salient-pole machine.

4. The amplitudes of the tangential surface field strength $\left|\dot{H}_{xo}\right|$ for the low-order waves are beyond the knee of the normal magnetisation curve for mild steel (fig.4.7), being greater than about 1000 A/m. The turbo-generator values tend to be greater than the salient-pole machine values because of its higher current loading. (The 5th harmonic of the salient-pole machine is eliminated by the 4/5 pitch, although, because of the lower current loading, it would never be as large as in the turbo-generator.)

5. The values of $\left|\dot{H}_{xo}\right|$ for the higher harmonics in the turbo-generator are very low, because of (3), but the values for the first pair of slot harmonics in the salient-pole machine are similar to the low-order values.

6. Practically all of the loss in the turbo-generator is produced by the low-order waves, whereas in the salient-pole machine the low-order waves and first pair of slot harmonics each produce about 50% of the total loss.

7. The stator current sheet for the slot harmonics is not equal to the fundamental current loading (table6.1) because of the inclusion of the slot-width factor k_s . In the salient-pole machine this factor is approximately equal to 0.75 for the first pair of slot harmonics, so that its inclusion reduced the calculated

tangential field strength and loss for these harmonics by about 25% and 50% respectively, and, because of (6), reduced the calculated total loss by about 1/3. Adderley[7] commented on the importance of k_s in machines where the loss of the high-order waves is significant. It was especially important in his work because he used the eddy-current coupling theory of Davies[129,130] and found that for the higher harmonics in the salient-pole machine $P \propto k_s^{2.7}$, rather than $P \propto \hat{K}^2 \propto k_s^2$ given by the linear theory.

8. The influence of the stator on the eddy-current reaction factor, given by $1/\tanh\beta g$, is small for the high-order and slot harmonics but significant for the low-order harmonics. In other salient-pole machines, however, with slot pitch to air gap ratios at the extreme of the range suggested by Lawrenson et al.[125], the influence may also be significant for the slot harmonics.

9. With $\mu_r = 100$, $\mu_r \tanh\beta g \gg 1$ so that Q is the ratio of the eddy-current field to the total field at the rotor surface (eqn.6.37)

6.3.3 Variation of winding-harmonic field strength and loss with μ_r and ρ

6.3.3.1 Surface tangential field strength

The influence of μ_r and ρ on $|\dot{H}_{xo}|$ is given by the relation between K_H and Q (eqn. 6.44, fig. 6.2). Since $Q \propto 1/\sqrt{\rho\mu_r}$ the effect of μ_r and ρ is the same, and decreasing either increases the eddy-current reaction and hence $|\dot{H}_{xo}|$. For the particular value of $\rho = 2.37 \times 10^{-7} \Omega m$, fig. 6.4 shows the variation with μ_r of $|\dot{H}_{xo}|$ for the 5th and 11th harmonics in the turbo-generator, and for the 7th and 29th harmonics in the salient-pole machine, these being the two harmonics in each machine with the highest values of $|\dot{H}_{xo}|$. There is a considerable variation of $|\dot{H}_{xo}|$ with μ_r, because $Q \not\gg 1$.
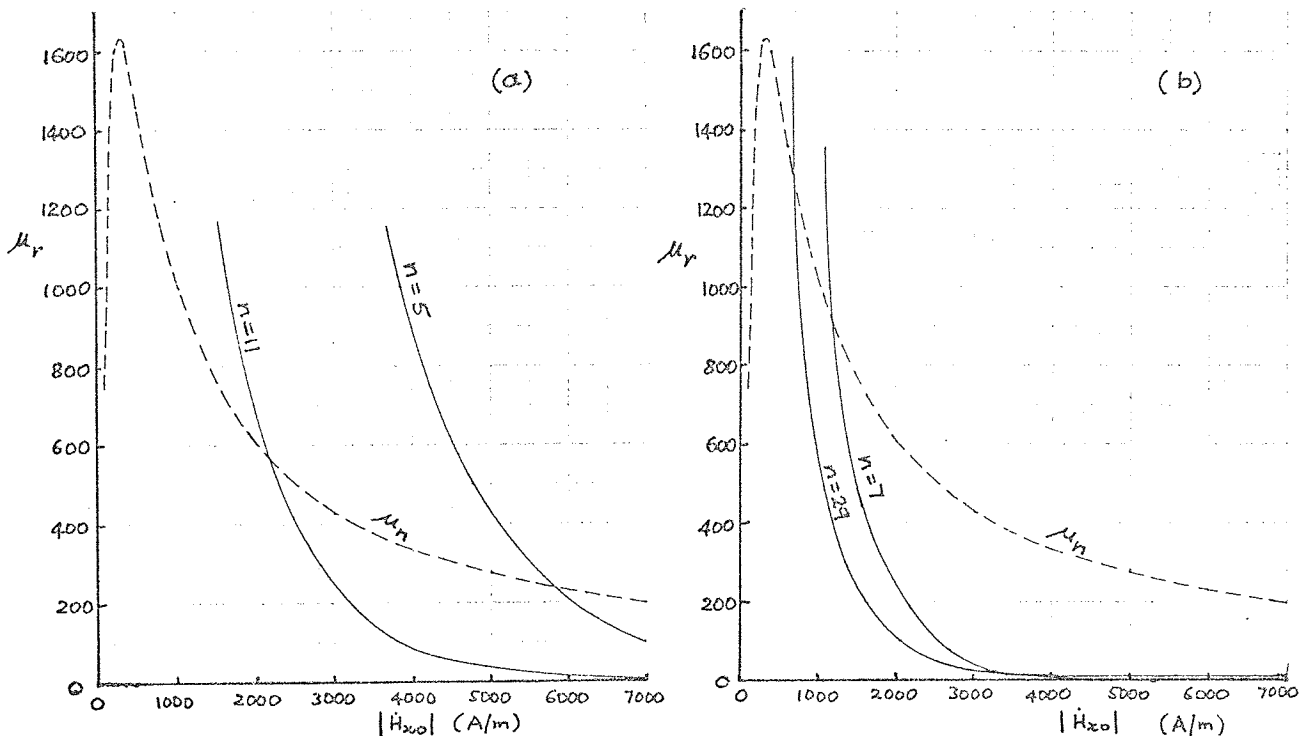

Fig. 6.4   Variation of surface field strength with μ_r

——— $\mu_r - |\dot{H}_{xo}|$ curves for each harmonic (for $\rho = 2.37 \times 10^{-7} \Omega m$)

- - - - - normal permeability curve for EN1A mild steel (from fig.4.8)

(a) turbo-generator   (b) salient-pole machine

To give an idea of possible operating points the normal permeability curve for EN1A mild steel is also given in fig. 6.4. Neglecting all superposition effects, it can be seen that the appropriate values of permeability would be different for each harmonic and each machine, being about 200 and 600 for n = 5 and 11

in the turbo-generator and about 900 and 1300 for n = 7 and 29 in the salient-pole machine. Also, while the values of $\left|\dot{H}_{xo}\right|$ might be a little less than the values for $\mu_r = 100$ given in table 6.2, they would still be beyond the knee of the normal magnetisation curve. The presence of a superposed field, however, is likely to reduce μ_r (chapter 3) resulting in increased values of $\left|\dot{H}_{xo}\right|$. (The use of the normal permeability curve to give an operating point is an approximation as it assumes that the appropriate permeability is the one corresponding to the tangential field strength on the surface. As a linear theory has been used this is only true if there is no change of permeability with depth and if the waveforms are sinusoidal. To be more exact a non-linear theory, such as that of Nejman[131] or MacLean[115] for the 1-dimensional semi-infinite slab with known surface field strength problem, would have to be applied to the 2-dimensional multi-region travelling-wave problem. When a superposed steady field is present, however, there tends to be less variation of permeability with field strength and the linear theory becomes more appropriate. There is also the superposition of the harmonic fields themselves to be considered.)

6.3.3.2 Loss

The variation of the total winding-harmonic loss with rotor permeability and resistivity for the two example machines is shown in fig. 6.5. The loss is plotted against $\sqrt{\rho' \mu_r}$, ρ' being the rotor resistivity relative to $1.72 \times 10^{-8} \Omega\,m$, the resistivity of international standard annealed copper. On this resistivity scale, likely values for rotor steels are from 8 to 18, corresponding to ρ in the approximate range $1.5 - 3.0 \times 10^{-7} \Omega\,m$. A scale of permeability is also given, corresponding to $\rho = 2.37 \times 10^{-7} \Omega\,m$ ($\rho' = 13.8$), the value used for table 6.2 .

The losses for the two most significant harmonics in each machine are also plotted in fig. 6.5. The shape of these curves is the same as the shape of the curve for K_p in fig. 6.2, for reasons

discussed in section 6.2.5.2.

It can be seen that the loss in the turbo-generator is dominated by the low-order waves, which have a peak loss in the range under consideration, so that the total loss has a peak at $\mu_r = 180$ (for $\rho = 2.37 \times 10^{-7} \Omega m$) and may either increase or decrease as $\sqrt{\rho \mu_r}$ increases. The peak loss is about 50% higher than the loss at either end of the range. On the other hand, the loss in the salient-pole machine is dominated by the 1st pair of slot harmonics, for which the eddy-current reaction tends to be weak, so that the total loss decreases as $\sqrt{\rho \mu_r}$ increases. (This is why circumferential grooving of the pole-face, which tends to increase the effective ρ, is used in such machines.) The maximum loss in the range is about 3 times the minimum.

The effect of permeability and resistivity is therefore likely to be more noticeable in the salient-pole machine, as far as the total winding-harmonic loss is concerned. In the next section the addition of slot-ripple and negative-sequence losses is considered, and it is shown that the slot ripple will not change the above picture, but that a normal amount of negative-sequence current may.

6.3.4 Slot-ripple and negative-sequence losses

The calculation of slot-ripple and negative-sequence losses for the two example machines is illustrated in table 6.3, of similar-form to table 6.2. For the purposes of illustration, the slot-ripple calculations are for a main gap flux density in the absence of slots (B_o) of 1.0 T and the negative-sequence calculations are for a 5% negative-sequence current (5% is a typical design value for turbo-generators[2]).

Prints of the curves given by Neville[128] were used to calculate the applied slot-ripple flux-density harmonics $(B_1$ and $B_2)$ as the values of s/g are below those considered by Freeman[127]. To calculate an equivalent stator current sheet $\hat{K}$, eqn. 6.47 was used

with the value of $\dot{B}_{ym}$ equal to the applied density, as explained

in section 6.2.4.2. ($\hat{K}$ is not critical to the calculations, as the

loss can be obtained via eqn. 6.56 with $|\dot{B}_{yo}| = K_B|\dot{B}_{ym}|$, as well as

via eqn. 6.57 with $|\dot{H}_{xo}| = K_H \dot{H}_{xm}$, where $\dot{H}_{xm}$ can be calculated

directly by combining eqns. 6.47 and 6.43:

$$\dot{H}_{xm} = \frac{|\dot{B}_{ym}|\tanh\beta g}{\mu_o} \qquad (6.61)$$

Because of the small air gap to pole pitch ratio for the

negative-sequence wave in each machine, the eddy-current reaction

is strong ($Q \gg 1$), and there is little difference between $\hat{K}$ and

$\dot{H}_{xm}$, and therefore there is almost complete reflection of the

stator current sheet in the rotor. Further, because $Q \gg 1$, there

is little variation of $|\dot{H}_{xo}|$ with μ_r , as shown in fig. 6.6. The

eddy-current reaction for the slot-ripple harmonics is much

weaker, however, being almost the same as for the winding slot-

harmonics, so that there is a large variation of $|\dot{H}_{xo}|$ with μ_r ,

as illustrated by the plot in fig. 6.6 of $|\dot{H}_{xo}|$ for the 1st slot-

harmonic in the salient-pole machine.

The curves of $|\dot{H}_{xo}|$ for the winding harmonics which were

given in fig. 6.4 are also shown in fig. 6.6. It can be seen that

a small unbalanced current in either machine will produce a

negative-sequence field on the rotor surface which is 2 or 3 times

larger than the largest winding-harmonic field, but that all

harmonic fields in the salient-pole machine may be overshadowed

by the 1st slot-ripple harmonic (table 6.3 shows that the slot-

ripple harmonics in the turbo-generator and the higher slot-ripple

harmonics in the salient-pole machine are fairly small).

The effect of the slot-ripple and negative-sequence waves on

the losses is shown in fig. 6.7. In the turbo-generator, the

negative-sequence loss tends to dominate the winding-harmonic loss

so that the total loss increases as $\sqrt{\rho\mu_r}$ increases, whereas in the

salient-pole machine the negative-sequence loss merely reduces the

dependence of the loss on $\sqrt{\rho \mu_r}$. The slot-ripple loss, however, has practically no effect in the turbo-generator because it is so small, but in the salient-pole machine it is large so that the total loss still decreases as $\sqrt{\rho \mu_r}$ increases.

6.4   Superposition effects

6.4.1   Superposition of the main field

The calculations of the previous section showed that for the waves travelling relative to the rotor in typical large machines the depth of penetration is much less than the pole pitch ($1/\beta d \gg 1$ in tables 6.2 and 6.3) so that in a smooth rotor the travelling fields are confined to a thin surface layer and are mainly in a tangential direction. On the other hand, the main field is stationary relative to the rotor and is mainly radial near the rotor surface, with the possible exception of regions where the main flux density changes sign (e.g. the short-circuit condition of fig. 2.13). Therefore, in a smooth rotor, the superposed steady field is predominantly perpendicular to the travelling fields.

An idea of the behaviour of steel when subjected to perpendicular fields can be obtained from calculations of the resultant field neglecting hysteresis, as suggested by Sugiura (section 3.3.2). Curves for EN1A steel obtained by this method are given in appendix 8.4, and the permeability curves for constant transverse flux densities of 1.0 T and 1.8 T are also plotted with the curves of surface field strength for the two example machines in fig. 6.6. It is assumed that any saturation of the surface layer by the travelling fields does not affect the harmonics of the main flux density wave, because the layer is in series with the air gap, and that the fundamental of the main flux density wave is given by the output voltage, so that the main flux density is a fixed quantity.

The curves in appendix 8.4 show that for values of alternating field strength beyond the knee of the normal magnetisation curve ($\geqslant 300$ A/m) the permeability is reduced by the transverse field, but that the reduction is not large until the transverse flux density is beyond the knee of the normal magnetisation curve ($\geqslant 0.6$ T). Even

when $B_b = 1.0$ T, the reduction is still small and fig. 6.6 shows that the appropriate values of permeability for each harmonic in the example machines are still different and only a little below the values without the superposed field. When $B_b = 1.8$ T, however, the reductions in permeability are significant and there is much less variation of permeability with the alternating field strength. The appropriate values of permeability for the winding harmonics in each machine are then about the same ($\simeq$ 100 in the turbo-generator and $\simeq$ 150 in the salient-pole machine) and the values for the negative-sequence wave in the turbo-generator and for the slot-ripple wave in the salient-pole machine are only about half these. The reduction of permeability would cause a decrease of eddy-current loss in the turbo-generator and and increase in the salient-pole machine (fig. 6.7).

The superposed main field would probably also cause a decrease in hysteresis loss. Although a reduction of permeability causes an increase in tangential field strength, this increase is at most proportional to $\mu^{-1/2}$ and its effect is likely to be offset by the marked reduction of hysteresis loss caused by a superposed perpendicular steady field for a given value of alternating field strength, noted by earlier workers (e.g. fig. 3.42 (b)). The hysteresis loss in a solid rotor and its significance would be difficult to evaluate at present because (a) hysteresis has not been included in the travelling-wave theory, and this needs to be done, possibly using complex permeability on the lines of Pohl[112] or Aspden[111] (see chapter 5, section 5.2.2) and (b) no law has been discovered for calculating the hysteresis loss as a function of alternating field strength or flux density with a superposed perpendicular steady field, and relatively few experiments have been conducted (chapter 3, section 3.3).

A further difficulty in allowing for the presence of the main field is that its value is not constant over the pole face, as

dicussed in chapter 2, section 2.5. The behaviour may be nearly linear in one region where the main flux density is high, and non-linear in other regions. The effect is likely to be different on different waves. The variation of the rotor properties occurs within a wavelength of the negative-sequence wave, but mainly over several wavelengths of the winding and slot-ripple harmonics. Also, the winding harmonics beat together in pairs (chapter 2 and next section) with the possibility of the maximum resultant being in different regions for different pairs of harmonics, whereas the resultant of the slot-ripple harmonics must reach a maximum where the main flux density is highest.

The above discussion has assumed that the rotor surface is smooth and of infinite length. When these restrictions are removed the problem of allowing for the main field is even more difficult because there may be regions where the travelling fields and the main field are not perpendicular, and where the main flux density cannot be considered fixed. For example, along the walls of a slot the travelling fields in the iron may be parallel to the surface. The main field in the tooth may then not be perpendicular to the travelling fields, and its flux density will depend on the relative reluctances of the inner and surface regions of the tooth and of the slot. As the tooth reluctance may be significantly altered by the effect of the travelling fields on the permeability (chapter 4, fig. 4.28), there could be a complicated interaction between the steady and travelling fields. In regions where the fields are parallel, the behaviour of the iron with respect to the travelling fields may be linear with a low value of permeability, or non-linear with unsymmetrical magnetisation, depending on the relative values of the varying and steady fields (chapter 5).

6.4.2 Superposition of the travelling waves

6.4.2.1 Winding harmonics

It was shown in section 6.3.2 that the eddy-current reaction for the winding-harmonics of two typical large machines is neither very strong nor very weak. Therefore in such machines, apart from the effect of the air gap, the resultant tangential surface field strength is not equal to the stator current loading relative to the rotor shown in chapter 2, figs. 2.6 - 2.8, and neither is the resultant radial flux density equal to the maximum applied flux density, which is proportional to the m.m.f. variations relative to the rotor shown in chapter 2. The diagrams in chapter 2, however, do indicate possible features about the resultant fields. For example, figs. 2.2 and 2.3 show that the resultant m.m.f. variations for a full-pitched, infinitely-distributed winding are likely to be unsymmetrical, having larger positive peaks than negative peaks where the fundamental armature m.m.f. is positive ($\vartheta_2 = -90°$ to $+90°$), and vice versa where the fundamental m.m.f. is negative ($\vartheta_2 = 90°$ to $270°$), and that the dominant frequency is the same ($6f_1$) at all points on the rotor. On the other hand, when the pitch is changed to 5/6, figs. 2.4 and 2.5 show that the variations still have some asymmetry of the peaks, but that the dominant frequency changes from $6f_1$ at $\vartheta_2 = 90°$ to $12f_1$ at $\vartheta_2 = 0°$. This change of frequency is accomplished in stages, so that at points near $\vartheta_2 = 0°$ there is a secondary peak in the m.m.f. variation with time (fig. 2.4) which may produce an incremental loop in the magnetisation of the rotor at such points. Other incremental loops may appear for a winding with discrete conductors, owing to the slot harmonics. This could be shown by determining the variations with time of the m.m.f. or current loading caused by the slots (possibly via the space variations shown in fig. 2.8) and adding these to the phase-band variations.

In practice, however, the effect of the air gap and the

reaction of the eddy currents must be considered. A part of the effect of the air gap can be studied without making assumptions about the rotor permeability, by determining the maximum applied flux density harmonics $\dot{B}_{ym}$ or the maximum surface field strength harmonics $\dot{H}_{xm}$, using eqns. 6.47 or 6.43. The tangential field strength is more important inside the iron, so the effect of the air gap on $\dot{H}_{xm}$ in the two example machines is illustrated in table 6.4, where the reduction factor $\dot{H}_{xm}/\hat{K} = 1/\cosh\beta g$ is shown, and the product of this with the winding factor is expressed as a fraction of the value for the first phase-band harmonic to show the relative values of $\dot{H}_{xm}$. These values are small for harmonics beyond the 13th in the turbo-generator and beyond the 31st in the salient-pole machine, and the relative values of the actual surface field strength $\dot{H}_{xo}$ will be even lower. The problem in the turbo-generator is therefore reduced to the superposition of the first 2 pairs of phase-band harmonics, but is rather more difficult in the salient-pole machine where the first pair of slot harmonics are important as well as the first few pairs of phase-band harmonics.

The superposition of a pair of winding harmonics which induce the same frequency in the rotor was discussed in chapter 2, section 2.4, and it was shown that there is a $\cos 2\vartheta$ type of variation superposed on the mean resultant amplitude (eqn. 2.8). Some resultant values of $\dot{H}_{xm}$ are shown in table 6.5, calculated from the sums $(\vartheta_2 = \dot{0})$ and differences $(\vartheta_2 = 90^\circ)$ of the individual values given in table 6.2. In the turbo-generator, the resultant of the second pair of harmonics is dominant at $\vartheta_2 = 0$ and the first pair at $\vartheta_2 = 90^\circ$ (as expected since the pitch is 5/6). Therefore, at $\vartheta_2 = 90^\circ$ the rotor is magnetised at a frequency of $6f_1$ with a small second harmonic component, and as ϑ_2 approaches 0° the second harmonic increases, beginning the formation of incremental loops, until finally at $\vartheta_2 = 0^\circ$ the incremental magnetisation is at a frequency of $12f_1$ with a small bias varying at $6f_1$. In the

salient-pole machine, there are incremental loops at both
$\vartheta_2 = 0°$ and $90°$; at $\vartheta_2 = 90°$ they are formed by the large
slot-harmonic component at a frequency of $30f_1$, the smaller bias
varying at (mainly) $6f_1$, and at $\vartheta_2 = 0°$ they are formed by the
second pair of phase-band harmonics and possibly also by the
higher harmonics.

With the possibility of such complicated patterns of
magnetisation it is difficult to see how a representative value
of permeability can be chosen for use in the linear theory, whether
it is desired to use one value for all harmonics or a different
value for each harmonic. When there are incremental loops with a
bias of smaller amplitude, the incremental permeability is equal
to the normal (unbiased) permeability, (chapter 4) but the loss is
affected by the asymmetry of the loops (chapter 5, section 5.4),
and as the bias varies, its effect will also vary. Apart from this,
there is the question of the appropriate permeability for the
varying bias. When there are no incremental loops, the
magnetisation may be non-sinusoidal and of unequal positive and
negative peaks, depending on the relative magnitudes and phases of
the resultant waves, and the calculation of the eddy-current loss
under such conditions is not well understood. There is, therefore,
the difficult nature of the variation with time at each point on
the rotor, the shape of which varies from point to point. Some
simplification may possibly be achieved in future studies of this
problem, however, as table 6.5 shows that the amplitudes of the
resultant values of $\dot{H}_{xm}$ are large, being generally greater than
1000 A/m, so that hysteresis effects will be small and calculations
may be based on the normal magnetisation curve, or some
representation of this.(There will be an exception at points
where incremental loops are just beginning, where μ_Δ depends on
the magnetic history as shown in chapter 4, figs. 4.32 - 4.35).

The above discussion, being based on values of $\dot{H}_{xm}$, needs no

modification if the eddy-current reaction is very strong. When this is not so, however, the surface field strength will be less than $\dot{H}_{xm}$. The exact reduction for each harmonic is difficult to calculate because of the non-linear magnetisation curve and the non-sinusoidal waveforms with time and space. An estimate of the effect for the two example machines is given in table 6.5, where resultant values of $\left|\dot{H}_{xo}\right|$ are shown, calculated from the linear theory values of $\left|\dot{H}_{xo}\right|$ for each harmonic with $\mu_r = 100$ given in table 6.2. With this uniform value of permeability, the reduction increases as the harmonic order increases, so there is less tendency to form incremental loops. The general pattern of behaviour is still the same, however, and the resultant values of surface field strength are still large.

Besides the reduction of amplitude of $\dot{H}_{xo}$ when the eddy-current reaction is not very strong, there is also a phase shift between $\dot{H}_{xo}$ and $\dot{H}_{xm}$ (or $\hat{K}$) (fig. 6.3). The effect of this on the combination of a pair of harmonics which induce the same frequency in the rotor may be shown by writing

$$\left.\begin{array}{l} H_{6k-1} = \hat{H}_{6k-1} \cos\left(6k\omega t + (6k-1)\vartheta_2 + \phi_{6k-1}\right) \\ H_{6k+1} = \hat{H}_{6k+1} \cos\left(6k\omega t + (6k+1)\vartheta_2 + \phi_{6k+1}\right) \end{array}\right\} \quad (6.62)$$

where ϕ is the phase shift of each harmonic and H refers to the surface values of field strength. The resultant is given by

$$H_{6k\omega} = \hat{H}_{6k\omega} \cos\left(6k\omega t + 6k\vartheta_2 + \eta_k\right) \quad (6.63)$$

where

$$\hat{H}^2_{6k\omega} = \hat{H}^2_{6k+1} + \hat{H}^2_{6k-1} + 2\hat{H}_{6k+1}\hat{H}_{6k-1}\cos 2(\vartheta_2 + \phi_{dk}) \quad (6.64)$$

$$\eta_k = \phi_{sk} + \arctan\left[\frac{\hat{H}_{6k+1}\sin(\vartheta_2+\phi_{dk}) - \hat{H}_{6k-1}\sin(\vartheta_2+\phi_{dk})}{\hat{H}_{6k+1}\cos(\vartheta_2+\phi_{dk}) + \hat{H}_{6k-1}\cos(\vartheta_2+\phi_{dk})}\right] \quad (6.65)$$

$$\phi_{sk} = \left(\phi_{6k+1} + \phi_{6k-1}\right)/2$$

$$\phi_{dk} = \left(\phi_{6k+1} - \phi_{6k-1}\right)/2$$

A comparison of eqn. 6.64 with eqn. 2.8 shows that one effect of

the phase shift is to move the points of maximum and minimum amplitude backwards by ϕ_{dk} elec deg. Taking the turbo-generator as an example, and using values of Q given in table 6.2 for $\mu_r = 100$, fig. 6.3 gives $\phi_5 = +16.5°$ and $\phi_7 = +22.8°$, so that the movement for the first pair of harmonics is only $\phi_{d1} = 3.1°$. The figure for the second pair of phase-band harmonics is $0.9°$ and in general it will be low because (a) the values of Q for a pair of harmonics are similar, and (b) there is only an appreciable variation of phase with Q for $0.1 < Q < 1.0$. A second effect of the phase shift is that the phase of the resultant wave (eqn. 6.65) is ϕ_{sk} plus a term depending on ϑ_2, ϕ_{dk} and the harmonic amplitudes. There will only be small differences between the values of this second term for different pairs of harmonics, because of the small values of ϕ_{dk}, but there may be larger differences between the values of ϕ_{sk} (in the turbo-generator $\phi_{s1} = 19.6°$ and $\phi_{s2} = 26.9°$ for $\mu_r = 100$, a difference of $7.3°$) so that there may be some influence on the total waveform worth considering.

Any careful attempt to allow for the non-linear magnetisation curve would also have to include the time and space harmonics caused by the non-linearity, even when the excitation is purely sinusoidal, and the variation of the waveform with depth. As explained in the previous section the superposed main field may cause more linear behaviour in regions where it is strong, but there is also the possible influence of slot-ripple and negative-sequence waves to consider, and this is discussed in the next section. Should the linear theory be considered appropriate in some particular machine, the loss of a pair of harmonics which induce the same frequency in the rotor may be calculated by substituting the expression for the resultant surface field strength amplitude (eqn.6.64) in eqn.6.57, since the wave impedance factor $\dfrac{\rho}{\sqrt{2}\,d}$ is independent of wavelength:

$$P_{6k\omega} = \frac{1}{2} \frac{\rho}{\sqrt{2}d_{6k}} \hat{H}^2_{6k\omega} \tag{6.66}$$

(eqn. 6.56 may also be used with the resultant amplitude of $vB_{yo} = E_{zo}$). This gives the local power loss per unit surface area, which varies around the rotor because of the variation of $\hat{H}_{6k\omega}$. Barello[122] showed that the total loss could be obtained by summing the losses of the individual components, but it was implicit in his argument that the pole arc was $180°$. If this is not so, the result is only true for certain load angles, as shown below.

The total loss over a pole arc α is given by

$$P'_{6k\omega} = \frac{1}{2} \frac{\rho}{\sqrt{2}d_{6k}} \frac{L\tau_1}{\pi} \times$$

$$\int_{-\frac{\alpha}{2}}^{\frac{\alpha}{2}} (\hat{H}^2_{6k+1} + \hat{H}^2_{6k-1} + 2\hat{H}_{6k+1} \hat{H}_{6k-1} \cos2(\vartheta_3 + 90 + \psi + \phi_{dk}))d\vartheta_3 \tag{6.67}$$

where ϑ_2 has been replaced by $\vartheta_3 + 90 + \psi$ to allow for the position of the rotor relative to the fundamental armature m.m.f., as explained in chapter 2, section 2.5. Carrying out the integral gives

$$P'_{6k\omega} = \frac{1}{2} \frac{\rho}{\sqrt{2}d_{6k}} L\tau_1 \times$$

$$\left[\frac{\alpha}{\pi}(\hat{H}^2_{6k+1} + \hat{H}^2_{6k-1}) + \frac{2}{\pi}\hat{H}_{6k+1}\hat{H}_{6k-1} \cos2(90 + \psi + \phi_{dk}) \sin\alpha\right] \tag{6.68}$$

If the pole arc is $180°$, the loss is equal to the sum of the component losses. If the pole arc is less than $180°$, the loss depends on the rotor angle ψ for all values of ψ except $\pm 45° = \psi + \phi_{dk} \simeq \psi$, for which $\cos2(\vartheta_3 + 90 + \psi + \phi_{dk})$ is an odd function about $\vartheta_3 = 0°$. Then the loss is independent of ψ, being $\frac{\alpha}{\pi}$ times the smooth-rotor value. (It may be noted from chapter 2, fig.2.13, that $\psi = 45°$ occurs at rated load and unity power factor for a machine with $X_q = 1.0$ p.u.)

Under short-circuit conditions, when $\psi = 90°$,

$$P'_{6k\omega} = \frac{1}{2} \frac{\rho}{\sqrt{2}d_{6k}} L\tau_1 \times$$

$$\left[\frac{\alpha}{\pi}(\hat{H}^2_{6k+1} + \hat{H}^2_{6k-1}) + \frac{2}{\pi}\hat{H}_{6k+1}\hat{H}_{6k-1}\cos 2\phi_{dk}\sin\alpha\right] \qquad (6.69)$$

and the loss is more or less than the $\psi = 45°$ value, depending on the signs of the winding factors. The same signs, i.e. a peak resultant at $\vartheta_2 = 0°$, will give more, and opposite signs, i.e. a peak resultant at $\vartheta_2 = 90°$, will give less. The total effect in a particular machine will depend on the proportion of the total winding-harmonic loss caused by each type of harmonic pair, the rotor angle on load, and the effective pole arc (which is approximately $180°$ for turbo-generators with magnetic slot wedges, rather indefinite for turbo-generators with non-magnetic slot wedges, and $< 180°$ for salient-pole machines).

6.4.2.2 Slot-ripple and negative-sequence waves

As for the winding-harmonic waves, the tangential component of the field of the slot-ripple and negative-sequence waves is the larger component inside a smooth rotor. This was shown for the two example machines in table 6.3, where $\frac{1}{\beta d} \gg 1$. Therefore these waves are predominantly parallel to one another and to the winding harmonics. It was also shown in table 6.3, and illustrated in fig. 6.6, that these waves may have field strengths of the same order or larger than the winding harmonics, and by referring to tables 6.5 and 6.3 it can be seen that this is still true with respect to the resultant amplitudes of the winding-harmonic pairs.

The effect of the negative-sequence wave on the rotor magnetisation would be to introduce a bias varying at a frequency of $2f_1$ and of a known constant field strength amplitude at all points on the rotor (the amplitude is relatively independent of μ_r as explained in section 6.3.4), so that the permeability of a winding harmonic superposed on this would follow a curve such as

the μ_Δ - H_b curve for H_Δ = 1000 A/m in fig. 4.32 . Hysteresis effects would be small because of the large winding-harmonic amplitudes, but the incremental loops would be nearly linear and of low permeability when $H_b \gtrsim H_\Delta$, and non-linear and unsymmetrical when $H_b \lesssim H_\Delta$ (chapter 4). Both the linear and non-linear types of behaviour discussed in chapter 5 would therefore occur for the winding harmonics during a cycle of the negative-sequence wave. The distortion of the negative-sequence wave caused by the winding harmonics would also affect the appropriate permeability for the calculation of the negative-sequence loss, in a rather complicated fashion. The superposed steady field would make the behaviour more linear, but, as discussed in section 6.4.1, a large value of steady flux density is required, and this may occur at only a few points on the rotor surface.

In a rotor which is not smooth, the flux paths of the negative-sequence and winding-harmonic waves may be different, owing to the different values of depth of penetration and wavelength, so that the interaction between the two may also be different.

The slot-ripple wave is unlikely to be important in machines with a high air gap to slot pitch ratio, as shown in section 6.3.4 for the turbo-generator example, but in machines where it is important the winding slot harmonics are also likely to be significant, as illustrated by the salient-pole machine example. It was shown in chapter 2 that the resultant slot-harmonic amplitude is a maximum at points of zero fundamental armature m.m.f., which is where the main flux density and hence slot ripple tends to be large. Since currents of the same frequency are induced in the rotor by the two types of travelling wave, there is interference between the two. The pattern of this interference will depend on the main flux density distribution, because this determines the slot-ripple amplitude. The resultant magnetisation will be affected by the (relatively) slowly varying bias of the negative-sequence

wave or the low-order harmonics, and by the perpendicular main field, in the ways already described.

6.4.3 Present methods of allowing for superposed fields

The methods in common use at present for the calculation of winding-harmonic losses are based on the linear theory, and do not allow for superposition in detail. Bratoljic (1966)[9] stated that in order to calculate with a representative constant permeability, an average value of the broad range between the extreme values of normal permeability and reversible permeability is used. Kuyper (1943)[120] recommended using a value of permeability such that the flux density at the rotor surface is about twice the saturation point of common steels, and to assume linear superposition of the losses of each harmonic. His examples, however, did not include a test in which more than one harmonic was significant. Barello (1955)[122] and Postnikov (1959)[123] recommended values of $\sqrt{\rho \mu_r}$ based on measurements of total losses, which imply $\mu_r \simeq 800$ (appendix 8.5). The above authors did not allow for the combination of harmonics which induce the same frequency in the rotor, yet this had been mentioned earlier by Pollard (1935)[13]. He, however, believed that the peak amplitude of all phase-band harmonics occurred at the peak of the fundamental armature m.m.f., although he did mention the effect of the rotor angle on the loss. Some of the authors[9,123] mentioned that the main field could reduce the permeability, but they did not say that the behaviour could become more linear. No-one noted the possible influence of the negative-sequence or slot-ripple waves.

Slot-ripple losses in solid rotors are usually calculated by the methods of Carter (1916)[133] or Gibbs (1947)[132], both based on the linear theory. Gibbs' contribution was to present curves by which the losses of all harmonics of the ripple could be rapidly summed, assuming linear superposition, and to suggest a method of substituting for permeability to make it correspond to

the normal permeability for the tangential surface field strength.
Carter considered only the fundamental of the ripple and put
$\mu_r = 1000$. The slot-ripple waveform is smooth with no secondary
peaks to form incremental loops. Gibbs made an allowance for
the difference between the peak of the ripple and its fundamental
amplitude in the substitution for μ_r by increasing the applied flux
density by the loss factor $\beta_2 = \sqrt{\sum_{n=1}^{\infty} (b_n^2 / \sqrt{n})}$, where b_n is the
amplitude of the n'th applied flux density harmonic as a fraction
of the mean flux density, resulting in a lower value of μ_r. No
justification was given for this step, and it is difficult to see
one.

Both Gibbs and Carter suggested calculating hysteresis loss
by Ball's formula for parallel superposed fields[41], because of the
biasing effect of the main field. Apart from the fact that Ball's
formula was known in 1915 to be valid only at alternating flux
densities much lower than those existing in the rotor surface
(chapter 3, sections 3.2.2 and 3.2.3.6), neither author explained
why the travelling and steady fields were parallel in the iron,
nor did they suggest using an incremental permeability. Gibbs,
however, said in the discussion of his paper that the fields were
perpendicular, and because of this he had used normal permeability
rather than incremental permeability (which he had found to give
incorrect results) presumably having no values of permeability for
superposed perpendicular fields.

Weak eddy-current reaction was assumed by both authors in
the derivation of their final formulae, which encouraged the use of
a high value of μ_r to get agreement with test results. Lawrenson
et al (1966)[125] recommended the inclusion of the eddy-current
reaction, saying that the permeability is often considerably less
than 1000, as incremental permeabilities are the ones to be
considered. This seems to indicate a preference for parallel
travelling and steady fields in the iron, although this was not

discussed, and neither did they indicate how one should choose a value of μ_r in a particular example.

The problem of the superposed steady field was recognised to some extent by Greig et al. (1971)[136] and earlier workers[134,135] at King's College in their work on slot-ripple losses in laminated poles. The values of permeability used, however, were not related to the conditions of magnetisation in their tests. For each material, the same value of μ_r was used (210 or 275) regardless of the steady or alternating field amplitudes, the values being measured by Sathirakul[134] with parallel fields for a bias of 0.8 T and for very small values of alternating flux density ($\simeq$ 0.02 T). At the same time Sathirakul measured the fundamental component of tooth-ripple flux density to be 0.35 T in a test with a main flux density of 0.8 T, and later Freeman[135] calculated that the tangential flux density could be much larger than this in thick laminations with the resultant travelling field nearly perpendicular to the main field.

Greig et al. thought that the exact value of permeability would not be important, because the loss is a function of $\sqrt{\mu_r}$. It can be seen from appendix 8.4, fig. 8.8 , however, that there may be a factor of 10 difference between the values of permeability for parallel and perpendicular superposed fields at low values of alternating field strength, leading to an uncertainty factor of 3 in the loss. At high values of alternating field strength the permeability decreases as both the steady and alternating fields increase, and an increase of steady flux density by a factor of 5 (e.g. from 0.2 to 1.0 T as in the tests of Greig et al.), causing at least a corresponding increase in the alternating field strength, decreases the permeability by about the same factor, leading to a possible uncertainty factor of about 2 in the loss. In fact, Beevers[137] measured a larger change than this in the percentage reduction of applied flux density with solid poles, a quantity

which is also a function of $\sqrt{\mu_r}$ (at the most, see K_B in fig. 6.2).

Possible differences between the no-load slot ripple loss and the loss on load, for example due to the effect of the armature reaction on the main flux density, the interaction between the winding slot harmonics and the slot-ripple harmonics, and the parallel varying bias of the low-order winding harmonics and the negative-sequence wave, were not discussed in any of the above papers on slot-ripple loss.

6.5. Conclusion

When the skin effect is strong ($\frac{1}{\beta^2 d^2} \gg 1$) and the stator permeability is sufficiently high (eqn. 6.28) the linear theory for the travelling-wave problem of fig. 6.1 may be discussed in terms of an eddy-current reaction factor. This is the ratio of the eddy-current field to the total field at the rotor surface (if $\mu_r \gg 1/\tanh\beta g$, as is usually true) and is given by $Q=1/\beta d\mu_r \tanh\beta g$, the factor $1/\tanh\beta g$ giving the effect of the stator iron.

The total pole-face loss in a particular machine tends to be proportional to $\sqrt{\rho\mu_r}$ or $1/\sqrt{\rho\mu_r}$, depending on whether harmonics with a strong or a weak eddy-current reaction dominate, this being well known[112]. For the winding and slot-ripple harmonics in typical large machines the eddy current reaction is unlikely to be either very strong or very weak. In salient-pole machines the losses of the slot-ripple and winding slot harmonics are likely to be larger than those of the low-order harmonics, and the total loss is likely to decrease as $\sqrt{\rho\mu_r}$ increases, the decrease being significant considering the uncertainty surrounding μ_r. On the other hand, in turbo-generators a few low-order phase-band harmonics will probably have the larger loss and the total winding-harmonic loss is likely to be almost independent of $\sqrt{\rho\mu_r}$, but when a normal amount of negative-sequence loss is included in these machines there may be a significant increase in total loss as $\sqrt{\rho\mu_r}$ increases.

The tangential component of the travelling fields inside the rotor iron, long recognised as the more important component for normal smooth solid pole machines, is very likely to be beyond the knee of the normal magnetisation curve for those harmonics which cause significant loss. Alternating field strength amplitudes up to about 10000 A/m are not impossible, especially when the resultants of pairs of harmonics which induce currents of the same frequency in the rotor are considered, and the amplitudes of

typical slot-ripple or negative-sequence waves may exceed those
of the winding harmonics. It is therefore possible for the
behaviour to be highly non-linear.

The problem of superposition in a smooth rotor is one of
parallel fields varying in time and space (the winding, slot-ripple
and negative-sequence waves) with a perpendicular steady field
varying in space (the main field) and the problem has not yet been
satisfactorily tackled. The total variation with time of the
parallel fields may not be the same at all points around the rotor
periphery, because of the interaction between pairs of winding
harmonics, the variation of the slot ripple with the main field
and its interaction with the winding slot harmonics, and the effect
of the main field on the magnetic characteristics of the iron,
although not all these may be present in every machine. The effects
of the main field are to reduce the permeability and to make the
behaviour more linear, but as a large value of the main flux density
is needed for the effects to be significant, under normal load
conditions there will be large regions where the behaviour is
non-linear.

In such regions there will be the problem of calculating the
loss of a rapidly-varying field with a time-varying parallel bias,
and that of calculating the loss caused by the varying bias. The
bias may be the negative-sequence wave or, if this is absent or
small, some low-order winding harmonics, with slot-ripple and
higher-order winding harmonics forming the rapidly-varying field.
The effects of the winding factor, air gap and eddy-current reaction
may reduce many of the higher harmonics in some machines
(e.g. turbo-generators), so that only a few harmonics need to be
considered. The formation of secondary peaks in the total
waveform, and the consequent incremental magnetisation, will
depend on the relative frequencies, magnitudes and phase shifts of
the component waves, although in machines where more than one wave

is significant it is certain that such peaks will be formed at some points on the rotor. During a cycle of the bias, the incremental magnetisation may be linear if the bias is larger than the incremental amplitude, and non-linear and unsymmetrical otherwise. At points where incremental loops are not formed, the calculation of the loss of a smoothly distorted sine wave will still be of interest. Because of the large amplitudes of the fields, hysteresis effects are likely to be insignificant in the calculation of eddy-current loss, although in practice there may be a small discontinuity where an incremental loop is just beginning to be formed. It is considerably more difficult to calculate the effects of superposition in a rotor which is not smooth, because the relative directions of the fields are uncertain.

The total pole-face loss may depend on the angle ψ between the rotor and the armature m.m.f., because of the interaction between pairs of winding harmonics. This was known earlier, although it was not realised that the phase-band losses may not all reach a maximum at the peak of the fundamental armature m.m.f. The smooth-rotor linear theory may be applied to calculate the loss as a function of ψ, although its application in practice may be difficult because, apart from the non-linearities, the contribution of the slotted region of a turbo-generator rotor to the loss and the interference between the slot-ripple and winding slot harmonics in a salient-pole machine are not well understood.

7. CONCLUSIONS AND FUTURE WORK

In normal large synchronous machines the fields travelling relative to the rotor which cause a significant loss have a fairly large tangential field strength on the rotor surface, and so it is likely that the superposed steady field will not be strong enough to cause linear behaviour, except in a few regions of the rotor under normal load conditions. The resultant field variations in the rotor caused by the travelling waves may have secondary peaks, especially if a significant negative-sequence or slot-ripple wave is present, and the waveform is likely to be different at different points on the rotor. A study of the eddy-current losses induced in a simple sample of mild steel by various fairly strong non-sinusoidal fields (i.e. superposed parallel alternating fields) representing the waveforms appearing in a machine should be made as a first step towards solving the travelling-wave problem (earlier experiments on non-sinusoidal waveforms were confined to hysteresis losses[46,144,145]).

The superposed main field is mainly perpendicular to the travelling fields in a smooth rotor. Few experiments have been performed to measure the effect on permeability of a superposed perpendicular field of constant flux density, and no measurements or calculations of eddy-current losses have been made. Difficulties were experienced by one author (Dietrich, see section 3.3.3) in determing the transverse flux density inside the iron. A uniform transverse flux density could be achieved by using a cylindrical specimen between the poles of an electromagnet, although this uniform density could be altered by the skin-effect of an alternating longitudinal field during the subsequent study of eddy-current losses. This saturation of the surface skin would be a problem with all the samples mentioned in chapter 3, section 3.3, and could only be avoided with a configuration in which the

transverse flux was forced to go through the skin, e.g. a large plate (or group of plates) between the poles of the electromagnet with the alternating field provided by a C core on the exposed thin side of the plate. Further tests would also be required with travelling waves, especially to study the relation between the wavelength of a wave and the effect of the variation of the steady field around the rotor (although it was implied above that the superposed steady field tends to make the behaviour more linear, this is only true with respect to time at one point on the rotor. As the permeability depends on the amplitude of the steady field, a variation of this field around the rotor makes the behaviour non-linear in space).

It appears that improvements need to be made to the method of calculating the main flux density which neglects saturation (appendix 8.2), although better test results are required. Numerical methods may be employed[146,147], and these have shown that high values of main flux density may be achieved in salient-pole machines when ψ is negative[146] (zero of the fundamental armature m.m.f. leading the d-axis.) (as would also be predicted by the analytical theory) and in the teeth adjacent to the poles in some large turbo-generators under normal load conditions[147], such teeth sometimes being given extra thickness for this reason.

The calculation of the total loss in slotted or salient-pole rotors is complicated by the interference between pairs of winding harmonics which induce the same frequency in the rotor, so that the loss depends on the rotor angle. Even if the linear theory is assumed valid, more work needs to be done on the contribution to the loss of the slotted region in a turbo-generator and on the interaction between the slot-ripple and winding slot harmonics in a salient-pole machine. The effect of the main field and the superposition of waves of different frequencies may also be different in a slotted rotor, because the relative directions of the

fields are not so clearly defined.

Some interesting earlier experimental work by Adderley[7] was with a stationary trunnion-mounted solid 'rotor' and a laminated rotating 'stator'. The machine was designed to accentuate m.m.f.-harmonic losses by having a small air gap and high winding factors (table 6.1) and some thought may be given as to how it might be used in future. The choice of an armature winding with only 1 slot per pole and phase resulted in all the m.m.f. harmonics being slot harmonics (for which $\left|k_{wn}\right| = k_{w1} = 1$) with a maximum resultant at the zero of the fundamental m.m.f. and having no secondary peaks at any point on the rotor (chapter 2, fig. 2.8 and Adderley, fig. 7.5). The winding-harmonic waveforms were therefore not typical of normal machines. In addition, the slot ripple was strong, of the same frequency as the m.m.f. harmonics, and sinusoidally modulated by the fundamental armature m.m.f. (there being no field winding) producing the equivalent of pairs of harmonics rotating in opposite directions with wavelengths equal to those of the m.m.f. harmonics. The machine could therefore be used for a study of the superposition of slot ripple and winding slot harmonics, with the disadvantages that the sources of the two types of wave could not be varied independently in either magnitude or position. Adderley concentrated on separating the slot-ripple and winding harmonics, with some success, but did not compare measured and calculated search coil waveforms. Simple measurements of the electric field strength on the 'rotor' surface could be made with a search wire returned around the core, in which the total induced voltage would be $V = \sum_n \dot{E}_n L = \sum_n (v\dot{B}_{yo}) L$. The radial flux density $\dot{B}_{yo}$ could be calculated for each m.m.f. and slot-ripple harmonic using the theory outlined in chapter 6 (together with Adderley's analysis of the slot-ripple applied flux density) and the summation of $\dot{E}$ formed for several points on the 'rotor'.

Measurements of total losses in the experimental

machine were made by Adderley, and the magnitude of these agreed with theory to within about 20%, although different methods were used for the slot-ripple and m.m.f. harmonic losses (eddy-current reaction being neglected in the slot-ripple calculations) and each of these loss components formed about 1/3 of the total. Any slight miscalculation of one component would severely upset the observed variations of the other with changes of current, resistivity or frequency, and indeed the variation of m.m.f. harmonic loss (after subtraction of the calculated slot-ripple and armature losses) showed a steep decrease with increase of resistivity ($P \propto \rho^{-0.75}$) where the maximum possible rate of decrease according to the linear theory is $P \propto \rho^{-0.5}$ when the eddy current reaction is weak. The eddy current reaction should be strong in this machine, however, because of the small air gap to pole pitch ratio. (It may be shown for the 5th harmonic and $\mu_r = 100$, that $Q \simeq 7.0$) Future work could include a calculation of both types of 'rotor' surface loss by the same method, although it is felt that the results may not be applicable to other machines because of the different waveforms and main field distributions. Work should first concentrate on configurations in which some separate control may be exercised over the harmonics and the main field. The model machine could be modified in this regard by enlarging the air gap and inserting two air gap windings of pole pitch $\tau_1/5$ and $\tau_1/7$ for example, the windings and armature to remain stationary. By exciting the original winding with d.c. and the two extra windings with a.c., various combinations of travelling and steady fields could be produced. It may also be possible to arrange for changes to be made to the pole pitches of the air gap windings.

Such experiments should be complemented, however, by work on the losses of superposed parallel alternating fields and by further studies of the loss caused by a single travelling wave. It would be useful, for example, to perform some measurements which

would indicate the magnitude of the tangential magnetic field

inside the solid rotor, on which much of the above argument is

based (such measurements would have to be performed on a rotor of

sufficient length to avoid end effects, and are much more difficult

than measurements of the radial magnetic field or axial electric

field). Once a suitable theory is established for a single wave,

work on superposed waves could proceed with more confidence.

8. APPENDICES

8.1 Appendix 1: Slot-width factor

If it is assumed that the m.m.f. increases linearly with distance over the slot width s, it may bé shown[120] that the slot-width factor of the n'th harmonic is given by

$$k_{sn} = \frac{\sin\left(\frac{ns}{2}\right)}{\frac{ns}{2}} \tag{8.1}$$

where s is in electrical radians. This is equivalent to a distribution factor for an infinitely distributed winding over a width s.

For a 60°-spread integral-slot winding with q slots per pole and phase, the slot pitch is $\lambda_s = \frac{\pi}{3q}$ elec rad giving

$$k_{sn} = \frac{\sin x}{x} \qquad \text{where} \qquad x = \pi \frac{n}{6q} \frac{s}{\lambda_s} \tag{8.2}$$

Thus, as shown by Adderley[7], k_{sn} may be plotted as a function of n/q for several values of s/λ_s (fig. 8.1), showing that it remains positive over the practical range and may cause significant reduction in the amplitude of the higher harmonics.
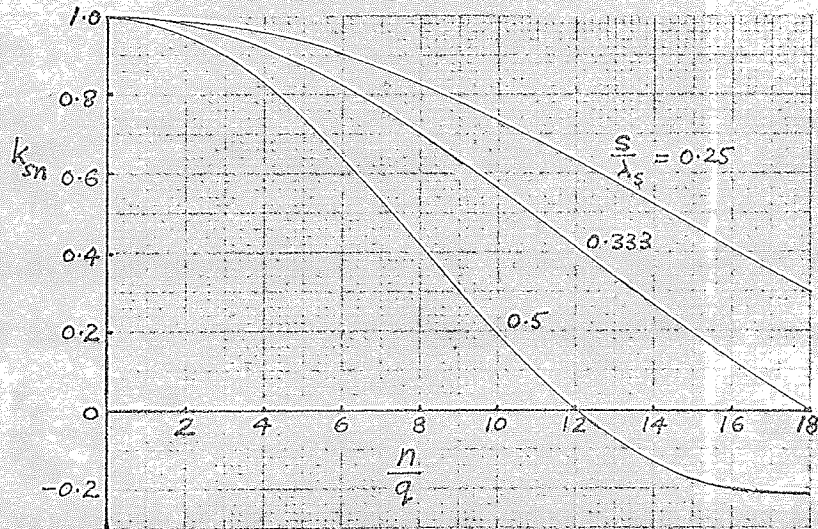

Fig. 8.1 Slot-width factor for 60°-spread, integral-slot winding ($n/q \simeq 6$ for 1st slot harmonics)

8.2 Appendix 2: Main flux density

8.2.1 Theory

In this section an expression is derived for the main flux density in the air gap, based on the resultant of those m.m.f.s which are stationary relative to the rotor, i.e. the fundamental armature m.m.f. and the total rotor m.m.f. It is similar to an expression derived by Pollard[13] in terms of direct and quadrature axis components. It assumes that saturation is small so that the whole m.m.f. is impressed on the air gap; and that the fundamental wavelength is large compared with the air gap so that the permeance of the gap is the same for both m.m.f.s.

If one per-unit m.m.f. is that peak value of the rotor m.m.f., $\hat{F}_{fo}$, which would produce the terminal voltage V on no load, then the per-unit peak fundamental armature m.m.f. is given by[138,139]

$$\frac{\hat{F}_{a1}}{\hat{F}_{fo}} = \frac{I\,X_{ad}}{V\,C_m} \tag{8.3}$$

where X_{ad} is the direct axis magnetising reactance and C_m is the ratio of the field m.m.f. to the armature m.m.f. (when this is in the d axis) for the same fundamental flux density. The variation of the fundamental armature m.m.f. relative to the rotor (fig. 2.10) is therefore

$$\frac{F_{a1}}{\hat{F}_{fo}} = \frac{I\,X_{ad}}{V\,C_m} \cos\left(\vartheta_3 + 90° + \psi\right) \tag{8.4}$$

The rotor m.m.f. is proportional to the voltage induced by the rotor field alone, so the per-unit peak rotor m.m.f. is given by

$$\frac{\hat{F}_f}{\hat{F}_{fo}} = \frac{E_f}{V} \tag{8.5}$$

and if the variation of the rotor m.m.f. around the rotor is represented by a function $f(\vartheta_3)$ then the per-unit rotor m.m.f. is

$$\frac{F_f}{\hat{F}_{fo}} = \frac{E_f}{V} f(\vartheta_3) \tag{8.6}$$

The total air-gap m.m.f. may be obtained by summing eqns.

8.4 and 8.6 to give

$$\frac{F}{F_{fo}} = \frac{E_f}{V} f(\vartheta_3) + \frac{I\,X_{ad}}{V\,C_m} \cos(\vartheta_3 + 90° + \psi) \qquad (8.7)$$

The main flux density distribution is then obtained from eqn. 8.7 and some known field form, for example the no load field, giving

$$B = F\,\frac{B_{fo}}{F_{fo}} = B_{fo}\,\frac{\hat{F}_{fo}}{F_{fo}}\left[\frac{E_f}{V} f(\vartheta_3) + \frac{I\,X_{ad}}{V\,C_m} \cos(\vartheta_3 + 90° + \psi)\right](8.8)$$

where B_{fo} is the no-load flux density caused by F_{fo} at the point ϑ_3.

This equation may be applied to a salient-pole machine of pole arc α electrical degrees, with the convention that the no-load flux density is positive over the pole at whose centre line $\vartheta_3 = 0$, using $f(\vartheta_3) = 1$ and $F_{fo} = \hat{F}_{fo}$ over this pole, so that

$$B = B_{fo}\left[\frac{E_f}{V} + \frac{I\,X_{ad}}{V\,C_m} \cos(\vartheta_3 + 90° + \psi)\right] \quad \text{for} \quad -\frac{\alpha}{2} < \vartheta_3 < \frac{\alpha}{2} \quad (8.9)$$

The expression for B over the adjacent pole $(180° - \frac{\alpha}{2} < \vartheta_3 < 180° + \frac{\alpha}{2})$ is the reverse of this (see fig. 2.10), as may be shown by putting in eqn. 8.8 $f(\vartheta_3) = -1$, $F_{fo} = -\hat{F}_{fo}$ and B_{fo} negative.

8.2.2 Experimental check

Ginsberg and Jokl[140] gave some test results for a 30kW salient-pole machine which enable some check to be made on eqn. 8.9. Unfortunately they did not give absolute scales for the flux density waveforms, so the exact level of saturation is not known. The assumption of a large pole pitch to air gap ratio is satisfactory, however, as may be seen from the machine data given by the authors, reproduced in table 8.1.

The no-load field form was given in fig. 3 of the paper, from which $B_{fo}/\hat{B}_{fo}$ can be obtained, where $\hat{B}_{fo}$ is the peak no-load flux density. This ratio is equal to 1 over most of the pole face $(-52° < \vartheta_3 < 52°)$ and drops to 0.8 at the pole tips $(\vartheta_3 = \pm 56°)$. From table V of the paper it may be deduced that the rated power factor of the machine is 0.8 lagging, so that at unity power factor

with rated voltage and rated output power, the current is 0.8 p.u.

Using eqns. 2.18 and 2.20 to calculate ψ and $\dfrac{E_f}{V}$, the following

expressions are obtained from eqn. 8.9 for the flux density over the

pole face $(-56° < \vartheta_3 < 56°)$ at rated voltage and rated output power:

Unity power factor ($\psi = 34.2°$):

$$\frac{B}{\bar{B}_{fo}} = \frac{B_{fo}}{\bar{B}_{fo}} \left[1.65 + 1.62 \cos (\vartheta_3 + 90° + 34.2°) \right] \qquad (8.10)$$

0.8 lagging power factor ($\psi = 61.1°$):

$$\frac{B}{\bar{B}_{fo}} = \frac{B_{fo}}{\bar{B}_{fo}} \left[2.49 + 2.02 \cos (\vartheta_3 + 90° + 61.1°) \right] \qquad (8.11)$$

Using the aforementioned values of $\dfrac{B_{fo}}{\bar{B}_{fo}}$, these expressions have

been plotted as dotted lines in fig. 8.2.

The full curves shown in fig. 8.2 are the field forms

measured with a stator-search coil, suitably scaled to agree with

the calculated curves at the pole centre (as no scales were given).

Also, the position of the measured curves relative to the pole

had to be deduced from the sharp drop of flux density at the pole

tips.

The comparison between the calculated and measured curves

shows that the theory seems to be only approximately correct. Large

discrepancies occur on the trailing pole edges where the calculated

load flux density rises to about twice the no-load flux density.

Saturation of the stator teeth and rotor pole would obviously reduce

this flux density closer to the measured value, but it is hard to

see how the large reduction required can be obtained if the machine

is a normal one with $\hat{B}_{fo} \simeq 1$ T. The smaller discrepancies which

occur on the leading pole edges would also be reduced by taking

saturation into account, as saturation reduces the angle ψ,

advancing the armature m.m.f. relative to the pole. The odd dips

which occur in the measured curves can be attributed to harmonic

armature currents, as the dips occur at 5th harmonic frequency and

harmonic currents were allowed to flow in the tests. The dips do

not then represent actual dips in the main flux density
as the fields of such currents rotate relative to the rotor.

TABLE 8.1   Ginsberg and Jokl generator no. 4 data

Rating (kW)	30	X_d	1.82
Frequency (Hz)	60	X_q	0.85
No. phases	3	X_{ad}	1.76
No. poles	4	C_m	0.87
Pole arc (elec deg)	112	Coils per group	5
Ratio $\dfrac{\text{max. air gap}}{\text{min. air gap}}$	1	% pitch	66.7
Ratio $\dfrac{\text{pole pitch}}{\text{max. air gap}}$	134	% pitch of search coil	100

8.3   Appendix 3: Feedback circuits

Two feedback circuits have been used[50,105,141] for obtaining

sinusoidal flux, and they can also be used for sinusoidal current,

as shown below. Waveforms other than sinusoidal can also be

obtained, and it was one of these circuits which was used for a

square waveform of $\frac{d\phi}{dt}$ in the uniformly-varying method of chapter 4

(section 4.3.1.2).

8.3.1   Steady-state analysis

The two circuits can be reduced to the form shown in fig. 8.3.

(a)   (b)
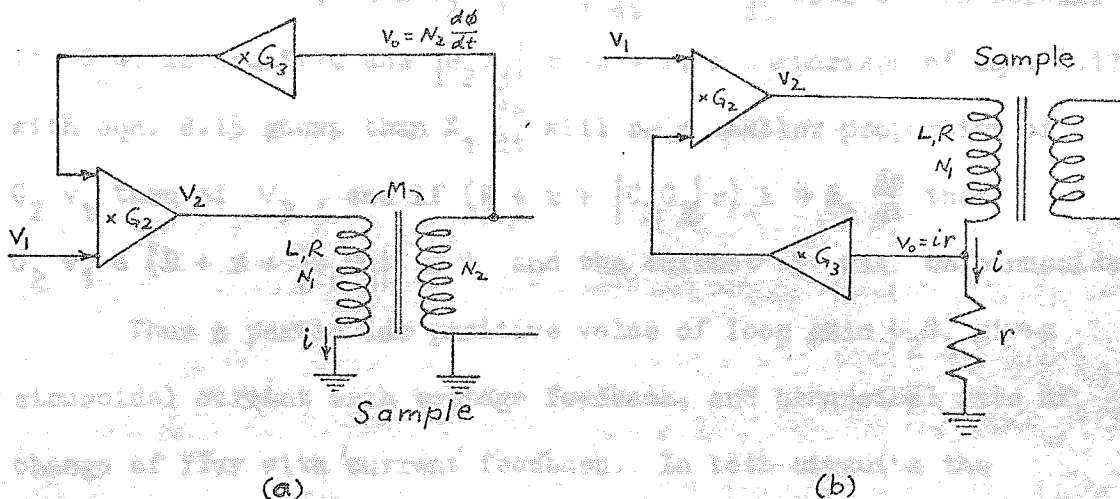
Fig. 8.3 Feedback circuits for magnetisation of an iron sample
   (a) Voltage feedback
   (b) 'Current' feedback

The voltage feedback circuit (fig. 8.3 (a)) may be used to

obtain sinusoidal flux or current as explained below, where the

input v_1 is assumed to be sinusoidal. Two equations for v_2 are

$$v_2 = Ri + N_1 \frac{d\phi}{dt} \qquad\qquad (8.12)$$

$$v_2 = G_2 \left(v_1 + G_3 N_2 \frac{d\phi}{dt} \right) \qquad (8.13)$$

Eliminating v_2 and rearranging gives

$$G_2 v_1 = Ri + (N_1 - G_2 G_3 N_2) \frac{d\phi}{dt} \qquad (8.14)$$

Therefore if $G_2 G_3 N_2 = N_1$, then $G_2 v_1 = Ri$ and the current i will

be sinusoidal. On the other hand, if $G_2 G_3$ is negative and

$|G_2 G_3| N_2 \gg N_1$, a comparison of eqn. 8.14 with eqn. 8.12 shows that

Ri will be a smaller proportion of $G_2 v_1$ than of v_2 , and if

$(N_1 + |G_2G_3| N_2) \frac{d\phi}{dt} \gg Ri$, then $G_2 v_1 = (N_1 + |G_2G_3| N_2) \frac{d\phi}{dt}$ and $\frac{d\phi}{dt}$ will be sinusoidal.

The analysis of the 'current' feedback circuit (fig. 8.3 (b)) follows similar lines. The two equations for v_2 are

$$v_2 = (R + r) i + N_1 \frac{d\phi}{dt} \left.\vphantom{\begin{matrix}a\\b\end{matrix}}\right\} \qquad (8.15)$$

$$v_2 = G_2 (v_1 + G_3 ri) \qquad (8.16)$$

which give

$$G_2 v_1 = (R + r - G_2G_3 r) i + N_1 \frac{d\phi}{dt} \qquad (8.17)$$

If $G_2G_3 r = R + r$, then $G_2 v_1 = N_1 \frac{d\phi}{dt}$ and $\frac{d\phi}{dt}$ will be sinusoidal. If G_2G_3 is negative and $|G_2G_3| r \gg R + r$, a comparison of eqn. 8.17 with eqn. 8.15 shows than $N_1 \frac{d\phi}{dt}$ will be a smaller proportion of $G_2 v_1$ than of v_2, and if $(R + r + |G_2G_3| r) i \gg N_1 \frac{d\phi}{dt}$ then $G_2 v_1 = (R + r + |G_2G_3| r) i$ and the current i will be sinusoidal.

Thus a particular positive value of loop gain G_2G_3 gives sinusoidal current with voltage feedback, and sinusoidal rate of change of flux with 'current' feedback. In both circuits the required gain can be made low (N_1/N_2 and $(R+r)/r$ respectively).

On the other hand, a large negative loop gain gives the opposite effects, i.e. a sinusoidal rate of change of flux with voltage feedback and sinusoidal current with 'current' feedback.

If v_1 has some waveform other than sinusoidal, the same conclusions apply with this waveform replacing the sinusoidal one.

8.3.2 Transient analysis

The circuits of fig. 8.3 are shown in block diagram transfer function form in fig. 8.4.

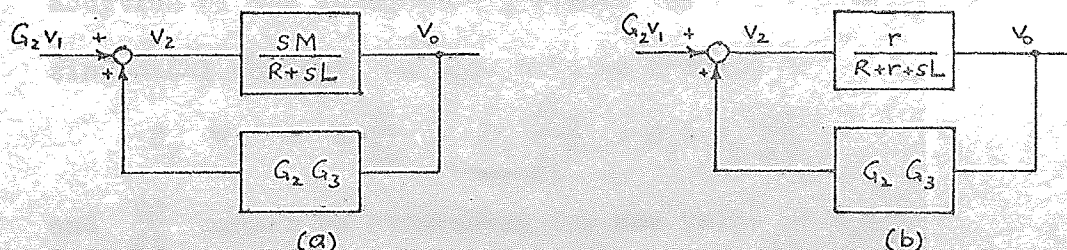(a)   (b)

Fig. 8.4 Feedback circuits in block form
   (a) Voltage feedback
   (b) 'Current' feedback

The transfer function for the voltage feedback circuit is

$$\frac{V_o}{V_1} = \frac{sM/(R+sL)}{1 - sMG_2G_3/(R+sL)} = \frac{s\,M/(L-MG_2G_3)}{s + R/(L-MG_2G_3)} \qquad (8.18)$$

which has a pole at $s = -R/(L-MG_2G_3)$. If G_2G_3 is negative and $|G_2G_3|$ is large, as required for sinusoidal $\frac{d\varnothing}{dt}$, the pole will be close to the origin and instability will be likely. If $G_2G_3 = N_1/N_2 = L/M$, as required for sinusoidal current, the pole will be at $\pm\infty$, instability being likely if G_2G_3 exceeds N_1/N_2 by a small amount.

The transfer function for the 'current' feedback circuit is

$$\frac{V_o}{V_1} = \frac{r/(R+r+sL)}{1 - rG_2G_3/(R+r+sL)} = \frac{r/L}{s + (R+r-rG_2G_3)/L} \qquad (8.19)$$

which has a pole at $s = -(R+r-rG_2G_3)/L$. If G_2G_3 is negative and $|G_2G_3|$ is large, as required for sinusoidal current, the pole will be far from the origin in the negative half plane and the circuit will be stable. If $G_2G_3 = (R+r)/r$, as required for sinusoidal voltage, the pole will be at the origin and instability will be likely if G_2G_3 exceeds $(R+r)/r$ by a small amount.

The voltage feedback circuit may be made more stable for sinusoidal $\frac{d\varnothing}{dt}$ by adding an integrator (transfer function $\frac{1}{s}$) to the forward path. Then eqn. 8.18 becomes

$$\frac{V_o}{V_1} = \frac{M/L}{s + (R - MG_2G_3)/L} \qquad (8.20)$$

and the pole is moved to $s = -(R - MG_2G_3)/L$, which is far away from the origin if G_2G_3 is negative and $|G_2G_3|$ is large. The addition of the integrator prevents the circuit being used for sinusoidal current, as eqn. 8.14 is changed to

$$G_2\,V_1 = R\frac{di}{dt} + N_1\frac{d^2\varnothing}{dt^2} - G_2G_3N_2\frac{d\varnothing}{dt}$$

and $\frac{d\varnothing}{dt}$ cannot be eliminated for any value of $G_2G_3N_2$.

Instability problems with the voltage feedback circuit for a high negative loop gain were encountered by MacFarlane and

Harris[105]. These were overcome with an integrator in the forward path by Warner[103] and by Mazzetti and Soardo[102], but no analysis was given. Instability problems with the 'current' feedback circuit for sinusoidal voltage (with fixed positive loop gain) were not mentioned by Harris and Cooter[141] nor by Choudhury et al.[50]. The circuits they actually used contained extra components, however, such as d.c. blocking capacitors and isolating transformers, and a complete analysis of these final circuits would be needed to see how stability was achieved and to determine the stable region.

8.4 Appendix 4: Superposed perpendicular fields

The known effects of a superposed perpendicular steady field on the normal magnetisation curve for an alternating field were described in chapter 3, section 3.3, and the experiments of Sugiura[35] were the most extensive. Some calculated curves for EN1A mild steel, using the method suggested by Sugiura, are given in this section, and it can be seen from fig. 3.40 in chapter 3 that such curves give a fairly good idea of the effect of the perpendicular field.

As mentioned in chapter 3, the method is based on the normal magnetisation curve (with no superposed field) and neglects hysteresis. With a given steady perpendicular field H_t and given longitudinal alternating field of peak amplitude H_{lm}, the resultant field strength at the instant when H_l is a maximum is calculated from

$$H = \sqrt{H_t^2 + H_{lm}^2} \qquad (8.21)$$

The value of B corresponding to this value of H is then read from the normal magnetisation curve and resolved to give the peak alternating flux density in the longitudinal direction

$$B_{lm} = B \cdot \frac{H_{lm}}{H} \qquad (8.22)$$

The curves of B_{lm} against H_{lm} for several values of the perpendicular field H_t are given in fig. 8.5, based on the normal magnetisation curve for EN1A steel given in chapter 4, fig. 4.7. Values of relative permeability $\mu_\perp$ calculated from these curves are plotted in fig. 8.6, where

$$\mu_\perp = \frac{B_{lm}}{\mu_o H_{lm}} \qquad (8.23)$$

The curves show that $\mu_\perp$ is greater than the normal permeability for low values of the alternating and transverse fields, and less than the normal permeability for high values of the fields. As the amplitude of the alternating field increases for a fixed value of transverse field, $\mu_\perp$ remains equal to the reversible permeability

for that value of H_t , until H_{lm} begins to exceed H_t when $\mu_\perp$ tends to the normal value. For high values of H_t , however, the magnetisation curve is more linear than the normal curve. In addition, Sugiura's measurements show that the magnetisation curve with a high value of H_t is a better representation of the corresponding hysteresis loops than is the case with no superposed perpendicular field. (This may be seen by comparing the loops in fig. 3.41 with the magnetisation curves in fig. 3.40)

A curve showing the permeability with a parallel superposed field of 5000 A/m (from fig. 4.17) is also plotted in fig. 8.6, showing that a parallel steady field may reduce the permeability much more than a perpendicular steady field.

The permeability with a given fixed value of perpendicular flux density is also of interest, as explained in chapter 6, section 6.4.1. For a fixed transverse field strength, the transverse flux density B_t varies during a cycle of the longitudinal field, as discussed in chapter 3, section 3.5.2, the variation with time depending on the magnetic properties of the iron, the strength of the transverse field and the amplitude and waveform of the alternating longitudinal field. The value of B_t at the instant when the longitudinal field is at its maximum may, however, be easily obtained by resolving the resultant flux density at that time

$$B_t = B \cdot \frac{H_t}{H}$$

where B has the same value as in eqn. 8.22. The curves of B_t against H_t for fixed values of H_{lm} are therefore the same as the curves of B_{lm} against H_{lm} for fixed values of H_t, and this is shown by the labels in brackets in fig. 8.5.

If the transverse flux density is fixed, the transverse field strength will vary during a cycle of the longitudinal field, but at the instant when the longitudinal field is a maximum the resultant and transverse fields will be the same as if the

transverse field strength were fixed, for the same values of H_{1m} and B_t (hysteresis being neglected). Therefore a value of B_t may be calculated for each value of $\mu_\perp$ plotted in fig. 8.6, and curves of $\mu_\perp$ plotted against B_t for several values of H_{1m}, as shown in fig. 8.7. For values of H_{1m} below the knee of the normal magnetisation curve, the permeability $\mu_\perp$ increases at first as B_t increases (as found by Gans, fig. 3.39) and decreases again when B_t exceeds about 0.6 T. For larger values of H_{1m}, $\mu_\perp$ decreases slowly as B_t increases, until B_t exceeds about 1.0 T when the decrease is more significant.

A cross-plot of the curves in fig. 8.7 is given in fig. 8.8, showing the variation of $\mu_\perp$ with H_{1m} for several fixed values of B_t. For small values of H_{1m} it can be seen that $\mu_\perp$ varies less with H_{1m} than the normal permeability, the value of $\mu_\perp$ being equal to the reversible permeability for the particular value of B_t, but that for values of H_{1m} beyond the knee of the normal magnetisation curve, $\mu_\perp$ decreases as H_{1m} increases, at about the same rate as the normal permeability, unless B_t is larger than about 1.0 T, when the decrease of $\mu_\perp$ is at first not so rapid. The magnetisation curve for a fixed value of B_t is therefore only more linear than the normal magnetisation curve for large values of H_{1m} if the value of B_t is high.

Some curves of the permeability with a parallel superposed field of fixed flux density (from fig. 4.19) are also plotted in fig. 8.8, showing that the permeability is reduced more by the parallel field, but that the magnetisation curves with a perpendicular field may be more linear for the lower values of steady flux density.

Some previous expressions for the loss of one winding harmonic

8.5.1 Introduction

It was pointed out by Greig et al.[137] that the methods of Kuyper[120], Barello[121], Postnikov[123] and Bratoljic[9] for calculating the loss of one winding harmonic are essentially the same, although this was not noted by Adderley[7]. The expressions developed by these authors are discussed so that the similarities may be seen, and it is shown that there is a factor of 4 error in Barello's formula. The work of Davies[129,130] is also discussed, as his approach is different from that of the other authors, and as the results were applied by Adderley to the calculation of winding-harmonic losses.

8.5.2 Kuyper (1943)[120]

Kuyper extended the work of earlier authors to include the effect of the stator at any distance from the rotor. His analysis followed the method used by Concordia and Poritsky (1937)[119], who were concerned with the transient behaviour of solid rotor machines, which has become the standard linear theory described in chapter 6. He obtained expressions for the electric and magnetic field strengths in the air gap and rotor, and, using the electric field strength E_z on the stator surface where the current sheet was placed, calculated the impedance $Z = -\dfrac{E_z}{K}$ met by the current. Since there was no loss in the stator ($\rho = \infty$) the rotor loss per unit area was calculated from $P = \frac{1}{2} \hat{K}^2 \, \mathrm{Re}(Z)$. He next defined a dimensionless factor R given by

$$R = \frac{P}{\frac{1}{2} \hat{K} \mu_o \lambda f} = \frac{\mathrm{Re}(Z)}{\mu_o \lambda f} = \frac{q_i \, (1 - \tanh^2 \beta g)}{(\tanh \beta g + q_r)^2 + q_i^2} \qquad (8.24)$$

where $q_r = \mathrm{Re}(\frac{\hat{\gamma}}{\mu_r})$, $q_i = \mathrm{Im}(\frac{\hat{\gamma}}{\mu_r})$, $\hat{\gamma}$ being given by eqn. 6.19, so that the loss was given by

$$P = \frac{1}{2} \hat{K}^2 \mu_o \lambda f R \qquad (8.25)$$

for all values of the parameters. If μ_r was relatively large,

however, he found that $q_r = q_i$ very often, enabling curves of R to be drawn against q_r for fixed values of g/λ . The equality $q_r = q_i$ is equivalent to the assumption of strong skin effect $(\frac{1}{\beta^2 d^2} \gg 1)$, as shown in eqn. 6.30. Therefore, in the symbols of this thesis,

$$q_r = q_i = \frac{1}{\sqrt{2}\beta d\mu_r} \qquad \text{if} \quad \frac{1}{\beta^2 d^2} \gg 1 \qquad (8.26)$$

and so, by substituting this in eqn. 8.24, or by comparing eqn. 8.25 with eqn. 6.59,

$$R = \frac{K_p}{\sqrt{2}\ \cosh\beta g\ \sinh\beta g} \qquad (8.27)$$

The velocity $v = f\lambda$ is very nearly the same for all the winding harmonics, so eqn. 8.25 shows that R gives the variation of the loss with g, λ , ρ and μ_r. In his fig. 2 , Kuyper plotted curves of R against the dimensionless parameter $q_r = \frac{1}{\sqrt{2}\beta d\mu_r} = \sqrt{\frac{\mu_o}{4\pi}\frac{v\lambda}{\rho\mu_r}}$ (mksA units, cgs units being used by Kuyper) for fixed values of g/λ . It may be shown that these have maxima where $1/\beta d\mu_r \tanh\beta g = 1$, in agreement with fig. 6.2, and that the maximum values of R are given by

$$R_{max} = \frac{1}{(2+\sqrt{2})\ \sqrt{2}\ \cosh\beta g\ \sinh\beta g} \qquad (8.28)$$

as they should be, since the maximum value of K_p is $\frac{1}{2+\sqrt{2}} = 0.292$. In his fig. 3, Kuyper plotted R_{max} against $\frac{1}{2}\beta g$, and recommended that the maximum values of R should be used in calculating the winding-harmonic loss of normal turbo-generators, and it is evident from fig. 6.5 that the loss for each significant harmonic is likely to be near the maximum for such machines.

Kuyper's final formula for the loss (his eqn. 24) is in terms of m.m.f., rather than current loading, and inch units were introduced to give the formula a neat form. Strictly it should be multiplied by 1.02, but apart from this it is correct.

Kuyper was also concerned with the tangential magnetic field strength on the rotor surface as a guide to the choice of a value of rotor permeability, and he gave curves of a factor

$S = \left|\dot{H}_{xo}\right|/\hat{K}$, which is equivalent to $K_H/\cosh\beta g$ (eqns. 6.44 and 6.43). Allowing for the different units, and the omission of a square root sign in the denominator of his eqn. (26),

$$S = 0.4\pi K_H \quad \text{if} \quad \frac{1}{\beta^2 d^2} \gg 1 \tag{8.29}$$

8.5.3 Barello (1947,1955)[121,122]

Barello, like the later authors, Postnikov and Bratoljic, does not appear to have been aware of Kuyper's work. He published two papers, one in Italy (1947) and one in France (1955). In the first he derived an expression for the loss, assuming strong skin effect, and in the second he added some discussion on the application and meaning of the equations.

As mentioned by Postnikov, Barello made an error. Postnikov did not say where the error lay, but it can be traced to his expression for the m.m.f. of one phase of a polyphase winding, eqn. 8 in the Italian paper:

$$i_a \psi(x_1) = i_a \cdot \sum_{n=1}^{\infty} C_n \cos\left(\frac{n\pi}{\tau_1} \cdot x_1\right) \tag{8.30}$$

where

$$C_n = \frac{4}{\pi} \cdot \frac{1}{n} \cdot N k_{wn} \tag{8.31}$$

He defined N as the number of conductors in series per pole and phase, when it should be the number of turns, half the number of conductors. Barello's equations in terms of the stator m.m.f. are therefore incorrect, the flux density by a factor of 2 and the loss by a factor of 4 (which agrees with Postnikov's example, where the loss calculated by Barello's formula is about 4 times larger than the loss by Postnikov's own formula, when Postnikov's extra factor of 1.4 is removed). Barello's expression for the radial flux density in terms of the stator current loading is correct, in the present symbols being

$$\left|\dot{B}_{yo}\right| = \frac{\mu_o \hat{K}}{\sqrt{\left(\sinh\beta g + \frac{1}{\sqrt{2}\beta d\mu_r}\cosh\beta g\right)^2 + \left(\frac{1}{\sqrt{2}\beta d\mu_r}\cosh\beta g\right)^2}} \tag{8.32}$$

which is equivalent to the expression given by eqns. 6.47 and 6.48.
The loss was calculated from eqn. 6.56. (A second error was made
by Barello, although this does not affect the results. He thought
that $\frac{1}{\beta^4 d^4} \gg 1$, rather than $\frac{1}{\beta^2 d^2} \gg 1$, was necessary for the
assumption of strong skin effect and consequent simplification
of the equations.)

Although Barello gave expressions for the tangential field
strength on the rotor surface, he did not calculate it. As a
guide to a suitable value of rotor permeability, he relied on a
comparison of calculated and measured losses. But his recommended
value of the product $\rho\mu_r \simeq 3 - 4 \times 10^{-4}$ Ωm ($\mu_r \simeq 2000$,
$\rho \simeq 2 \times 10^{-7}$ Ωm) came out on the high side, because of the factor
of 4 error in his formula (fig. 6.5 shows that $\mu_r \simeq 2000$ is
likely to give a calculated loss much less than the maximum,
compensating for the x 4 error).

Barello also discussed the eddy-current reaction, saying
that it was embodied in the $\frac{1}{\sqrt{2}\beta d\mu_r} \cosh\beta g$ terms in eqn. 8.32, and
that by putting these terms equal to zero (e.g. $\rho = \infty$) the applied
flux density could be obtained. This procedure is not strictly
valid because the equation is only valid for $\frac{1}{\beta^2 d^2} \gg 1$, but the
error introduced is normally small as it results in the omission
of the factor K_μ (eqn. 6.49) which is equal to unity for
$\mu_r \tanh\beta g \gg 1$. He noted that the remaining term in the denominator
of eqn. 8.32 when $\rho = \infty$ is $\sinh\beta g$, which allows for air-gap
leakage (eqn. 6.47 may be presented in terms of a leakage factor K_L:

$$\dot{B}_{ym} = j \frac{\mu_o \hat{K}}{\beta g} K_L \qquad\qquad (8.33)$$

where $K_L = \beta g/\sinh\beta g$ is equal to 1 when βg is small, and
$\mu_o \hat{K}/\beta g = \mu_o \hat{F}/g$ is the flux density with no leakage). For the
effect of the eddy-current reaction on the loss, he defined a factor
Δ given by

$$\Delta = \frac{(\sinh\beta g + \frac{1}{\sqrt{2}\beta d\mu_r}\cosh\beta g)^2 + (\frac{1}{\sqrt{2}\beta d\mu_r}\cosh\beta g)^2}{\sinh^2\beta g} \qquad (8.34)$$

so that eqn. 6.48 gives

$$\Delta = \frac{1}{K_B^2} \qquad (8.35)$$

He found that Δ could be as high as 2 for low-order phase-band harmonics, but was usually near 1 for the higher harmonics. These figures would have been higher had Barello used smaller values of $\rho\mu_r$.

8.5.4 Postnikov (1958)[123]

Postnikov is possibly the standard Russian author on the winding-harmonic pole-face loss, as his work was used by Anempodistov et al.[3]. Postnikov's paper begins '.... in one recent work (Barello, 1955) we find an erroneous determination of the induction of the rotor surface due to eddy currents ...... the reasons why the formulae of individual authors lead to widely divergent answers are explained by a different evaluation of the screening effect and variable permeability.' Postnikov knew, however, that the error in Barello's paper was only in the determination of the fundamental m.m.f., because he followed the French paper almost line by line to arrive at eqn. 32 for $|\dot{B}_{yo}|$, identical to Barello's eqn. 32 (eqn. 8.32 in the previous section), even making the same mistake that $\frac{1}{\beta^4 d^4} \gg 1$, rather than $\frac{1}{\beta^2 d^2} \gg 1$, is required for equality of the real and imaginary parts of $\dot{\gamma}$. Postnikov also used the same method as Barello to obtain an expression for the loss, which contained the terms $k_{r\nu}$, $k_{\nu 1}$ and A_1. The terms $k_{r\nu}$ and $k_{\nu 1}$ come from Barello's discussion of the eddy-current reaction and air-gap leakage, $k_{r\nu}$ being equal to $1/\sqrt{\Delta} = K_B$ (eqn. 8.35) and $k_{\nu 1}$ being equal to $\beta g/\sinh\beta g = K_L$ (eqn. 8.33). (The term A_1 was defined by Postnikov in his eqn. 41 as $A_1 = \hat{F}_1\pi/\sqrt{2}\tau_1 k_{w1}$, the symbols on the right hand side having the same meaning as in this thesis, so that A_1 is the r.m.s. value of

the total stator current loading, rather than the effective value
of the fundamental loading as described by Postnikov.)

After giving an expression for the loss of one harmonic,
Postnikov considered the sum of the losses of several harmonics,
for values of parameters such that $k_{r\nu}^2 \simeq k_{\nu 1}^2 \simeq 1$, and for
values such that $k_{r\nu}^2$ is approximately the same for all harmonics.
He appeared to conclude that there is little point in such
approximations, going on to consider rearrangements of the formula
for the loss of one harmonic. He combined $k_{r\nu}$ and $k_{\nu 1}$ to form a
new factor $\phi_{x\nu}$, related to Kuyper's factor R by $\phi_{x\nu} = \beta g R$
(expressing $\phi_{x\nu}$ in terms of $\alpha_{\nu 1}$ $(=\beta g)$ and $x_\nu = \delta_\nu'/\sqrt{\rho'\mu'}$
$(=g/\sqrt{2}d\mu_r)$ where δ_ν' was the ratio of the air gap to the skin
depth in copper). By differentiating $\phi_{x\nu}$ with respect to x_ν
for fixed $\alpha_{\nu 1}$ he showed the maxima occurred when $x_\nu = \alpha_{\nu 1} \tanh\alpha_{\nu 1}/\sqrt{2}$
i.e. when $Q = 1/\beta d\mu_r \tanh\beta g = 1$ in the present symbols, agreeing
with the earlier discussion of R and K_p. For calculating the
loss with small air gap to pole pitch ratios, Postnikov considered
another factor $C_{\mu\nu}'$ more convenient. This is related to K_H by
$C_{\mu\nu}' = \frac{1}{2}(K_H \cosh\beta g)^2$, and tends to 0.5 for small values of βg.
Postnikov's expressions for the loss in terms of $\phi_{x\nu}$ and $C_{\mu\nu}'$ (his
eqns. 48 and 51) were based on the use of c.g.s. units and the
assumption that the skin depth in copper $(\delta_{cu} = \sqrt{2\rho_{cu}/\mu_o\omega_1})$ is
1 cm at the fundamental frequency ω_1 (his eqn. 47). To make the
equations exact and valid in any rationalised units, eqn. 48
should be multiplied by δ_{cu} and eqn. 51 by δ_{cu}^2. (In fact
$\delta_{cu} = 0.9$ cm with Postnikov's values of $\rho_{cu} = 1.6 \times 10^{-8}$ Ωm,
$f_1 = 50$ Hz, so that his equations if used as intended would give
results about 10% (eqn. 48) and 20% (eqn. 51) too high.)

Postnikov suggested that a modification factor of 1.4 be
included in the loss expressions to account for the variation of
permeability with depth in the rotor and for hysteresis loss.
This was based on the work of Nejman[131], who considered the

1-dimensional problem of a semi-infinite slab excited by a known sinusoidal tangential field strength, and showed that, for most ferromagnetic materials used in normal electrical machines when working in the region of strong saturation, the effects of both non-linearity and hysteresis are to increase the loss by a factor of 1.4 beyond the value calculated by the linear theory neglecting hysteresis. Postnikov's suggestion may therefore be appropriate for a machine in which an individual wave is particularly pronounced, the rotor is smooth, the main field is small, and the eddy-current reaction is strong, when the tangential field strength will be sinusoidal and of known amplitude and the magnetisation characteristic of the rotor will be the normal one. He did not dicuss in detail the problem of choosing a value for μ_r, however, merely saying that for approximate calculations a value of $\sqrt{\rho'\mu_r} = 100$ may be taken, implying $\mu_r = 600 - 1000$ for $\rho = 1.5 - 3.0 \times 10^{-7}$ Ωm (ρ' being the resistivity relative to copper), because of the comparatively small field strength of the harmonics and the saturation due to the fundamental field.

This discussion of Postnikov's paper is given in some detail because the paper is rather confusing. The English translation contains several errors, including some pages out of order and a critical sentence missing from the numerical example. Also the naming of the harmonics is different from that used in the West, the phase-band harmonics sometimes being called 'space' harmonics and sometimes 'higher' harmonics, and the winding slot harmonics being called 'ripple' harmonics.

8.5.5 <u>Bratoljić (1966)</u> [9]

While Bratoljić was mainly concerned with the effects of finite length, axial slots and tangential grooves, he also gave a summary of the classical linear theory for smooth rotors. This followed the lines of Barello's work, with the loss being calculated

from eqn. 6.56 (making the correct assumption that $\frac{1}{\beta^2 d^2} \gg 1$ for strong skin effect). He then added something new, for by comparing the expressions for $|\dot{H}_{xo}|$ and P he saw that the loss could be given by eqn. 6.57, reminiscent of the expression for losses in a thick plate with a known sinusoidal tangential magnetic field H_t ($P = \frac{1}{2}\sqrt{\pi\mu_o\mu_r\rho f}\ \hat{H}_t^2$), and he defined a factor $K_H = |\dot{H}_{xo}|/\hat{K}$ (equal to the K_H defined in eqn. 6.44 divided by $\cosh\beta g$) from which $|\dot{H}_{xo}|$ and hence the loss could be found. K_H was plotted against $\frac{\sqrt{2}}{\pi}\beta d\mu_r$ for fixed values of τ/g .

Bratoljić noted that the tangential field was the larger component inside the rotor iron, but did not give any values for this. He did, however, discuss the results of some experiments to determine the effect of saturation on the loss of a single wave. He found that the loss calculated by the linear theory (with μ_r equal to the normal value corresponding to $|\dot{H}_{xo}|$) should be multiplied by a saturation factor between 1.0 and 1.3 for $|\dot{H}_{xo}|$ in the range 0 to 20000 A/m.

8.5.6 Davies (1963, 1966)[129,130]

8.5.6.1 General comments

The theory developed by Davies was an extension of the work of Gibbs[142] and arose from a representation of the normal magnetisation curve in the form $B = aH^b$ around and above the knee. A linear theory was used to develop an equation for the loss in terms of the tangential field strength on the rotor surface (eqn. 6.57 in fact). It was assumed that the skin effect was strong ($\frac{1}{\beta^2 d^2} \gg 1$) so the tangential field was approximately equal to the resultant field inside the rotor (and he mentioned that the resultant H vector follows an ellipse with time). The rotor permeability was then assigned to be the normal value corresponding to the surface tangential field strength by substituting $(\mu_o\mu_r)^{1/4}H = k_1 H^m$ (equivalent to $B = aH^b$) into the loss equation. Expressions for the resultant (i.e. total) m.m.f. and the eddy-

current reaction m.m.f. were then obtained in terms of the loss, so that the loss could be found by equating the phasor difference of these two m.m.f.s to the applied m.m.f., with due allowance for the reluctance of each flux path in the air gap.

These last steps are important, because in principle any shape of stator surface can be allowed for, the only previous assumption about the iron surfaces being that the rotor is smooth. The requirement that μ_r and $|\dot{H}_{xo}|$ should be consistent with the normal permeability curve is of doubtful validity, however, with regard to the experiments of Bratoljić (section 8.5.5) the work of Nejman (mentioned in section 8.5.4) and the paper by Lim and Hammond[143], all of which suggest that the loss will be greater than the linear theory value by a factor K_s between 1.0 and 1.7, depending on the level of saturation. It is possible that such a factor could be included in Davies' theory, but this could not be justified when more than one significant wave is present, because of the superposition effects on the magnetisation curve discussed in chapter 6, section 6.4.

Adderley[7] applied Davies' theory to the calculation of winding-harmonic loss in several industrial machines, and compared the results with those obtained by the classical theory (Kuyper, Barello). Since both theories are linear, any differences must be due to the assignment of the permeability for each harmonic and to the treatment of the air gap. (It is shown below that when these are handled in the same way for both theories the results are in fact the same.) For example, when the values of the tangential field strength for the high-order winding harmonics are less than those for the low-order harmonics, Davies' method applied to each harmonic in turn ensures that the values of μ_r for the high-order harmonics are greater than those for the low-order harmonics. As the losses of the high-order harmonics usually decrease as μ_r increases (e.g. the 29th harmonic for the salient-pole

machine in fig. 6.5), the method results in a lower loss for these harmonics than is given by the classical theory with the same value of μ_r for all harmonics. (This effect can be seen in Adderley's results when some corrections are made to his calculations by Kuyper's formula and the calculations by Barello's formula are divided by 4 (as discussed in section 8.5.3).) Because of the uncertainty surrounding the calculation of the losses of several superposed waves, there is no basis at present for assuming that it is better to assign a value of μ_r to each harmonic in accordance with the normal value corresponding to its surface field strength, as implied by Davies' method, than to use a uniform value of μ_r for all harmonics, based on some assessment of the surface saturation.

Davies' work resulted in some normalised curves for torque, total flux and eddy-current reaction m.m.f. (presented in his second paper) which are similar in form to the curves given here in chapter 6, fig. 6.2. It is shown below that such curves can be derived in a more general way than was done in chapter 6 or by Davies, that the main parameter is the ratio of the eddy-current reaction field to the total field, and that when constant permeability and a uniform air gap are assumed the results are the same as those given in chapter 6. Some expressions are then derived for the terms in Davies' theory for a machine with a uniform air gap of any length, a necessary preliminary to the application of the theory to normal synchronous machines and which was not done correctly by Adderley (Davies being concerned with complicated stator shapes which occur in eddy-current couplings.).

8.5.6.2 Normalised curves

It is assumed that the field variations are sinusoidal in space and time, so that the complex number representation may be used, as in chapter 6. Let the components of the radial flux density on the rotor surface be as follows

$\dot{B}_{yo}$ = total flux density

$\dot{B}_{ya}$ = applied flux density

$\dot{B}_{ye}$ = eddy-current reaction flux density

Then

$$\dot{B}_{ya} = \dot{B}_{yo} - \dot{B}_{ye} \qquad (8.36)$$

and

$$\left|\dot{B}_{ya}\right|^2 = \left|\dot{B}_{yo}\right|^2 + \left|\dot{B}_{ye}\right|^2 - 2\left|\dot{B}_{yo}\right|\left|\dot{B}_{ye}\right|\cos\phi_e \qquad (8.37)$$

where ϕ_e is the angle between $\dot{B}_{yo}$ and $\dot{B}_{ye}$

The eddy current reaction flux density may be written in terms of the tangential field strength on the rotor surface, since, for strong skin effect, this is equal to the total induced current per unit length[112,129]. Thus

$$\left|\dot{B}_{ye}\right| = C'\left|\dot{H}_{xo}\right| \qquad (8.38)$$

where C' depends on the air gap reluctance and the stator and rotor permeabilities. This may be substituted in eqn. 6.5 3 for the loss per unit area ($P = \frac{1}{2} v \left|\dot{B}_{yo}\right|\left|\dot{H}_{xo}\right| \cos\vartheta$) to give

$$P = \left|\dot{B}_{yo}\right| \left|\dot{B}_{ye}\right| \frac{v \cos\vartheta}{2C'} \qquad (8.39)$$

which may also be written in terms of the torque per unit area T, using $P/v = 2T/D$ where D is the rotor diameter,

$$T = \left|\dot{B}_{yo}\right| \left|\dot{B}_{ye}\right| \frac{D \cos\vartheta}{4C'} \qquad (8.40)$$

Thus the product $\left|\dot{B}_{yo}\right|\left|\dot{B}_{ye}\right|$ is proportional to the torque, or to the power loss if v is constant. Eqn. 8.37 may be used to give this product in terms of the ratio of the eddy-current reaction field to the total field, $\left|\dot{B}_{ye}\right| / \left|\dot{B}_{yo}\right|$,

$$\frac{\left|\dot{B}_{ya}\right|^2}{\left|\dot{B}_{yo}\right|\left|\dot{B}_{ye}\right|} = \frac{\left|\dot{B}_{yo}\right|}{\left|\dot{B}_{ye}\right|} + \frac{\left|\dot{B}_{ye}\right|}{\left|\dot{B}_{yo}\right|} - 2\cos\phi_e$$

Inverting this equation gives the required product

$$\left|\dot{B}_{yo}\right| \left|\dot{B}_{ye}\right| = \frac{\left|\dot{B}_{ya}\right|^2}{Q^{-1} + Q + C_3} \qquad (8.41)$$

where $\quad Q = |\dot{B}_{ye}| \,/\, |\dot{B}_{yo}|$ $\qquad\qquad$ (8.42)

$\qquad C_3 = -2\cos\phi_e$ $\qquad\qquad\qquad\qquad$ (8.43)

$\qquad$ The R.H.S. of eqn. (8.42) is symmetrical about $Q = 1$, where it has a maximum value of $|\dot{B}_{ya}|^2 \,/\, (2 + C_3)$. Using the subscript m to denote maximum,

$$\left(|\dot{B}_{yo}| \, |\dot{B}_{ye}|\right)_m = \frac{B_{ya}^{\;2}}{2 + C_3}$$

So that eqns. 8.39 and 8.40 give

$$T_m = \frac{|\dot{B}_{ya}|^2}{2 + C_3} \; \frac{D\cos\vartheta}{4\,C'} \qquad\qquad (8.44)$$

$$P_m = \frac{|\dot{B}_{ya}|^2}{2 + C_3} \; \frac{v\cos\vartheta}{2\,C'} \qquad\qquad (8.45)$$

The general expression for the normalised torque, or loss at constant velocity, with strong skin effect, is therefore given by

$$\frac{T}{T_m} = \frac{P}{P_m} = \frac{2 + C_3}{Q^{-1} + Q + C_3} \qquad\qquad (8.46)$$

$\qquad$ Expressions can also be obtained for the normalised total flux density and eddy-current reaction flux density, as follows

$$|\dot{B}_{yo}|^2 = \frac{|\dot{B}_{yo}| \, |\dot{B}_{ye}|}{Q} = \frac{|\dot{B}_{ya}|^2 \, Q^{-1}}{Q^{-1} + Q + C_3} \qquad\qquad (8.47)$$

which has a maximum when $Q \ll 1$

$$|\dot{B}_{yo}|_m = |\dot{B}_{ya}| \qquad\qquad (8.48)$$

so that

$$\frac{|\dot{B}_{yo}|}{|\dot{B}_{yo}|_m} = \frac{Q^{-1/2}}{(Q^{-1} + Q + C_3)^{1/2}} \qquad\qquad (8.49)$$

Similarly, when $Q \gg 1$

$$|\dot{B}_{ye}| = |\dot{B}_{ye}|_m = |\dot{B}_{ya}| \qquad\qquad (8.50)$$

so that

$$\frac{|\dot{B}_{ye}|}{|\dot{B}_{ye}|_m} = \frac{|\dot{H}_{xo}|}{|\dot{H}_{xo}|_m} = \frac{Q^{1/2}}{(Q^{-1} + Q + C_3)^{1/2}} \qquad\qquad (8.51)$$

8.5.6.3 Application to a uniform air-gap machine

Eqn. 8.46 is the same as that derived by Davies, and, as indicated by him, the maximum torque, or loss at constant velocity, occurs when $\left| \dot{B}_{yo} \right| = \left| \dot{B}_{ye} \right|$ (i.e. $Q=1$), although he did not note that Q is the ratio of $\left| \dot{B}_{yo} \right|$ and $\left| \dot{B}_{ye} \right|$. To obtain quantitative results from the equations, Q, C_3, C', $\cos\vartheta$ and B_{ya} must be expressed in terms of known quantities. This may be done as follows for a solid-rotor machine with a uniform air gap and to which linear theory is assumed to be applicable. The theory could also be applied to give the generalised curves for an induction motor with discrete conductors on the rotor $\left(\varnothing_e \simeq 180°, C_3 \simeq 2 \right)$.

The flux density produced by a current sheet in the absence of eddy currents may be found by solving Poisson's equation (eqn. 6.18 with $\rho = \infty$). For a current sheet K' at the rotor surface, with the geometry of fig. 6.1, it may be shown that if $\mu_r \tanh\beta g \gg 1$ and $\mu_s \tanh\beta g \gg 1$ then the radial flux density at the rotor surface is given by

$$\dot{B}_{yo}' = j \frac{\mu_o}{\tanh\beta g} \hat{K}' \qquad (8.52)$$

Therefore the radial flux density produced at the rotor surface by the eddy currents in the original problem is

$$\dot{B}_{ye} = -j \frac{\mu_o}{\tanh\beta g} \dot{H}_{xo} \qquad (8.53)$$

which is independent of μ_r and μ_s if $\mu_r \tanh\beta g \gg 1$ and $\mu_s \tanh\beta g \gg 1$. A relation between the total radial flux density and the tangential field strength may be found from the knowledge that the field inside the iron varies with y as $e^{\beta\gamma y}$ (where y is negative, fig. 6.1) and with x as $e^{-j\beta x}$, and this was given previously in eqn. 6.54. With strong skin effect the relation was given in eqn. 6.55,

$$\dot{B}_{yo} = \sqrt{j}\, \beta d \mu_o \mu_r \dot{H}_{xo} \qquad \text{if } \frac{1}{\beta^2 d^2} \gg 1 \qquad (8.54)$$

The ratio of the eddy-current reaction flux density to the total

flux density from eqns. 8.53 and 8.54 is

$$\frac{\dot{B}_{ye}}{\dot{B}_{yo}} = - \frac{\sqrt{j}}{\beta d \; \mu_r \tanh\beta g} \tag{8.55}$$

so that

$$Q = \frac{|\dot{B}_{ye}|}{|\dot{B}_{yo}|} = \frac{1}{\beta d \mu_r \tanh\beta g} \tag{8.56}$$

and the angle between $\dot{B}_{ye}$ and $\dot{B}_{yo}$ is $\phi_e = 135°$ so that

$$C_3 = -2\cos\phi_e = \sqrt{2} \tag{8.57}$$

These results for Q and C_3 enable the normalised curves to be drawn and used, and it can be seen that Q is the same as Q used in chapter 6 and that with $C_3 = \sqrt{2}$ the expressions 8.46, 8.49 and 8.51 are the same as $K_p (2+\sqrt{2})$, K_B and K_H respectively.

To obtain a physical value for the torque or loss, the applied flux density, the parameter C' and the rotor power factor $\cos\theta$ are required, so that T_m and P_m may be found. The applied flux density may be obtained in similar fashion to eqn. 8.52 and with $\mu_r \tanh\beta g \gg 1$ and $\mu_s \tanh\beta g \gg 1$ is

$$\dot{B}_{ya} = j \; \frac{\mu_o \hat{K}}{\sinh\beta g} \tag{8.58}$$

The rotor power factor with strong skin effect is

$$\cos\theta = 1/\sqrt{2} \qquad \text{if } \frac{1}{\beta^2 d^2} \gg 1 \tag{8.59}$$

and C' may be obtained be comparing eqns. 8.53 and 8.38

$$C' = \frac{\mu_o}{\tanh\beta g} \tag{8.60}$$

Substituting these expressions into eqns. 8.44 and 8.45 gives

$$T_m = \frac{|\dot{B}_{ya}|^2}{2+\sqrt{2}} \; \frac{D \tanh\beta g}{4\sqrt{2}\,\mu_o} = \frac{1}{2}\mu_o \hat{K}^2 \cdot \frac{D}{2\sqrt{2}\cosh\beta g \sinh\beta g} \cdot \frac{1}{2+\sqrt{2}} \tag{8.61}$$

$$P_m = \frac{|\dot{B}_{ya}|^2}{2+\sqrt{2}} \; \frac{v \tanh\beta g}{2\sqrt{2}\,\mu_o} = \frac{1}{2}\mu_o v \hat{K}^2 \frac{1}{\sqrt{2}\cosh\beta g \sinh\beta g} \cdot \frac{1}{2+\sqrt{2}} \tag{8.62}$$

This expression for P_m agrees with the expression obtained in chapter 6, eqn. 6.59.

8.5.6.4 Substitution for permeability

In the above treatment the parameter Q depends on the rotor permeability. Davies eliminated μ_r by linking it with the tangential field strength on the rotor surface, and the expression for Q may be derived as follows. Eqn. 6.57 for the loss per unit area $(P = \frac{1}{2}\sqrt{\pi\mu_o\mu_r\rho f}\left|\dot{H}_{xo}\right|^2)$, based on the linear theory and assuming strong skin effect, may be combined with the representation of the normal magnetisation curve, with $H = \left|\overset{\circ}{H}_{xo}\right|$,

$$(\mu_o\mu_r)^{1/4}\left|\dot{H}_{xo}\right| = k_1\left|\dot{H}_{xo}\right|^m \tag{8.63}$$

to give

$$\left|\dot{H}_{xo}\right| = \left(\frac{2P}{k_1^2\sqrt{\pi\rho f}}\right)^{\frac{1}{2m}} = \left(\frac{4\sqrt{\lambda}}{Dk_1^2\sqrt{\pi\rho}}\right)^{\frac{1}{2m}} \cdot T^{\frac{1}{2m}} \cdot v^{\frac{1}{4m}} \tag{8.64}$$

so that eqn. 8.38 gives

$$\left|\dot{B}_{ye}\right| = C_1'\, T^{\frac{1}{2m}}\, v^{\frac{1}{4m}} \tag{8.65}$$

where $\quad C_1' = C'\left(\dfrac{4\sqrt{\lambda}}{Dk_1^2\sqrt{\pi\rho}}\right)^{\frac{1}{2m}}$ $\tag{8.66}$

The general expression for the loss, eqn. 6.53, may be written

$$\left|\dot{B}_{yo}\right| = \frac{2P}{v\left|\dot{H}_{xo}\right|\cos\vartheta} = \frac{4T}{D\left|\dot{H}_{xo}\right|\cos\vartheta}$$

and on substituting for $\left|\dot{H}_{xo}\right|$ from eqn. 8.64 this gives

$$\left|\dot{B}_{yo}\right| = C_2'\, T^{1-\frac{1}{2m}}\, v^{-\frac{1}{4m}} \tag{8.67}$$

where $\quad C_2' = \dfrac{4}{D\cos\vartheta}\left(\dfrac{4\sqrt{\lambda}}{Dk_1^2\sqrt{\pi\rho}}\right)^{-\frac{1}{2m}}$ $\tag{8.68}$

Therefore eqns. 8.65 and 8.67 give

$$Q = \frac{\left|\dot{B}_{ye}\right|}{\left|\dot{B}_{yo}\right|} = \frac{C_1'}{C_2'}\, T^{\frac{1}{m}-1}\, v^{\frac{1}{2m}} \tag{8.69}$$

Since the maximum torque T_m occurs at a speed v_m when $Q = 1$,

$$\frac{C_2'}{C_1'} = T_m^{\frac{1}{m}-1}\, v_m^{\frac{1}{2m}} \tag{8.70}$$

and

$$Q = \left(\frac{T}{T_m}\right)^{\frac{1}{m} - 1} \left(\frac{v}{v_m}\right)^{\frac{1}{2m}} \tag{8.71}$$

The curve of T/T_m against Q given by eqn. 8.46 may be used with eqn. 8.71 to plot T/T_m against v/v_m, as done by Davies.

For a uniform air gap, T_m is given by eqns. 8.61 as before, since this is independent of the value of μ_r, and v_m may be found from eqn. 8.70, using eqns. 8.61, 8.60, 8.59, 8.66 and 8.68,

$$v_m = \left(\frac{2 + \sqrt{2}}{|\dot{B}_{yo}|^2}\right)^{2-2m} \left(\frac{\tanh\beta g}{\mu_o}\right)^{4m-2} \frac{k_1^4 2\pi\rho}{\lambda} \tag{8.72}$$

Thus, for $m \neq 1$, v_m depends on the applied flux density and the shape of the normal magnetisation curve embodied in k_1 and m. If $m = 1$, eqn. 8.63 implies that μ_r is independent of H, with $\mu_o \mu_r = k_1^4$, and eqn. 8.71 gives $Q = (v/v_m)^{1/2}$, and eqn. 8.72 gives $v_m = (2\pi\rho\mu_r \tanh^2\beta g)/\mu_o\lambda$, which may be shown to agree with the expression for v derived from eqn. 8.56 when $Q = 1$.

The above expressions for T_m and v_m could have been derived from Davies' equations. Care is required, however, because his equations were expressed in terms of m.m.f., with a factor f to allow for different flux paths of the applied and eddy-current fields. For a uniform air gap with sufficiently high stator and rotor permeabilities, a comparison of eqns. 8.53 and 8.58 shows that $f = 1/\cosh\beta g$.

8.5.6.5 Allowance for non-linearity

An allowance for the effect of a non-linear normal magnetisation curve on eqn. 6.57 for P and on the rotor power factor could be made by including a saturation factor K_s in eqn. 6.57 and by using a new value of $\cos\vartheta$ (e.g. $K_s \simeq 1.4$ and $\cos\vartheta \simeq 0.85$, as suggested by Nejman[131], noting that $\phi_e = 90° + \vartheta$ (eqn. 8.53) so that $C_3 = -2\cos\phi_e = 2\sin\vartheta \simeq 1.05$). To verify this suggestion, a

comparison of measured and calculated values of T_m and v_m would be needed as well as a comparison of the normalised curves, and so a machine with sinusoidal excitation and small end effects should be used.

REFERENCES

1. Chalmers, B.J.: 'Electromagnetic problems of a.c. machines'
        (Chapman and Hall, 1965)

2. Wiedemann, E.: 'Fully water-cooled turbogenerators', Brown Boveri
        Review, 1966, 53, pp 501 - 511

3. Anempodistov, V.P., Kasharskii, E.G., and Urusov, I.D.: 'Problems
        in the design and development of 750 MW turbo-
        generators' (Pergamon, 1960)

4. Symons, H.D.:   'The heat paths in electrical machinery', J.IEE,
        1912, 48, pp 674 - 718

5. Bausch, H. and Jordan, H.: 'Zusatzverluste in den Läuferkappen von
        Turbogeneratoren', E.T.Z.-A, 1969, 90, pp 126 - 130

6. Rahman, M.A., Copeland, M.A. and Slemon, G.R.: 'An analysis of the
        hysteresis motor Part III: Parasitic losses',
        IEEE Trans., 1969, PAS-88, pp 954 - 961

7. Adderley, K.J.: 'A study of the pole face loss caused by armature
        reaction m.m.f. harmonics' M.Sc. Thesis, The
        University of Aston in Birmingham, 1968

8. Taegen, F. and van de Graaf, J.T.: 'Der Einfluss der Krümmung des
        Luftspaltes auf die Zusatzverluste in massiven
        Rotoreisen von synchronmaschinen', Arch.
        Elektrotech., 1969, 53, pp 45 - 52

9. Bratoljić, T.: 'Recent studies of stray losses in solid pole-
        pieces of synchronous machines', Brown Boveri
        Review, 1966, 53, pp 521 - 530

10. Carter, F.W.:   'Air-gap induction', Electrical World and
        Engineer, 1901, 38, pp 884 - 888

11. Adams, C.A., Lanier, A.C., Pope, C.C. and Schooley, C.O.: 'Pole-
        face losses', Trans. AIEE, 1909, 28 II,
        pp 1133 - 1156

12. Rüdenberg, R.: 'Zusätsliche Verluste in Synchronmaschinen und
        ihre Messung', E.T.Z., 1924, 45, pp 37 - 41 and
        59 - 63

13. Pollard, E.I.:   'Load losses in salient pole synchronous machines',
        Trans. AIEE, 1935, 54, pp 1332 - 1340

14. Richardson, P.: 'Stray losses in synchronous electrical machinery',
        Proc.IEE, 1945, 92 II, pp 291 - 301

15. Gault, J.S.: 'Rotor-bar currents in squirrel-cage induction motors', Trans. AIEE, 1941, 60, pp 784 - 791

16. Say, M.G.: 'Performance and design of alternating current machines' (Pitman, 1936)

17. Liwschitz-Garik, M.: 'Winding alternating-current machines' (Van Nostrand, 1950)

18. Rowland, H.A.: 'On magnetic permeability, and the maximum of magnetism of iron, steel and nickel', Phil. Mag., 1873, 46, pp 140 - 159

19. Searle, G.F.C.: 'Studies in magnetic testing', J.IEE, 1904, 34, pp 55 - 118

20. Ewing, J.A.: 'Magnetic Induction in iron and other metals', (The Electrican, 1891, 3rd. ed. 1900), also Phil. Trans. Roy. Soc., 1885, 176, pp 523 - 641

21. Lord Rayleigh: 'Notes on electricity and magnetism - III. On the behaviour of iron and steel under the operation of feeble magnetic forces', Phil. Mag., 1887, 23, 5th series, pp 225 - 245

22. Bozorth, R.M.: 'Ferromagnetism' (Van Nostrand, 1951) pp 538 - 553

23. Spooner, T.: 'Permeability', J.AIEE, 1923, 42, pp 42 - 47

24. Lanchester, F.W.: 'The air-gap transformer and choke', J.IEE, 1933, 73, pp 413 - 418

25. Gans, R.: 'Magnetisch korrespondierende Zustände', Physik. Zeitschr., 1910, 11, pp 988 - 991

26. Gans, R.: 'Die Gleichung der Kurve der reversiblen Suszeptibilität', Physik. Zeitschr., 1911, 12, pp 1053 - 1054

27. Ebinger, A.: 'Untersuchung über die Permeabilität des Eisens bei Wellenstrommagnetisierung', Zeitschr. für Techn. Physik, 1930, 11, pp 221 - 227

28. Sizoo, G.J.: 'Über die effektive und die reversible Permeabilität', Annalen der Physik, 1929, 3, 5th series, pp 270 - 276

29. Nicholls, C.R., Morsztyn, K., and Bonwick, W.J.: 'The influence of residual magnetism in current transformers on the operation of differential protection systems', IE Aust., Elect. Eng. Trans., 1969, EE5, pp 271 - 276

30. Johnson, W.C., Merrell, B.C., and Alley, R.E.: 'Universal curves for d.c. controllable reactors', Trans. AIEE, 1949, 68, pp 31 - 40

31. Chernovets, A.K. and Kozulin, V.S.: 'The magnetisation curves for electrical steels when a direct field is superposed upon a rotating field', (In Russian), Elektrotekhnika (USSR), 1966, 37, pp 45 - 48

32. Chernovets, A.K. and Kozulin, V.S.: 'An experimental study of the magnetisation characteristics of electrical sheet steel when a direct field is superposed upon a rotating field', (In Russian), Izvestiya V.U.Z. - Energetika, 1967, no. 1, pp 23 - 29

33. Chubb, L.W. and Spooner, T.: 'The effect of displaced magnetic pulsations on the hysteresis loss of sheet steel', Proc. AIEE, 1915, 34, part 2, pp 2321 - 2342

34. Spooner, T.: 'Tooth frequency losses in rotating machines', J. AIEE, 1921, 40, pp 751 - 756

35. Sugiura, J.: 'On the magnetic properties of iron polarized in any direction', Researches of the Electrotechnical Laboratory, Tokyo, 1931, no. 300 (In Japanese)

36. Sims, L.G.A. and Clay, D.L.: 'Incremental Magnetisation', Wireless Engineer, 1935, 12, pp 238 - 245 and 312 - 320

37. Ewing, J.A. and Klaassen, H.G.: 'Magnetic qualities of iron', Phil. Trans. Roy. Soc. A, 1893, 184, pp 985 - 1039

38. Wilson, E., O'Dell, G.F., and Jennings, H.W.K.: 'On the effect of previous magnetic history on magnetisation', Proc. Royal Soc. of London, 1909, 83A, pp 1 - 9

39. Holm, F.: 'Untersuchungen über magnetische Hysteresis' Zeitschrift des Vereines deutscher Ingenieure, 1912, 56, pp 1746 - 1751 (October, no. 43)

40. Rosenbaum, M.: 'Hysteresis loss in iron taken through unsymmetrical cycles of constant amplitude', J.IEE, 1912, 48, pp 534 - 545

41. Ball, J.D.: 'The unsymmetrical hysteresis loop', Trans. AIEE, 1915, 34, pp 2695 - 2715

42. 'Magnetic permeability of iron and steel', B.S. 2454 : 1954

43. Hughes, E.: 'Errors in the magnetic testing of ring specimens',
     J.IEE, 1927, 65, pp 932 - 943

44. Stroude, F.: 'An accurate examination of the Steinmetz index
     for transformer iron, stalloy and cast iron',
     Proc. Phys. Soc. London, 1912, 24 IV, pp 238 - 249

45. 'Discussion on papers by Ball and by Chubb and
     Spooner', Proc. AIEE, 1916, 35, pp 506 - 510

46. Greig, J. and Shurmer, H.V.: 'Iron losses under superimposed
     alternating inductions', in 'Soft magnetic materials
     for telecommunications', Eds. Richards, C.E. and
     Lynch, A.C. (Pergamon, 1953) pp 27 - 37

47. 'Magnetic materials for use under combined d.c.
     and a.c. magnetisation', B.S. 933 : 1941

48. Carter, R.O. and Richards, D.L.: 'The incremental magnetic
     properties of silicon-iron alloys', Proc. IEE,
     1950, 97 II, pp 199 - 214

49. Mondal, R.K., Bhattacharyya, S.N., and Choudhury, J.K.:
     'Measurement of incremental magnetic loss by bridge
     and wattmeter methods', J.Instn. Engrs. (India),
     Elect. Engng. Div., 1966, 46, EL 6, pp 464 - 477.

50. Choudhury, J.K., Mondal, R.K., and Bhattacharyya, S.N.: 'A current
     feedback method for correction of flux-wave
     distortion in incremental magnetic testing',
     J. Instn. Engrs. (India), Elect. Engng. Div.,
     1967, 47, EL 3, pp 81 - 94

51. Charlton, O.E. and Jackson, J.E.: 'Losses in iron under the action
     of superposed alternating - and direct - current
     excitations', Trans. AIEE, 1925, 44, pp 824 - 831

52. Edgar, R.F.: 'Loss characteristics of silicon steel at 60 cycles
     with d.c. excitation', Trans. AIEE, 1933, 52,
     pp 721 - 726

53. Niwa, Y. and Asami, Y.: 'Magnetic properties of sheet steel under
     superposed alternating field and unsymmetrical
     hysteresis losses', Researches of the
     Electrotechnical Laboratory, Tokyo, 1923, no. 124

54. Niwa, Y., Sugiura, J, and Matura, J.: 'Further study on the
     magnetic properties of electrical sheet steel under
     superposed alternating field and unsymmetrical
     hysteresis losses', Researches of the
     Electrotechnical Laboratory, Tokyo, 1924, no. 144

55. Kresadlo, Z.: 'Vliv stejnosměrné předmagnetizace na magnetizační ztráty', Electrotech. Obzor (Czech.), 1969, 58, pp 146 - 153

56. Coales, J.D.: 'On a method of using transformers as choking coils and its application to the testing of alternators', J.IEE, 1908, 42, pp 412 - 454

57. Boyajian, A.: 'Theory of d.c. excited iron-core reactors and regulators', Trans. AIEE, 1924, 43, pp 919 - 936

58. Vallauri, G.: 'Hysteresis in iron for asymmetric cycle of magnetisation', Atti dell' Assoc. Elettr. Ital., 1911, 15, pp 79 - 92

59. Choudhury, J.K., Mondal, R.K. and Bhattacharyya, S.N.: 'New type of sample for incremental magnetic testing', Proc. IEE, 1966, 113, pp 1692 - 1694

60. Shiner, P.G.: 'New type of sample for incremental testing', Proc. IEE, 1967, 114, pp 419 - 420 (Correspondence)

61. Goldschmidt, R.: 'Zur Überlagerung starker und schwacher Felder in magnetischen Materialen', Zeitschrift für Technische Physik, 1930, 11, pp 8 - 12

62. Carter. G.W.: 'The electromagnetic field in its engineering aspects', (Longmans, 1954)

63. Webb, C.E. and Ford, L.H.: 'Alternating-current permeability and the bridge method of magnetic testing', J.IEE, 1935, 76, pp 185 - 194

64. Bishop, J.E.L. and Lee, E.W.: 'The behaviour of ferromagnetic sheets in alternating electric and magnetic fields. (I) A domain theory of the skin-effect impedance and complex permeability', Proc. Roy. Soc. A, 1963, 276, pp 96 - 111

65. Bloor, D. and Martin, D.H.: 'Ferromagnetic domain sizes in polycrystalline silicon-iron', Proc. Phys. Soc., 1957, 73, pp 694 - 695

66. Martin, D.H.: 'Surface structures and ferromagnetic domain sizes', Proc. Phys. Soc., 1957, (B), 70, pp 77-84

67. Boon, C.R. and Robey, J.A.: 'Effect of domain-wall motion on power loss in grain-oriented silicon-iron sheet', Proc. IEE, 1968, 115, pp 1535 - 1540

68. Overshot, K.J. and Thompson, J.E.: 'Magnetic properties of grain-oriented silicon-iron, part 4', Proc. IEE, 1970, 117, pp 865 - 868

69. Bishop, J.E.L.: 'Magnetic domain structure and losses in Goss-textured silicon iron', Proc. IEE, 1970, 117, pp 2191 - 2193

70. Beckley, P. and Thompson, J.E.: 'Influence of inclusions on domain-wall motion and power loss in oriented electrical steel', Proc. IEE, 1970, 117, pp 2194 - 2200

71. Peterson, E. and Wrathall, L.R.: 'Eddy currents in composite laminations', Proc. IRE, 1936, 24, pp 275 - 286

72. Smith, A.W.: 'The effect of a superposed constant field upon the alternating current permeability and energy loss in iron', Phys. Rev., 1921, 17, pp 416 - 418

73. Fondiller, W., and Martin, W.H.: 'Hysteresis effects with varying superposed magnetising forces', Trans. AIEE, 1921, 40, pp 553 - 587

74. Sims, L.G.A. and Spinks, J.: 'Ballistic measurements in incremental magnetism', Engineering, 1938, 146, pp 406 - 408

75. 'Lysaght - Sankey electrical steel sheets', (Joseph Sankey & Sons Ltd., Albert St., Bilston, Staffs.) 1938

76. 'RTB electrical sheet and strip', (Richard Thomas and Baldwins, P.O. Box 13, Cookley Works, Brierley Hill, Staffs.)

77. 'SCW electrical steel sheet and strip', (The Steel Company of Wales, Orb Works, Newport, Mon.) 1959

78. Electrical Engineering staff of M.I.T.: 'Magnetic circuits and transformers', (Wiley, 1943) p. 200

79. Langman, R.: 'Measurement of reversible permeability using solid (nonlaminated) specimens', Proc. IEE, 1970, 117, pp 1887 - 1890

80. Greig, J. and Parton, J.E.: 'Harmonic power in iron testing', Engineering, 1938, 146, pp 431 - 433

81. Choudhury, J.K., Mondal, R.K., and Bhattacharyya, S.N.: 'A.C. magnetic testing under superposed transverse polarizing field', J. Instn. Engrs. (India), Elect. Engng. Div., 1967, 47, EL 4, pp 253 - 261

82. Winkelmann, A.: 'Handbuch der Physik', 2 Aufl., 5, pp 209 - 210 by F. Auerbach, (J.A. Barth, Leipzig, 1908)

83. Gans, R.: 'Die reversible longitudinale und transversale Permeabilität', Annalen der Physik, 1909, 29, 4th series, (7), pp 301 - 315

84. Goldschmidt, R.: 'Die Verkleinerung der Hystereseverluste durch Ströme hoher Frequenz und das Verhalten des Eisens bei Längs - und Quermagnetisierung', E.T.Z., 1910, 31, pp 218 - 221

85. Harrison, E.P., Turney, G.L., Rowe, H. and Gollop, H.: 'The electrical properties of high permeability wires carrying alternating current', Proc. Roy. Soc. A, 1936, 157, pp 451 - 479

86. Webb, J.S.: 'The variation in the high-frequency resistance and permeability of ferromagnetic materials due to a superimposed magnetic field', Proc. IRE, 1938, 26, pp 433 - 441

87. Beck, F.J. and Kelly, J.M.: 'Magnetisation in perpendicularly superposed direct and alternating fields', J. Appl. Phys., 1948, 19, pp 551 - 562

88. Libkind, M.S. and Dorzhko, L.I.: 'The electromagnetic characteristics of a controlled reactor with transverse magnetisation', Electric Technology, 1967, 1, pp 39 - 54

89. Zaitsev, I.A.: 'The magnetic characteristics of iron in the presence of additional magnetisation', Trud. Leningrad Polytechnical Institute, 1947, no. 2

90. Dietrich, H.: 'Magnetisches Verhalten ferromagnetischer Werkstoffe in gekreuzten Magnetfeldern', E.T.Z.-A, 1969, 90, pp 133 - 137

91. Marconi, G.: 'Note on a magnetic detector of electric waves, which can be employed as a receiver for space telegraphy', Proc. Roy. Soc. London, 1902, 70, pp 341 - 344

92. Finzi, G.: 'On hysteresis in presence of alternating currents', The Electrician, 1891, 26, pp 672 - 673

93. Ashworth, J.R.: 'The anhysteretic properties of iron and nickel. Part 1. The relation of magnetic intensity to field strength and temperature', Phil. Mag. 6th series, 1914, 27, pp 357 - 370

94. Williams, N.H.: 'Some effects of cross-magnetising fields upon hysteresis', Phys. Rev., 1917, (II), 9, p 339 (abstract of paper presented at Chicago meeting of the American Physical Society, Dec. 2, 1916)

95. Heartz, R.A. and Buelteman, H.: 'The application of perpendicularly superposed magnetic fields', Trans. AIEE, 1955, 74I, pp 655 - 660

96. Webb, C.E. and Ford, L.H.: 'The time-decrease of permeability at low magnetising forces', J.IEE, 1934, 75, pp 787 - 797

97. Astbury, N.F.: 'Industrial Magnetic testing', (Institute of Physics, London, 1952)

98. Jackson, W.J.: 'The effect of heat-treatment on the magnetic properties of carbon-steel castings', J. Iron and Steel Inst., 1960, 194 I, pp 29 - 36

99. Peck, J.S.: 'Testing large transformers', Elec. World and Engineer, 1901, 37, pp 1083 - 1086

100. Morris, J.T. and Langford, T.H.: 'The method of constant rate of change of flux as a standard for determining magnetisation curves of iron', Proc. Phys. Soc. (London), 1911, 23, pp 277 - 300

101. Ross, H.McG.: 'An automatic plotter for magnetic hysteresis loops', Proc. IEE, 1954, 101 II, pp 417 - 427

102. Mazzetti, P. and Soardo, P.: 'Electronic hysteresigraph holds dB/dt constant', Rev. Sci. Instr., 1966, 37, pp 548 - 552

103. Warner, J.M.: 'An improved hysteresis loop recorder', Australian Telecom. Res., 1967, 1, pp 52 - 58

104. Erdmann, P.: 'Ein elektronisches Präzisionsgerät zum automatischen Messen und Schreiben von Magnetisierungsschleifen', Techn. Mitt. Krupp, Forsch.-Ber., 1968, 26, pp 11 - 16

105. McFarlane, J. and Harris, M.J.: 'The control of flux waveforms in iron testing by the application of feedback amplifier techniques', Proc. IEE, 1958, 105 A, pp 395 - 402

106. Newbury, R.A.: 'Demagnetizer for solid specimens', J.Sci. Instr., 1969, series 2, 2, pp 315 - 318.

107. Burrows, C.W.: 'On the best method of demagnetising iron in magnetic testing', Bull. Bureau of Standards (Washington), 1907, 4, pp 205 - 274

108. Brailsford, F. and Bradshaw, C.G.: 'Iron losses at high magnetic flux densities in electrical sheet steels', Proc. IEE, 1955, 102 A, pp 463 - 471

109. British Steel Castings Research Association: 'Magnetic properties of plain carbon steel castings', Data Sheet 4.

110. McLachlan, N.W.: 'Bessel functions for engineers', (Oxford, 1934)

111. Aspden, H.: 'Eddy-currents in solid cylindrical cores having non-uniform permeability' J.Appl. Phys., 1952, 23, pp 523 - 528

112. Pohl, R.: 'Electromagnetic and mechanical effects in solid iron due to an alternating or rotating magnetic field', J. IEE, 1944, 91 II, pp 239 - 248

113. Copeland, M.A. and Slemon, G.R.: 'Minor loop loss predictions in devices using permanent magnet materials', IEEE Trans, 1966, MAG - 2, pp 420 - 423

114. Béland, B. and Robert, J.: 'Eddy-current losses in saturated cyclinders', IEEE Trans on Communications and Electronics, 1964, 83, pp 191 - 198

115. MacLean, W.: 'Theory of strong electromagnetic waves in massive iron', J. Appl. Phys. 1954, 25, pp 1267 - 1270

116. McConnell, H.M.: 'Eddy current phenomena in ferromagnetic materials', Trans. AIEE, 1954, 73 I, pp 226-235

117. Agarwal, P.D.: 'Eddy-current losses in solid and laminated iron', Trans. AIEE, 1959, 78 I, pp 169 - 181

118. Higa, W.H.: 'Theory of magnetic cross valves', Trans. AIEE, 1955, 74I, pp 204 - 208

119. Concordia, L. and Poritsky, H.: 'Synchronous machine with cylindrical rotor', Trans. AIEE, 1937, 56, pp 49 - 58

120. Kuyper, W.W.: 'Pole-face losses in solid-rotor turbine generators', Trans. AIEE, 1943, 62, pp 827 - 834

121. Barello, G.: 'Perdite per correnti parassite nelle espansioni polari massicce degli alternatori', L'Elettrotecnica, 1947, 34, pp 324 - 334

122. Barello, G: 'Courants de Foucault engendrés dans les pièces polaires massives des alternateurs par les champs tournants parasites de la reaction d'induit', Revue générale de l'Electricite, 1955, 64, pp 557 - 576

123. Postnikov, I.M.: 'Eddy currents in synchronous and asynchronous machines with unlaminated rotors', Elektrichestvo, 1958, no. 10, pp 7 - 14.In Russian (Translation: Electric Technology, 1959, 4, pp 463-479)

124. Stoll, R.L. and Hammond, P.: 'Calculation of the magnetic field of rotating machines, Part 4', Proc.IEE, 1965, 112, pp 2083 - 2094

125. Lawrenson, P.J., Reece, P. and Ralph, M.C.: 'Tooth-ripple losses in solid poles', Proc.IEE, 1966, 113, pp 657 - 662 . Correspondence: Proc.IEE, 113, pp 1846-1847 and 114, pp 275 - 276

126. Gibbs, W.J.: 'Conformal transformations in electrical engineering', (Chapman and Hall, 1958)

127. Freeman, E.M.: 'The calculation of harmonics, due to slotting, in the flux-density waveform of a dynamo-electric machine', Proc.IEE, 1962, 109C, pp 581 - 588

128. Neville, S.: 'Use of Carter's coefficient with narrow teeth', Proc.IEE, 1967, 114, pp 1245-1250

129. Davies, E.J.: 'An experimental and theoretical study of eddy-current couplings and brakes', Trans.IEEE, 1963, PAS-67, pp 401 - 417

130. Davies, E.J.: 'General theory of eddy-current couplings and brakes', Proc.IEE, 1966, 113, pp 825 - 837

131. Nejman, L.R.: 'Skin effect in ferromagnetic bodies', (Gosenergoizdat, Leningrad, 1949) (In Russian)

132. Gibbs, W.J.: 'Tooth-ripple losses in unwound pole-shoes', J.IEE, 1947, 94II, pp 2 - 12 Discussion: J.IEE, 1948, 95II, pp 545 - 549

133. Carter, F.W.: 'Pole-face losses', J.IEE, 1916, 54, pp 168 - 170

134. Sathirakul, K.: 'A study of tooth-ripple losses in dynamo-electric machines', Ph.D. Thesis, University of London, 1959

135. Freeman, E.M.: 'A study of tooth-ripple eddy current losses in laminated pole shoes', Ph.D. Thesis, University of London, 1964

136. Greig, J., Beevers, C.L. and ffoulkes, T.H.O.: 'Tooth-ripple losses in electrical machines', Proc.IEE, 1971, 118, pp 1269 - 1274

137. Greig, J., Beevers, C.L. and Freeman, E.M.: 'Tooth-ripple losses in solid poles', Proc.IEE, 1966, 113, p 1846 (Correspondence)

138. Kilgore, L.A.: 'Calculation of synchronous machine constants', Trans.AIEE, 1931, 50, pp 1201 - 1214

139. Ginsberg, D. and Jokl, A.L.: 'Voltage harmonics of salient-pole generators under balanced 3-phase loads - I', Trans.AIEE, 1959, 78 III, pp 1573 - 1580

140. Ginsberg, D. and Jokl, A.L.: 'Voltage harmonics of salient-pole generators under balanced 3-phase loads - II', Trans.AIEE, 1960, 79 III, pp 560 - 566

141. Harris, W.P. and Cooter, I.L.: 'Improved bridge method for the measurement of core losses in ferromagnetic materials at high flux densities', J. Research National Bureau of Standards, 1958, 60, pp 509 - 516

142. Gibbs, W.J.: 'Theory and design of eddy-current slip couplings', Beama J., 1946, pp 123 - 128, 172 - 177, 219 - 225

143. Lim, K.K. and Hammond, P.: 'Universal loss chart for the calculation of eddy-current losses in thick steel plates', Proc.IEE, 1970, 117, pp 857 - 864
Correspondence: Proc.IEE, 1971, 118, pp 277 - 280

144.   Lloyd, M.G.:   'Effect of waveform upon the iron losses in transformers', Bull. Bureau of Standards (Washington), 1907, 4, pp 477 - 510

145.   Schröter, F.:   'Eisenverluste durch gleichzeitige Magnetisierung bei zwei verschiedenen Frequenzen', Archiv für Elektrotechnik, 1924, 13, pp 30 - 34

146.   Erdelyi, E.A., Ahamed, S.V. and Hopkins, R.E.: 'Nonlinear theory of synchronous machines on-load', Trans.IEEE, 1966, PAS-85, pp 792 - 801

147.   Ray, A.K.:   'A study of flux distribution in electrical machines under non-linear conditions using finite-difference and finite-element methods', Ph. D. Thesis, University of London, 1971

Table 6.1   Data of two large industrial machines and
an experimental machine for the calculation
of pole-face losses

		500 MVA turbo-generator (Adderley ref.Y)	60 MVA salient-pole machine (Adderley ref.1E)	Experimental machine?
No. poles	$2p$	2	6	4
Frequency (Hz)	f_1	50	50	50
Rated phase current (A r.m.s.)	I_A	11000	2670	30
Conductors in series per slot	Z	1	1	8
Phase spread (deg)	w	60	60	60
Slots per pole and phase	q	10	5	1
Pitch (p.u.)	ε	0.833	0.800	1
Slot pitch (mm)	λ_s	57.1 [1]	54.5	76
Slot width (mm)	s	$\sim\lambda_s/2$	22	4
Effective air gap (mm)	g	85	19	0.305
Rotor diameter (mm)	D	1090	1560	288
Pole length (mm)	L	5200	2700	250
Gap/radius ratio	$2g/D$	0.156	0.0244	0.00246
Fundamental winding factor	k_{w1}	0.923	0.908	1
Fundamental current loading (A/m)	$\hat{K}_1 = \dfrac{\sqrt{2}\,I_A Zk_{w1}}{\lambda_s}$	252000	63000	4500

Note (1) Because of the high value of gap/radius ratio for the
turbo-generator the representation in rectangular
coordinates is approximate. For present purposes the
machine has been developed about the rotor, and the
stator slot pitch correspondingly reduced from 65 mm
to 57.1 mm.

Table 6.2   Linear theory calculation of winding-harmonic losses for the two large industrial machines of table 6.1

$\mu_r = 100$, $\rho = 2.37 \times 10^{-7}\,\Omega\text{m}$, $f_1 = 50$ Hz

	n	$\beta g = \dfrac{\pi g}{\tau}$	$\tanh\beta g$	$\dfrac{1}{\beta d}=\dfrac{\tau}{\pi d}$	Q	K_H	K_B	k_d	k_p	k_s	$\hat{K}$ (A/m)	$\hat{H}_{xm}$ (A/m)	$\hat{H}_{xo}$ (A/m)	P (W/m²)	P_{total} (W/m²)
	5	0.78	0.65	108.9	1.68	0.68	0.40	.193	.259	.996	13650	10300	6950	3930	3930
	7	1.09	0.80	77.8	0.97	0.53	0.55	-.140	.259	.994	-9850	-5950	-3170	815	4745
500 MVA	11	1.72	0.94	70.0	0.74	0.455	0.62	-.092	.966	.984	-23800	-8250	-3810	1680	6425
turbo-generator	13	2.03	0.96	59.2	0.62	0.410	0.66	.079	.966	.982	-20600	-5300	-2170	530	6955
	17	2.65	0.99	55.4	0.55	0.380	0.69	.064	-.259	.956	-4320	-620	-235	8	6963
	19	2.97	0.99	49.6	0.50	0.360	0.72	-.060	-.259	.952	4000	410	147	3	6966
	23	3.59	1.00	47.3	0.473	0.345	0.73	-.054	-.966	.940	13200	700	242	10	6976
	25	3.90	1.00	43.5	0.435	0.325	0.75	.052	-.966	.930	12700	485	156	5	6981
slot harmonics	59	9.21	1.00	29.2	0.292	0.242	0.82	-.955	.966	.646	-163000	-32	-8	0.02	6982
	61	9.53	1.00	28.2	0.282	0.235	0.83	-.955	.966	.624	157000	24	6	0.01	6982
	5	0.37	0.35	51.9	1.48	0.64	0.44	.200	0	.993	0	0	0	0	0
	7	0.51	0.47	37.1	0.79	0.470	0.60	-.149	.588	.986	-6000	-5360	-2518	516	516
60 MVA	11	0.81	0.67	33.4	0.51	0.360	0.71	-.109	.951	.966	-6960	-5160	-1660	398	914
salient-pole	13	0.95	0.74	28.2	0.38	0.295	0.77	.102	-.588	.953	-3980	-2670	-785	71	985
machine	17	1.25	0.84	26.4	0.312	0.255	0.81	.102	.588	.920	3820	2040	514	37	1022
	19	1.39	0.88	23.6	0.268	0.222	0.84	-.109	.951	.901	6480	3080	677	65	1087
	23	1.68	0.93	22.6	0.243	0.205	0.85	-.149	.588	.857	5200	1880	384	24	1111
	25	1.83	0.95	20.6	0.219	0.188	0.86	.200	0	.832	0	0	0	0	1111
slot harmonics	29	2.12	0.97	20.0	0.206	0.180	0.87	.957	-.951	.778	-49000	-11420	-2062	775	1886
	31	2.27	0.98	18.7	0.191	0.170	0.88	.957	.951	.749	47200	9520	1615	475	2361
"	59	4.32	1.00	13.9	0.139	0.125	0.90	.957	-.951	.267	-16800	-451	-56	0.65	2364
	61	4.46	1.00	13.4	0.134	0.123	0.92	.957	.951	.232	14600	316	41	0.45	2364

Note: Q, K_H, K_B: see fig. 6.2; $\hat{K} = K_1 k_p k_d k_s / k_{w1}$; $\hat{H}_{xm} = \hat{K}/\cosh\beta g$; $|\hat{H}_{xo}| = \hat{H}_{xm} K_H$; $P = \dfrac{1}{2}\sqrt{\pi\mu_0\mu_r\rho f}\;|\hat{H}_{xo}|^2$

Table 6.3 Linear theory calculation of negative-sequence and slot-ripple losses in the two large industrial machines of table 6.1 $\mu_r = 100$, $\rho = 2.37 \times 10^{-7}$ Ωm, $f_1 = 50$ Hz

	τ	f	βg	$\tanh\beta g$	$\dfrac{1}{\beta d}$	Q	K_H	K_B	$\hat{K}$ (A/m)	$\dot{H}_{xm}$ (A/m)	$|\dot{H}_{xo}|$ (A/m)	P (w/m²)
500 MVA turbo-generator												
negative sequence	τ_1	$2f_1$	0.156	0.155	315	20.3	0.966	0.047	12600	12450	12050	6610
1st slot ripple	$\dfrac{\tau_1}{60}$	$60f_1$	9.34	1.00	28.8	0.288	0.240	0.82	~20x10⁶	3200	770	155
60 MVA salient-pole machine												
negative sequence	τ_2	$2f_1$	0.0731	0.0730	150	20.6	0.966	0.046	3150	3140	3040	435
1st slot ripple	$\dfrac{\tau_1}{30}$	$30f_1$	2.19	0.975	19.4	0.199	0.172	0.88	~113000	45000	7750	10800
2nd slot ripple	$\dfrac{\tau_1}{60}$	$60f_1$	4.38	1.00	13.7	0.137	0.123	0.91	~240000	6000	750	145

Note: Negative sequence

turbo-generator:

$\hat{K} = 5\%$ of 252000 ($=\hat{K}_1$)

salient-pole machine:

$\hat{K} = 5\%$ of 63000 ($=\hat{K}_1$)

Slot ripple

turbo-generator:

$\dfrac{\lambda_s}{s} = 2$, $\dfrac{s}{g} = 0.33$ gives $\dfrac{B_1}{B_o} \simeq 0.004$ (from Neville[128], fig. 5)

$\hat{K} = \dfrac{|B_{ym}| \sinh\beta g}{\mu_o} \simeq \dfrac{0.004 \times 7000}{4\pi \times 10^{-7}} \simeq 20 \times 10^6$ A/m for $B_o = 1.0$ T   (eqn. 6.47)

$\dot{H}_{xm} = \dfrac{|B_{ym}| \tanh\beta g}{\mu_o} \simeq \dfrac{0.004 \times 1.00}{4\pi \times 10^{-7}} = 3200$ A/m for $B_o = 1.0$ T   (eqn. 6.61)

salient-pole machine:

$\dfrac{\lambda_s}{s} = 2.5$, $\dfrac{s}{g} = 1.16$ gives $\dfrac{B_1}{B_o} = 0.058$

$\dfrac{1}{2}\dfrac{\lambda_s}{s} = 1.25$, $\dfrac{s}{g} = 1.16$ gives $\dfrac{B_2}{B_o} = \dfrac{1}{2} \times 0.015 = 0.0075$

Table 6.4 Reduction of winding-harmonic maximum tangential field strength due to winding factor (k_w) and air gap $(1/\cosh\beta g)$ in the two industrial machines of table 6.1.

	500 MVA turbo-generator				60 MVA salient-pole machine				
n	βg	$\dfrac{1}{\cosh\beta g}$	$k_w=k_d k_p k_s$	$\dfrac{\lvert k_w\rvert}{\cosh\beta g}$ %	n	βg	$\dfrac{1}{\cosh\beta g}$	$k_w=k_d k_p k_s$	$\dfrac{\lvert k_w\rvert}{\cosh\beta g}$ %
5	0.78	.77	.0499	100	5	0.37	.93	0	0
7	1.09	.62	-.0359	58	7	0.51	.88	-.0865	100
11	1.72	.34	-.0872	80	11	0.81	.75	-.0100	96
13	2.03	.26	-.0754	51	13	0.95	.69	-.0572	50
17	2.65	.14	-.0160	6	17	1.25	.54	.0554	38
19	2.97	.10	.0147	4	19	1.39	.48	.0935	57
23	3.59	.05	.0486	7	23	1.68	.36	.0755	35
25	3.90	.03	.0465	5	25	1.83	.31	.0	0
					29	2.12	.24	-.709	215
					31	2.27	.21	.681	180
					35	2.56	.16	0	0
					37	2.71	.13	-.0575	10
					41	3.00	.10	-.0613	8
					43	3.15	.08	-.0333	4
59	9.21	.0002	-.596	0.3	59	4.32	.03	-.243	8
61	9.53	.0002	.575	0.2	61	4.46	.02	.212	6

Table 6.5 Resultant values of winding-harmonic tangential field strength at the peak of the stator fundamental m.m.f. $(\vartheta_2 = 0)$ and at the zero of the fundamental m.m.f. $(\vartheta_2 = 90°)$ for the two industrial machines of table 6.1

		k	n	$f=6kf_1$	$(\dot{H}_{xm})6k\omega$		$\lvert\dot{H}_{xo}\rvert\,6k\omega$	
					$\vartheta_2=0$	$\vartheta_2=90°$	$\vartheta_2+\phi_{dk}=0$	$\vartheta_2+\phi_{dk}=90°$
500 MVA turbo-generator		1	5, 7	$6f_1$	4350	16250	3780	10120
		2	11,13	$12f_1$	13550	2950	5980	1640
		3	17,19	$18f_1$	210	1030	88	382
		4	23,25	$24f_1$	1185	215	400	84
		5	29,31	$30f_1$	19	119	7	37
60 MVA salient-pole machine		1	5, 7	$6f_1$	5360	5360	2518	2518
		2	11,13	$12f_1$	7830	2490	2645	1075
		3	17,19	$18f_1$	5120	1040	1191	163
		4	23,25	$24f_1$	1880	1880	384	384
slot harmonics →		5	29,31	$30f_1$	1900	20940	447	3677

Note: At $\vartheta_2=0$, $H_{6k\omega}=\lvert H_{6k+1} + H_{6k-1}\rvert$ A/m

and at $\vartheta_2=90°$, $H_{6k\omega}=\lvert H_{6k+1} - H_{6k-1}\rvert$ A/m

where H_{6k+1} and H_{6k-1} are given in table 6.2;

ϕ_{dk} see eqn. 6.64
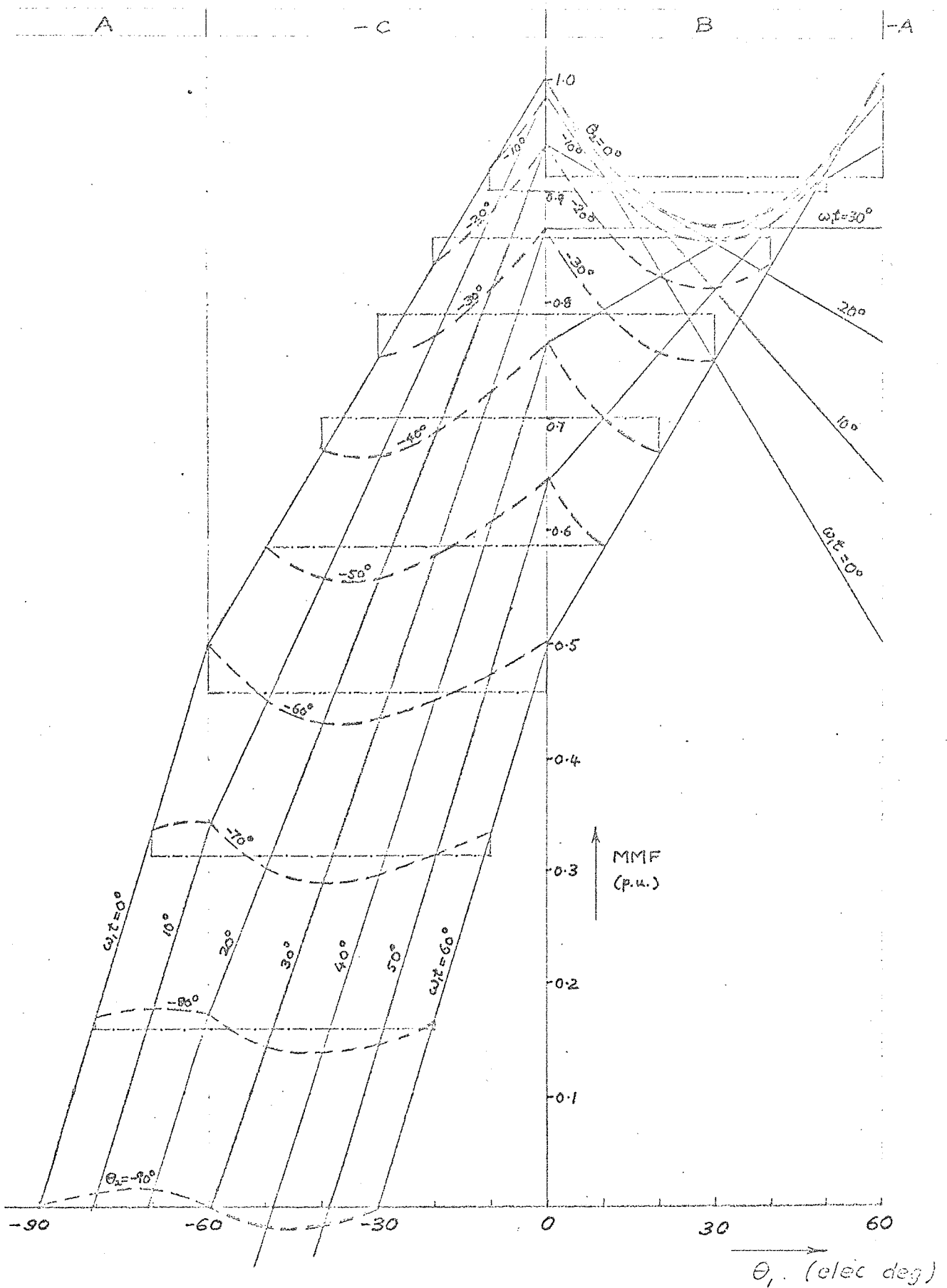
Fig. 2.2 M.m.f. of 3-phase, 60°-spread, infinitely-distributed, full-
pitched stator winding
———— variation in space at 10° intervals in time, relative to the
stator(ϑ_1 = position angle relative to the stator with origin
at ₵ of A-phase coils, $\omega_1 t$ = 0 when A-phase current is at
its maximum)
- - - - variation with time ($\omega_1 t$), relative to the fundamental (—·—),
at several positions on the fundamental (ϑ_2=0°, -10°, -20°....)
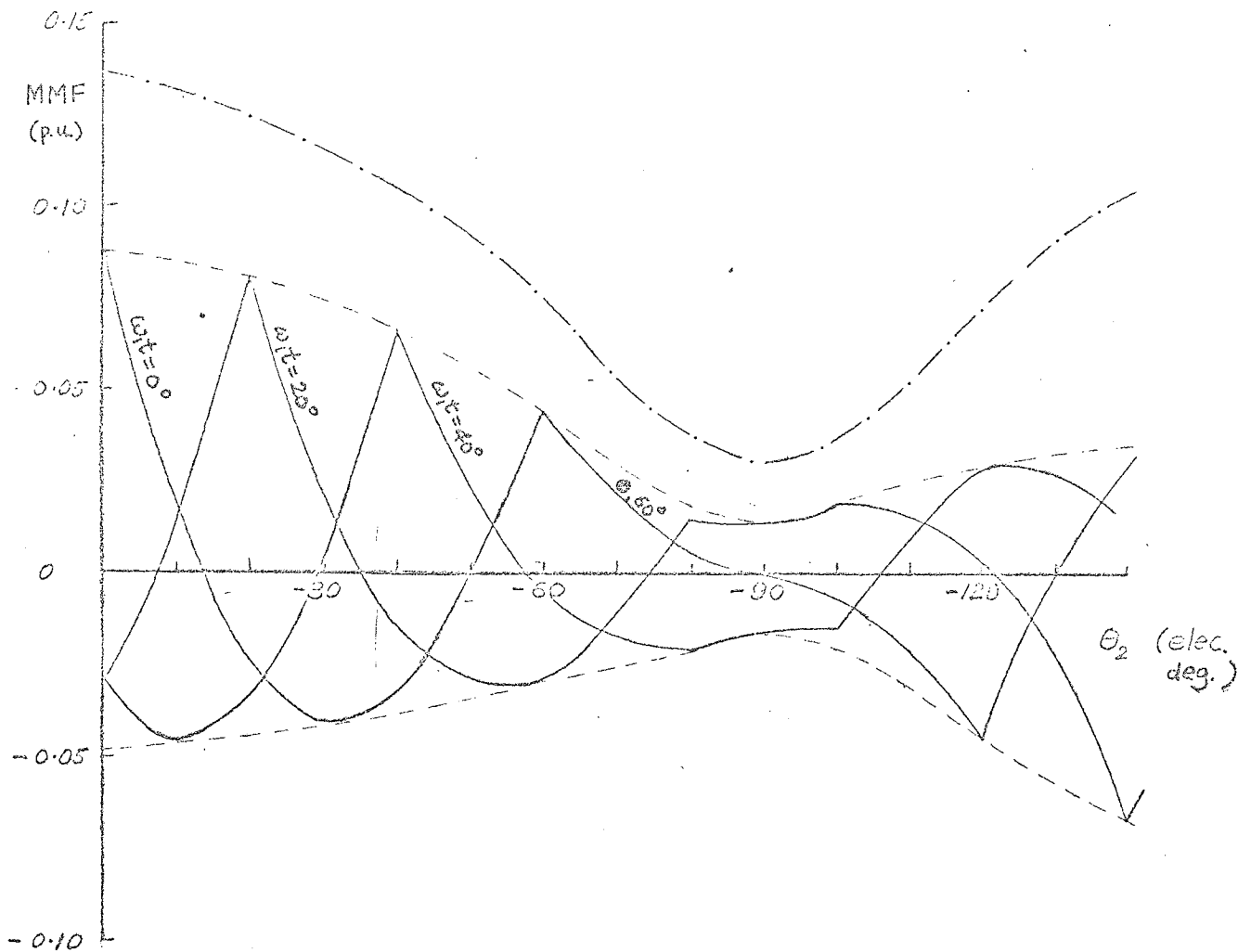
Fig. 2.3 M.m.f. of full-pitched, 3-phase, 60°-spread, infinitely-distributed stator winding

———— variation in space, at 20° intervals in time, relative to the fundamental (ϑ_2= position angle relative to the peak of the fundamental m.m.f.)

—·— peak-peak amplitude of the variation, i.e. the amplitude of the envelope (----) of the space variations
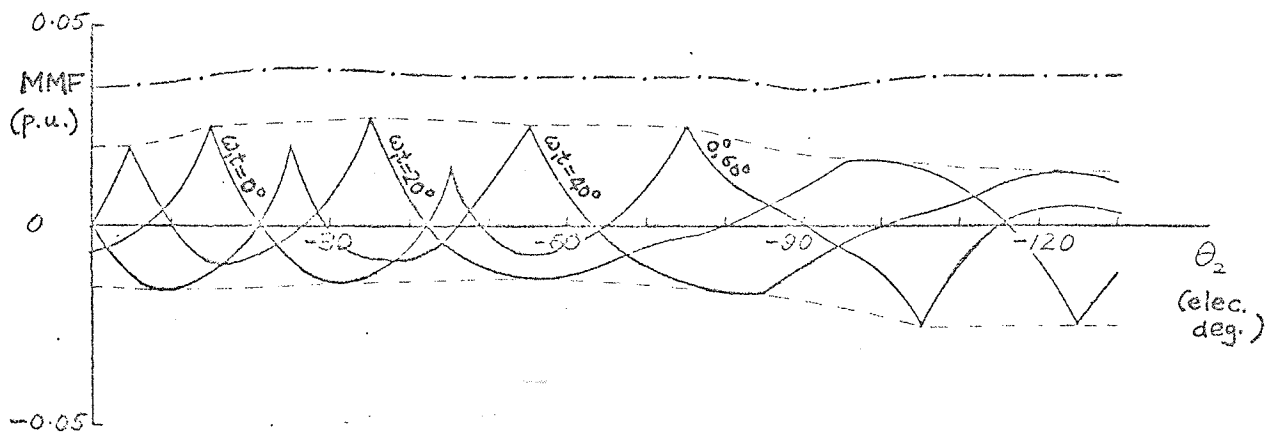
Fig. 2.5 M.m.f. of 5/6-pitched, 3-phase, 60°-spread, infinitely-distributed winding

——·— } as for fig. 2.3 above
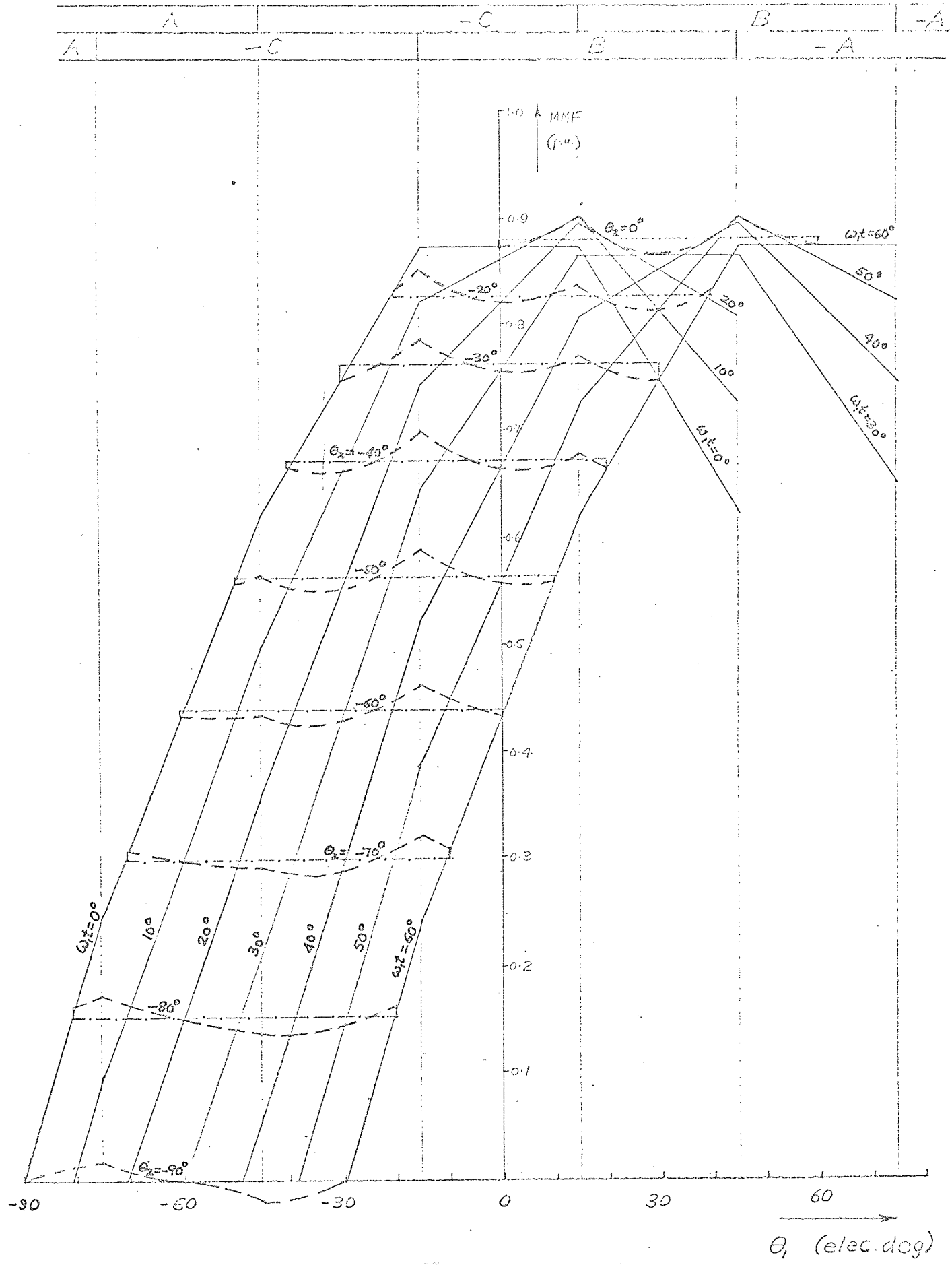
Fig. 2.4 M.m.f. of 5/6 pitched, 3-phase, 60°-spread, infinitely-
distributed stator winding

———
---- } as for fig. 2.2
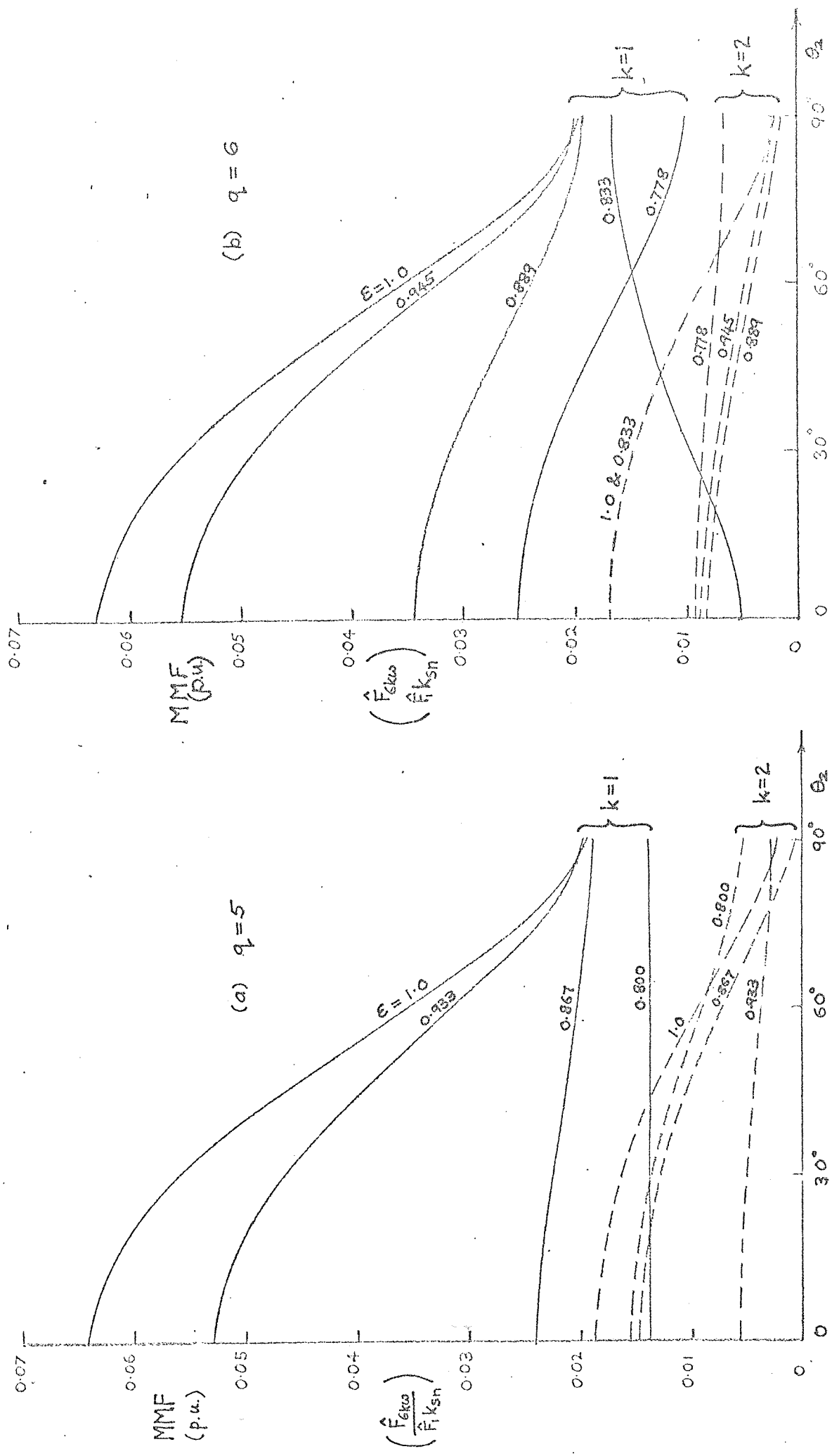
Fig. 2.9 Amplitude of the resultant m.m.f. of a pair of stator winding harmonics ($\hat{F}_{16k\omega}$) as a function of position relative to the peak of the fundamental m.m.f. for several practical pitches (ε) and for the first two pairs of harmonics

——— resultant of the 5th and 7th harmonics
— — — resultant of the 11th and 13th harmonics

(a) 5 slots per pole and phase
(b) 6 slots per pole and phase
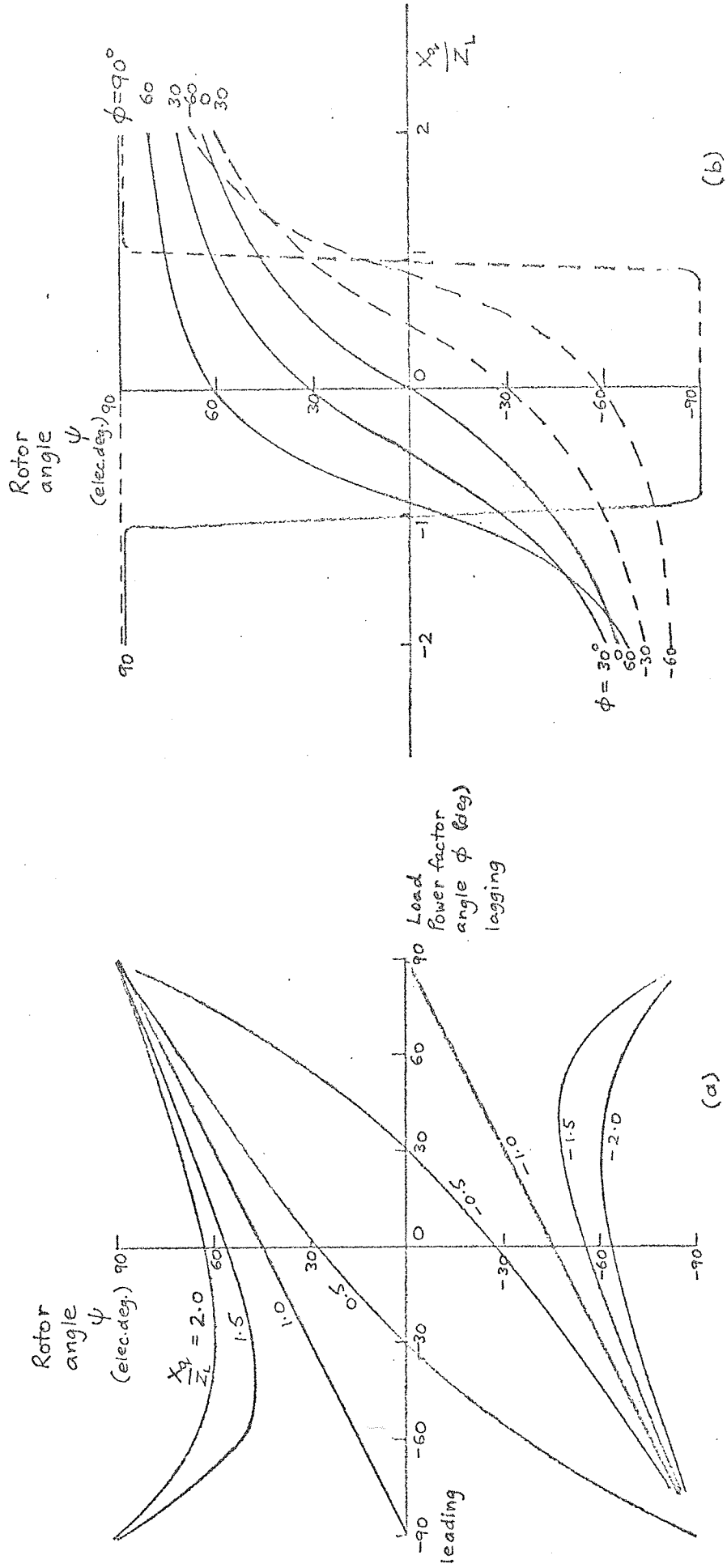
Fig. 2.12 Rotor angle relative to the stator fundamental m.m.f. (ψ) ($R_a/R_L \ll 1$ in eqn. 2.17)

(a) Variation of ψ with power factor angle ϕ (b) Variation of ψ with $X_q/X_L = IX_q/V$ for constant
for constant values of $X_q/Z_L = IX_q/V$ values of power factor angle ϕ
          —— lagging p.f.
          — — leading p.f.
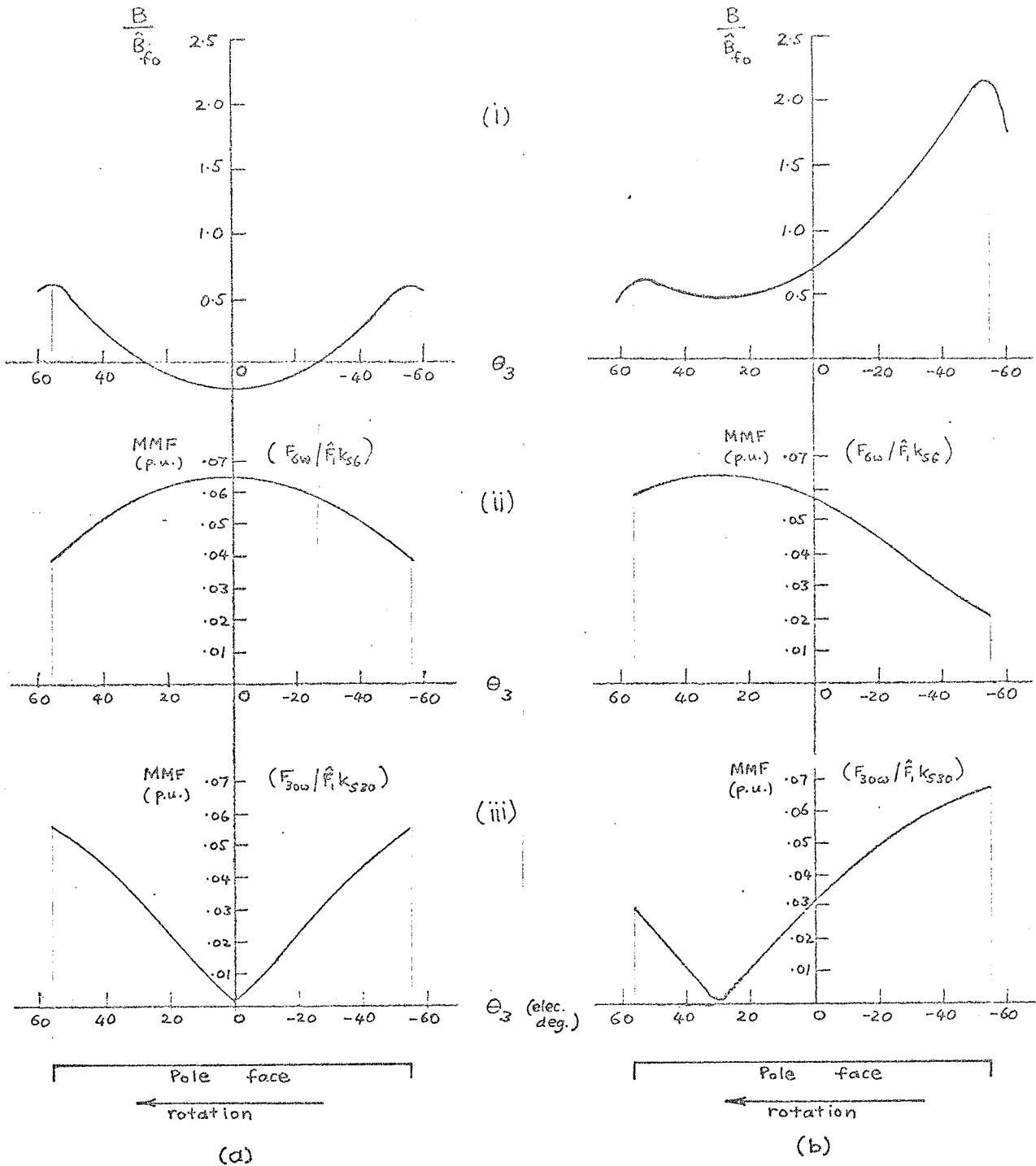
Fig. 2.13 Resultant amplitude of stator winding harmonic pairs and main flux density over the pole face (Ginsberg and Jokl 30 kW salient-pole machine no. 4)
(i) Calculated main flux density
(ii) Resultant of 1st phase-band pair (n = 5,7)
(iii) Resultant of 1st slot-harmonic pair (n = 29,31)

(a) Rated current short circuit   (b) Rated kW, 0.8 p.f. lagging

$$90^\circ + \psi = 180^\circ$$ $$90^\circ + \psi = 151^\circ$$
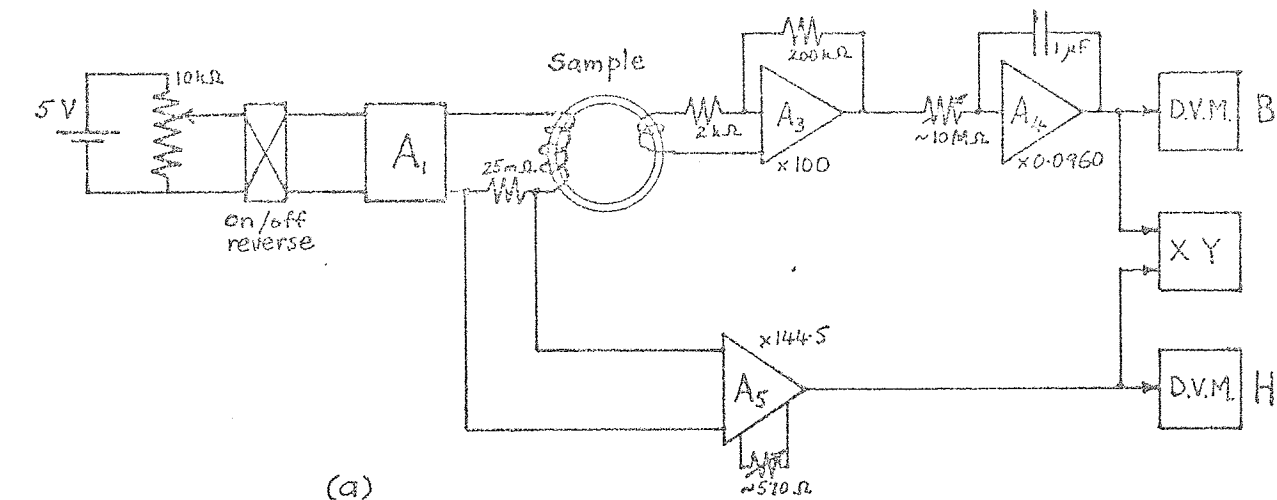
(a)
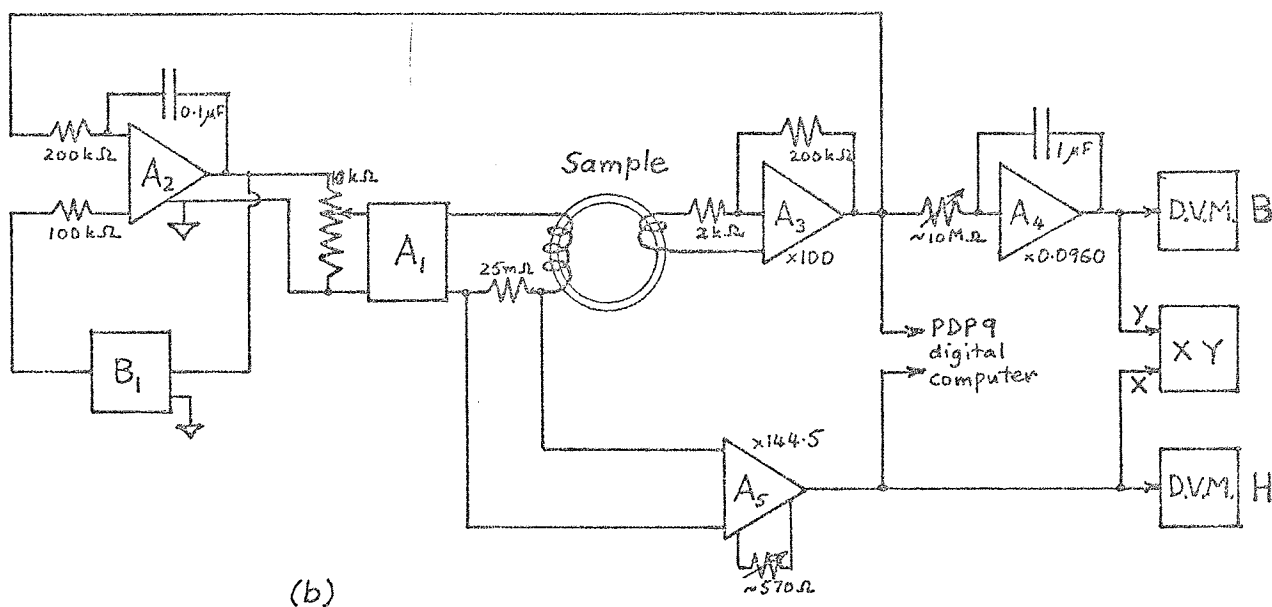
(b)

Fig. 4.1   Circuits for measurement of magnetic characteristics
(a)   Ballistic* and slowly-varying flux methods
(b)   Uniformly-varying flux method

A_1 Mazzetti and Soardo power amplifier (with dual
             input transistor S.G.S. BFX 16 612)

A_2 Burr Brown model 3010 chopper stabilised operational
             amplifier (low drift)

A_3, A_4 Burr Brown model 3071 chopper stabilised operational
             amplifier (low drift, low noise)

A_5 Burr Brown model 3061 instrumentation amplifier

B_1 Mazzetti and Soardo bistable (with 9.1 V zener diode
             input reference to give switching at 9.1 V and
             with Multiar circuit coupling transformer L_1 = 7 mH,
             $N_1 : N_2$ = 1:5, ferrite pot core)

D.V.M. Solartron digital voltmeter LM1402 $\left(\begin{array}{l}\text{lowest range } 0.00 \\ \text{to } 20.00 \text{ mV}\end{array}\right)$
XY   Houston Instrument model HR 92 X-Y recorder

*A_3 and A_4 were replaced by a single integrator of gain 9.60
             if the flux-coil ouput saturated A_3 in a ballistic
             test.

Maximum output of all amplifiers = 10 V

B (τ)

−1·5

−1·0

−0·5

0

−200

Br (τ)   Hc (A/m)
1·5   300

1·0   200

0·5   100

0   0

Hc

Br

0   0·5   1·0   1·5   2·0
Bm (τ)

H (A/m)

1000   800   600   400   200   2000   3000   4000   5000

Fig 4.2   Hysteresis loops by the uniformly-varying
          flux method
          $\frac{d\phi}{dt} = 0.015$ mWb/s

Inset   Coercive force and remanent flux density
        against loop maximum flux density
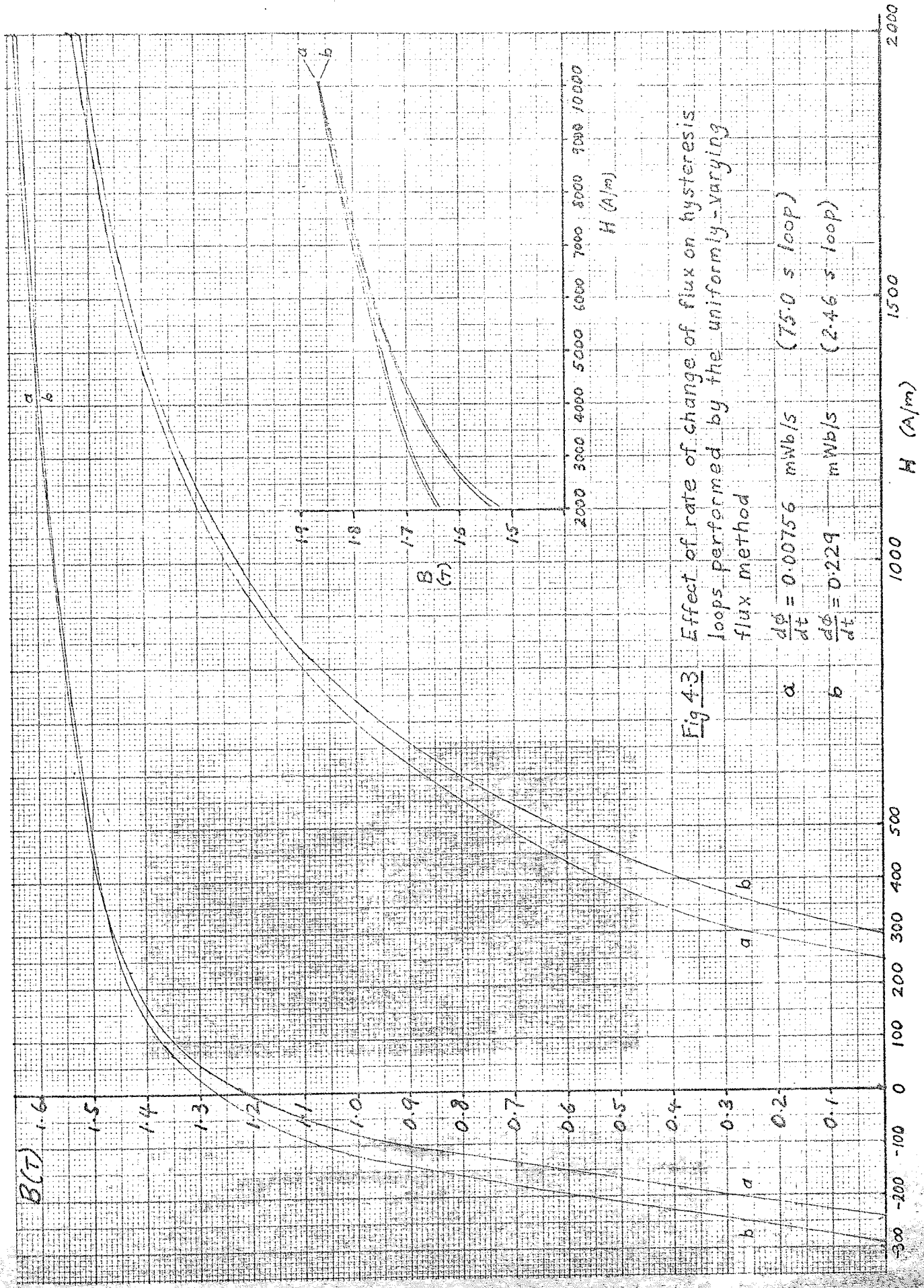
Fig 4.3 Effect of rate of change of flux on hysteresis loops performed by the uniformly-varying flux method

a $\dfrac{d\phi}{dt} = 0.00756$ mWb/s (75.0 s loop)

b $\dfrac{d\phi}{dt} = 0.229$ mWb/s (2.46 s loop)
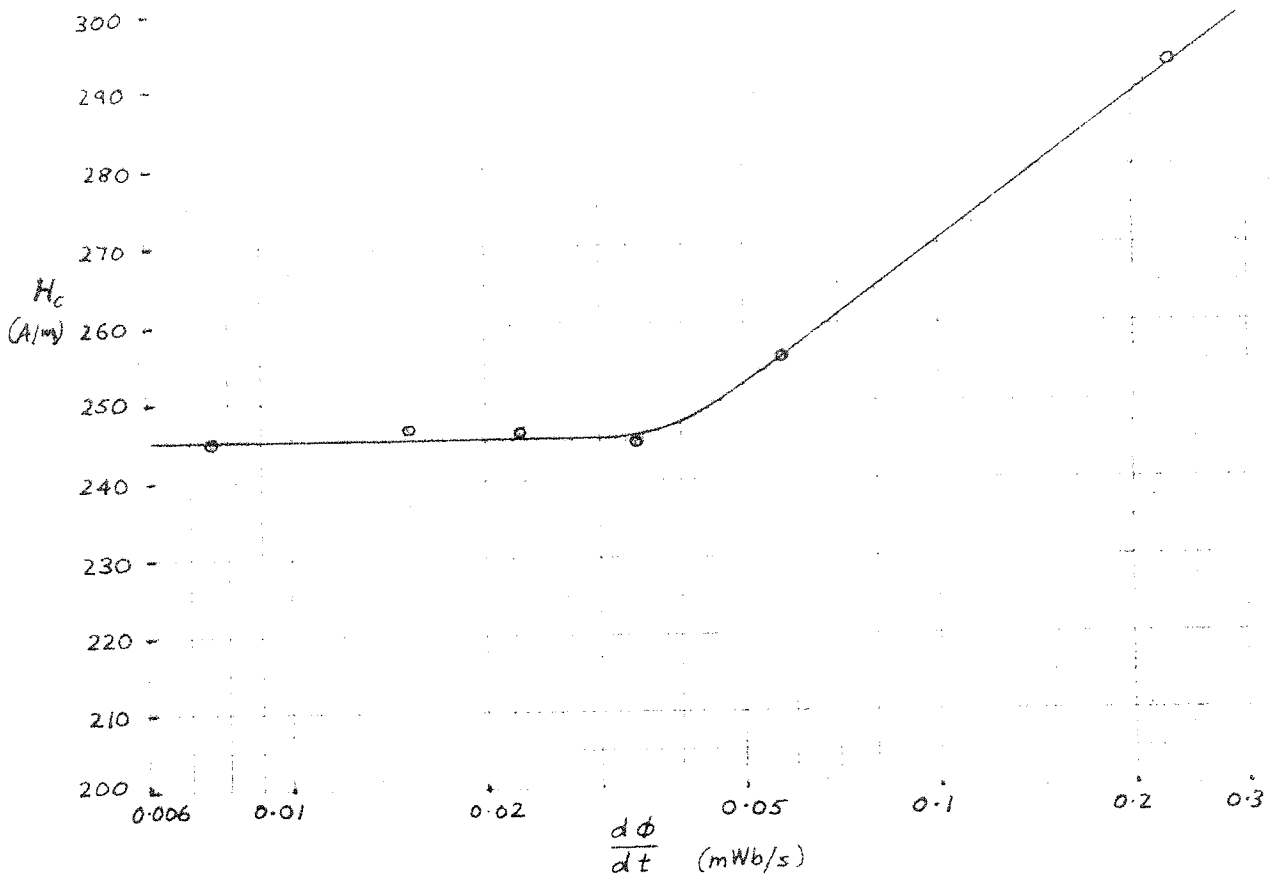
Fig. 4.4   Effect of rate of change of flux on apparent coercive force of a hysteresis loop (H_m = 10000 A/m, B_m = 1.86 T) taken by the uniformly-varying flux method
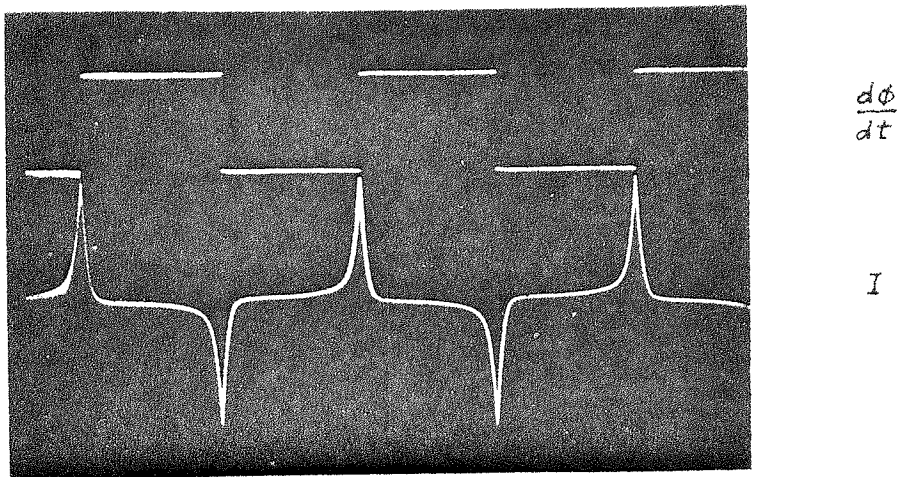
Fig. 4.5   Flux-coil output (proportional to $\frac{d\phi}{dt}$) and magnetising-coil current for the uniformly-varying flux method
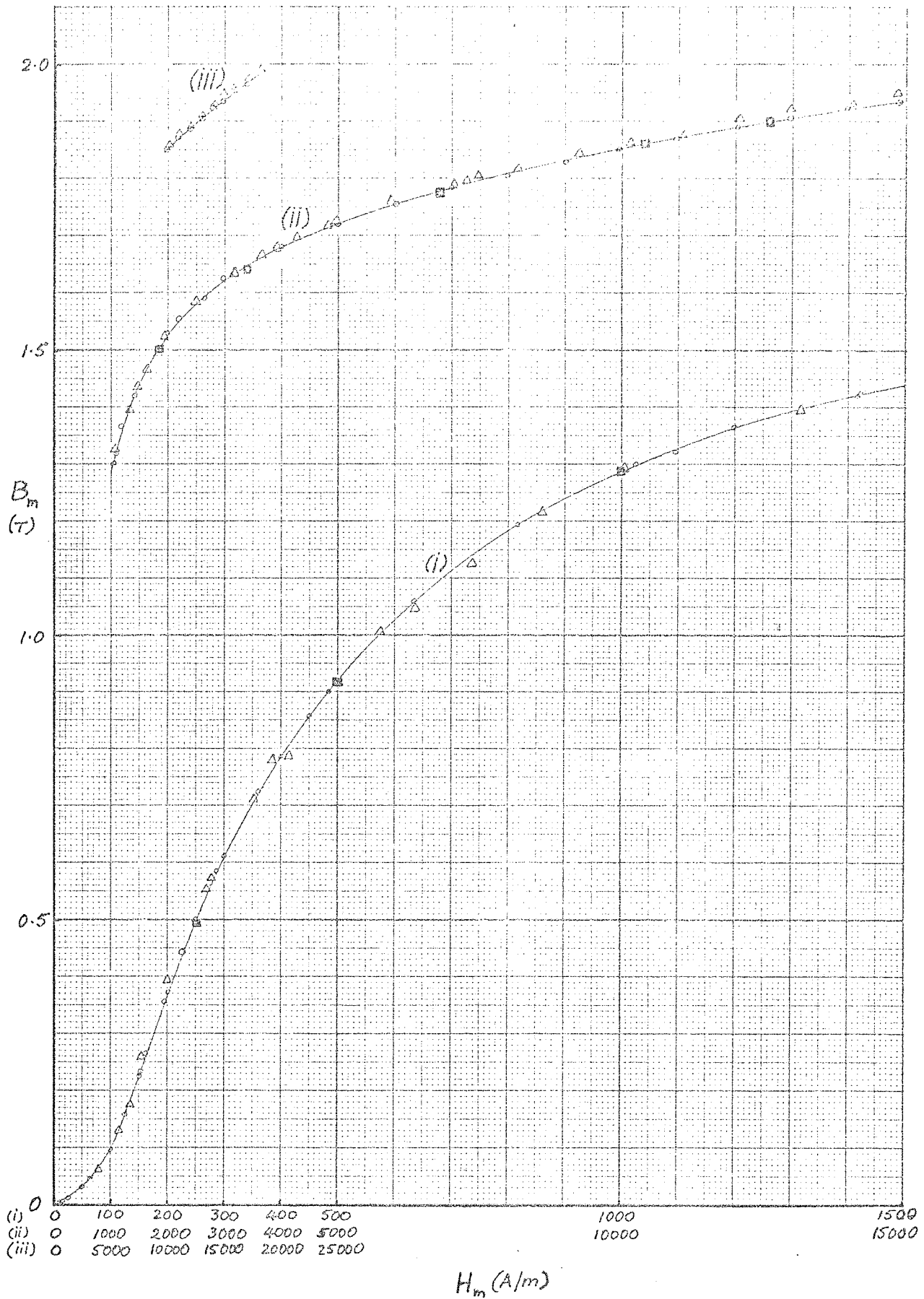
Fig. 4.7   Normal magnetisation curve from hysteresis loops
           performed by three methods

   o   Ballistic (sudden reversals)

   ▲   Uniformly-varying flux

   □   Slowly-varying flux
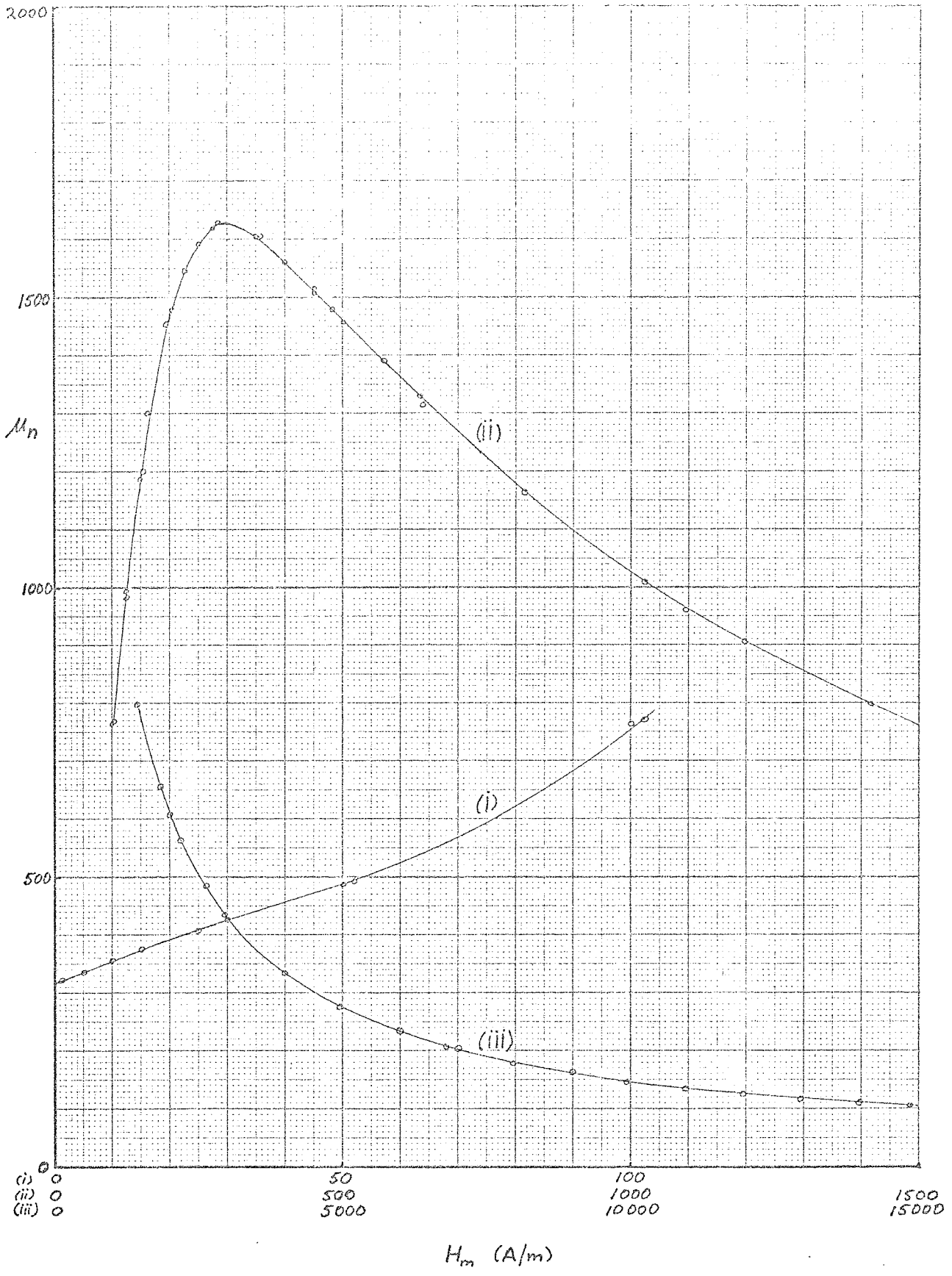
Fig. 4.8 Normal permeability calculated from the ballistic curve
of fig. 4.7 ($\mu_n = \frac{B_m}{\mu_0 H_m}$) plotted against H_m
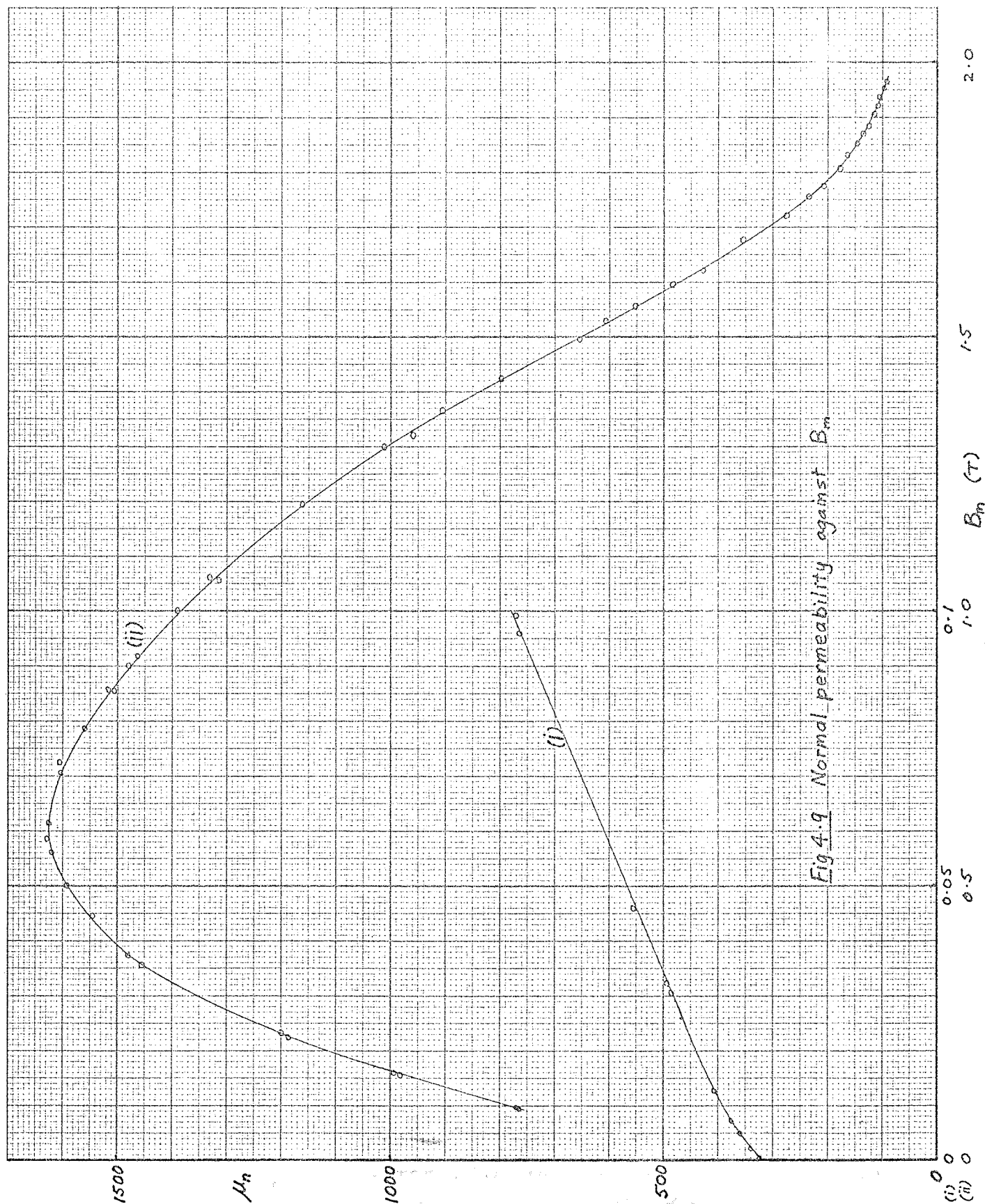
Fig 4.9 Normal permeability against B_m
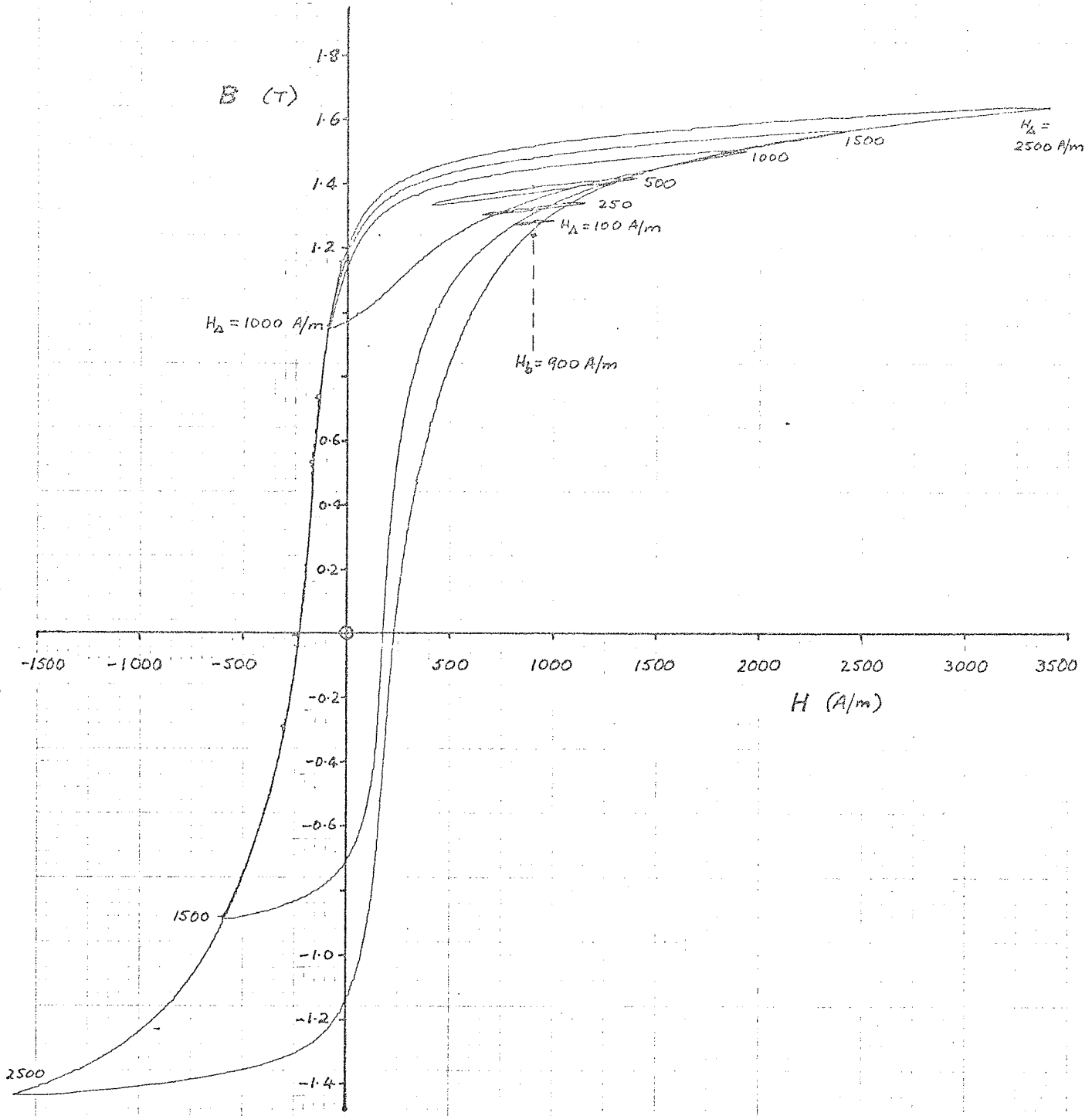
Fig 4.12   Incremental loops on the normal magnetisation
curve recorded with XY plotter using
slowly-varying flux method

$H_b = 900$ A/m

H_Δ as shown
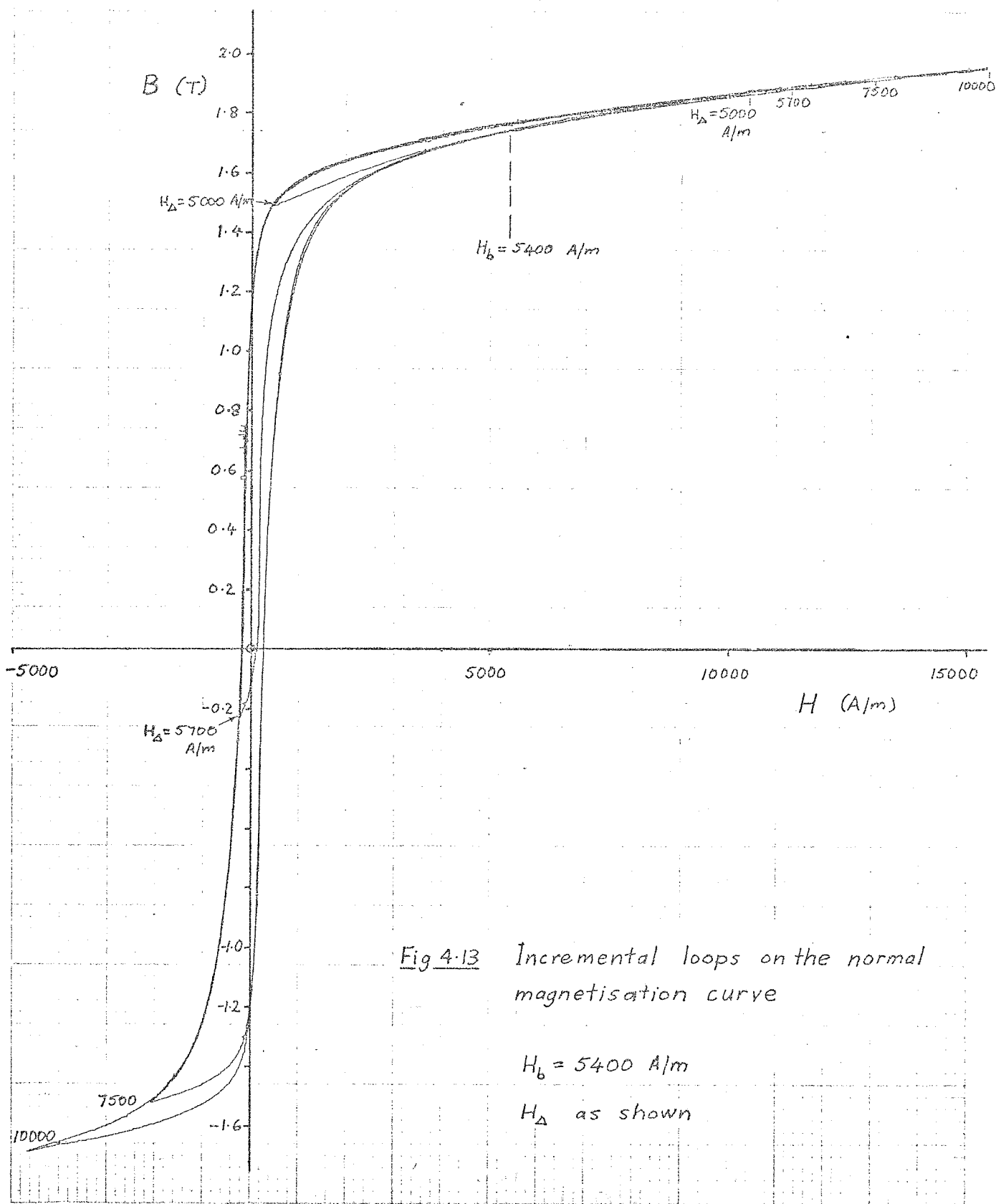
Fig 4.13   Incremental loops on the normal
magnetisation curve

$H_b = 5400$ A/m

H_Δ as shown
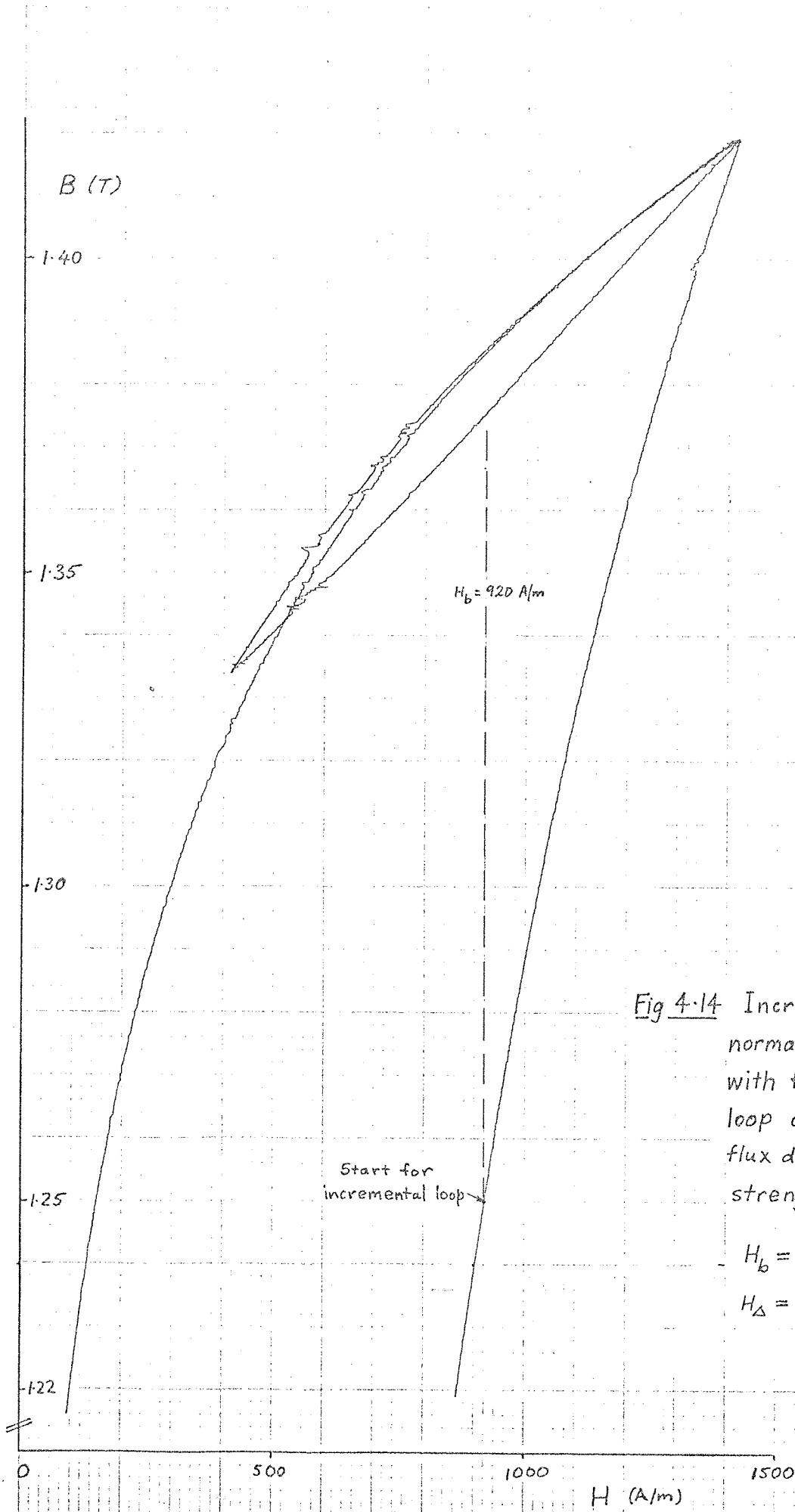
Fig 4.14 Incremental loop on the normal magnetisation curve, with the tip of the normal loop of the same peak flux density and field strength

$H_b = 920$ A/m

$H_\Delta = 500$ A/m
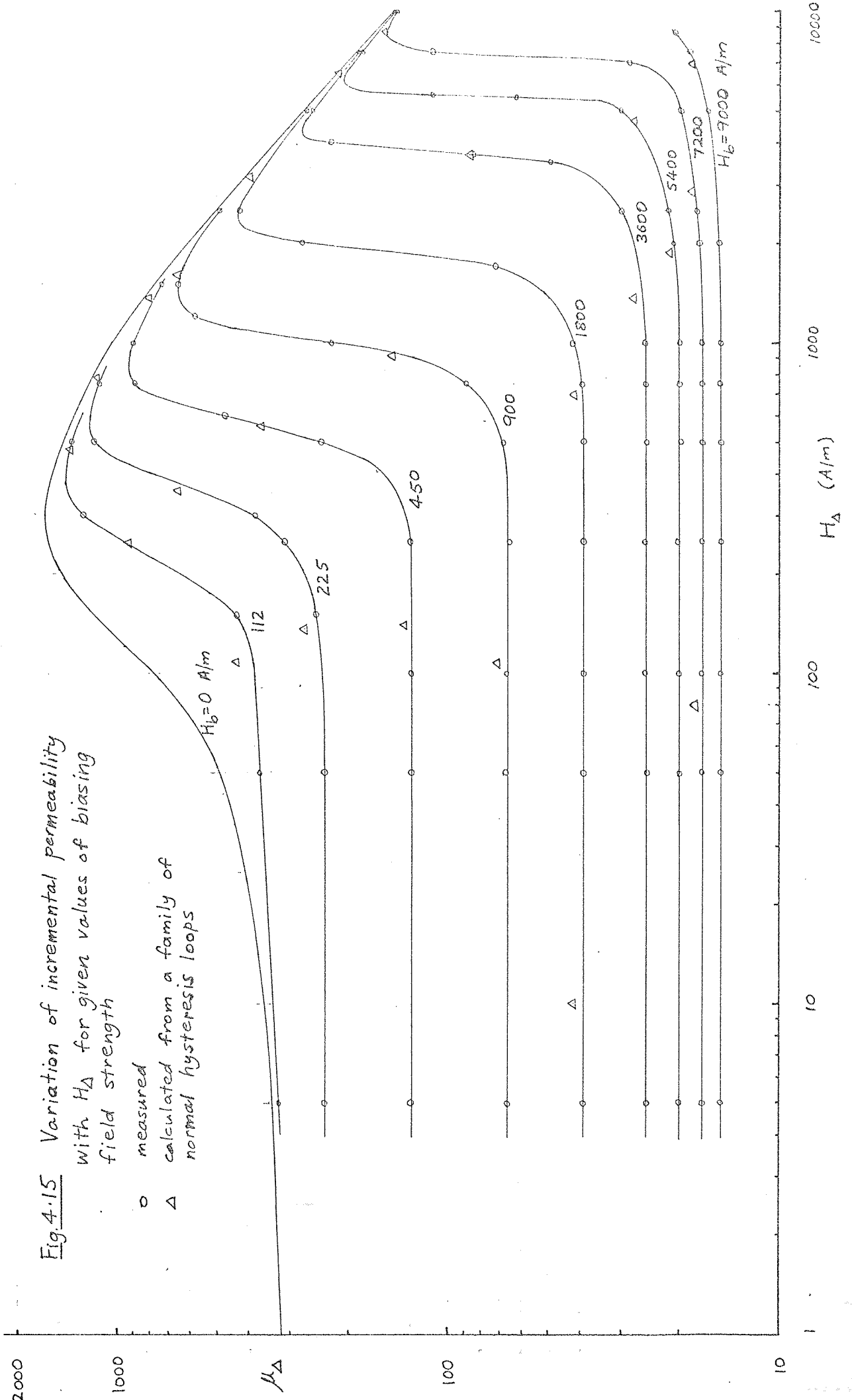
Fig. 4.15 Variation of incremental permeability with H_Δ for given values of biasing field strength

o   measured
△   calculated from a family of normal hysteresis loops

Fig.4.16 Variation of incremental permeability with B_Δ for given values of biasing field strength

o   measured

△   calculated from the normal magnetisation curve for $H_b = 900$ A/m

□   calculated from normal hysteresis loops for $H_b = 900$ A/m
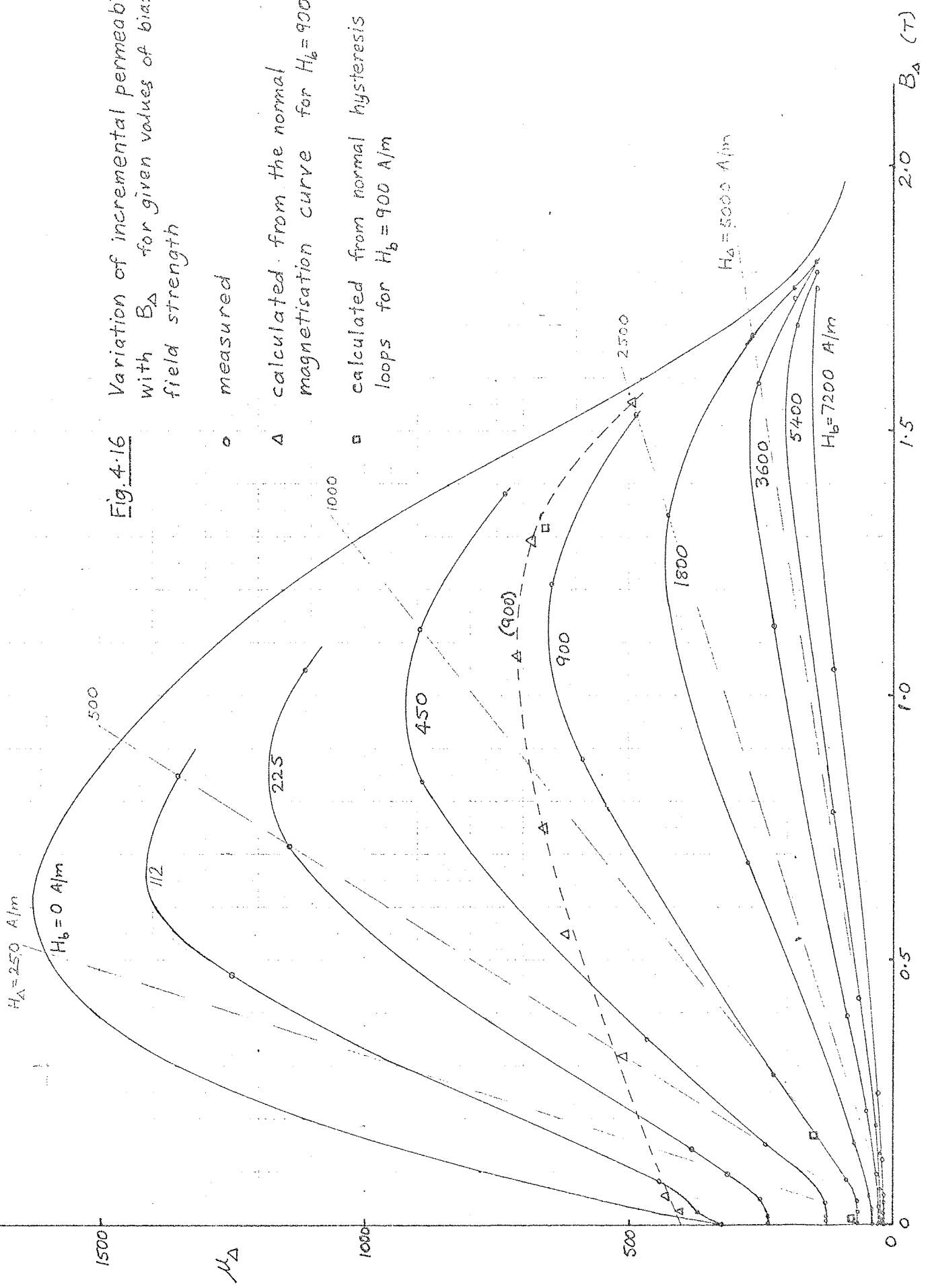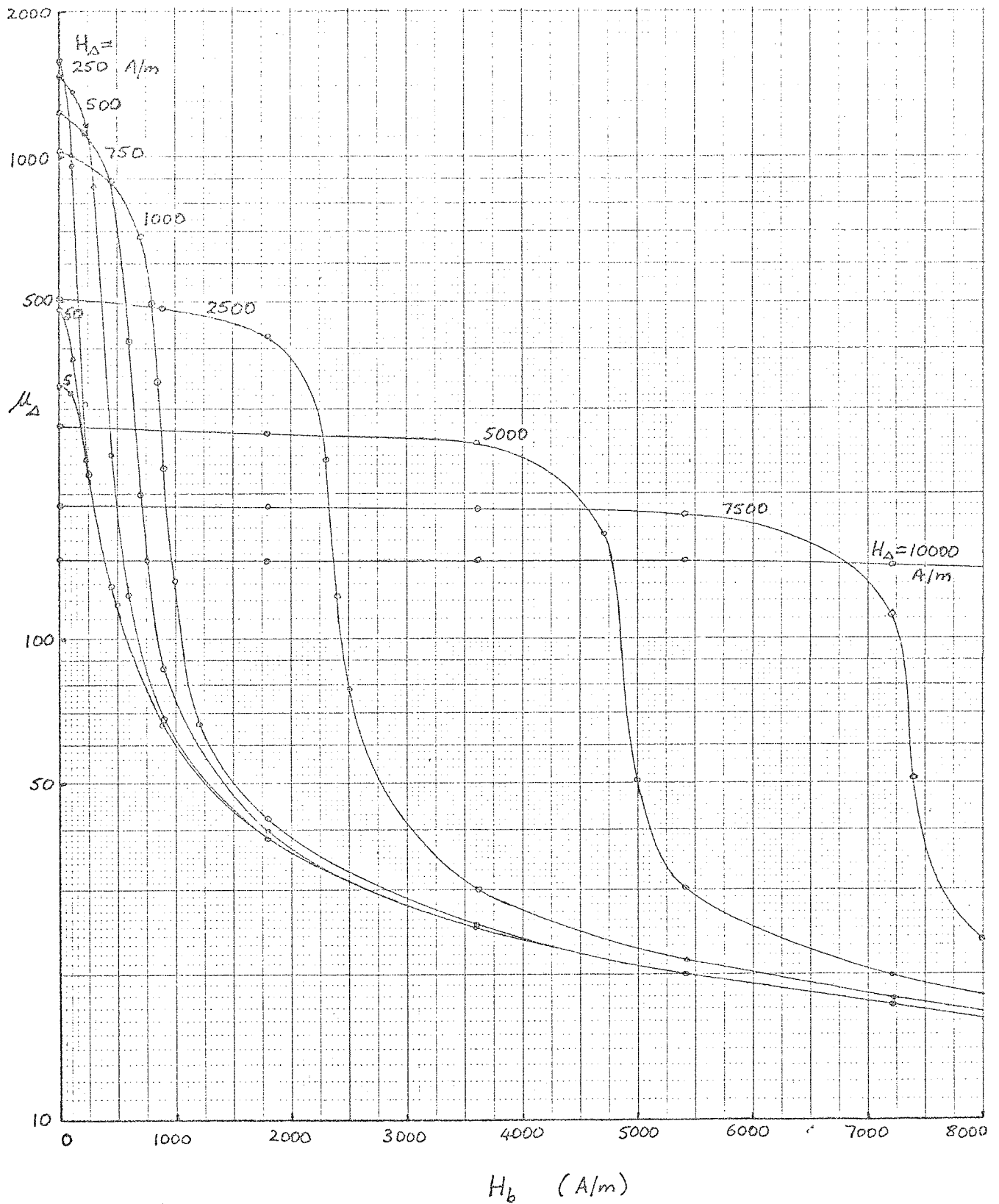
Fig. 4.17 Variation of incremental permeability with biasing field
strength for given values of H_Δ
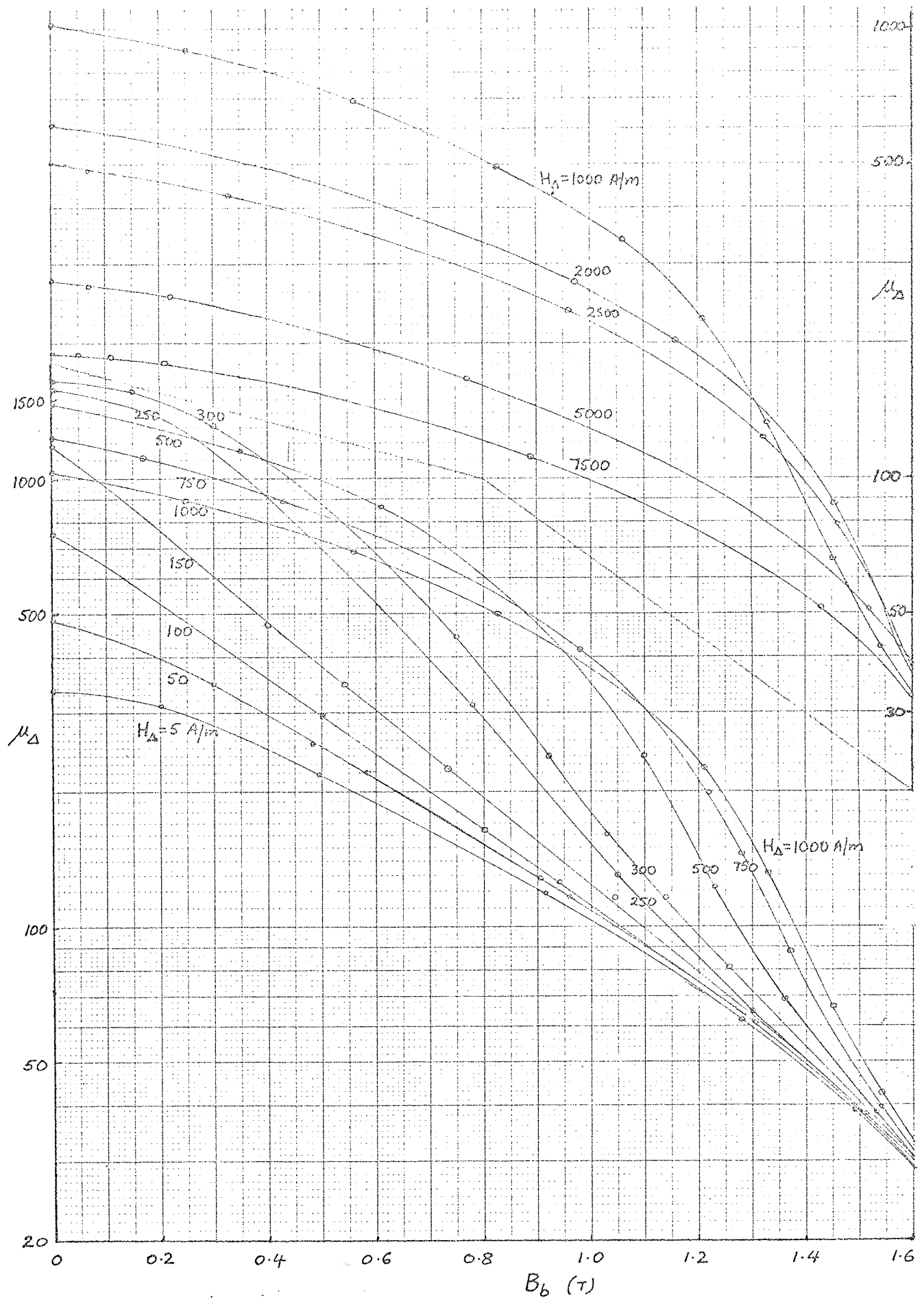
Fig. 4.18   Variation of incremental permeability with biasing flux
density for given values of H_Δ

Fig. 4.19 Variation of incremental permeability with H_Δ for given values of biasing flux density
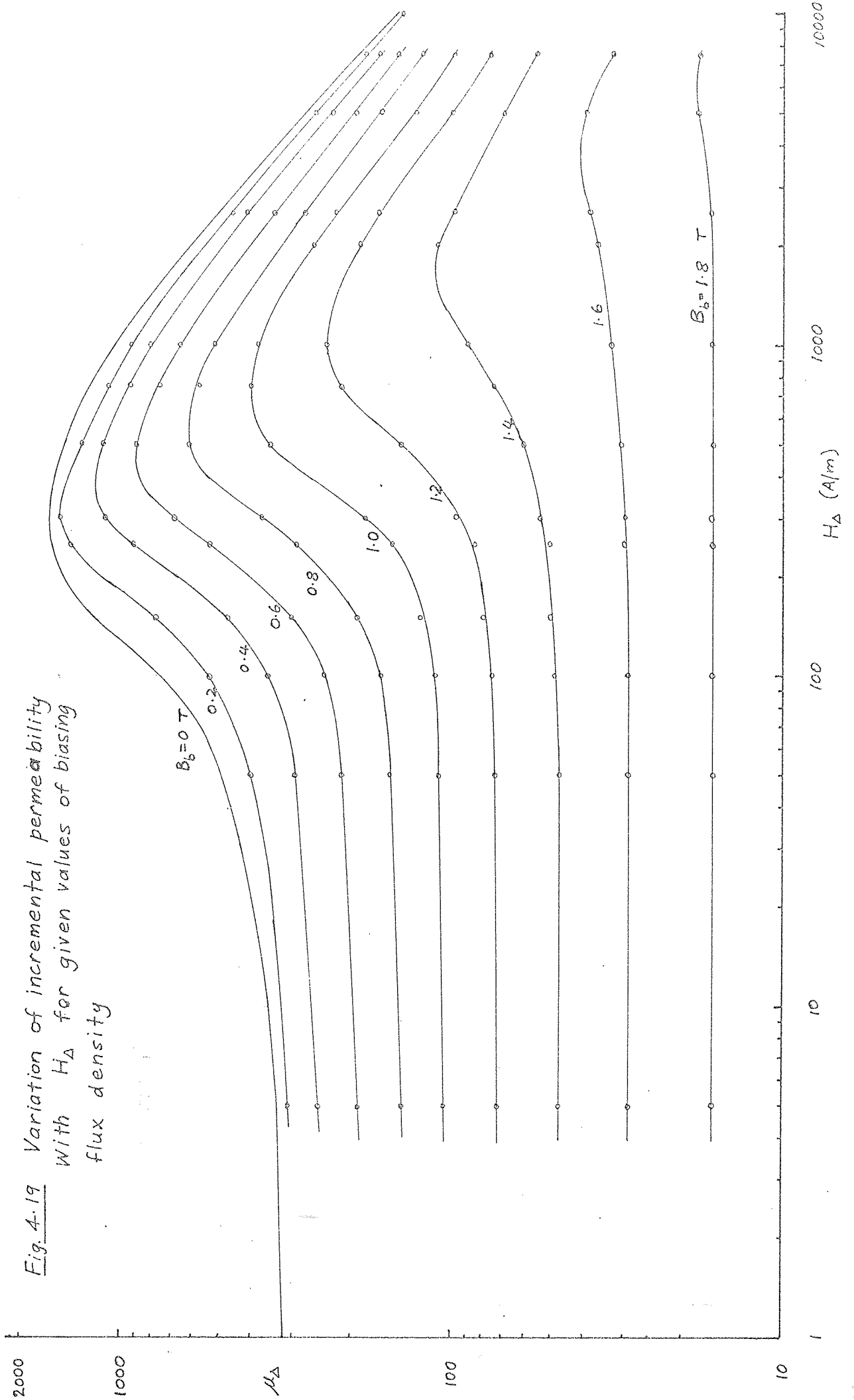
Fig. 4.20   Variation of incremental permeability
with B_Δ for given values of
biasing flux density
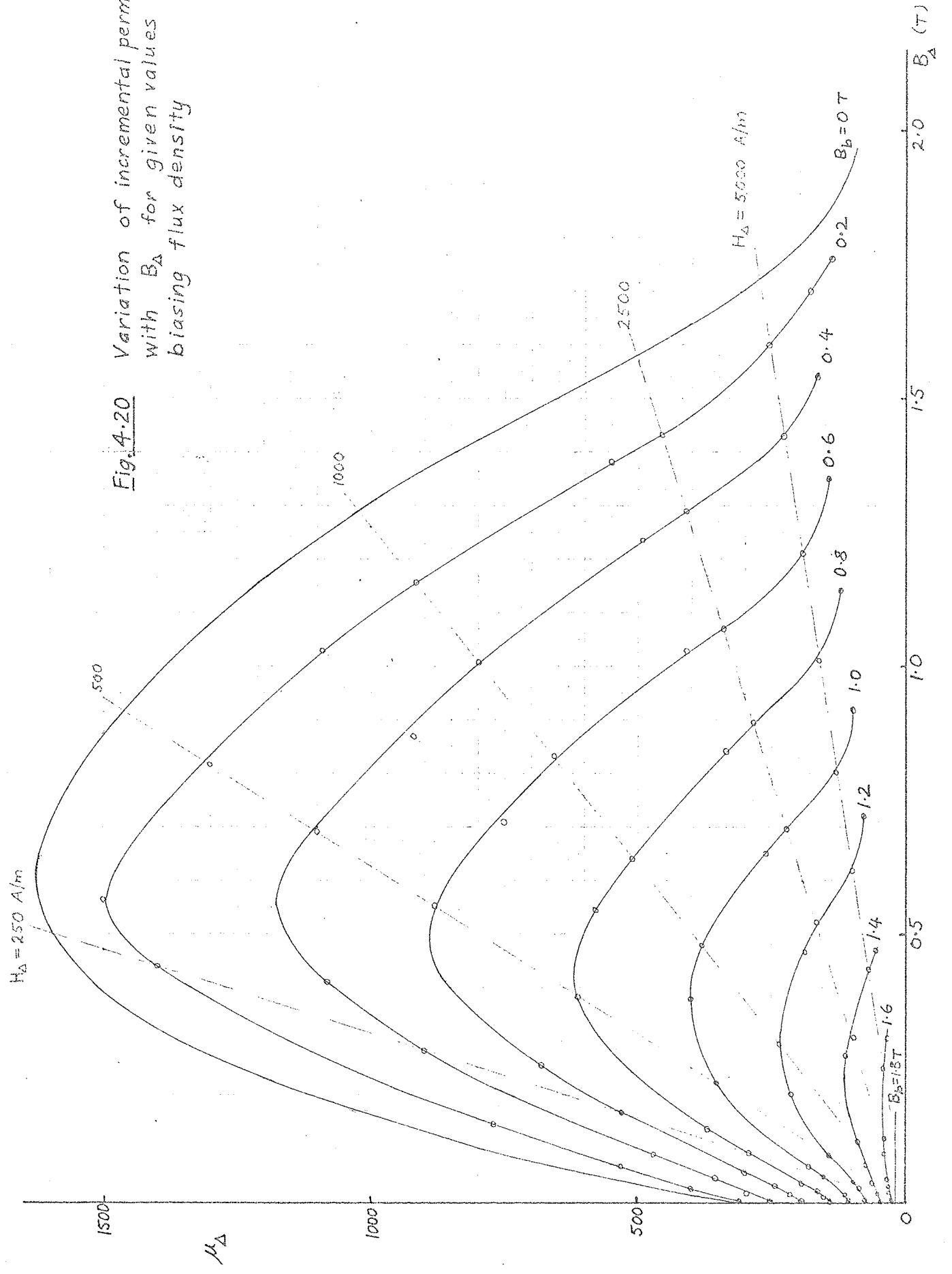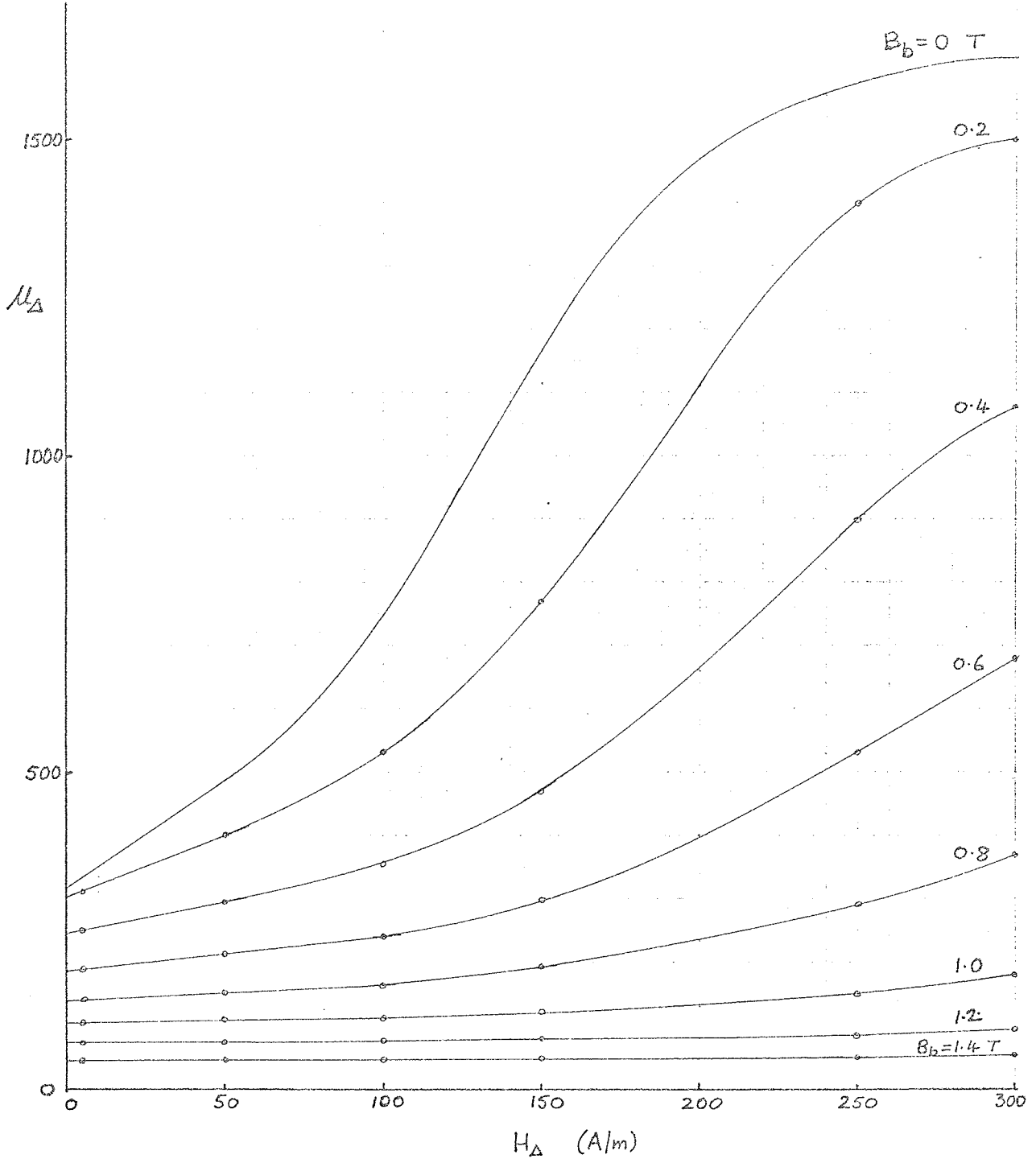
Fig. 4.21 Variation of incremental permeability with small H_Δ for given values of biasing flux density(the low H_Δ part of fig. 4.19, but with linear scales)

Fig 4.22   Variation of incremental permeability with B_Δ for given values of peak flux density

Normal permeability ($B_m = B_\Delta$)

$B_m = 1.8\,T$

1.6

1.4

1.2

1.0

0.8

0.6

0.4

0.2

μ_Δ

1500

1000

500

0

0.5   1.0   1.5   2.0 B_Δ (T)
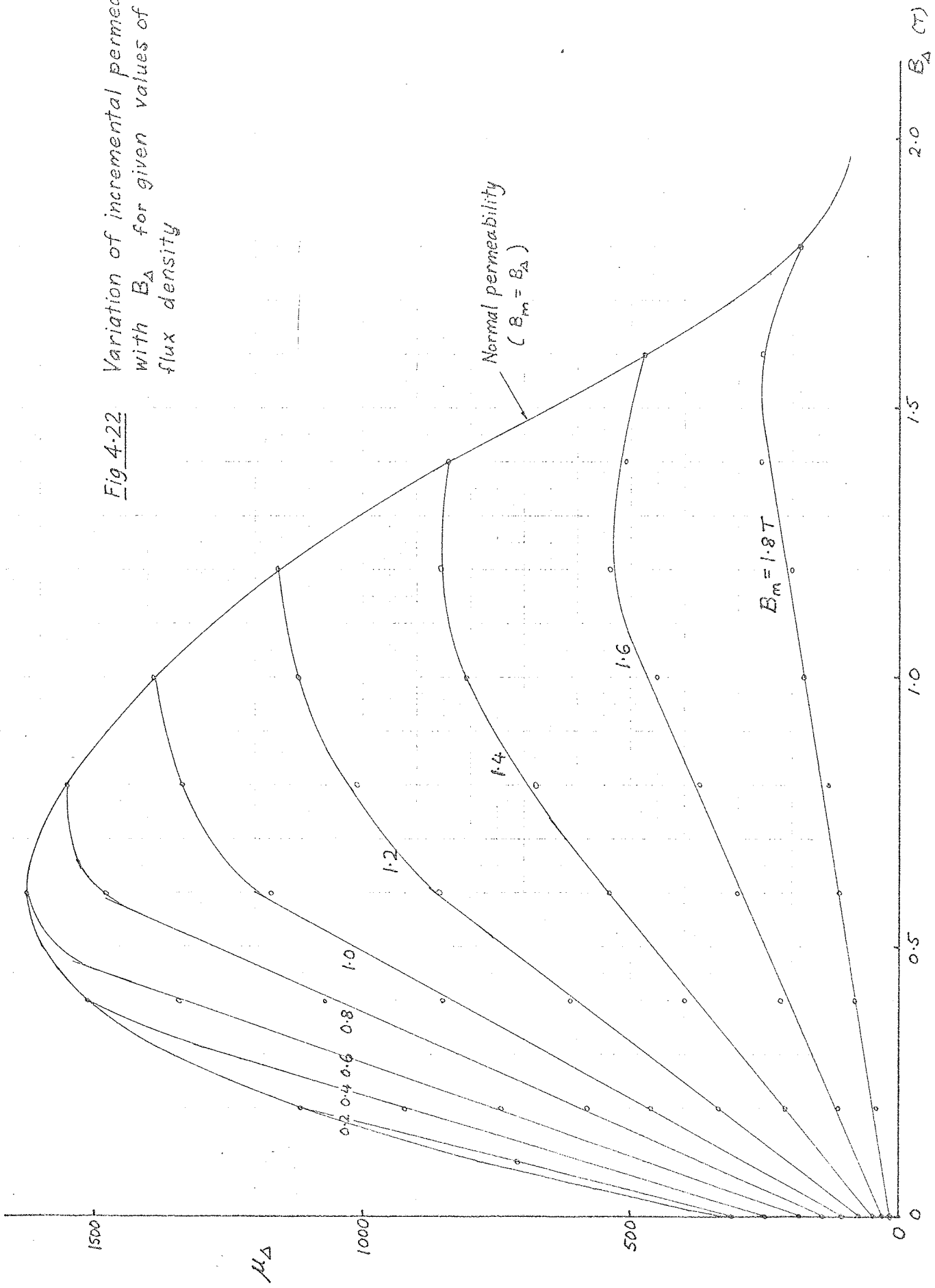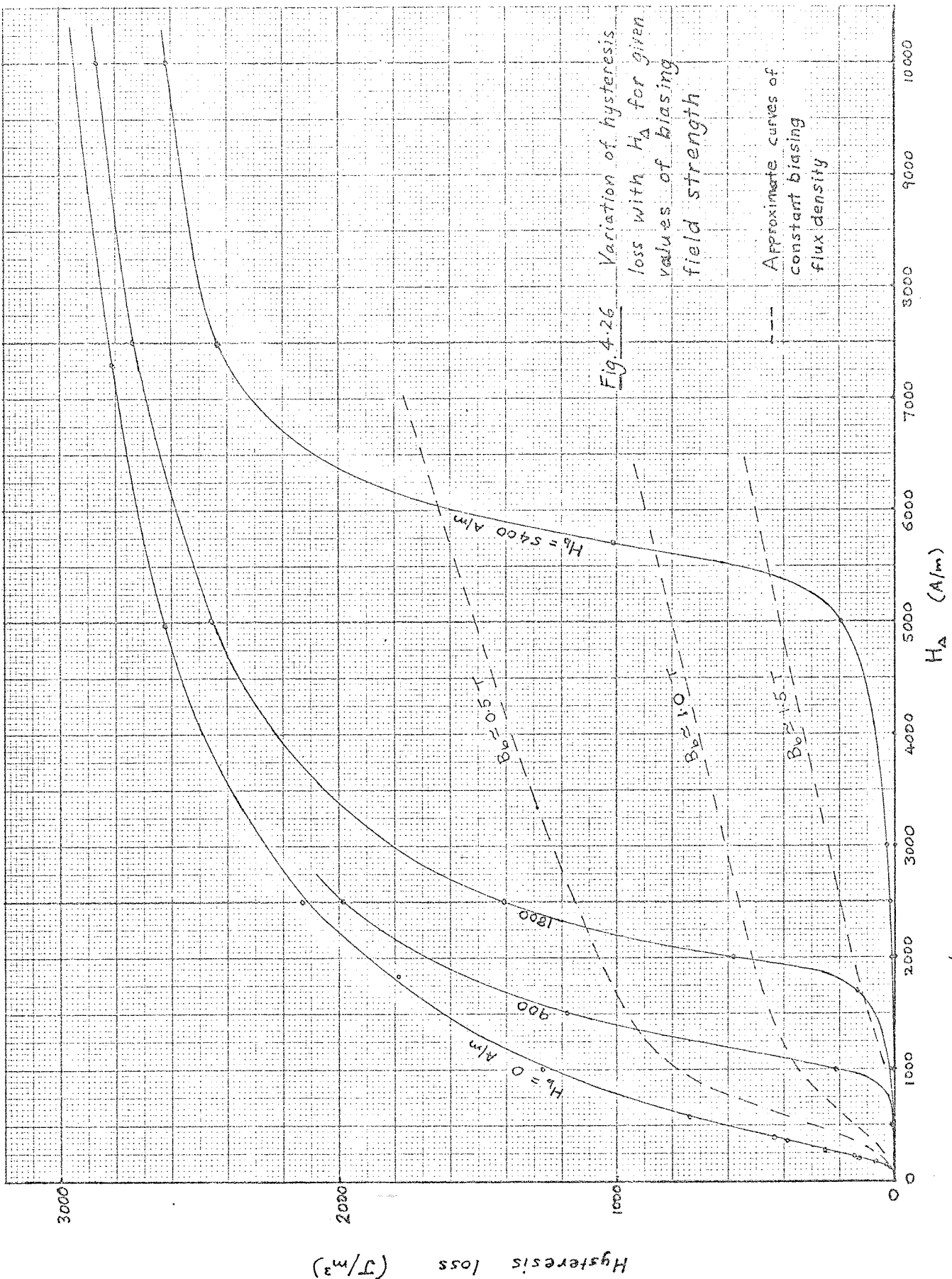
Fig. 4.26 Variation of hysteresis loss with H_A for given values of biasing field strength

——— Approximate curves of constant biasing flux density
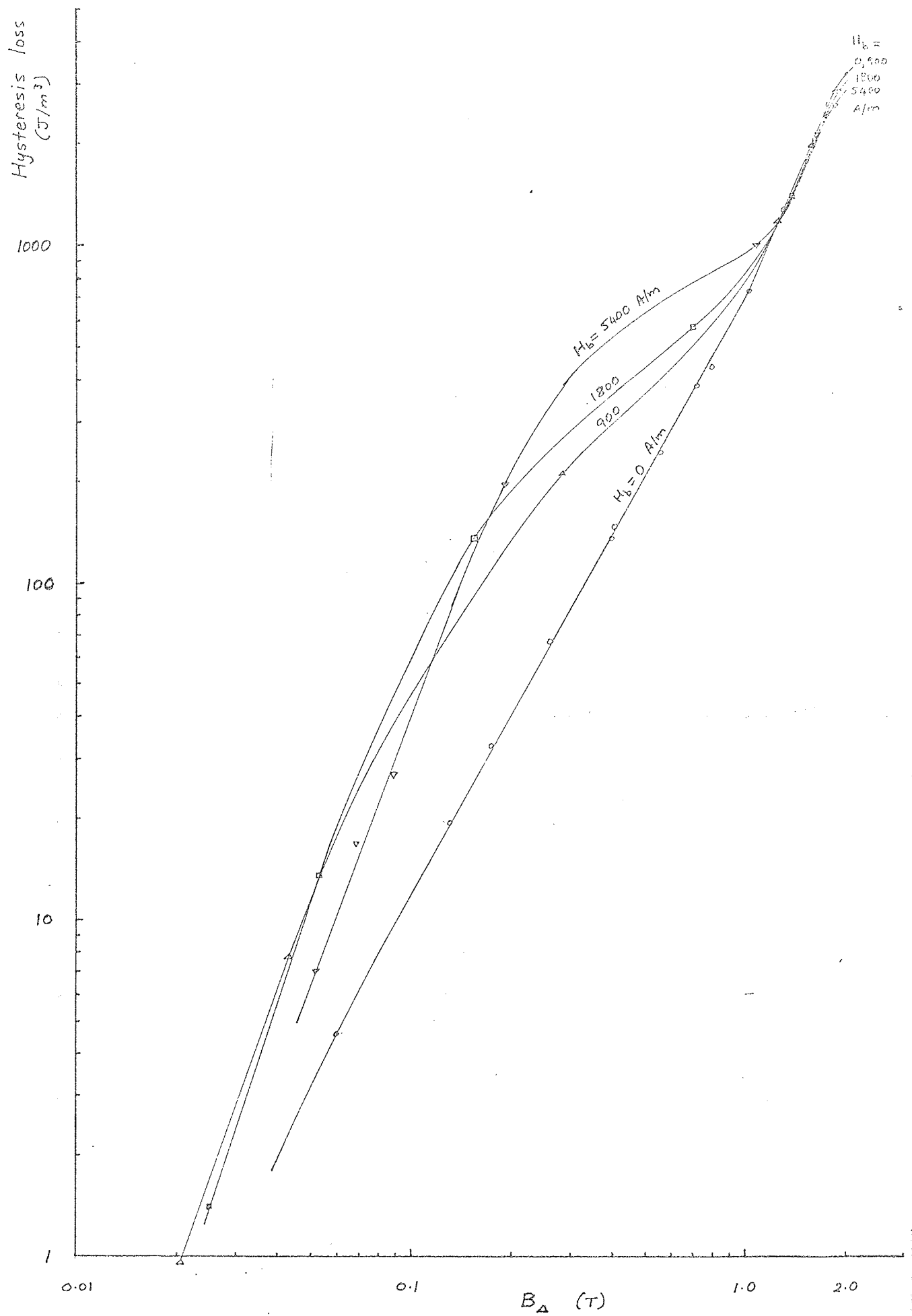
Fig. 4.27 Hysteresis loss as a function of B_Δ for given values
of biasing field strength
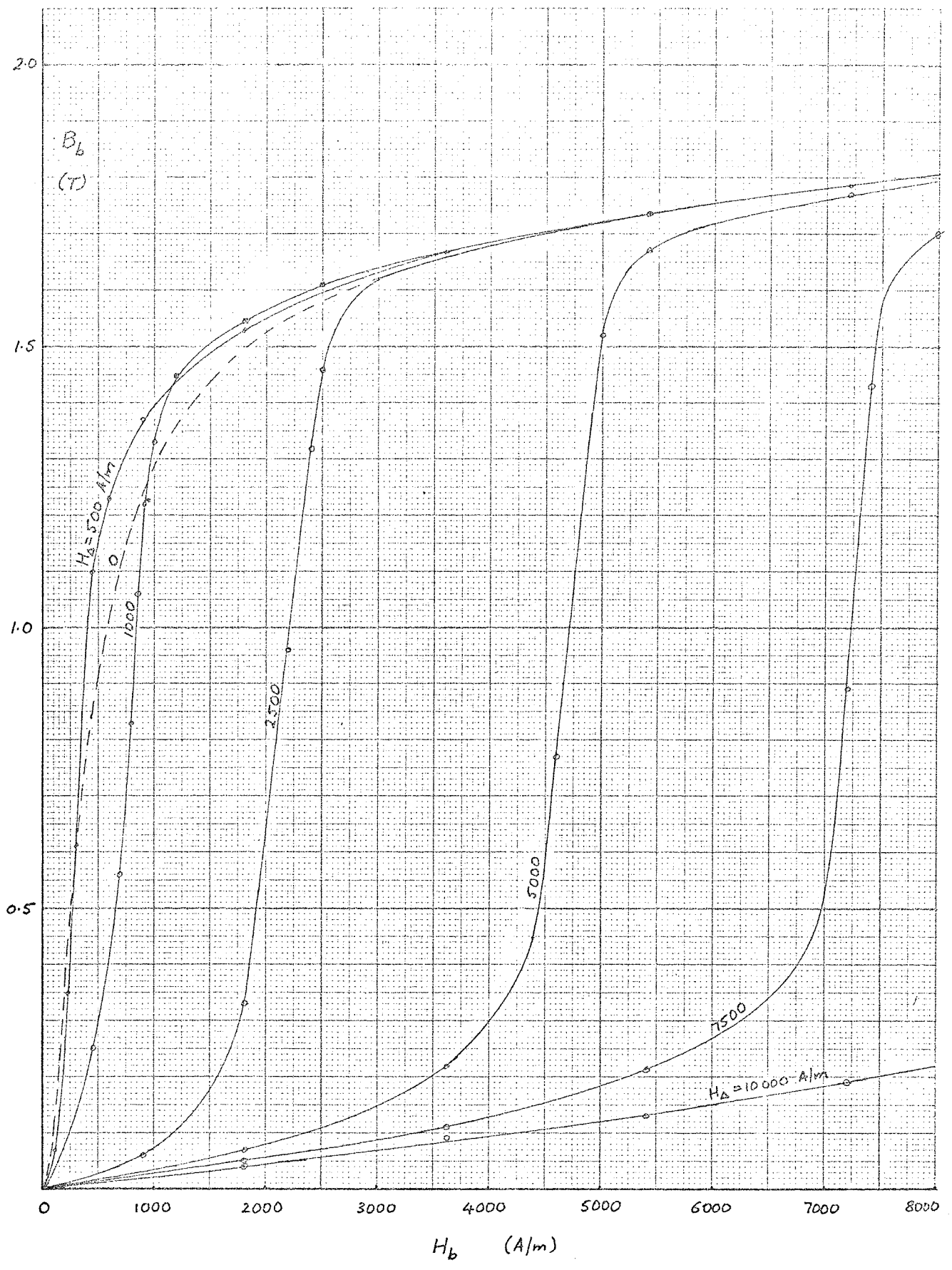
Fig. 4.28   Effect of the incremental field on the steady field:
biasing flux density against biasing field strength for
several values of H_Δ

Fig. 4.29 Incremental permeability against biasing field strength

$H_\Delta = 250$ A/m

—o— Uniformly-varying flux method, } on normal loop $H_m = 4000$ A/m
△ Ballistic method, } $B_m = 1.68$ T

--□-- Ballistic method, on normal magnetisation curve

H_b (A/m)

μ_Δ

2000

1000

100

10

100

1000

10000
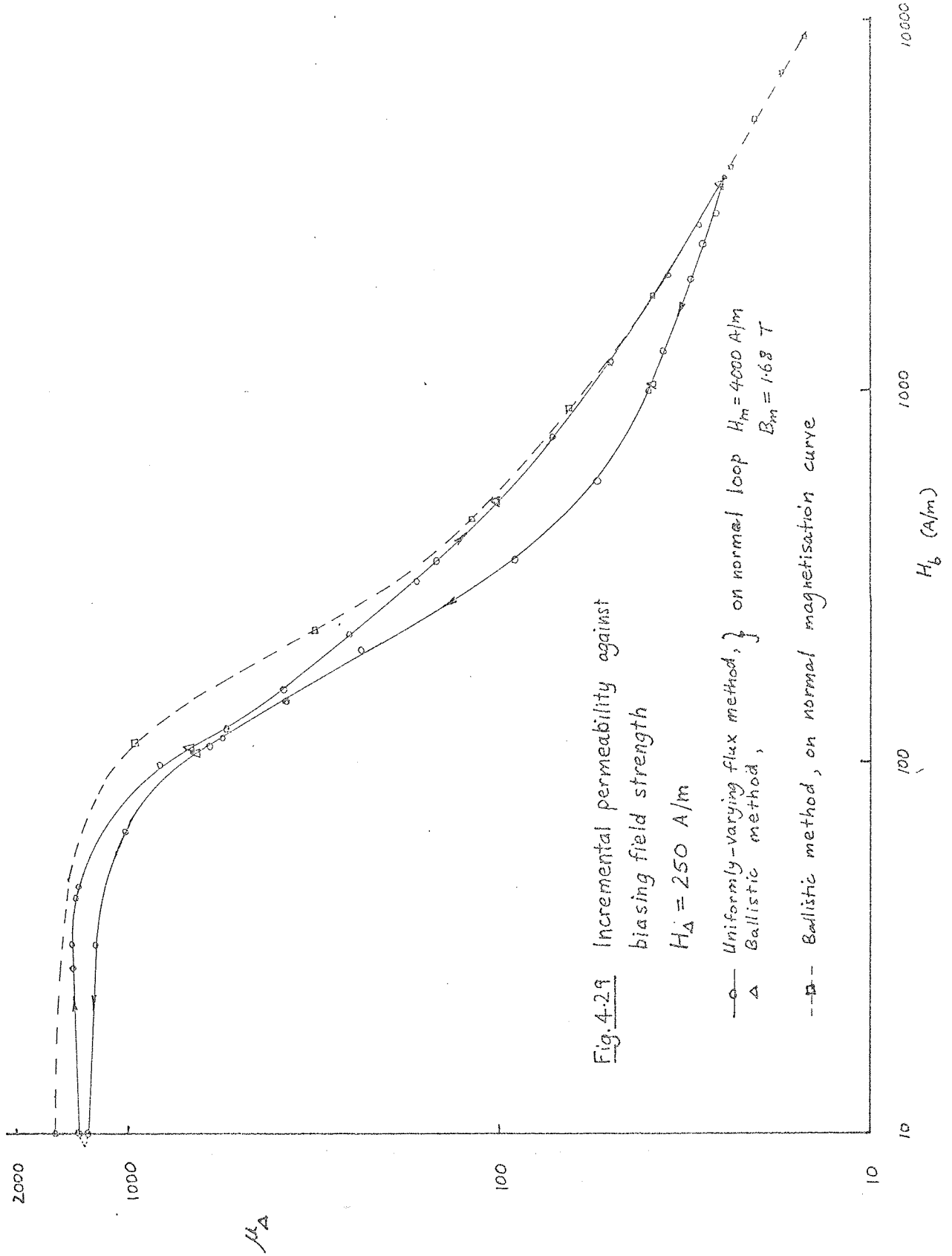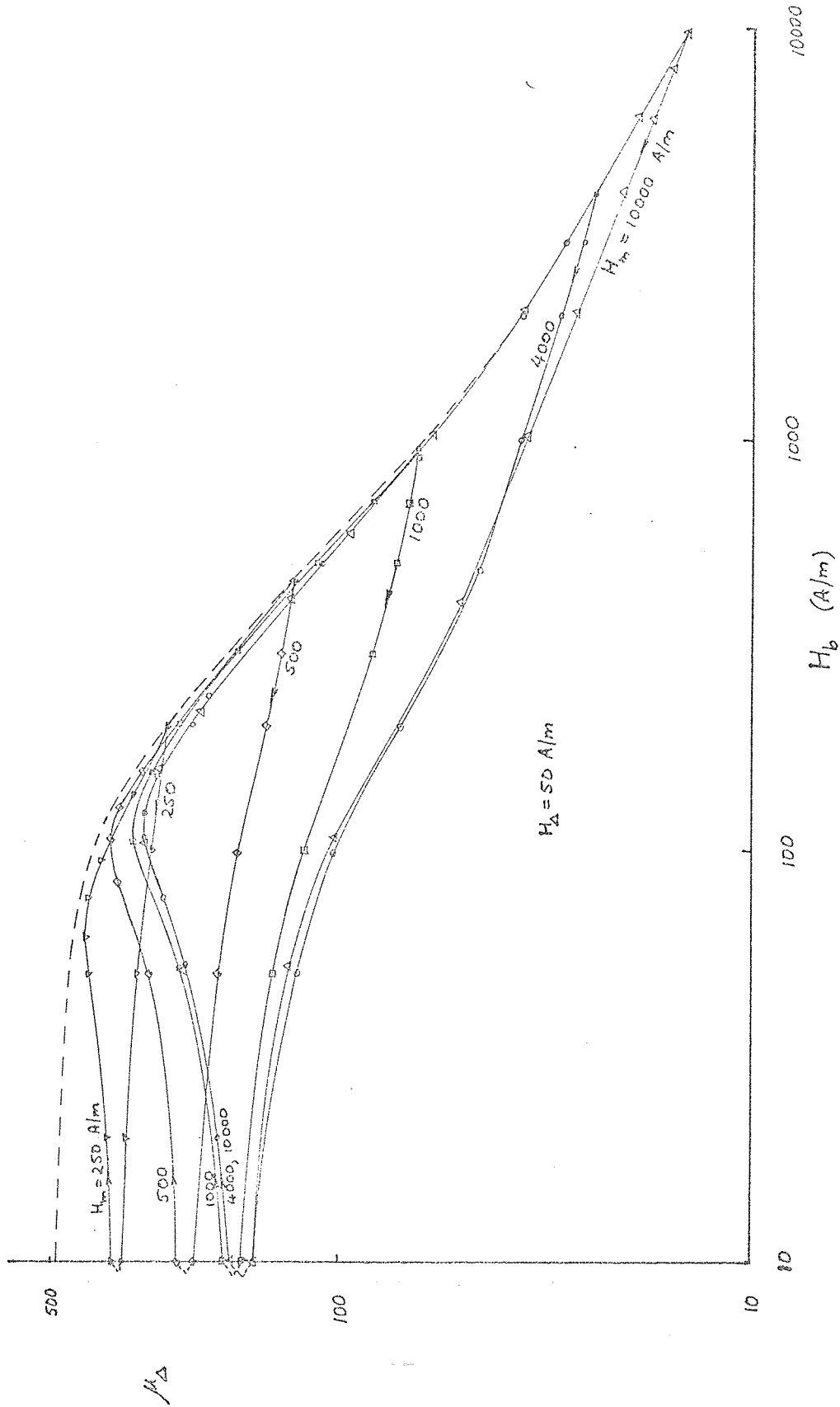
Fig. 4.30   Effect of amplitude of previous magnetic history: H_Δ against H_b for
incremental loops of constant H_Δ (50 A/m) on several normal loops

———   on normal loop of given peak value

– – –   on normal magnetisation curve

Fig.4.31 Effect of amplitude of previous magnetic history : μ_Δ against B_b for incremental loops of constant H_Δ on several normal loops

——— on normal loop of given peak value
— — — on normal magnetisation curve

$H_\Delta = 50$ A/m

$H_m = 250$ A/m
$B_m = 0.50$ T

$H_m = 500$ A/m
$B_m = 0.92$ T

$H_m = 1000$ A/m
$B_m = 1.29$ T

$H_m = 4000$ A/m, $B_m = 1.68$ T

$H_m = 10000$ A/m, $B_m = 1.85$ T

μ_Δ

B_b (T)

$H_\Delta = 1000$ A/m

300
150
1000
150
50
5
50
$H_\Delta = 5$ A/m

μ_Δ

2000
1000
100
10

100
1000
10000

H_b (A/m)

10

Fig 4.32 Effect of some previous magnetic history on incremental loops of different sizes : μ_Δ against H_b for given values of H_Δ

——— on normal loop $H_m = 4000$ A/m , $B_m = 1.68$ T

– – – on normal magnetisation curve
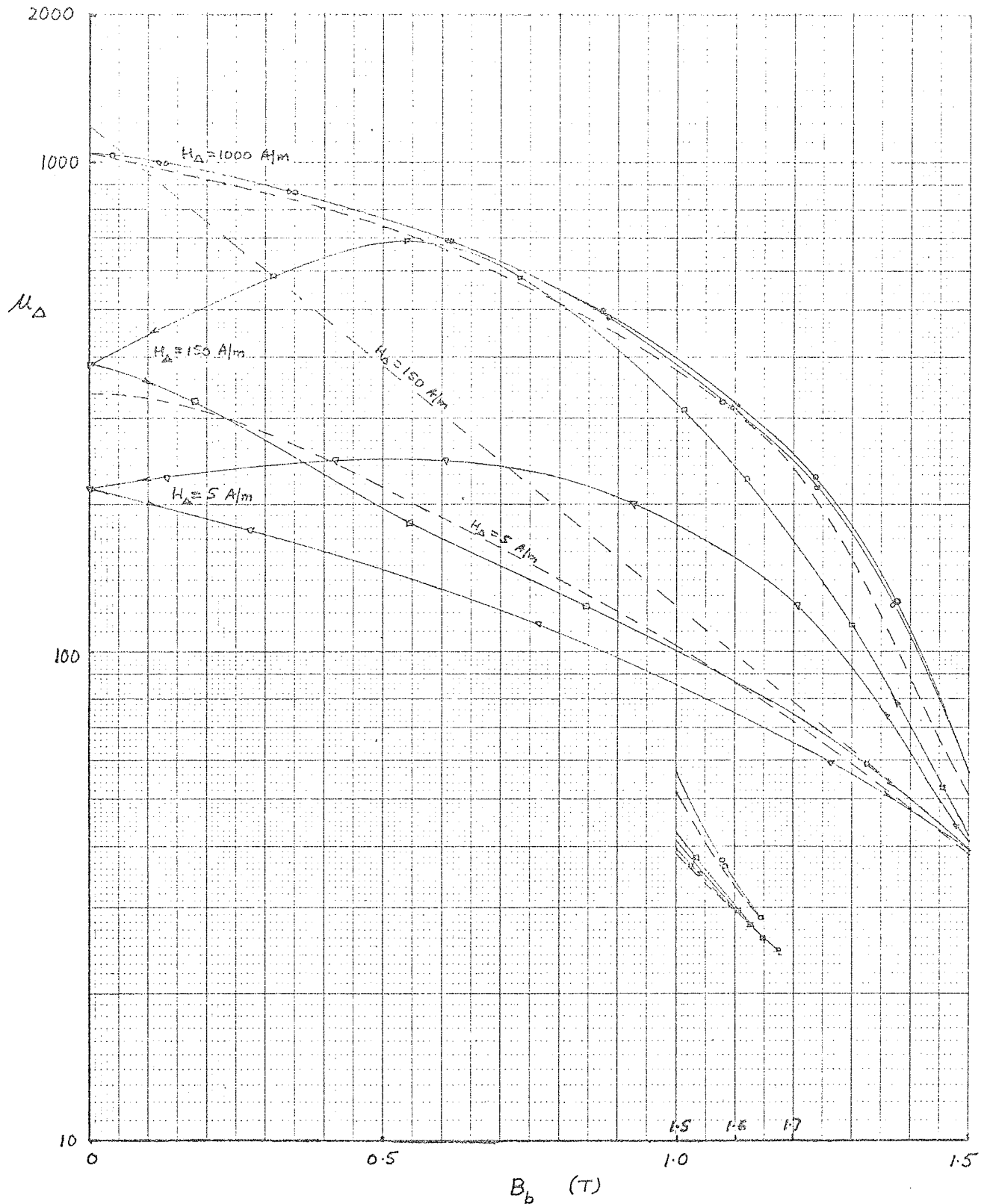
Fig. 4.33 Effect of same previous magnetic history on incremental
loops of different sizes: μ_Δ against B_b for given
values of H_Δ

———————— on normal loop $H_m = 4000$ A/m, $B_m = 1.68$ T

— — — — on normal magnetisation curve
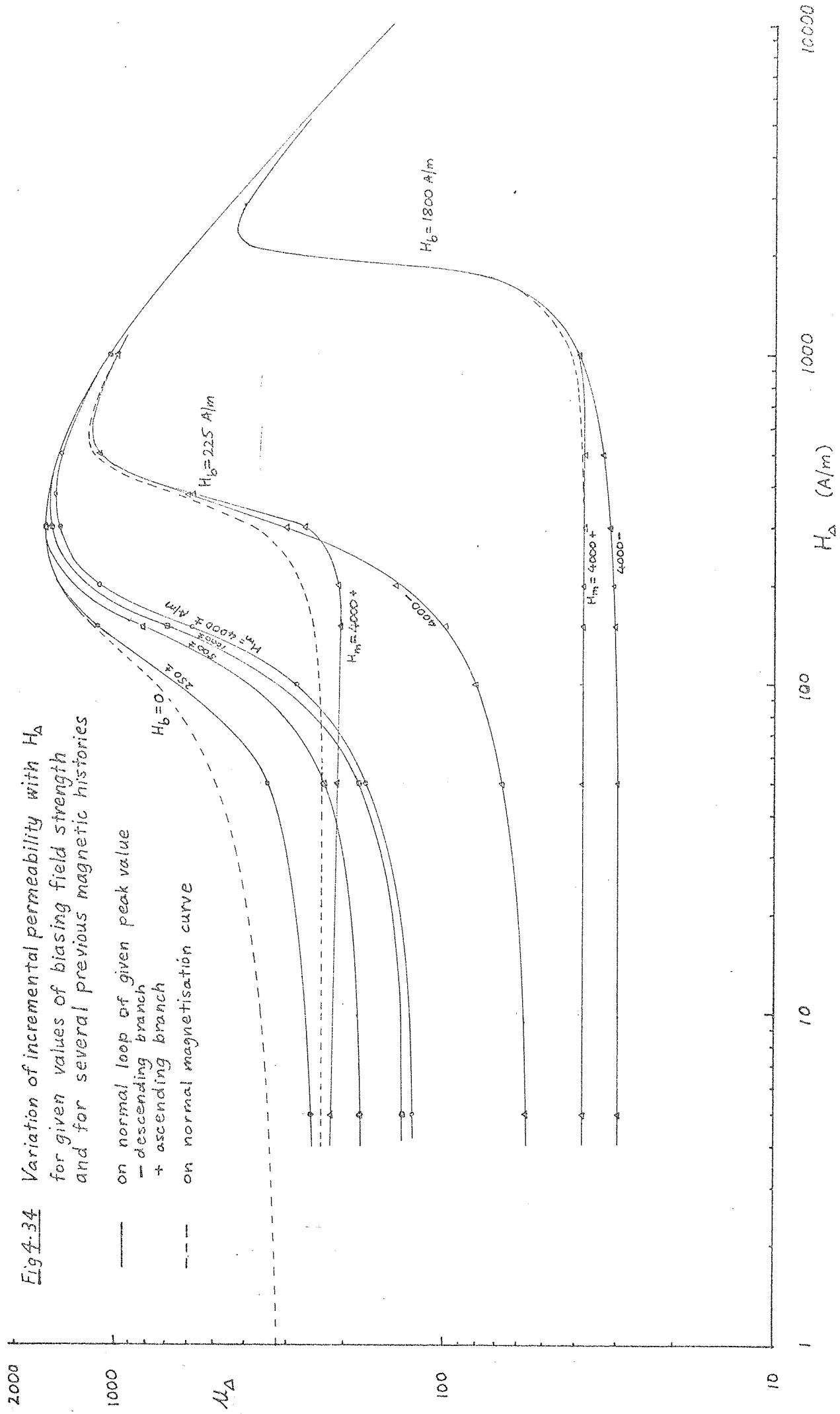
Fig 4.34   Variation of incremental permeability with H_Δ
for given values of biasing field strength
and for several previous magnetic histories

on normal loop of given peak value
— descending branch
+ ascending branch

$H_b = 0$

on normal magnetisation curve

$H_b = 1800$ A/m

$H_b = 225$ A/m

$H_m = 4000+$

$4000-$

$H_m = 4000+$

$4000-$

$H_m = 4000$ A/m

$H_b = 0$

450+

900+

1800+

μ_Δ

2000

1000

100

10

1   10   100   1000   10000

H_Δ (A/m)

Fig. 4.35   Variation of incremental permeability with H_Δ
for given values of biasing flux density
and for several previous magnetic histories

on normal loop of given peak value
−   descending branch
+   ascending branch

·—·—   on normal magnetisation curve

μ_Δ

H_Δ (A/m)

N ×10⁻⁶ (Ω)

W

500

100

0.4
0.3
0.2
0.1

W

Z

Z_∞

N

Slope = 1.0

10   2.5   4.0   5.6   8.0   12.5   17.8   25

178   100   1000   2000

$ma = \sqrt{\dfrac{\omega x_0 \mu_a \alpha}{\rho}}$

μ_Δ
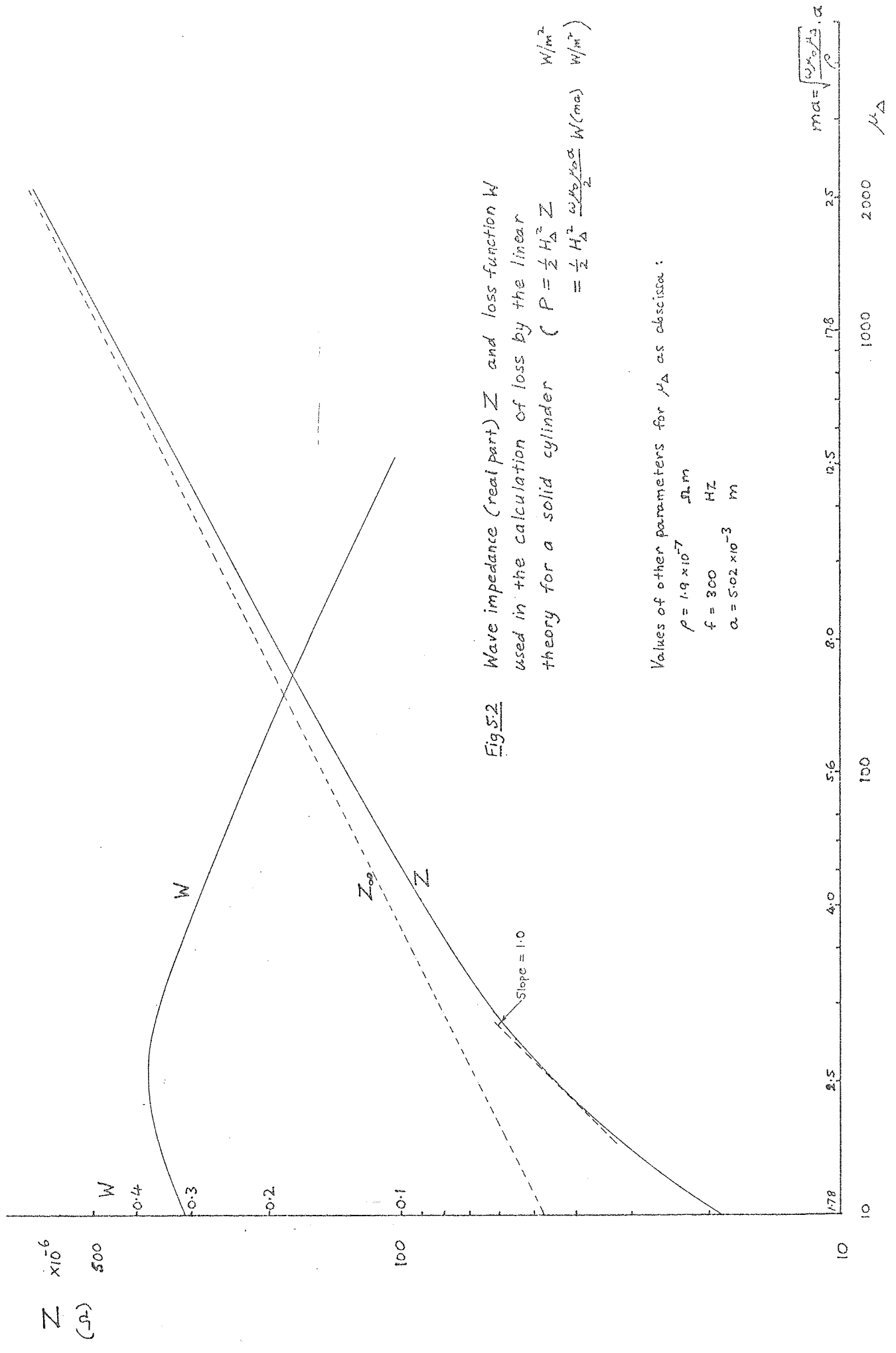
Fig 5:2   Wave impedance (real part) Z and loss function W used in the calculation of loss by the linear theory for a solid cylinder

$$\left(P = \frac{1}{2} H_\Delta^2 \, Z \qquad \text{W/m}^2 \right.$$

$$\left. = \frac{1}{2} H_\Delta^2 \, \frac{\omega x_0 \mu_0 \mu_a}{2} \, W(ma) \qquad \text{W/m}^2 \right)$$

Values of other parameters for μ_Δ as abscissa :

$\rho = 1.9 \times 10^{-7}$ $\Omega\,\text{m}$

$f = 300$ Hz

$\alpha = 5.02 \times 10^{-3}$ m
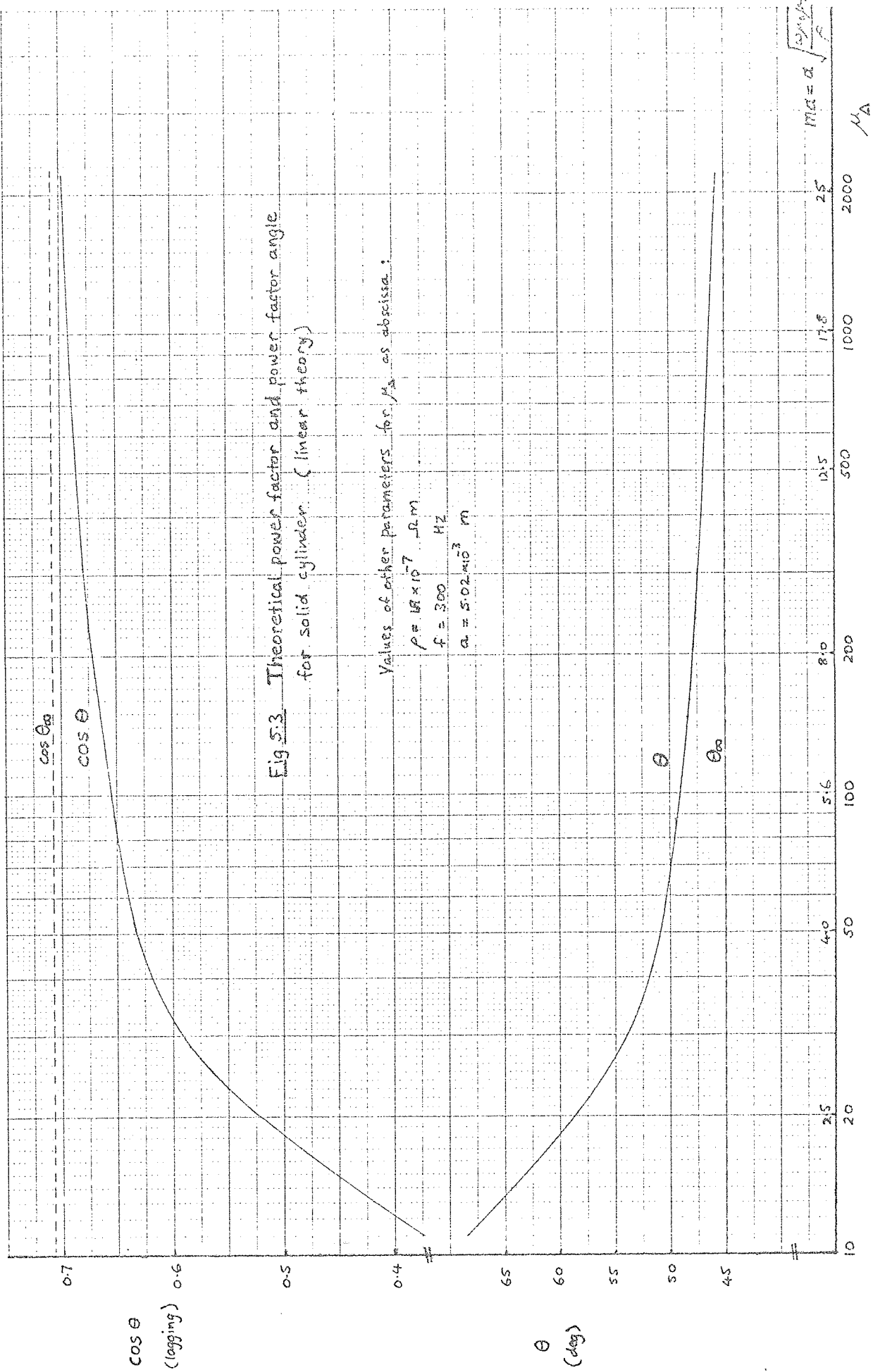
Fig 5.3   Theoretical power factor and power factor angle
for solid cylinder.   (linear theory)

Values of other parameters for μ_a as abscissa:

$\rho = 18 \times 10^{-7} \ \Omega m$

$f = 300 \quad Hz$

$a = 5.02 \times 10^{-3} \ m$

$m a = a \sqrt{\dfrac{2 \pi f \mu_a}{\rho}}$

μ_a

$\cos \theta$
(lagging)

θ
(deg)

$\cos \theta_a$

$\cos \theta$

θ

θ_a
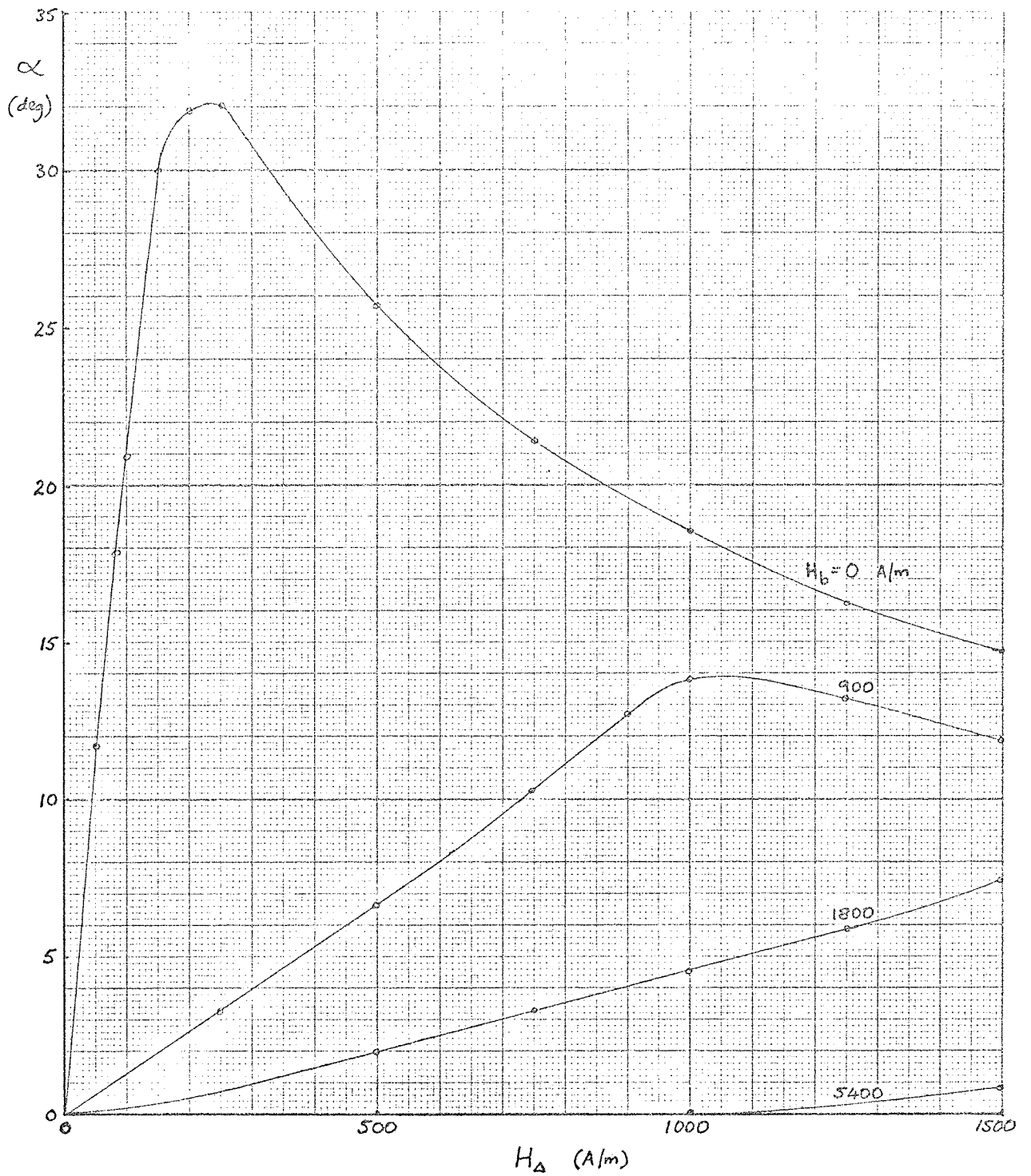
Fig. 5.4   Variation of measured hysteresis angle with H_Δ for given values of H_b
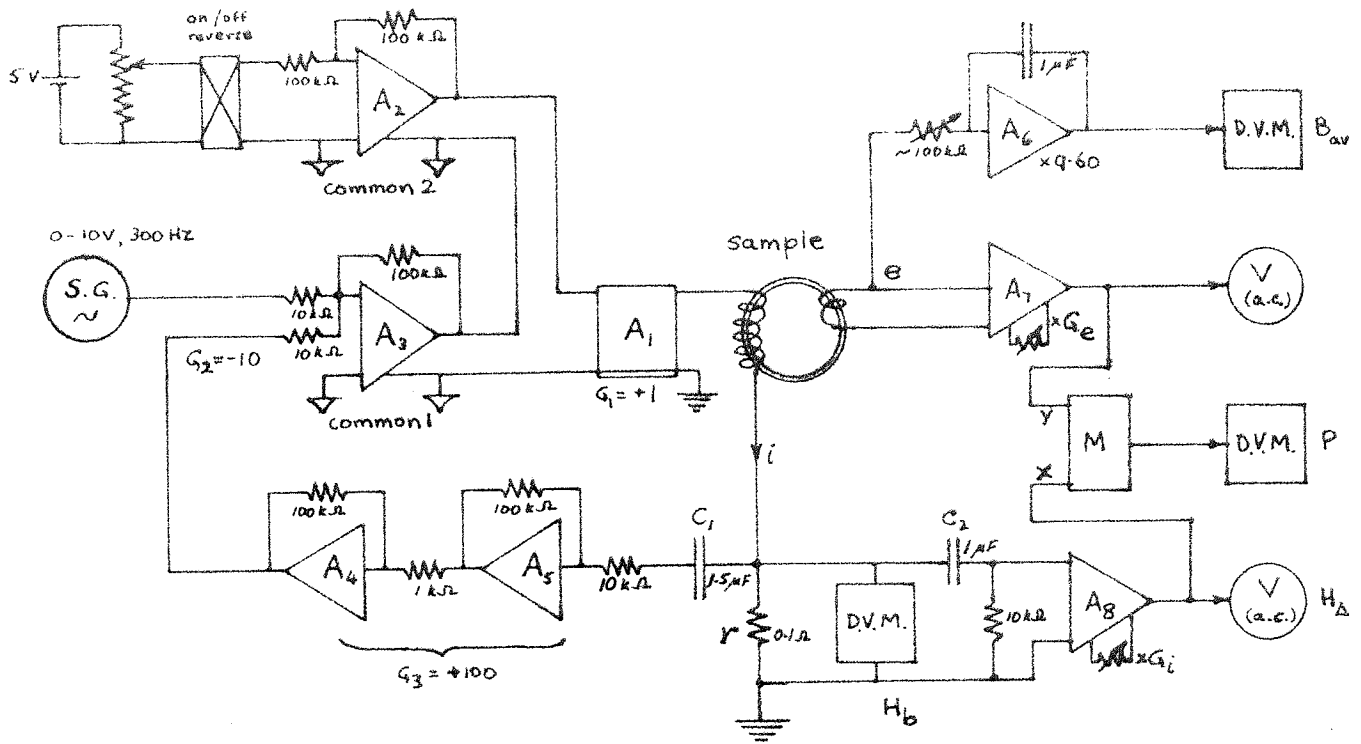
Fig. 5.6 Circuit for the measurement of a.c. loss with a superposed
d.c. field and with high-gain negative feedback proportional to
magnetising current.

A_1	Power amplifier (see fig. 4.1)
A_2, A_3, A_5	Burr Brown model 3010 chopper stabilised operational amplifier
A_4, A_6	Burr Brown model 3071 chopper stabilised operational amplifier
A_7, A_8	Burr Brown model 3061 instrumentation amplifier
M	Burr Brown model 4029 quarter-square multiplier
V	Solartron true-r.m.s. voltmeter VM1484
D.V.M.	Solartron digital voltmeter LM1402
S.G.	Prossor Scientific Instruments A100 waveform generator
r	0.1 Ω H.W. Sullivan d.c. resistance standard
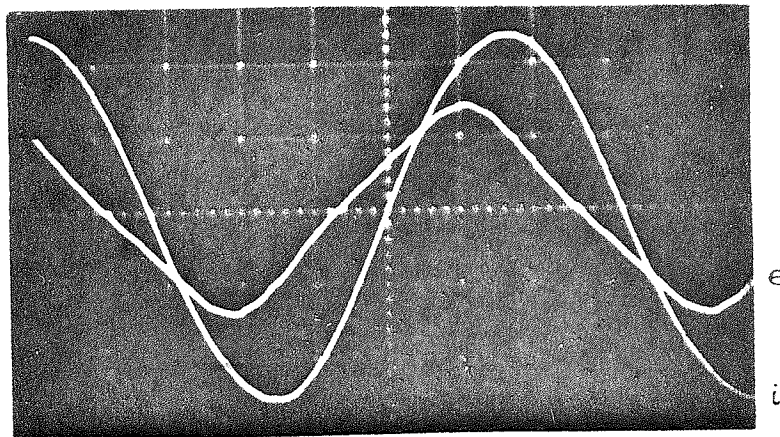
Fig. 5.7 Waveforms obtained with above circuit,
showing sinusoidal current. H_Δ = 250 A/m, H_b = 0
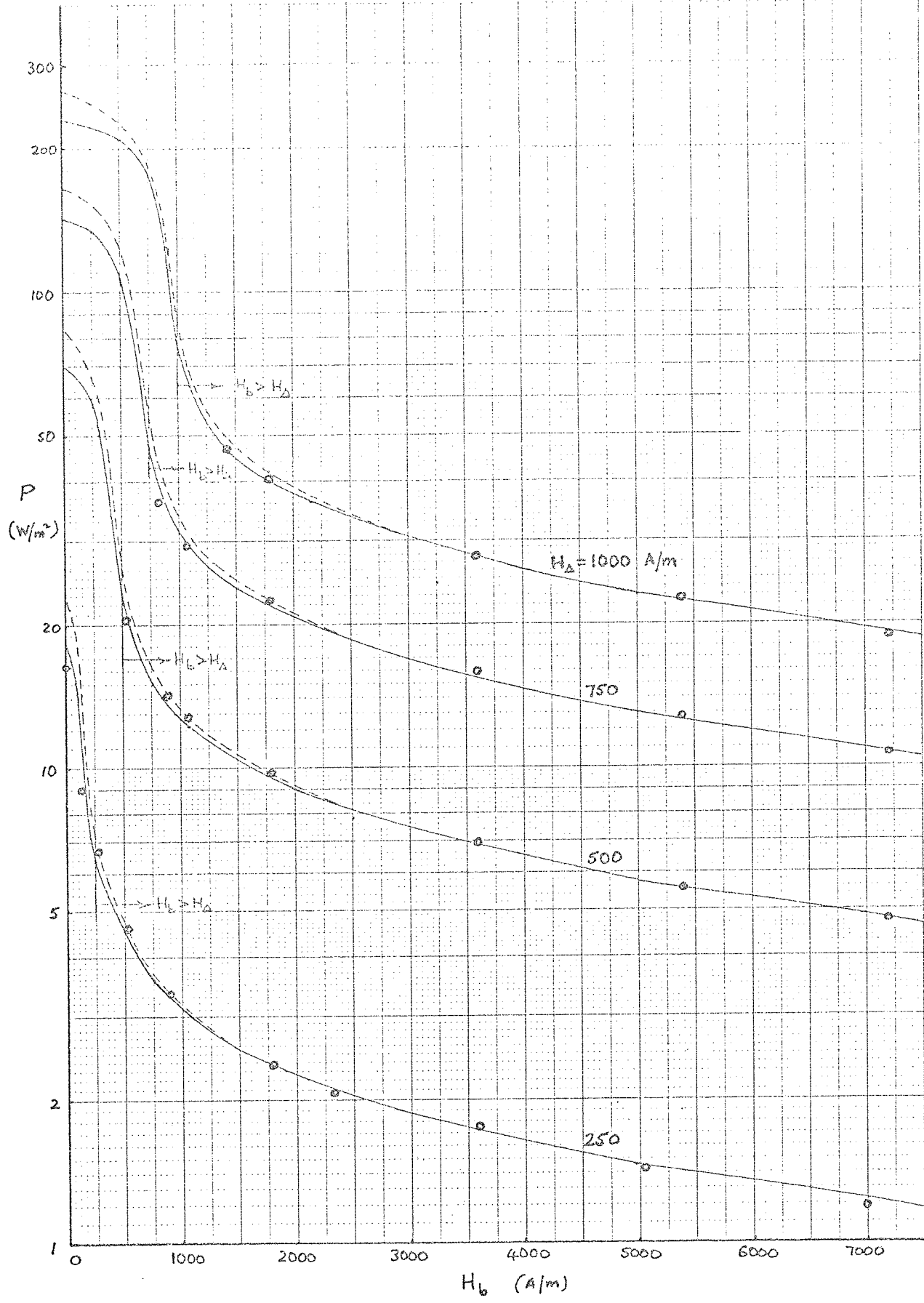
Fig. 5.8 Comparison of measured and calculated losses in solid mild-steel ring at 300 Hz with a superposed parallel field

    o   measured

―――――   calculated using linear theory,
                           neglecting hysteresis

– – – – –   calculated using linear theory,
                           including hysteresis

Fig. 5.9 Comparison of measured and calculated wave impedances

—— Calculated, linear theory neglecting hysteresis

Measured, $H_A = 250$ A/m
o
△   "   500   "
◇   "   750   "
□   "   1000 "

$H_A = 1000$ A/m
750
500
250

Z ($\mu\Omega$)
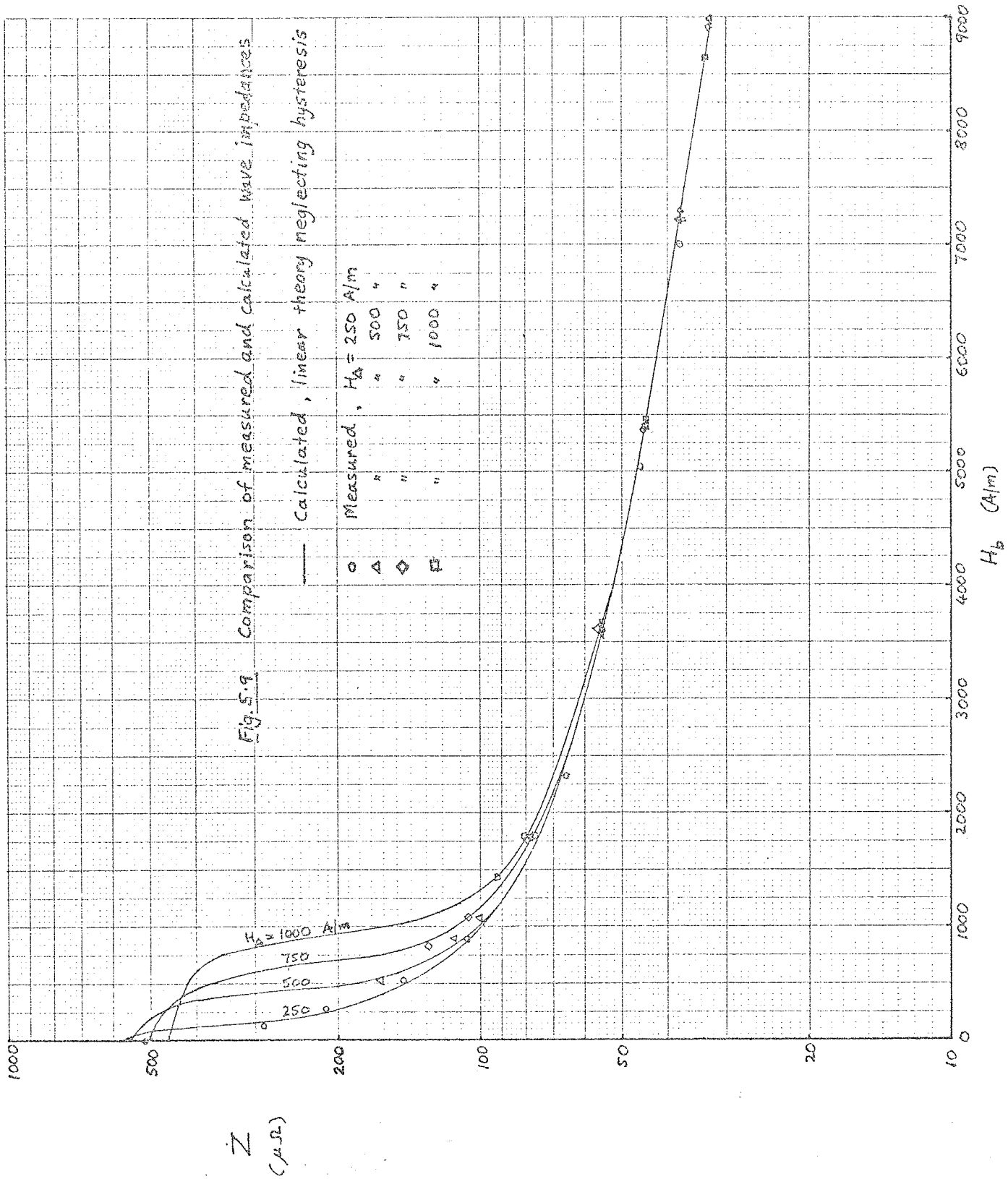
H_b (A/m)

Fig. 5.10   Comparison of measured and calculated power factors, neglecting hysteresis

— Calculated, using linear theory

Measured, $H_\Delta = 250$ A/m
" " 500 "
" " 750 "
" " 1000 "
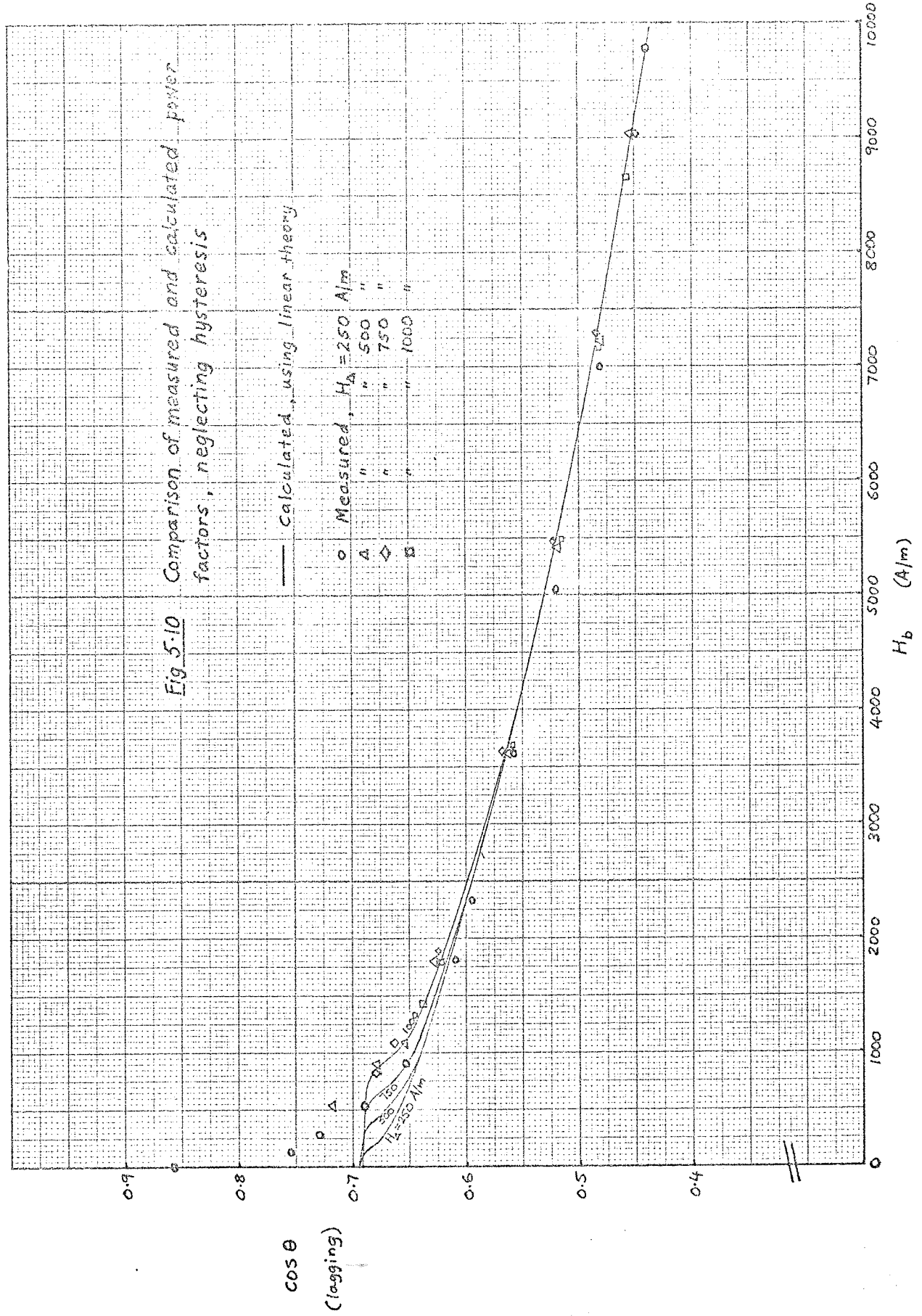
cos θ
(lagging)

H_b (A/m)
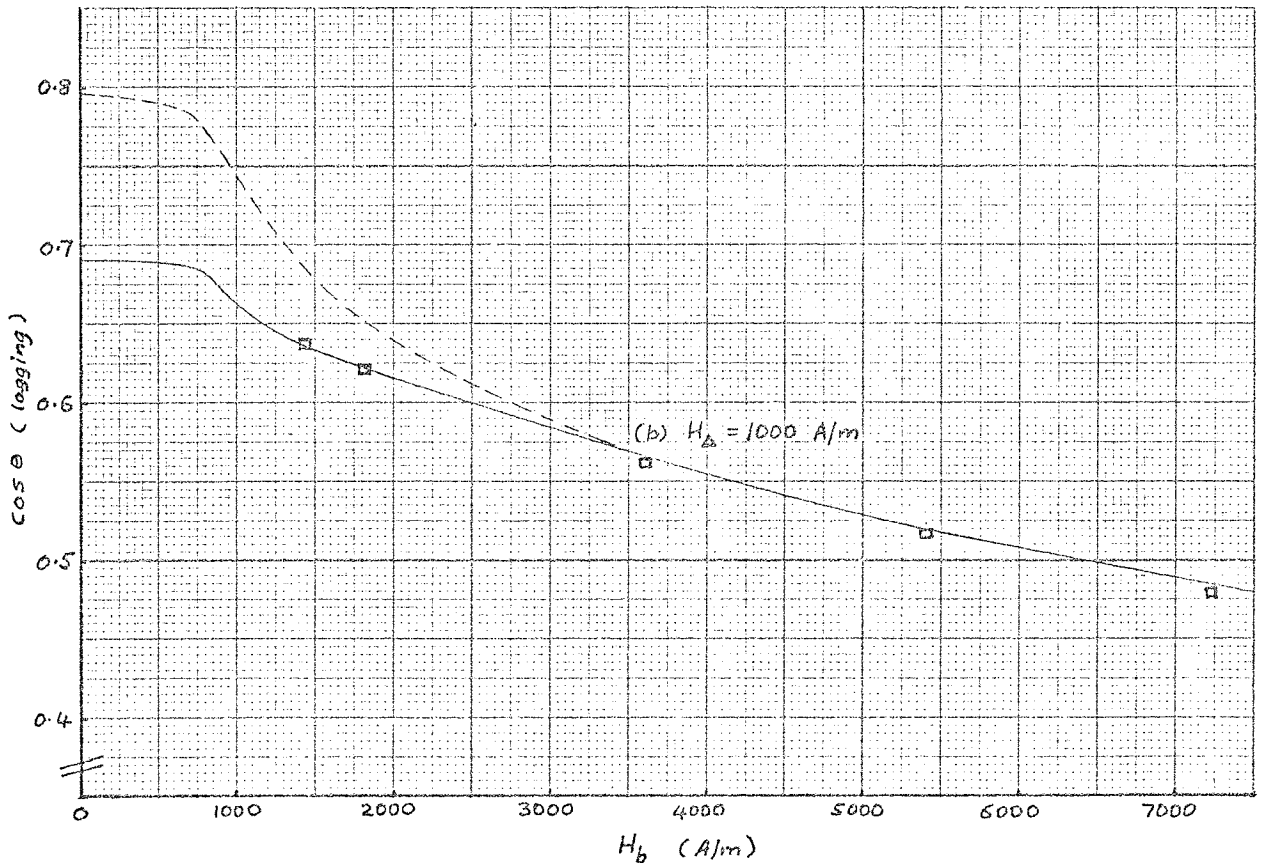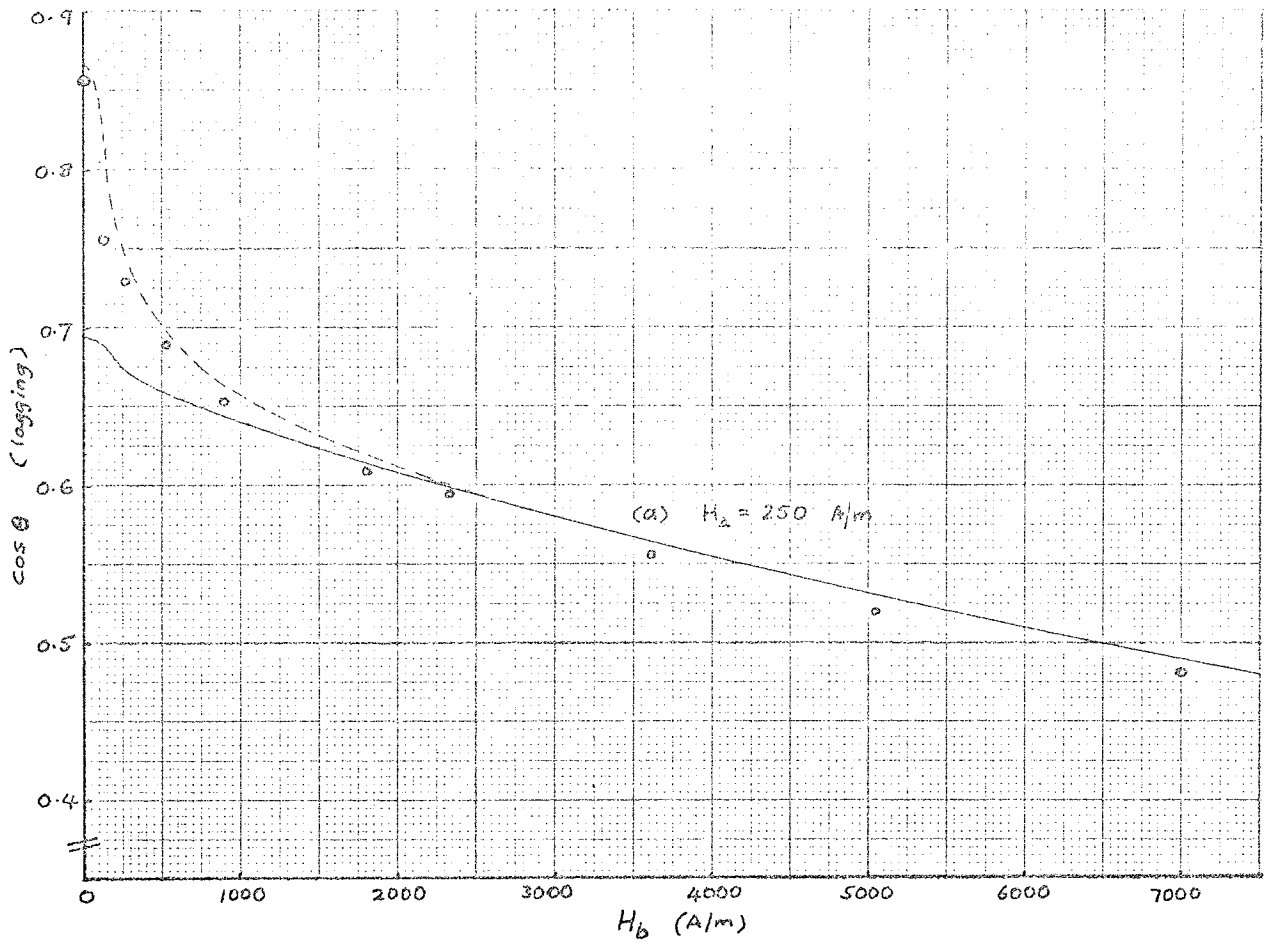
Fig. 5.11   Comparison of measured and calculated power factors
for two values of H_Δ (250 A/m and 1000 A/m)

———————   Calculated, neglecting hysteresis

— — — —   Calculated, including hysteresis
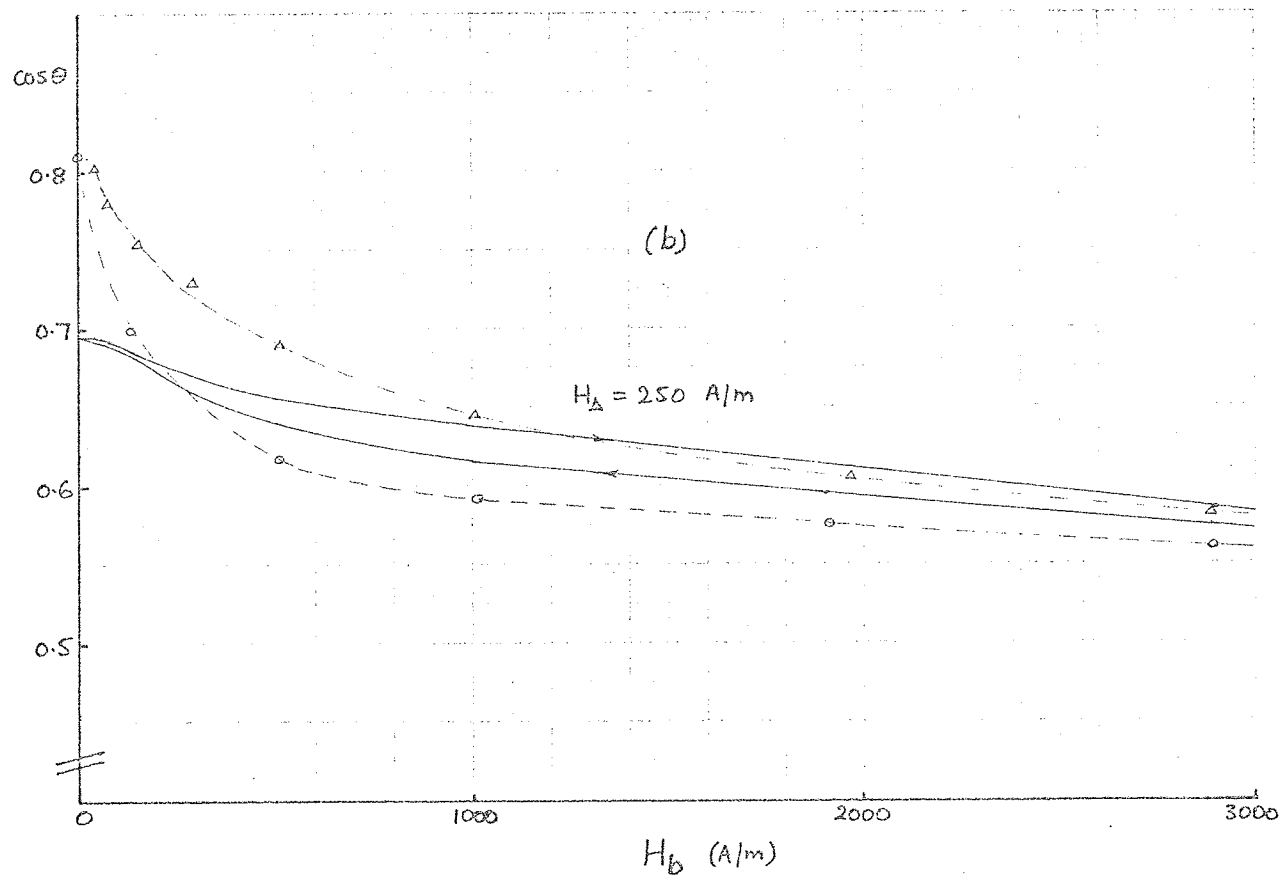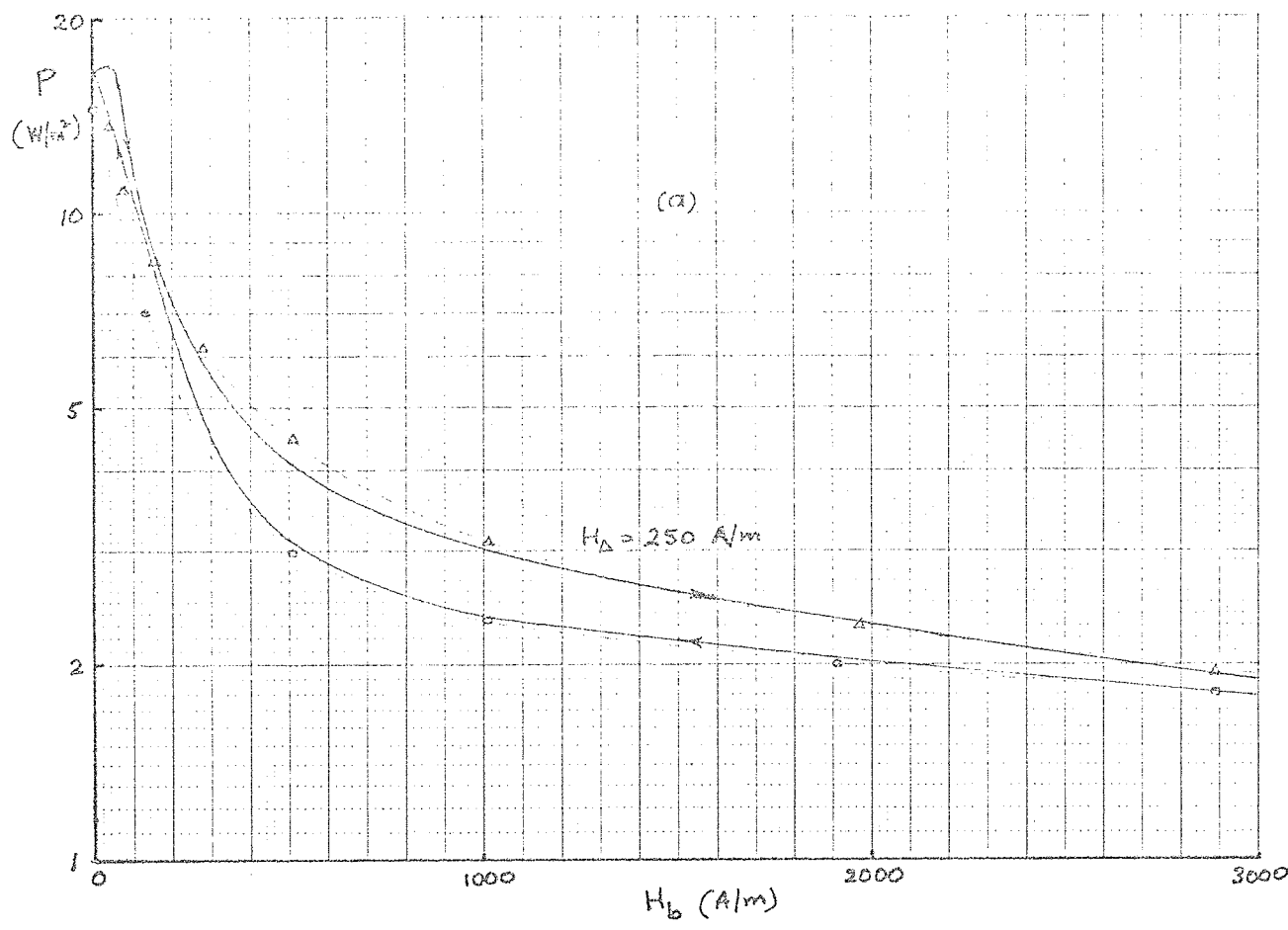
o   Measured

Fig. 5.12   Comparison of measured and calculated (a) a.c. losses and
(b) power factor for incremental loops on the normal loop
H_m = 4000 A/m (solid steel ring, f = 300 Hz)

———————   Calculated, linear theory neglecting hysteresis

--o--   Measured on descending branch of normal loop

--▲--   Measured on ascending branch of normal loop
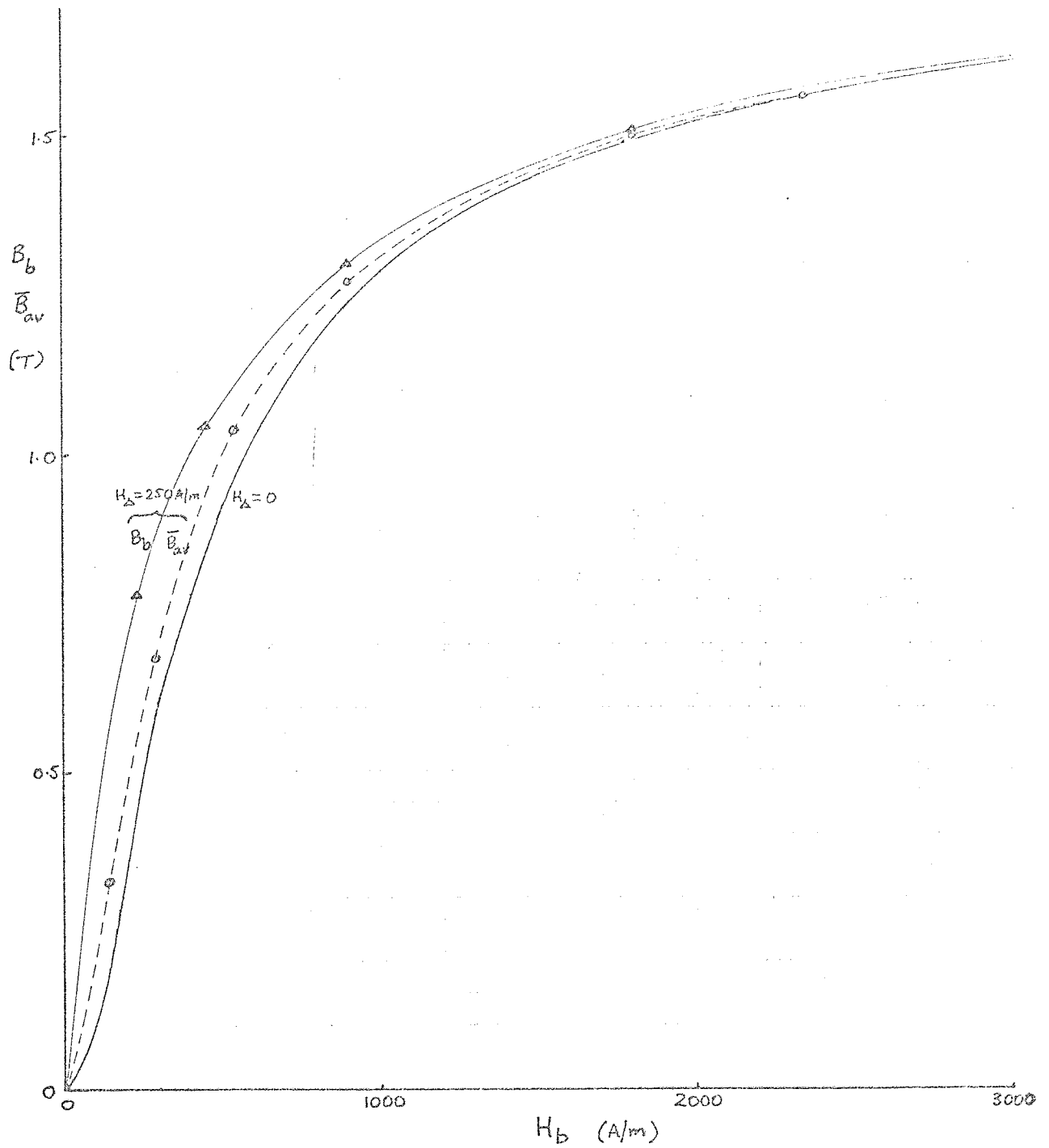
Fig. 5.13 Comparison of the steady flux density in the solid iron
ring under d.c. and a.c. conditions

	d.c. measurements (B_b), H_Δ = 250 A/m
	a.c. measurements $(\bar{B}_{av})$ at 300 Hz, H_Δ = 250 A/m
	Normal magnetisation curve $(H_\Delta = 0)$
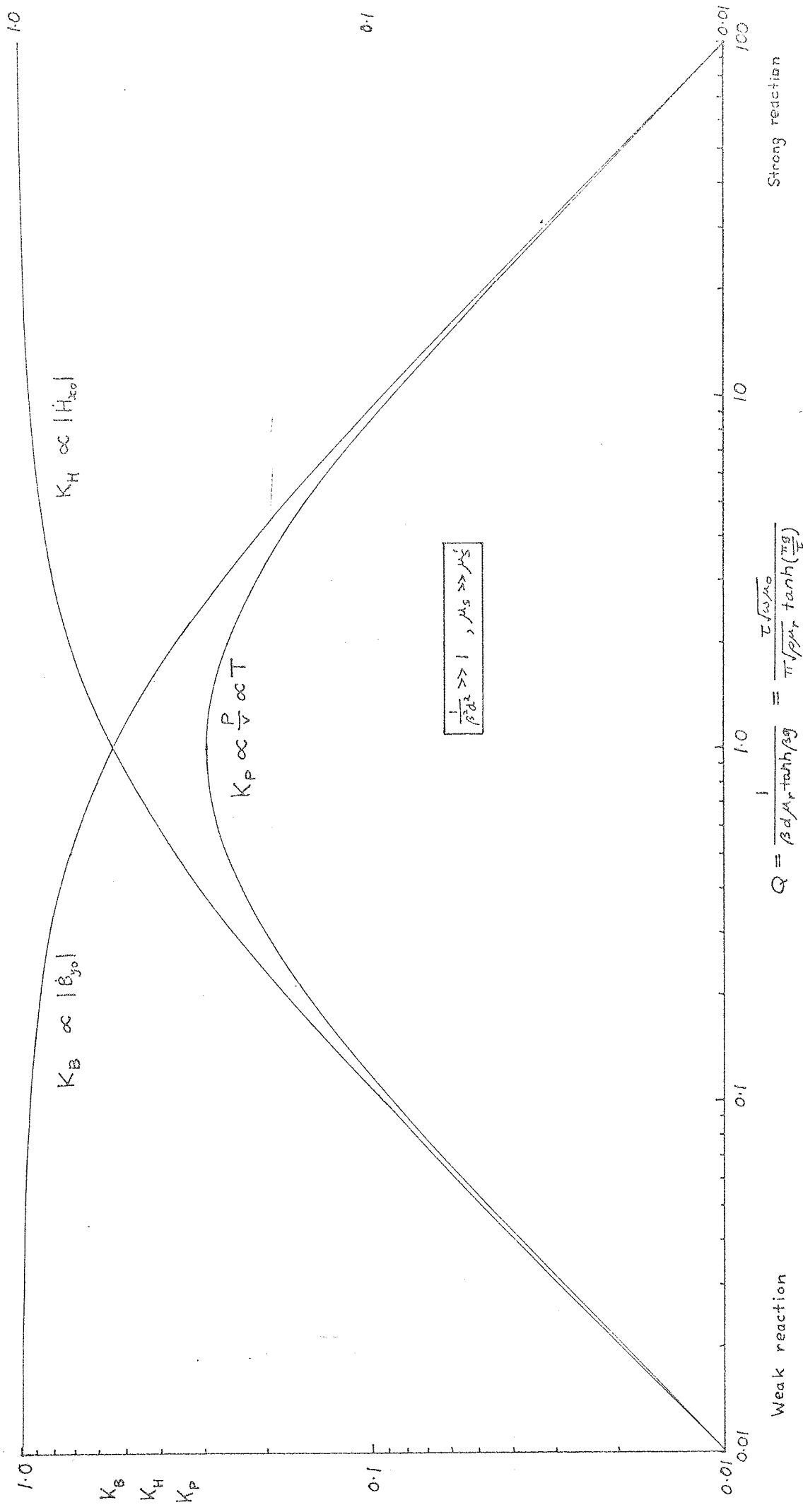
Fig. 6.2 Normalised curves for radial flux density, tangential field strength and loss (or torque) in a smooth solid rotor with strong skin effect as a function of the eddy-current reaction factor Q

$\angle \dot{B}_{yo}$ $\angle H_{zo}$

90°	45°
85°	40°
80°	35°
75°	30°
70°	25°
65°	20°
60°	15°
55°	10°
50°	5°
45°	0°

$$\frac{1}{\beta^2 d^2} \gg 1 \ , \ \mu_s \gg \mu_s'$$

Q

0.01   0.05   0.1   0.5   1.0   5   10
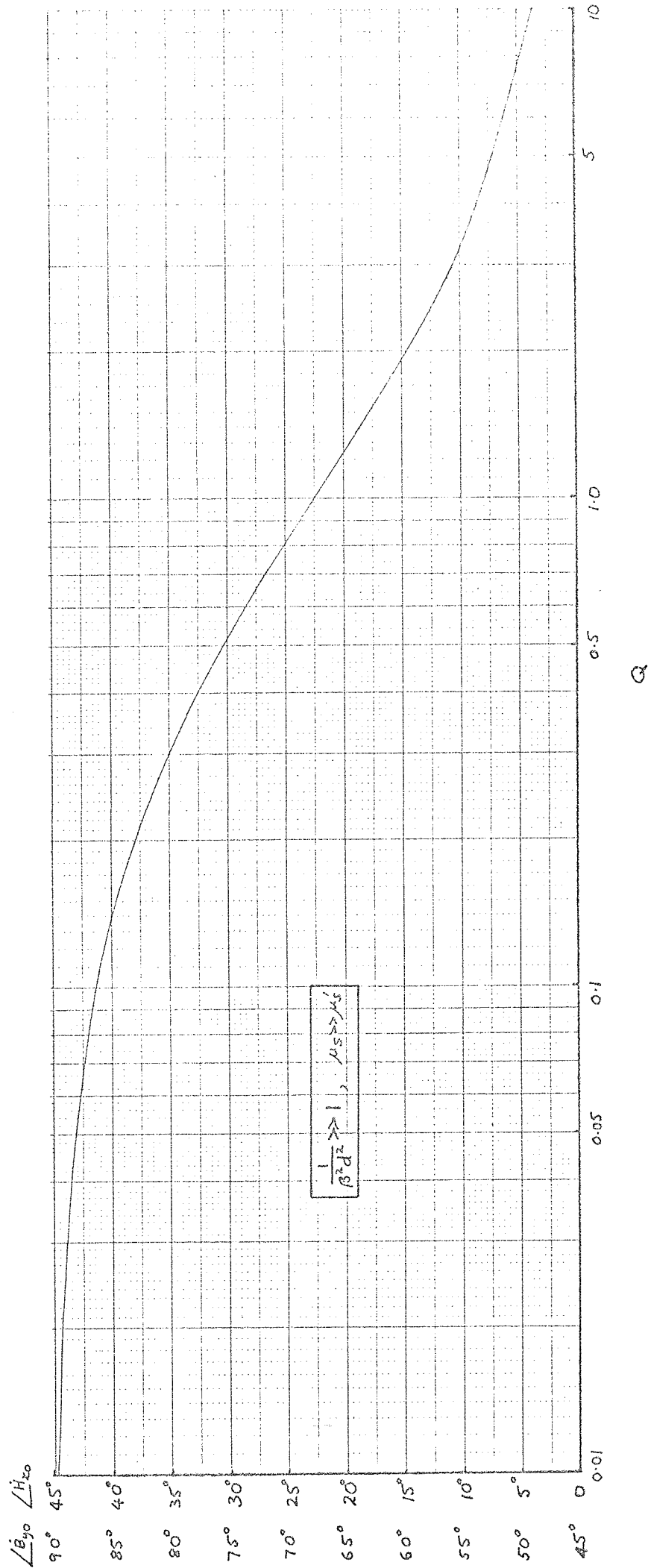
Fig. 6.3   Phase relative to the stator current of radial flux density and tangential field strength on the surface of a solid rotor with strong skin effect as a function of the eddy-current reaction factor Q
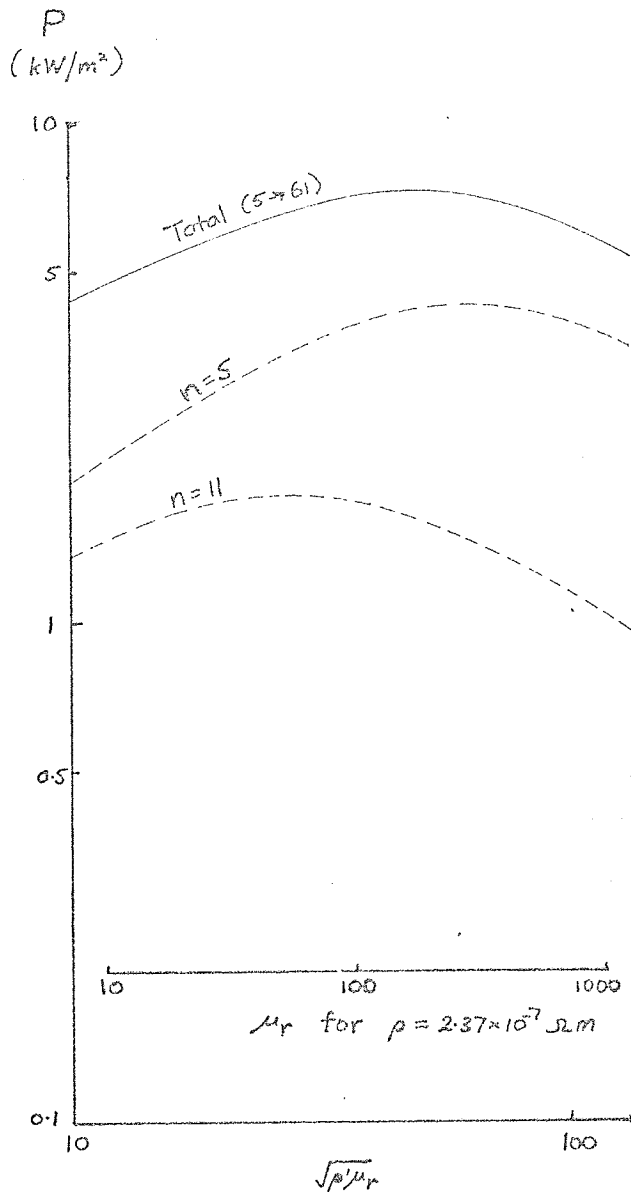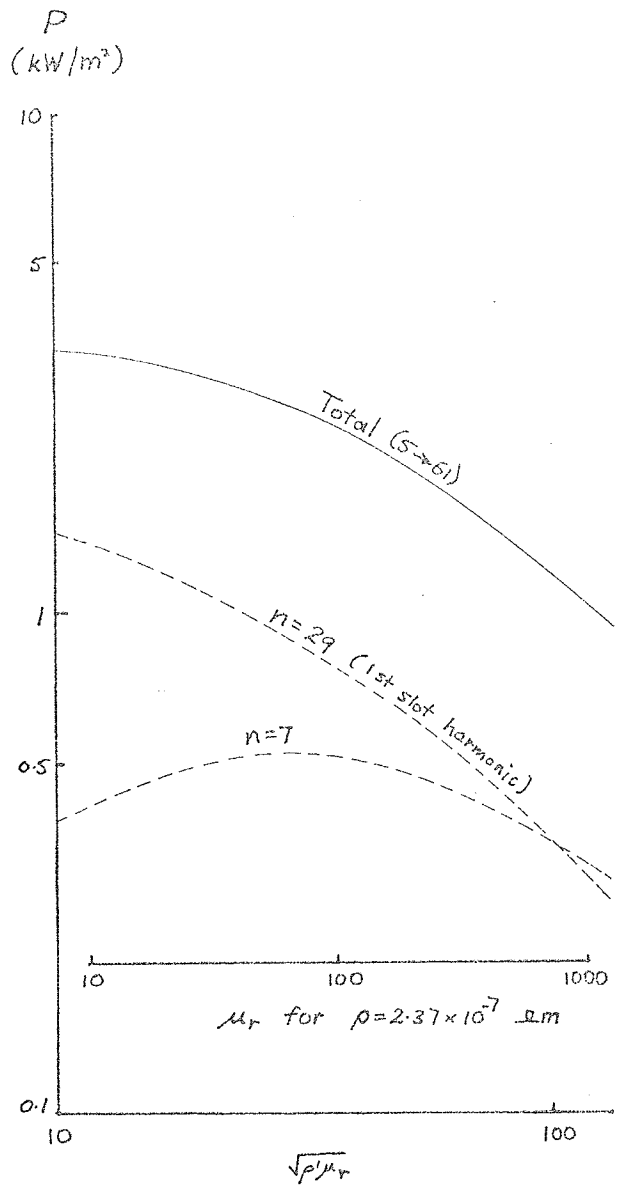
(a) 500 MVA turbo-generator   (b) 60 MVA salient-pole machine

Fig. 6.5 Variation with resistivity and permeability of the calculated winding-harmonic loss intensity for the two large industrial machines of table 6.1 (ρ'= resistivity relative to copper, ρ_{cu} = 1.72 x 10^{-8} Ωm)

——— total loss of 5th to 61st harmonics

----- individual losses of some important harmonics
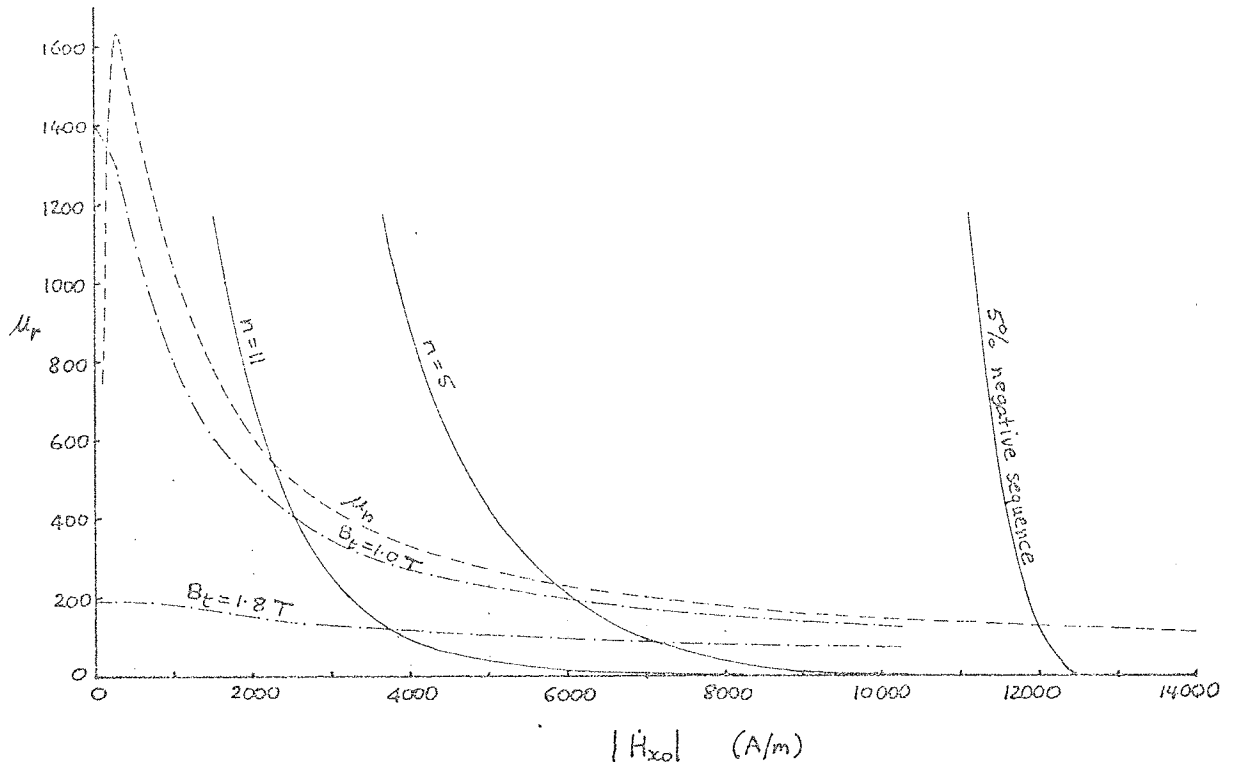
(a) 500 MVA turbo-generator
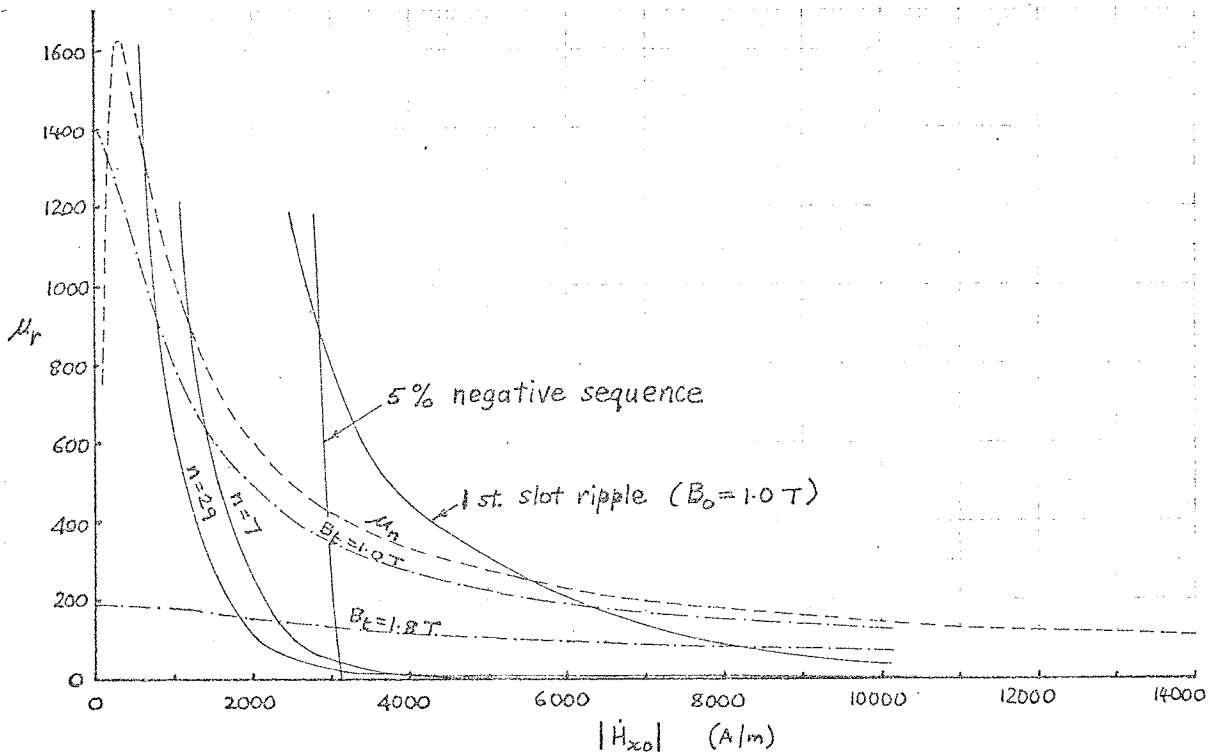
(b) 60 MVA salient-pole machine

Fig. 6.6 Variation with μ_r of the calculated surface tangential field strength in the two large industrial machines (table 6.1) for a 5% negative-sequence wave, a slot-ripple wave assuming a main flux density of ~1.0 T, and some important winding-harmonic waves, together with some curves showing the dependence of the permeability on field strength for EN1A mild steel with and without a superposed perpendicular steady field of fixed flux density

———— variation of travelling-wave field strength with μ_r

– – – – – normal permeability (from fig. 4.8)

—·—··— permeability with a superposed perpendicular field of given flux density (from fig. 8.8)
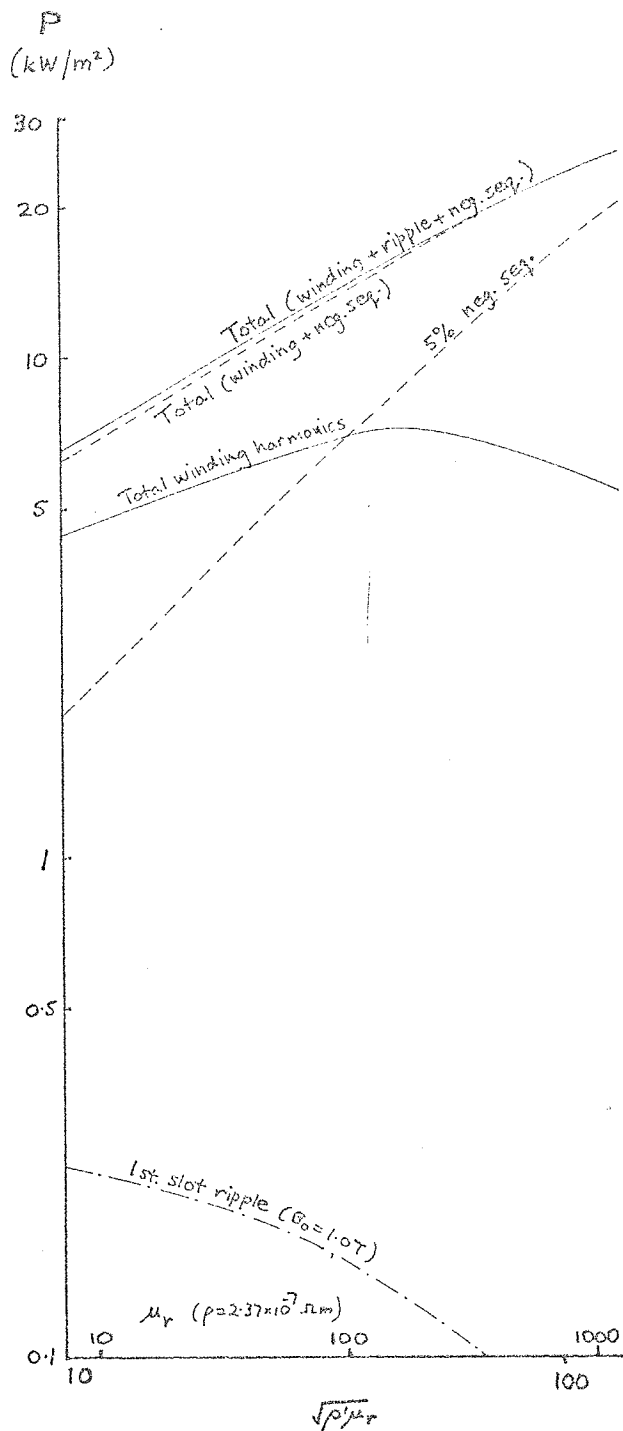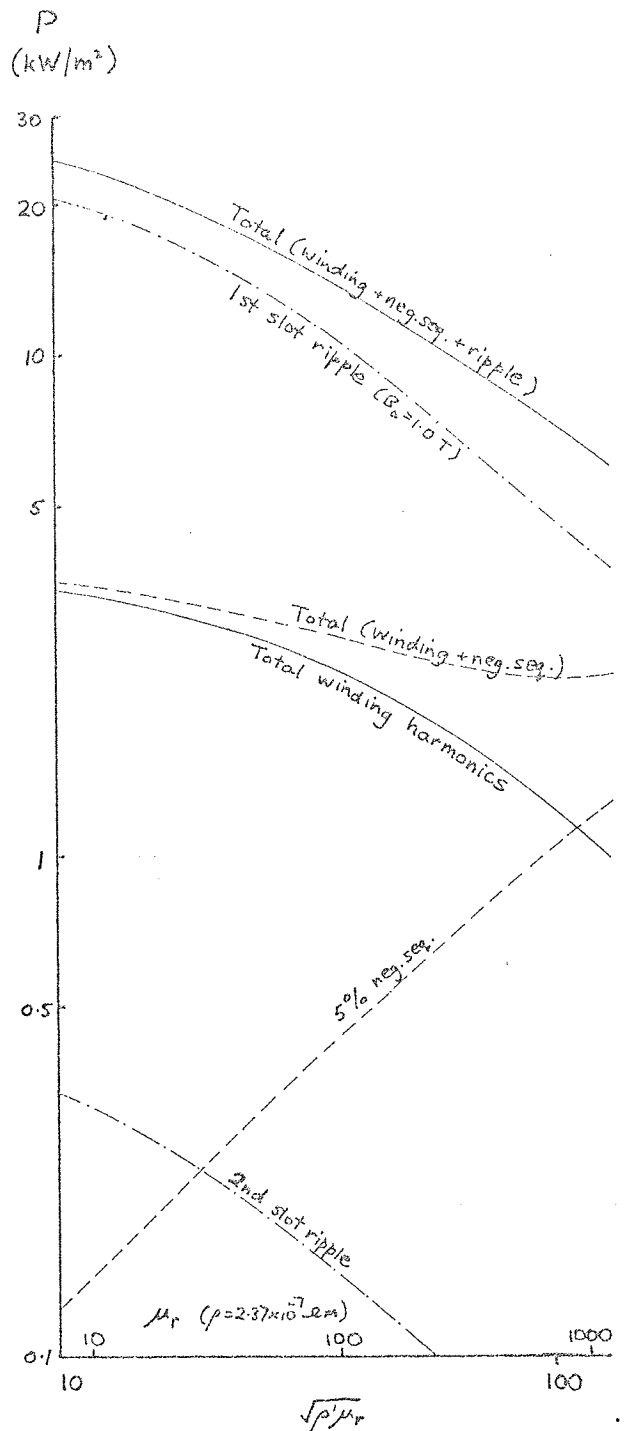
(a) 500 MVA Turbo-generator   (b) 60 MVA salient-pole
machine

Fig. 6.7   Variation with permeability and resistivity of the
calculated rotor surface loss intensity in the two
large industrial machines of table 6.1 including a
5% negative-sequence wave and a slot-ripple wave
(assuming a main flux density of ~1.0 T for the slot ripple)
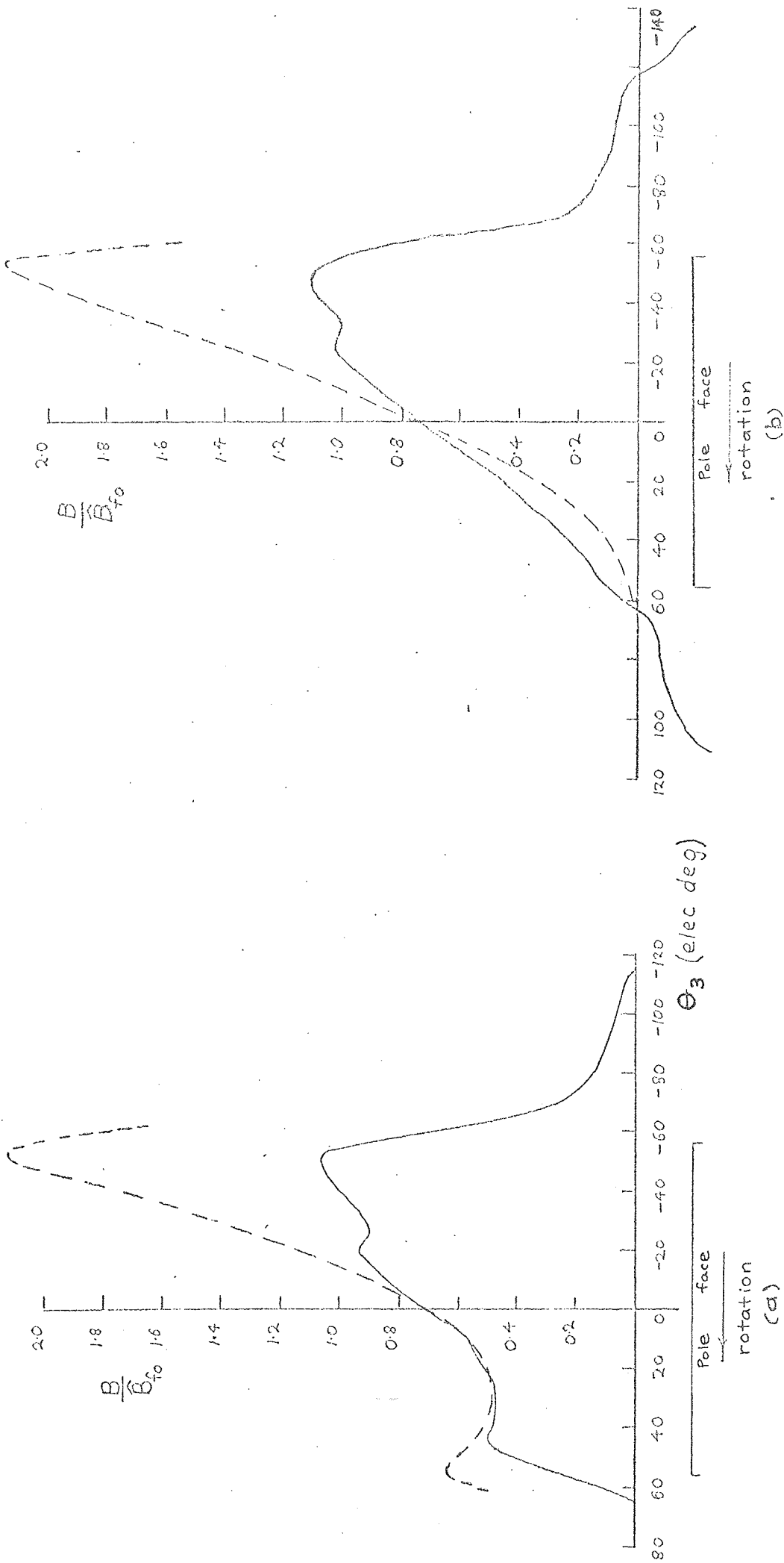(ρ' = resistivity relative to copper, ρ_{cu} = 1.72 x 10^{-8} Ωm)

Fig. 8.2 Main flux density in Ginsberg and Jokl 30 kW salient pole machine no. 4

——— measured
– – – calculated

(a) Rated kW, 0.8 p.f. lagging   (b) Rated kW, u.p.f.
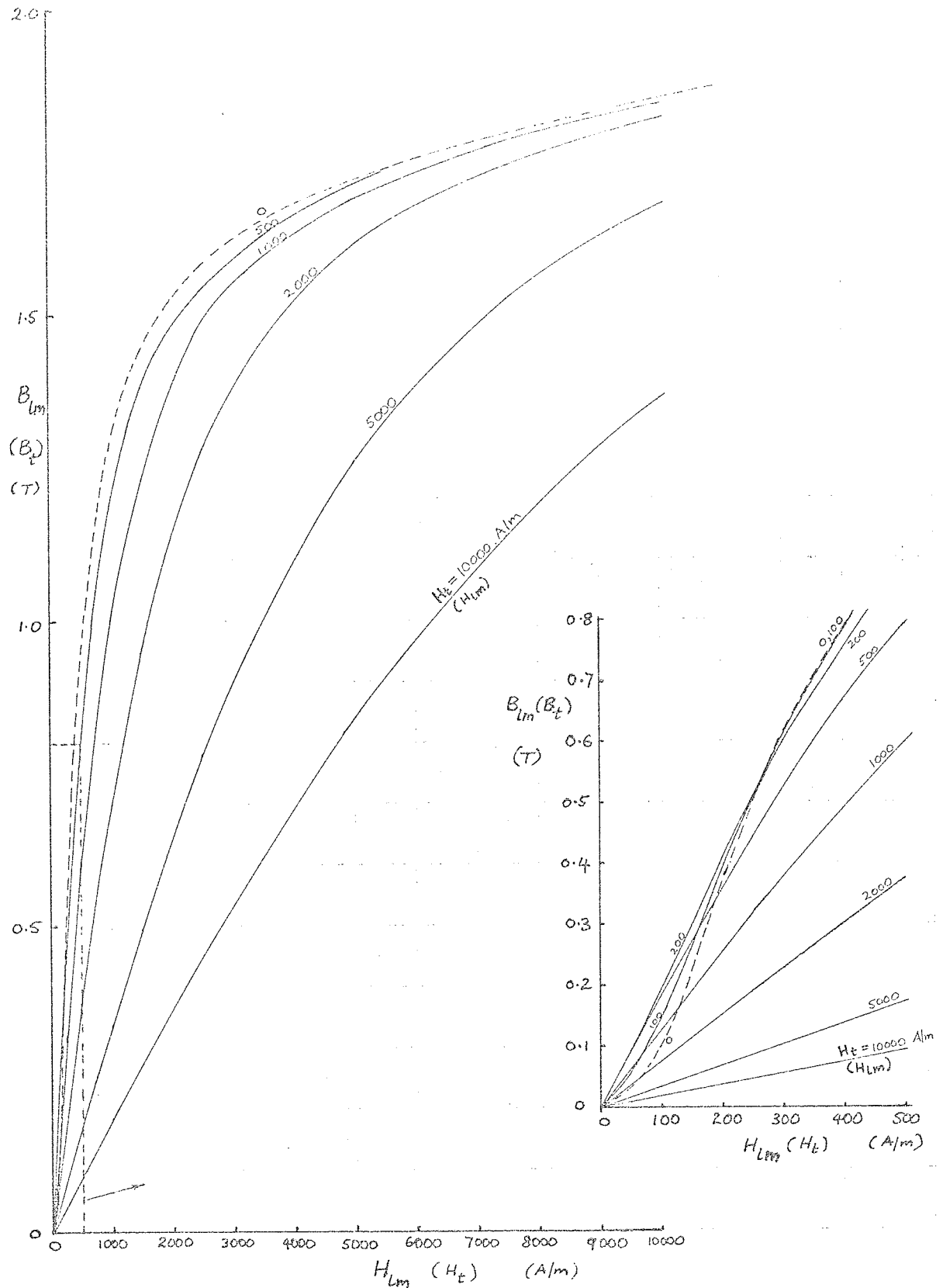 $90^\circ + \psi = 151^\circ$ $90^\circ + \psi = 124^\circ$

Fig. 8.5 Calculated magnetisation curves with a superposed perpendicular steady field for EN1A steel

B_{lm}, H_{lm} = peak values of reversing longitudinal field

H_t = field strength of transverse field when longitudinal field is at its peak

The curves may also be used to give B_t corresponding to H_t for a given balue of H_{lm}, as indicated by the labels in brackets.
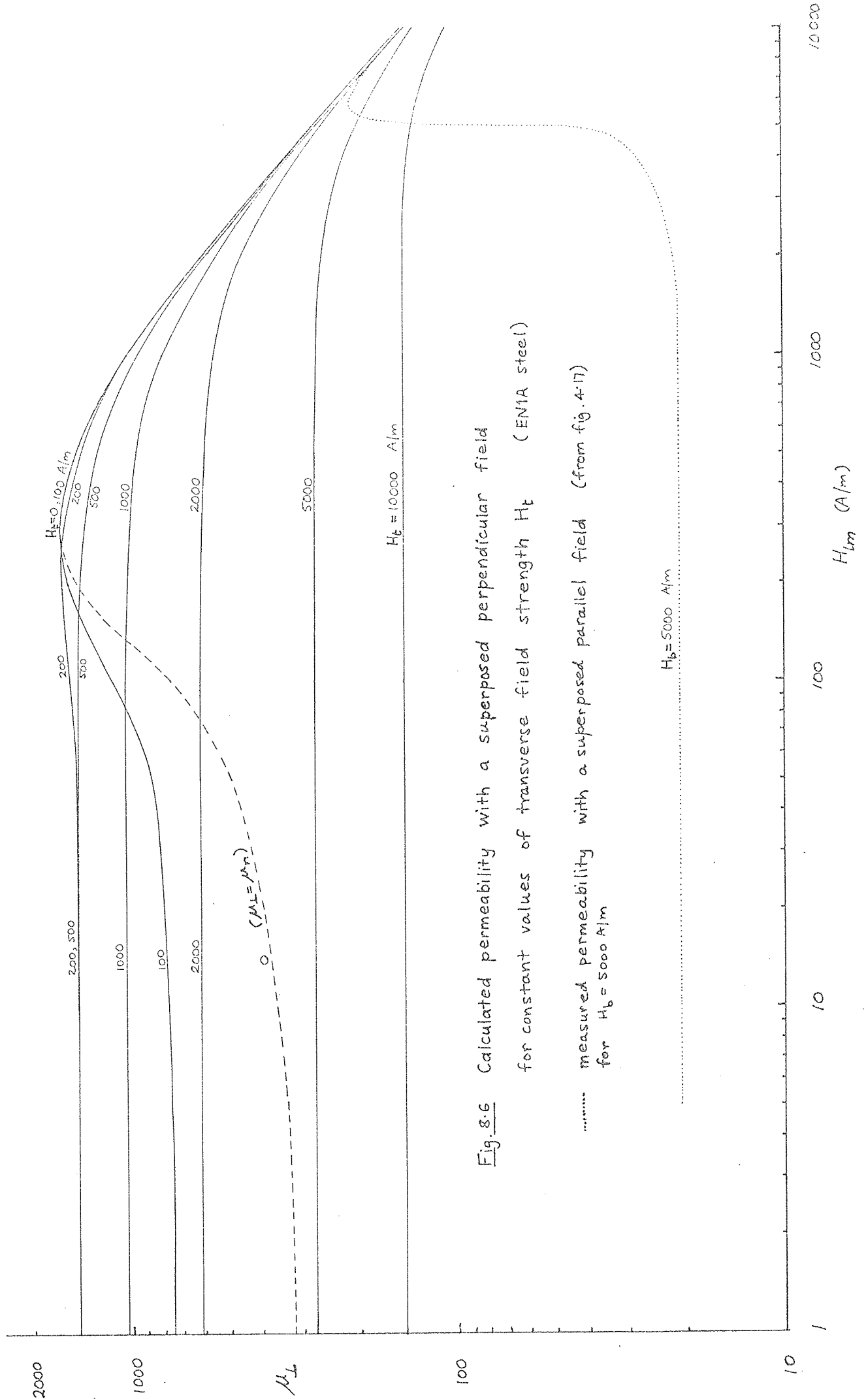
Fig. 8.6 Calculated permeability with a superposed perpendicular field
for constant values of transverse field strength H_t (EN1A steel)

——— measured permeability with a superposed parallel field   (from fig. 4·17)
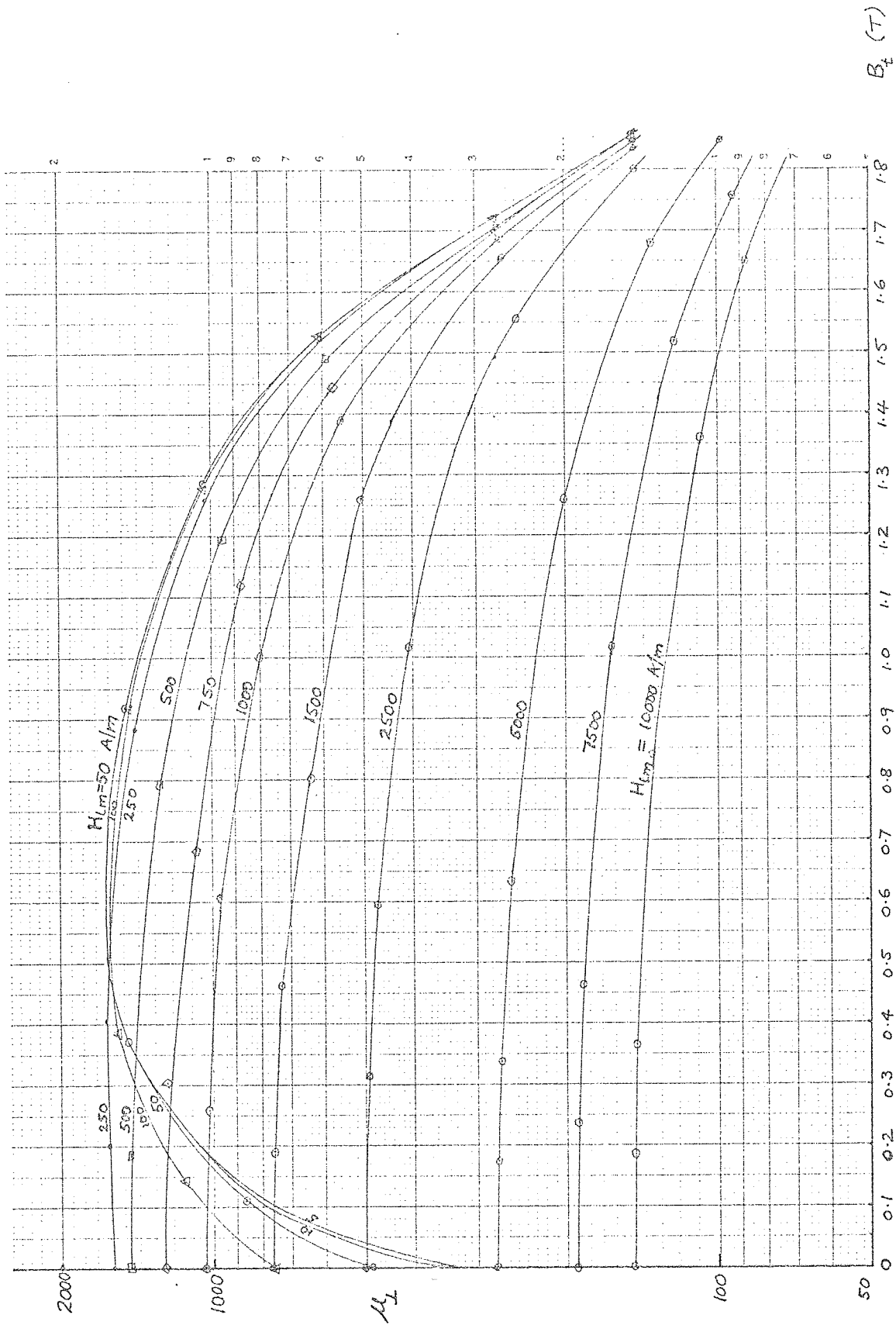for $H_b = 5000$ A/m

Fig. 8.7 Calculated permeability with a superposed perpendicular field as a function of transverse flux density B_t for several values of peak longitudinal field H_{lm} (EN1A steel)
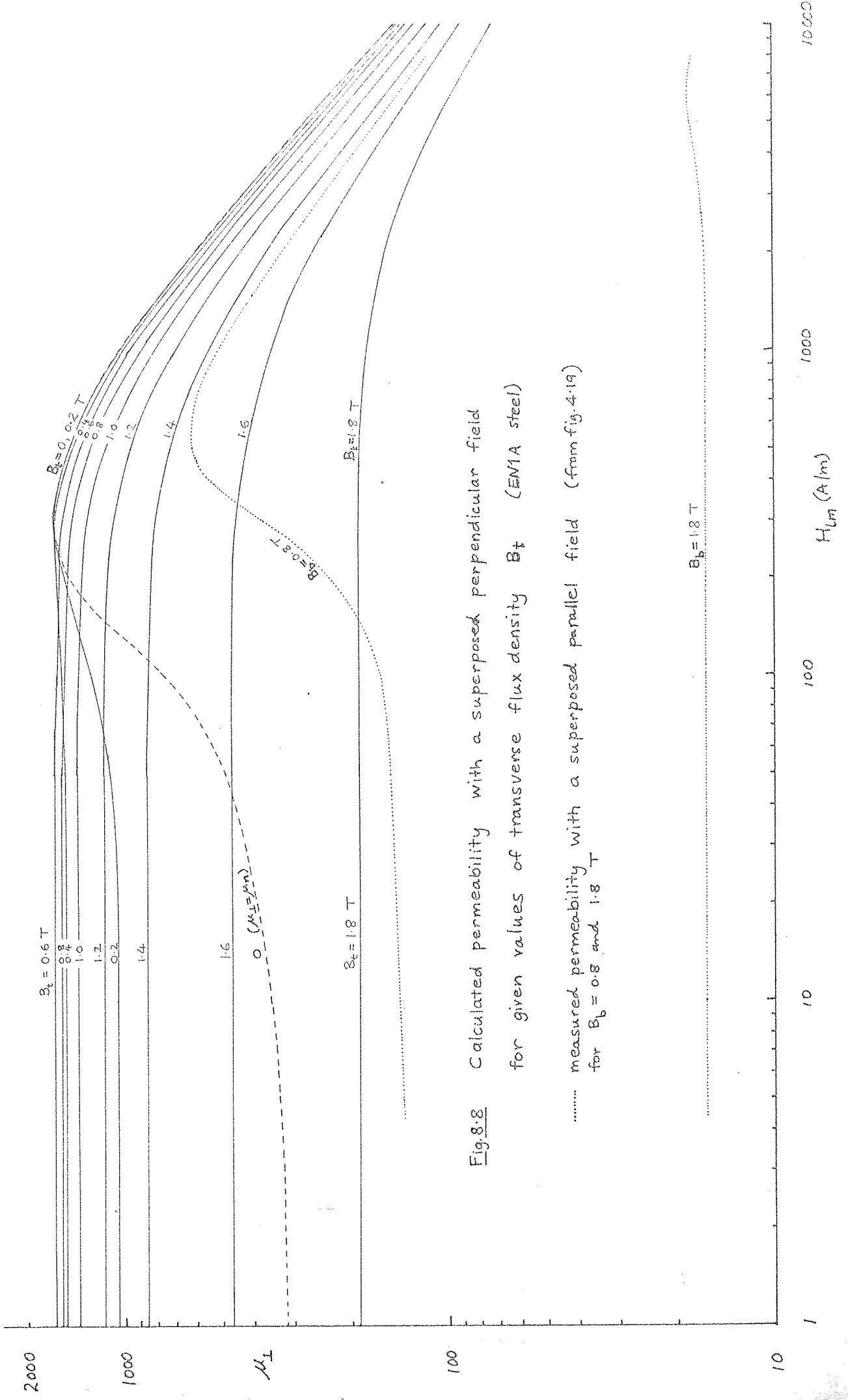
Fig. 8.8   Calculated permeability with a superposed perpendicular field

for given values of transverse flux density B_t (EM1A steel)

...... measured permeability with a superposed parallel field   (from fig. 4.19)

for $B_b = 0.8$ and 1.8 T